NEAR-INFRARED POLARIZATION OF ZODIACAL LIGHT OBSERVED BY FLYING OBJECTS TO STUDY INTERPLANETARY DUST

KWANSEI GAKUIN UNIVERSITY

DOCTORAL THESIS

NEAR-INFRARED POLARIZATION OF ZODIACAL LIGHT OBSERVED BY FLYING OBJECTS TO STUDY INTERPLANETARY DUST

Author:
Koji TAKIMOTO

Supervisor:
Prof. Doc. Shuji MATSUURA

A thesis submitted in fulfillment of the requirements for the degree of Doctor of Philosophy

in the

Shuji Matsuura Laboratory
Department of Physics

March 7, 2022

Declaration of Authorship

I, Koji TAKIMOTO, declare that this thesis titled, "NEAR-INFRARED POLARIZATION OF ZODIACAL LIGHT OBSERVED BY FLYING OBJECTS TO STUDY INTERPLANETARY DUST" and the work presented in it are my own. I confirm that:

- This work was done wholly or mainly while in candidature for a research degree at this University.
- Where any part of this thesis has previously been submitted for a degree or any other qualification at this University or any other institution, this has been clearly stated.
- Where I have consulted the published work of others, this is always clearly attributed.
- Where I have quoted from the work of others, the source is always given. With the exception of such quotations, this thesis is entirely my own work.
- I have acknowledged all main sources of help.
- Where the thesis is based on work done by myself jointly with others, I have made clear exactly what was done by others and what I have contributed myself.

Signed:

Date:

KWANSEI GAKUIN UNIVERSITY

Abstract

Graduate School of Science and Technology
Department of Physics

Doctor of Philosophy

NEAR-INFRARED POLARIZATION OF ZODIACAL LIGHT OBSERVED BY FLYING OBJECTS TO STUDY INTERPLANETARY DUST

by Koji TAKIMOTO

I report the first measurement of the zodiacal light (ZL) polarization spectrum in the near-infrared between 0.8 and 1.8 μm. Using the low-resolution spectrometer (LRS) on board the Cosmic Infrared Background Experiment ($CIBER$), calibrated for absolute spectrophotometry and spectropolarimetry, we acquire long-slit polarization spectral images of the total diffuse sky brightness toward five fields. To extract the ZL spectrum, we subtract the contribution of other diffuse radiation, such as the diffuse galactic light (DGL), the integrated star light (ISL), and the extragalactic background light (EBL). The measured ZL polarization spectrum shows little wavelength dependence in the near-infrared, and the degree of polarization clearly varies as a function of the ecliptic coordinates and solar elongation. Among the observed fields, the North Ecliptic Pole shows the maximum degree of polarization of $\sim 20\%$, which is consistent with an earlier observation from the Diffuse Infrared Background Experiment ($DIRBE$) aboard on the Cosmic Background Explorer ($COBE$). I also report the ZL polarization maps in the near-infrared bands at 1.25, 2.2, and 3.5 μm observed by $DIRBE$. I report the first new results on the dependence on ecliptic latitude, solar elongation, and wavelength. The measured degree of polarization and its solar elongation dependence are reproduced by the empirical scattering model in the visible band and also by an Mie scattering model for large absorptive particles, while a Rayleigh scattering model is ruled out. The wavelength dependence of the ZL polarization in wide wavelength range including the visible band is similar to that of comet, although further data are needed to constrain the compositions. The ZL brightness is also explained by large absorbing particles. All of these results suggest that the interplanetary dust is dominated by large particles.

Acknowledgements

I am very grateful to my supervisor Dr. Shuji Matsuura, for giving me a great opportunity to study the infrared astronomy. His dedication and support has helped me a lot not only in this thesis but also in many other challenges. I am proud to be a part of your laboratory. I am also grateful to him for inviting me to the *CIBER*-2 project and for his valuable guidance throughout my research activities.

I thank Dr. Toshiaki Arai (Hanazono) for the raw *CIBER*-1 data, and Dr. Kohji Tsumura, Dr. Kei Sano, and Dr. Aoi Takahashi for their discussions on the polarization observations of the *CIBER*-1 project. I would also like to thank Dr. James J. Bock, Dr. Michael Zemcov, Dr. Asantha Cooray, Dr. Phillip M. Korngut, Dr. Chi H. Nguyen, and Mr. Richard M. Feder for their help and support.

I would like to thank the members of *CIBER*-2 for their great support. Although there were many difficulties to reach the first launch, I am very proud of the fact that we were able to accomplish the launch with a total of about 50 wonderful people, and it will be an event I will never forget.

I wish to thank my colleagues in the Matsuura Laboratory for their support. I have wonderful memories of my time in the laboratory with about 50 people, all of which are nostalgic and all of which come back to me vividly.

I would like to thank NASA and the Space Telescope Science Institute for producing the photograph of the zodiacal light and allowing me to use it.

I would like to thank the most important people in my life, my parents and my brother.

This thesis is reviewed by Dr. Masumichi Seta, Dr. Junko Hiraga, Dr. Takafumi Ootsubo, and Dr. Shuji Matsuura.

Contents

List of Figures

List of Tables

List of Abbreviations

CIBER	**C**osmic **I**nfrared **B**ackground **E**xpe**R**iment
CIO	**C**alibrated **I**ndividual **O**bservations
COBE	**CO**smic **B**ackground **E**xplorer
CSC	*COBE* Quadrilaterilized **S**pherical **C**ube
DGL	**D**iffuse **G**alactic **L**ight
DIRBE	**D**iffuse **I**nfra**R**ed **B**ackground **E**xpepiment
EBL	**E**xtragalactic **B**ackground **L**ight
FIRAS	**F**ar **I**nfra**R**ed **A**bsolute **S**pectrophotometer
FOV	**F**ield **O**f **V**iew
IPD	**I**nter**P**lanetary **D**ust
IRAS	**I**nfra**R**ed **A**stronomical **S**atellite
IRC	**I**nfra**R**ed **C**amera
IRTS	**I**nfra**R**ed **T**elescope in **S**pace
ISL	**I**ntegrated **S**tar **L**ight
JFC	**J**upiter-**F**amily **C**omet
JFET	**J**unction **F**ield **E**ffect **T**ransistor
LRS	**L**ow-**R**esolution **S**pectrometer
NaN	**N**ot **a** **N**umber
NEP	**N**orth **E**cliptic **P**ole
NIRS	**N**ear **I**nfra**R**ed **S**pectrometer
SAA	**S**outh **A**tlantic **A**nomaly
SCL	**S**uper-**C**ontinuum **L**aser
SIRCUS	**S**pectral **I**rradiance and **R**adiance responsivity **C**alibrations using **U**niform **S**ources
2MASS	**2(Two)** **M**icron **A**ll-**S**ky **S**urvey
ZL	**Z**odiacal **L**ight

Chapter 1

Introduction

1.1 ZODIACAL LIGHT

Zodiacal light (ZL) arises from sunlight scattered by the interplanetary dust (IPD) in the optical and near-infrared (< 3 μm), and from thermal emission from the IPD in the mid- and far-infrared (> 3 μm). Figure 1.1 shows the ZL and the Milky Way. At lower left, a glowing patch extends to the upper right in the direction of Jupiter, the bright object left of center. The ZL is brighter as the observer looks along the ecliptic and closer to the Sun. Measuring the ZL is important to understand the structure of the IPD's distribution and the physical properties of the IPD, such as its size distribution, composition, shape, and complex refractive index. In addition, the information obtained from the ZL measurement is important for future studies of the dust disks of exoplanetary systems. Most of the ZL's brightness is from the IPD, with typical dust grain sizes from 1 to 100 μm, probably even less than 1 μm (Grun et al., 1985; Reach, 1988). Because the IPD grains of these sizes fall into the Sun due to Poynting-Robertson drag (Burns, Lamy, and Soter, 1979) within the age of the solar system, IPD dating to the early solar system is unlikely to exist today. Wyatt and Whipple (1950) found that all particles with a radius ≤ 1 cm, which were initially in a sphere with a radius of 1 au centered on the Sun, fall into the Sun within a period of 28 million years. Therefore, a continuous supply of IPD particles is necessary to maintain the zodiacal cloud.

Early studies of the ZL were motivated by the need to better understand the environment of solid matter surrounding the Earth, as well as by the fact that the ZL was a source of noise when studying faint and extended objects. The integrated brightness of the night sky includes the ZL, airglow, the integrated star light (ISL), the diffuse galactic light (DGL), and the extragalactic background light (EBL). Long-term surveys can isolate these different signal sources and extract their individual components. Cassini (1685) observed the visual pattern of night-sky brightness and first formulated the hypothesis of the IPD cloud. The spectra of these diffuse radiation are shown in Figure 1.2. In the visible part of the spectrum, the ZL shows a solar spectrum.

The ZL intensity depends on the observer's position in the Earth's orbit, the wavelength, and the direction from which the observer views the Sun. The IPD distribution is basically plane symmetric with respect to the ecliptic plane, although the Helios probes measurements between the orbits of the Earth and Venus indicate that it is inclined by $\sim 3^\circ$ from the ecliptic plane (Leinert et al., 1980). Figure 1.3 shows the ZL geometry of observation in helio-ecliptic coordinates. It is important to keep in mind that the ZL intensity observed in one direction corresponds to that integrated along the line of sight. According to Kelsall et al. (1998), the ZL intensity I_λ from sunlight scattered by the IPD observed at wavelength λ as the integral along

FIGURE 1.1: This very wide, multi-frame panorama was taken in October 2014 at Canyon de Chelly National Monument in northeast Arizona. The ZL is at left, with the northern Milky Way to the right. The Orion constellation is at top right. Jupiter is the brighter object left of center, while a similarly bright object to the right (below Orion) is Sirius. M44 (the Praesepe Cluster) is just above Jupiter. On the horizon, a yellow glow marks the location of the nearby town of Chinle, Arizona. (IMAGE: Zolt Levay Photography)

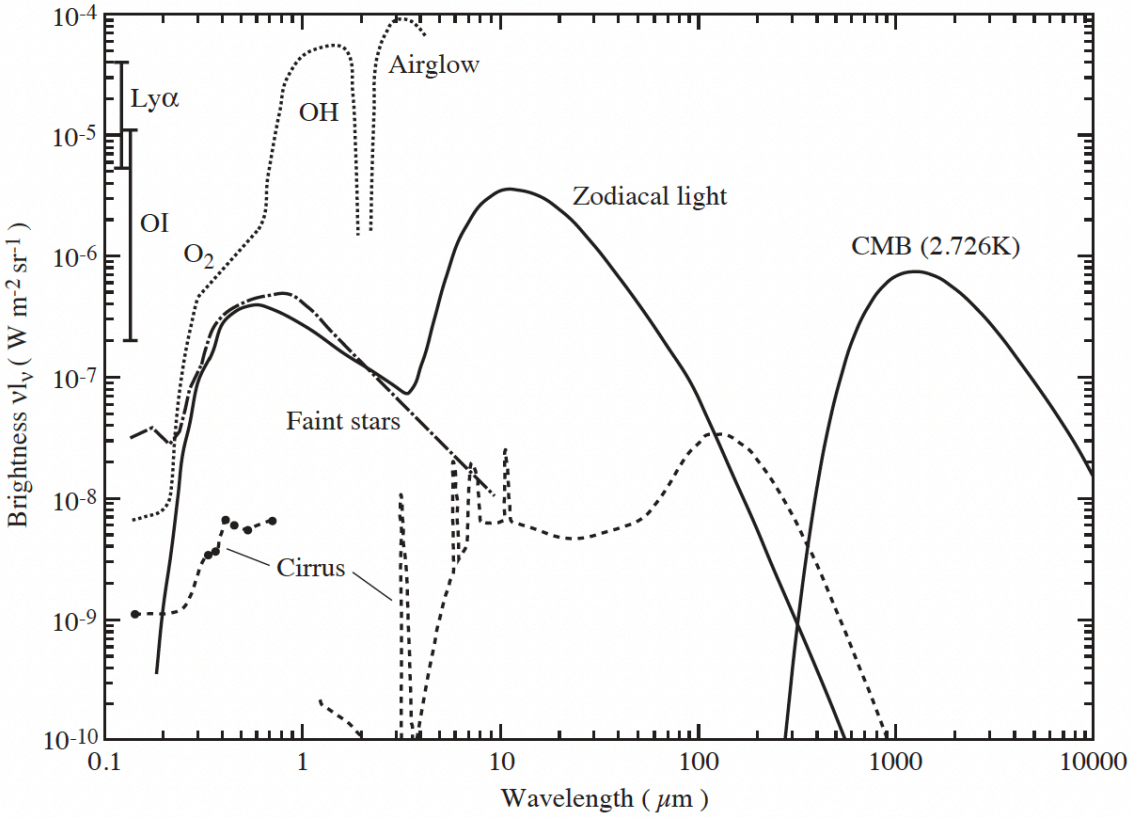

FIGURE 1.2: Overview on the brightness of the sky outside the lower terrestrial atmosphere and at high ecliptic and galactic latitudes. The zodiacal emission and scattering as well as the ISL are given for the South Ecliptic Pole ($l = 276°$, $b = -30°$). The bright magnitude cut-off for the stellar component is $V = 6.0$ mag for $0.3 - 1$ μm. In the infrared, stars brighter than 15 Jy between 1.25 and 4.85 μm and brighter than 85 Jy at 12 μm are excluded. No cut-off was applied to the ultraviolet data, $\lambda \leq 0.3$ μm. interstellar cirrus component is normalized for a column density of 10^{20} H-atoms cm^{-2} corresponding to a visual extinction of 0.053 mag. This is close to the values at the darkest patches in the sky. Source for the long-wavelength data, $\lambda \geq 1.25$ μm, are *COBE*/*DIRBE* and *COBE*/Far Infrared Absolute Spectrophotometer (*FIRAS*) measurements as presented by Désert et al. (1996). The IR cirrus spectrum is according to the model of Desert, Boulanger, and Puget (1990) fitted with Infrared Astronomical Satellite (*IRAS*) photometry. The short-wavelength data, $\lambda \leq 1.0$ μm, are from the following sources: ZL: Leinert and Grün (1990); ISL: $\lambda \leq 0.3$ μm, Gondhalekar (1990), $\lambda \geq 0.3$ μm, Mattila (1980); cirrus: $\lambda = 0.15$ μm, Haikala et al. (1995), $\lambda = 0.35 - 0.74$ μm, Mattila (1990), Mattila (1979). The geocoronal Lyman α (121.6 nm) and the OI (130.4, 135.6 nm) line intensities were as measured with the Faint Object Camera of the Hubble Space Telescope at a height of 610 km (Caulet, Hook, and Fosbury, 1994).

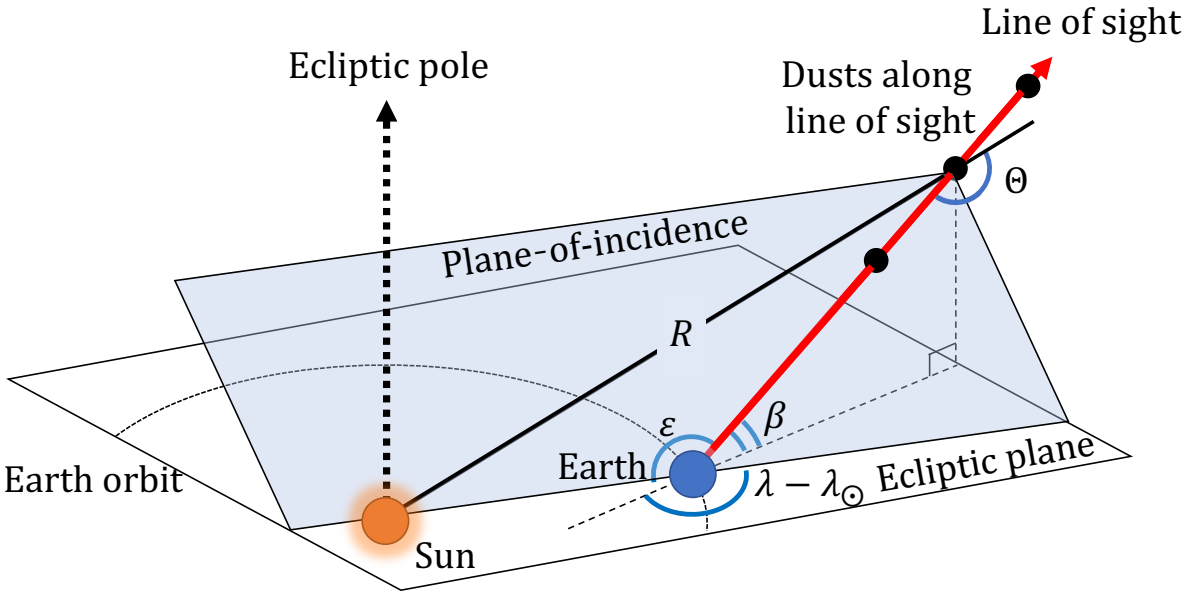

FIGURE 1.3: Basic geometry of the ZL observation with respect to the ecliptic latitude β and the helio-ecliptic longitude $(\lambda - \lambda_{\odot})$, where λ is the ecliptic longitude and $\lambda_{\odot}$ is ecliptic longitude of the Sun. The red arrow represents the line of sight from the Earth toward the IPD grain. The radial distance from the grain to the Sun is denoted by R, and the solar elongation is indicated by ϵ. The scattering angle is denoted by Θ.

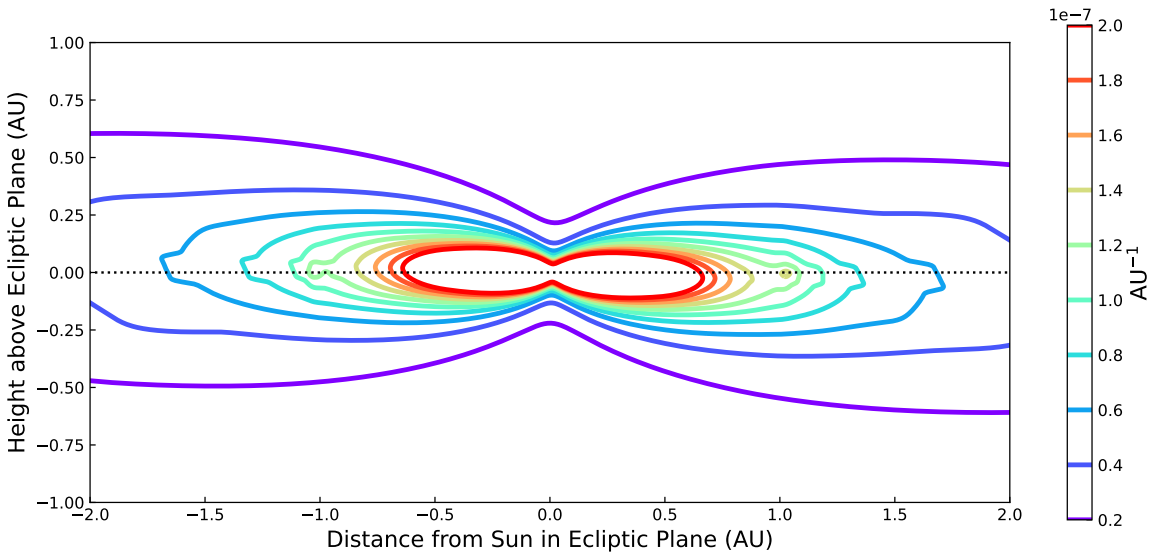

FIGURE 1.4: Three-dimensional density of the IPD. Isodensity contours of the IPD model components, shown for a cross-sectional slice perpendicular to the ecliptic plane: all components combined.

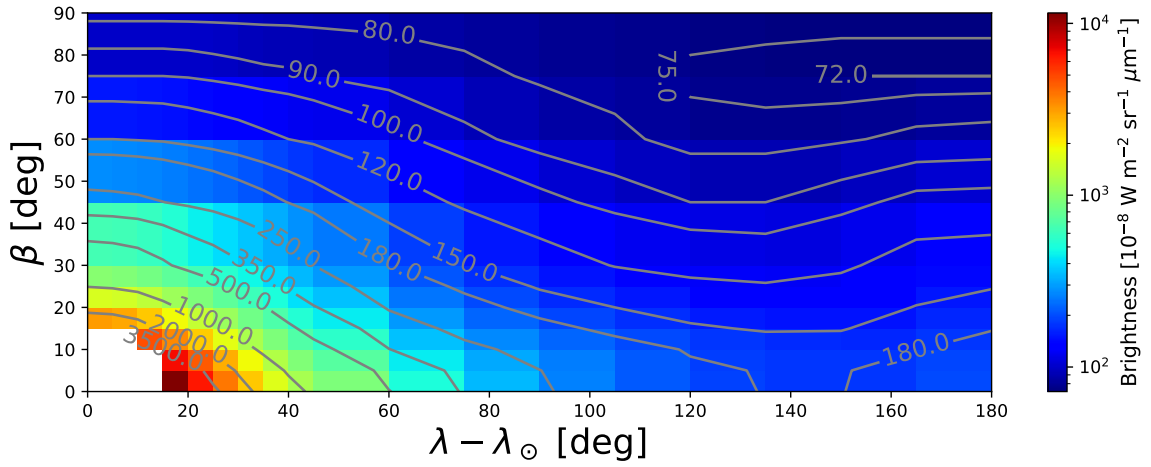

FIGURE 1.5: ZL brightness averaged over a year observed from the Earth at 500 nm (Levasseur-Regourd, 1996; Leinert et al., 1998).

the line of sight s is expressed as:

$$I_\lambda = \int n(X,Y,Z) A_\lambda F_\lambda^\odot \Phi_\lambda(\Theta) ds,$$

where $n(X,Y,Z)$ is the three-dimensional density of the IPD, A_λ is the albedo at wavelength λ, $F_\lambda^\odot$ is the solar flux, $\Phi_\lambda(\Theta)$ is the phase function at scattering angle Θ. Figure 1.4 shows the density distribution of the IPD determined by this method. The details of the physical IPD model are shown in Appendix A. Figure 1.5 shows average ZL brightness observed from the earth at a wavelength of 500 nm for a year (Levasseur-Regourd, 1996; Leinert et al., 1998). Towards the ecliptic pole, the brightness as given above is 7.7×10^{-7} W m^{-2} sr^{-1} μm^{-1}. The maximum brightness in the ecliptic plane is 1.2×10^{-4} W m^{-2} sr^{-1} μm^{-1} at $\lambda - \lambda_\odot = 15°$, and the minimum brightness is 1.8×10^{-6} W m^{-2} sr^{-1} μm^{-1} at $\lambda - \lambda_\odot = 135 \sim 150°$.

1.2 POLARIMETRIC PROPERTIES

If the incident light is 100% polarized, the scattered light will be polarized in the same way. However, since light in two different polarization states is scattered differently, if the incident light is unpolarized, the scattered light will be partially polarized. The ZL scattered by an optically thin cloud of IPDs presents a systematic polarization because Sunlight is natural light and is not polarized. The linear polarization P of sunlight scattered by IPD surfaces is usually defined differences between the intensities polarized along the planes perpendicular, $I_\perp$, and parallel, $I_\parallel$, to the scattering plane:

$$P = \frac{I_\perp - I_\parallel}{I_\perp + I_\parallel}.$$

where the degree of polarization of the scattered light, given incident unpolarized light, is $|P|$. A few studies report polarization measurements of the ZL. Leinert et al. (1998) summarized the ZL polarization measured from space in the visible and the near-infrared, and the degree of polarization is largely dependent on the helio-ecliptic longitude to first order. Figure 1.6 shows the ZL polarizaton observed from

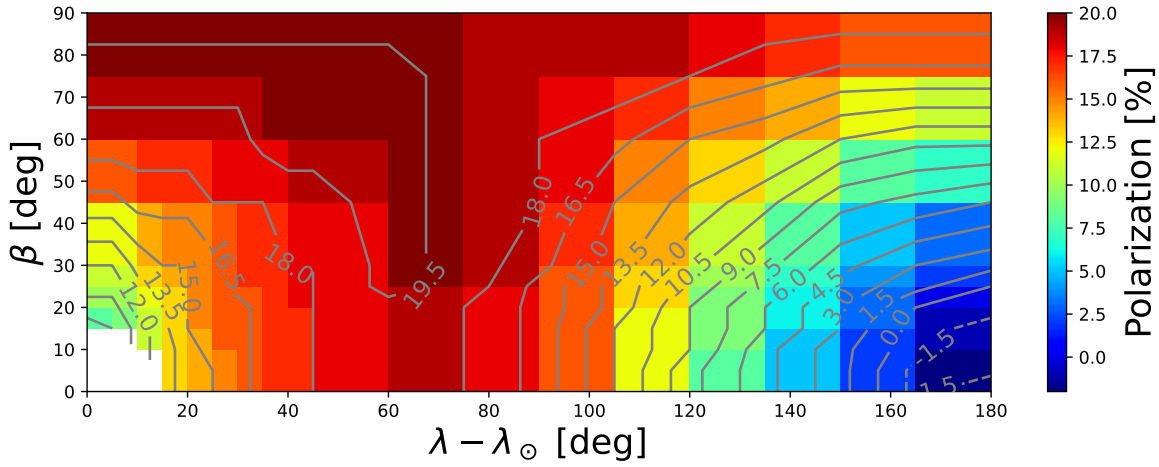

FIGURE 1.6: ZL polarization observed from the Earth at 500 nm (Levasseur-Regourd, 1996; Leinert et al., 1998). Positive values correspond to a direction of polarisation (E vector) perpendicular to the scattering plane (Sun-Earth-scattering particles), negative values correspond to a direction of the polarisation in the scattering plane. The negative values noticed in the Gegenschein region ($\lambda - \lambda_\odot = 180°$, $\beta = 0°$) correspond to a parallel component greater than the perpendicular component, as expected for the scattering by irregular particles at small phase angles.

the Earth at 500 nm. At visible wavelengths, integrated line of sight polarization on the sky varies from -3% to +20% depending on the elevation and azimuth of observation, and shows little wavelength dependence (Weinberg and Hahn, 1980; Pitz et al., 1979; Leinert and Blanck, 1982). In the near-infrared, only Berriman et al. (1994) has measured the polarization of the ZL from space by the Diffuse Infrared Background Experiment (*DIRBE*) aboard on the Cosmic Background Explorer (*COBE*) in discrete photometric bands at 1.25, 2.2, and 3.5 μm. This result shows that the degree of polarization of the ZL is about 10 $\sim$ 20% at solar elongation ϵ = 90°, and tends to decrease toward longer wavelengths.

1.3 SCATTERING PROPERTIES

The scattering function depends mainly on the size, complex refractive index, and shape of the IPD particles.

First, the general relationship between the scattering function and the size of the dust particle is well known (Bohren and Huffman, 1983). The size of a scattering particle is often parameterized by the ratio

$$x = \frac{2\pi r}{\lambda},$$

where r is the particle's radius, λ is the wavelength of the light, and x is a dimensionless parameter that characterizes the particle's interaction with the incident radiation. The Rayleigh scattering applies to the case when the scattering particle is very small ($x \ll 1$, with $r < 0.1\lambda$) and the whole surface reradiates with the same

phase. The Rayleigh scattering theory defines the degree of polarization as

$$P = \frac{1 - \cos^2 \Theta}{1 + \cos^2 \Theta}.$$

Since P is always positive, the scattered light will be partially polarized in the direction perpendicular to the scattering plane. If a sphere of sufficient size is irradiated with unpolarized light, the scattered light will be 100% polarized at a scattering angle of 90°. Figure 1.7 shows the Rayleigh scattering at different size parameters: assuming that x is sufficiently small compared to λ, the unpolarized scattering intensity is inversely proportional to the fourth power of the wavelength of the incident light, and the degree of polarization does not change. Figure 1.8 shows the polarization characteristics in Rayleigh scattering theory. At the intermediate $x \approx 1$ of Mie scattering, interference effects develop through phase variations over the object's surface. The Mie scattering theory defines the degree of polarization as

$$P = \frac{|S_1(\mu)|^2 - |S_2(\mu)|^2}{|S_1(\mu)|^2 + |S_2(\mu)|^2},$$

$$S_1(\mu) = \sum_{n=1}^{\infty} \frac{2n+1}{n(n+1)} (a_n(m,\ x)\pi_n(\mu) + b_n(m,\ x)\tau_n(\mu)),$$

$$S_2(\mu) = \sum_{n=1}^{\infty} \frac{2n+1}{n(n+1)} (a_n(m,\ x)\tau_n(\mu) + b_n(m,\ x)\pi_n(\mu)),$$

where S_1 and S_2 are complex amplitude functions, $\mu = \cos\theta$, a_n and b_n are Mie coefficients, and π_n and τ_n are angular-dependent functions. m $(= m_1 + im_2)$ is its complex refractive index relative to that of the surrounding medium. Figure 1.9 shows the Mie scattering at different particles: refractive material $(m = 2.0 + 0.03i)$ and absorptive material $(m = 3.0 + 2.0i)$ with the same size parameter $x = 1$. Figure 1.10 shows the polarization characteristics in Mie scattering theory with absorbing particles. An object with $x \gg 1$ scatters light according to its projected area, based on geometrical optics scattering. The geometrical optics scattering theory defines the degree of polarization as

$$P = \frac{R_\parallel - R_\perp}{R_\parallel + R_\perp},$$

$$R_\parallel = \left(\frac{\cos\Theta_t - m\cos\Theta_i}{\cos\Theta_t + m\cos\Theta_i} \right)^2,$$

$$R_\perp = \left(\frac{\cos\Theta_i - m\cos\Theta_t}{\cos\Theta_i + m\cos\Theta_t} \right)^2,$$

where $R_\parallel$ and $R_\perp$ are the reflectances for the two polarization states of the incident light. i and t indicate incident and transmission, respectively. m $(= m_1 + im_2)$ is its complex refractive index relative to that of the surrounding medium. Figure 1.11 shows the polarization characteristics in geometric optics scattering theory with absorbing particles.

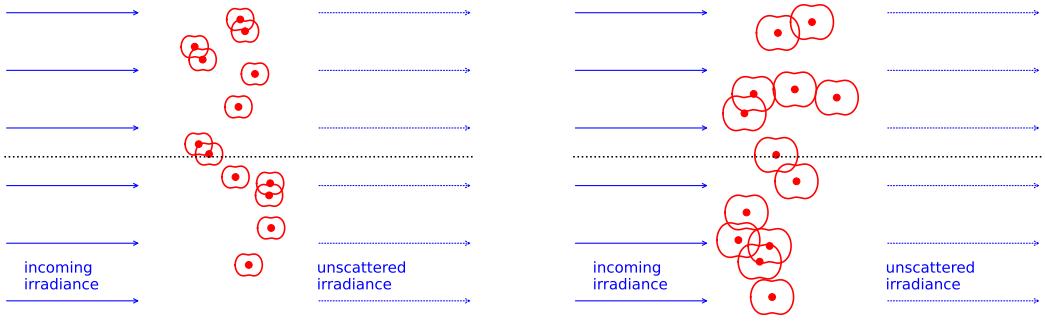

(A) $x = 0.005,\ m = 1.5 + 10^{-8}i$ (B) $x = 0.010,\ m = 1.5 + 10^{-8}i$

FIGURE 1.7: The Rayleigh scattering at different size parameters.

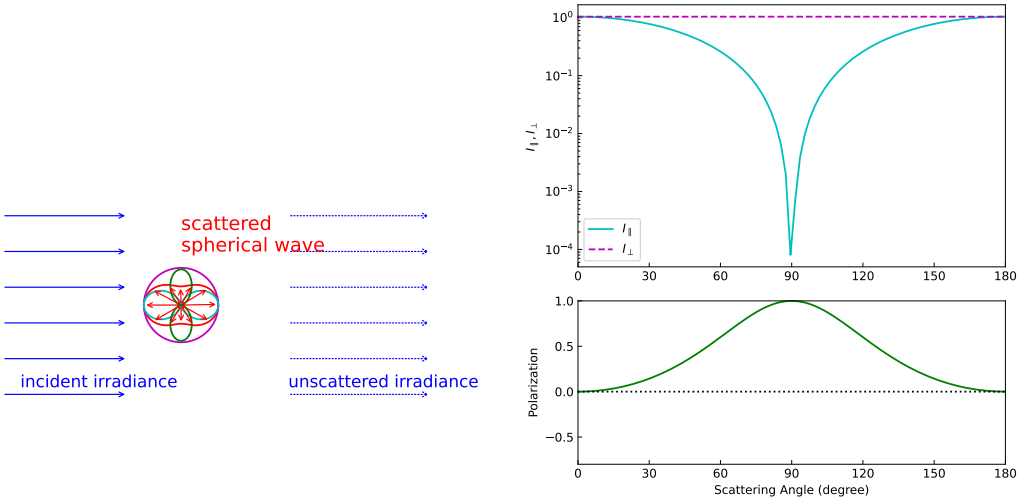

(A) Scattering pattern (B) The polarized intensities $I_{\perp}$, $I_{\parallel}$ and polarization P as a function of the scattering angle

FIGURE 1.8: Polarization characteristics in Rayleigh scattering theory.

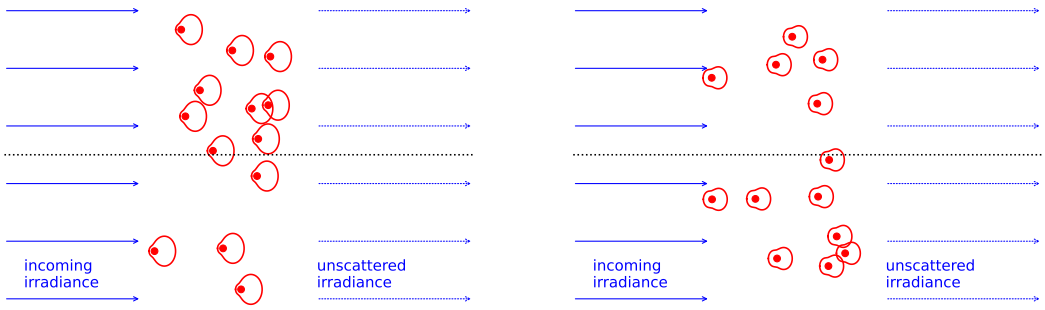

(A) $x = 1,\ m = 2.0 + 0.03i$ (B) $x = 1,\ m = 3.0 + 2.0i$

FIGURE 1.9: The Mie scattering at different particles.

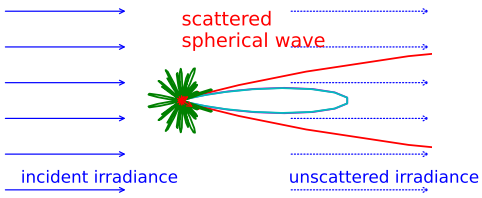

(A) Scattering pattern

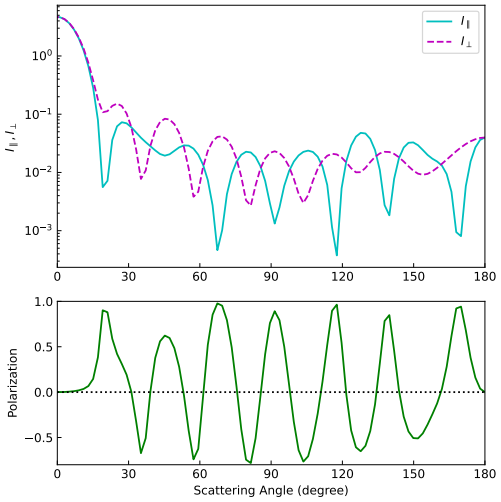

(B) The polarized intensities $I_\perp$, $I_\parallel$ and polarization P as a function of the scattering angle

FIGURE 1.10: Polarization characteristics in Mie scattering theory with absorbing particles.

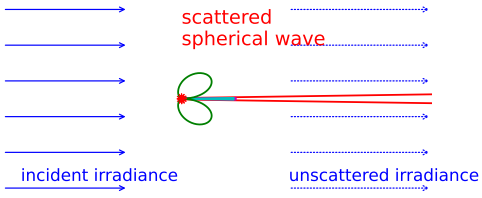

(A) Scattering pattern

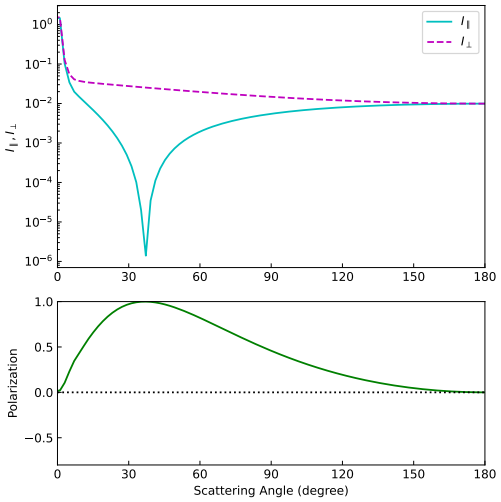

(B) The polarized intensities $I_\perp$, $I_\parallel$ and polarization P as a function of the scattering angle

FIGURE 1.11: Polarization characteristics in geometric optics scattering theory with absorbing particles.

1.4 ON THE ORIGINS OF INTERPLANETARY DUST PARTICLES

The intensity and polarization phase curve can be compared with numerical and experimental simulations to estimate the physical properties of the scatterer. The source of the IPD is assumed to comprise both comets and asteroids, but the relative importance of each has not been settled. Interstellar dust also contributes to the IPD at a level estimated to be less than 10% (Srama et al., 2011; Rowan-Robinson and May, 2013). According to findings from astronomical observations, IPD particles are made up of silicate and carbon compounds. In other words, the optical index of IPD can be both high in light absorption, as in carbonaceous compounds, and low, as in silicates.

Giese et al. (1978)'s model calculations and microwave analog measurements indicate that absorbing particles with fluffy structures may be an important component of IPD clouds. The properties of the ZL are consistent with a mixture of irregular fluffy particles and compact particles formed of silicates and carbonaceous materials. These properties are consistent with the properties of the IPD collected in the stratosphere (Flynn, Nittler, and Engrand, 2016). Nesvorný et al. (2010) and Nesvorný et al. (2011) compared their dynamical simulations of the IPD with data from *IRAS*, suggesting that 85 $\sim$ 95% of the observed mid-infrared emission is produced by particles from Jupiter-family comets (JFCs) and $<$ 10% by dust from long-period comets. Fernández et al. (2006) showed that the geometric albedo of the nucleus of comet 162P/Siding Spring (P/2004 TU_{12}), which has the largest radii known among JFCs, is 0.059 ± 0.023 in the H band, 0.037 ± 0.014 in the R band, and 0.034 ± 0.013 in the V band. Soderblom et al. (2002) also observed the nucleus of JFC 19P/Borrelly and derived a geometric albedo of 0.03 ± 0.05. IPD id also known to have a low albedo (Kelsall et al., 1998) and has similarities to the comet nucleus. Yang and Ishiguro (2015) derived the spectral gradient of IPD as $S' = 8.5 \pm 1.0\%/100$ nm at 460 nm and, combining with the albedo, showed that $>$ 90% of the IPD originates from comets or D-type asteroids. The ZL spectra measured by the Near Infrared Spectrometer (NIRS) on board the Infrared Telescope in Space (IRTS) and the Cosmic Infrared Background Experiment (*CIBER*) show silicate-like features at 0.9 and 1.6 μm (Matsumoto et al., 1996; Tsumura et al., 2010), comparable to fresh and active comets or S-type asteroids. A combination of amorphous and crystalline silicate grain features is found in ZL spectrum between 9 and 11μm (Ootsubo et al., 1998; Reach et al., 2003; Ootsubo et al., 2009). Crystalline silicate features have been observed in comet C/1995 O1 Hale-Bopp (Wooden et al., 1999; Wooden et al., 2000). Therefore, the silicate feature of the ZL has not been the key to determine the fraction of cometary and asteroid dusts in the IPD.

The polarization of ZL is another observable that can be used to probe the cause of IPD from the dust composition. Since the polarization properties of scattered light depend on the scattering angle and the composition of the IPD, the origin of the IPD can be investigated by the polarization spectrum of ZL at various fields. For example, the cometary dust ejected from comets is studied by polarization measurements. Zubko et al. (2014) studied dust in comet C/1975 V1 (West) and reproduced the polarization measurement by models with Mg-rich silicate and amorphous carbon. Lasue et al. (2009) also studied dust of comet C/1995 O1 Hale-Bopp and 1P/Halley based on the polarization measurement and implied that the cometary dust can be explained by mixture of a non-absorbing silicate-type material and a more absorbing organic-type material. As mentioned in Section 1.3, the polarization properties

of IPD vary with the size parameter and complex refractive index, so the size and composition of IPD particles can be studied by observing the polarization of ZL. In the *CIBER* experiment, we observed the polarization of ZL in the near-infrared region of 0.8-1.8 μm, where the scattering component of ZL is dominant, and used the polarization spectrum to constrain the properties of IPD, such as dust distribution, size, composition, and shape, in order to investigate the origin of IPD.

1.5 OUTLINE OF THIS THESIS

In this thesis, I report a ZL polarization-spectrum measurement from the Low Resolution Spectrometer (*LRS*) on board *CIBER* in Chapter 2. The purpose of polarization observation by the *LRS* was to separate polarized ZL from presumably unpolarized EBL, and to identify spectral features by studying the wavelength dependence of polarization. Our result is the first measurement of the ZL polarization spectrum in the near-infrared. Chapter 3 describes the ZL polarization in the near-infrared of the Weekly Sky Maps observed by *DIRBE*, one of the three instruments onboard the *COBE* satellite. This is the second time that the analysis of polarization observation data has been presented, after Berriman et al. (1994). I report the first new results on the dependence on ecliptic latitude, solar elongation, and wavelength. The size and composition of the IPD and future work are mentioned in Chapter 4. Summary of this thesis appears in Chapter 5.

Chapter 2

POLARIZATION SPECTRUM OF NEAR INFRARED ZODIACAL LIGHT OBSERVED WITH *LRS/CIBER*

2.1 OVERVIEW OF *LRS/CIBER*

CIBER, designed to study the diffuse near-infrared emission above the Earth's atmosphere (Zemcov et al., 2013), housed three instruments including a two broadband imagers (Bock et al., 2013), a narrowband spectrometer (Korngut et al., 2013), as well as the *LRS*, designed to measure the spectrum of diffuse light in $0.8 \leq \lambda \leq 1.8$ μm (Tsumura et al., 2013) with a wavelength resolution of $\lambda/\Delta\lambda = 15$-30. The fore optics of the *LRS* brings an image of the sky to focus on a mask containing five slits, as shown in Figure 2.1, each spanning a field of view (FOV) of $5^\circ \times 2.'7$ sampled by a 256×256 pixel HgCdTe array. This array hosts a cold-shutter assembly for dark-current measurement.

CIBER conducted observations four times, on 2009 February, 2010 July, 2012 March, and 2013 June. The payload was successfully recovered and refurbished after the first three flights. Because the polarizers were only installed in the third flight, we mainly use the third flight data in this paper. At the third flight, we used NASA Black Brant IX[1] two-stage vechicles launched from the White Sands Missile Range in New Mexico, USA. The apogee on the flight was 330km, providing a total exposure time of $\sim$ 240 s. The raw data, which are nondestructively sampled by the integrating detectors, were telemetered to the ground from the rocket during the flight. The celestial-attitude-control system achieved a pointing stability of $< 8''$. Details about the *CIBER* payload and flight performance are given in Zemcov et al. (2013); see Tsumura et al. (2013) and Arai et al. (2015) for details pertaining to the *LRS*.

To measure the polarization spectrum, we installed wire-grid polarization film [2] on the slit mask. Wire-grid polarization films with different transmittance axes were installed on eight different regions of the slit mask (Figure 2.1). Although the FOV of each polarizer is different, the ZL is smoothly distributed over the entire FOV and small field-to-field fluctuations, if any, can be corrected for. Therefore, if the ISL and DGL can be removed, ZL polarization can be measured with this instrument. The phase angles of the transmittance axis of the polarizer are labeled as $\theta = 0^\circ, 45^\circ, 90^\circ,$

[1] For details on the launch vehicles, see the Sounding Rocket Handbook (http://sites.wff.nasa.gov/code810/files/SRHB.pdf).

[2] Manufactured by Asahikasei E-materials corporation.

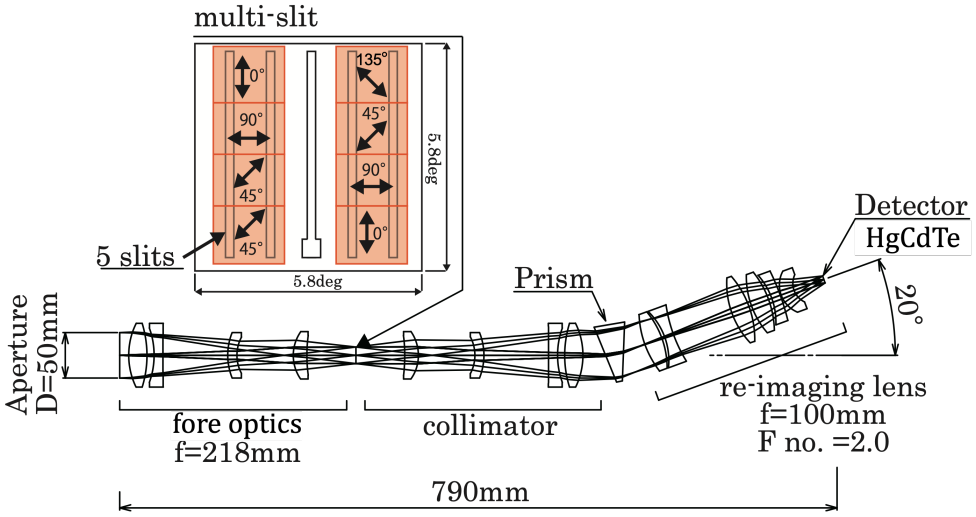

FIGURE 2.1: The *LRS* optics and wire-grid polarizing films. The *LRS* has five slits. A notch at the bottom of the center slit is for the focus adjustment experiments in the laboratory. The wire-grid polarizing films (orange) are installed on the slit mask except for the center slit. The transmittance axes are indicated by the black arrows. The direction of the transmittance axes are defined as $\theta = 0°, 45°, 90°$, and $135°$.

TABLE 2.1: Observed Fields of the *CIBER* Third Flight

Field Name	Exposure Time (s)	Payloads Altitude (km)	Ecliptic (λ, β) (deg)	Galactic (l, b) (deg)	Equatorial (α, δ) (deg)	Solar Elong. ϵ (deg)	ZL model $\lambda I_{\mathrm{ZL_{model}}}$ (nW m^{-2} sr^{-1})
Lockman Hole	47	202-265	(135.42, 45.49)	(149.41, 51.97)	(161.43, 58.21)	118.8	330.23
SWIRE/ELAIS-N1	45	284-315	(209.32, 72.32)	(84.31, 44.71)	(242.81, 54.59)	105.7	269.12
North Ecliptic Pole (NEP)	53	320-324	(311.48, 89.62)	(96.06, 29.56)	(270.63, 66.28)	90.0	280.55
Elat30 (β = 30 degree)	26	319-306	(234.38, 29.25)	(18.64, 44.89)	(236.98, 9.57)	124.1	403.53
BOOTES-B	50	296-244	(200.35, 44.82)	(55.13, 68.06)	(217.30, 33.27)	132.3	328.47

The coordinate systems are based on J2000.
The ZL brightness is estimated by using the ZL model (Kelsall et al., 1998) at 1.25 μm.

and 135° (Figure 2.1). The relative angles of the four *LRS* polarizers are determined with an accuracy of $\pm 0.°1$ and are taken into account when estimating the polarization bias. Note that the polarizing film in the lower left corner was mistakenly installed with the transmission axis rotated by 90° during the final installation, but it was calibrated and launched as it was. Because the polarizing films were not installed on the center slit, the total spectrum of the sky brightness was also measured.

The observed fields are listed in Table 2.1. For the ZL analysis, the fields are selected based on ecliptic coordinates and solar elongation. The low-ecliptic-latitude field, Elat30, shows high ZL brightness. On the other hand, the high-ecliptic-latitude fields exhibit low ZL brightness. The North Ecliptic Pole (NEP) field, where the solar elongation is 90°, is selected because the polarization is expected to be maximum. As the solar elongation increases, the polarization is expected to decrease.

2.2 BASIC DATA REDUCTION

At first, we make the *LRS* image from individual time-ordered array readout frames. In Figure 2.2, we give examples of the *LRS* images in the third flight. The five vertical

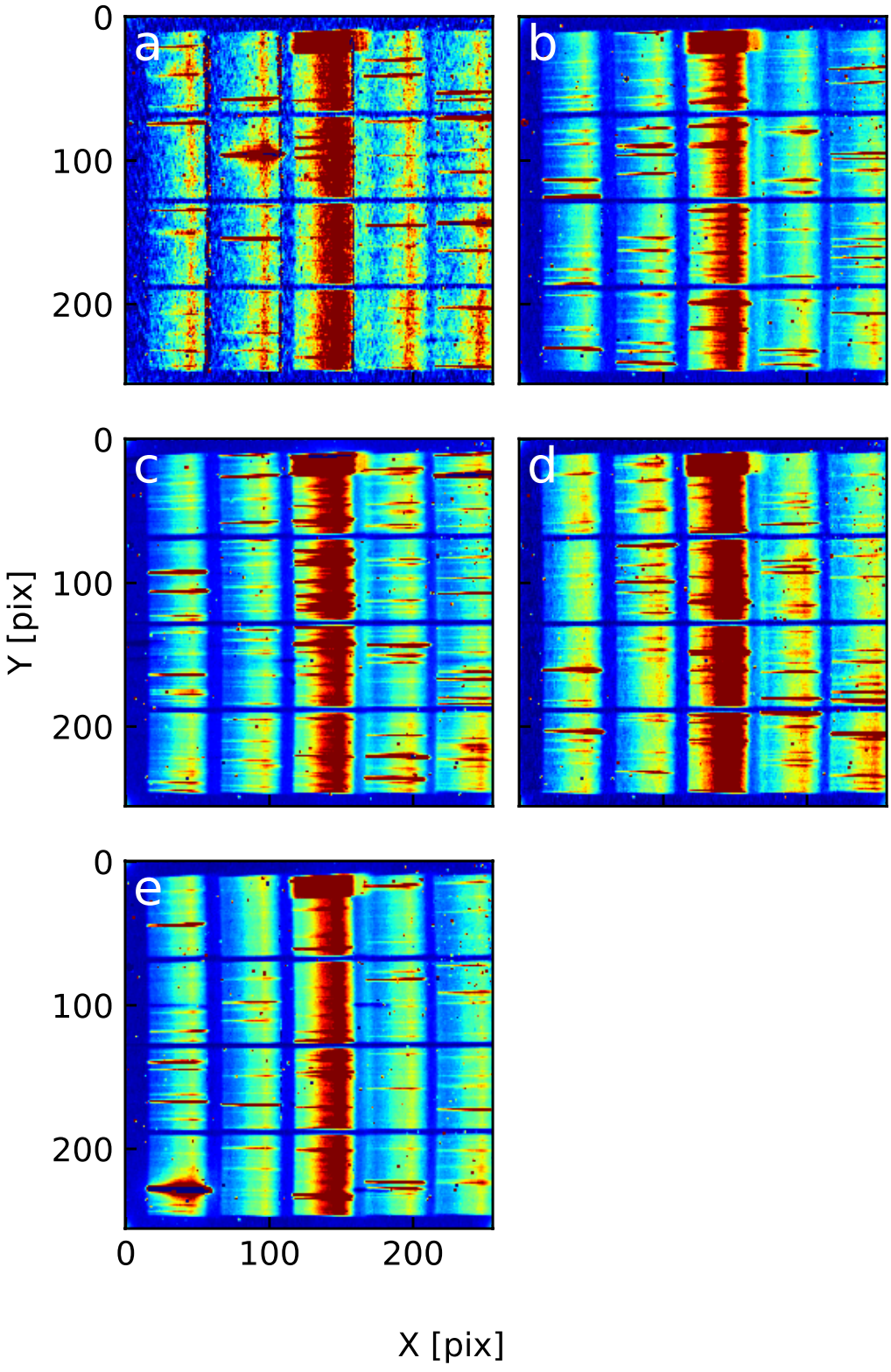

FIGURE 2.2: *LRS* raw images of the *CIBER* third flight in the photocurrent unit taken in each observation field (a: Lockman, b: SWIRE/ELAIS-N1, c: NEP, d: Elat30, e: BOOTES-B). The five vertical sections correspond to the images of the five slits dispersed toward the x-direction, and four parallel sections correspond to wire-grid polarizing films.

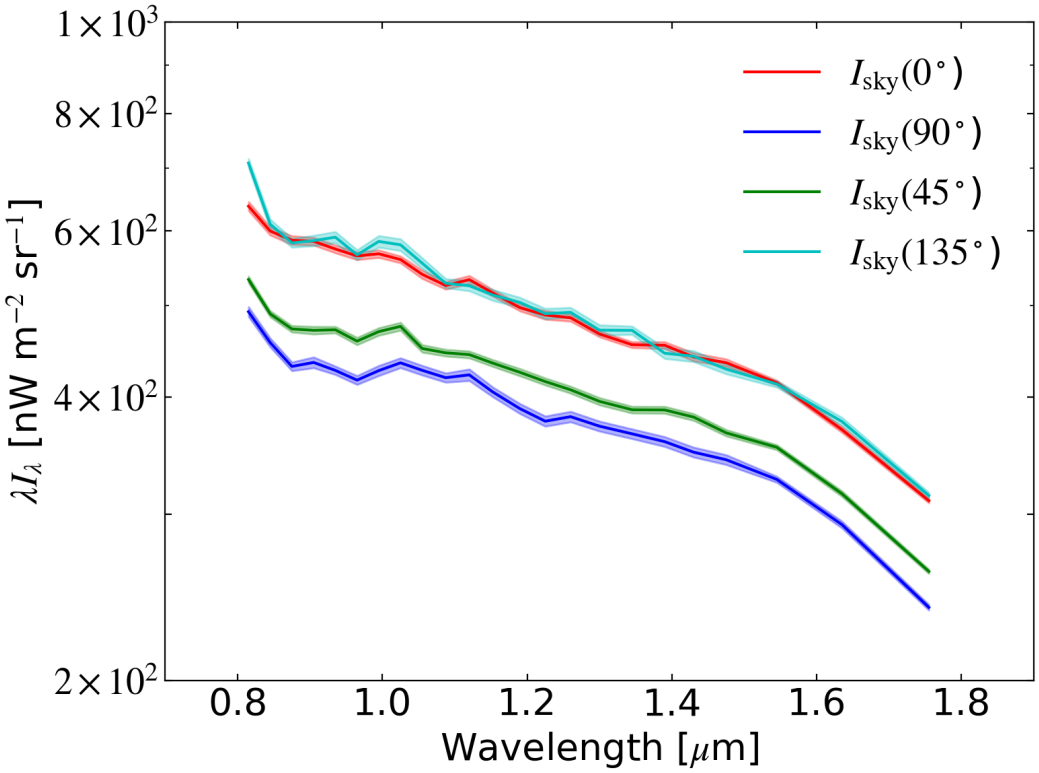

FIGURE 2.3: The sky spectrum, $I_{\rm sky}(\theta)$, through each polarization filter at the NEP field. The phase angles of the transmittance axis are labeled as $\theta = 0^\circ, 45^\circ, 90^\circ$, and 135°. The shaded regions are dominated by the flux calibration uncertainty, and the statistical uncertainty is negligible.

sections correspond to the five slits dispersed in the x-direction, and the four parallel sections correspond to the wire-grid polarizing films.

In order to measure the absolute spectrum of the sky brightness, we subtract the dark current and mask bright point sources from the *LRS* images. The dark current is estimated from the masked regions of each slit individually. The corners of the array are masked to avoid contamination by spurious signals emanating from the multiplexers of the detectors in the corners of each quadrant. To remove bright point sources, we average the photocurrent of each slit along the horizontal direction, then clip the pixels containing stars determined by the criterion that the band-averaged photocurrent is deviated from the mean of the band-average photocurrent of all pixels by 2 σ, where σ is the standard deviation of the photocurrent. We iterate this clipping procedure until the ratio of the number of rejected pixels to the remaining pixels is less than 0.1% of the total. To reject hot and dead pixels and the remaining faint point sources, pixels which are greater than 3 σ from the mean are also excluded. Finally, we derive the sky spectrum, $I_{\rm sky}(\theta)$, through each polarization filter as shown in Figure 2.3.

Further details on the basic data reduction are described in Tsumura et al. (2010) and Arai et al. (2015).

2.3 DATA ANALYSIS

After the basic data reduction, to derive the ZL polarization spectrum, we separate the mean ZL brightness, $I_{\rm ZL,mean}$, and the ZL brightness of the polarized component, $I_{\rm ZL,pol}$, from the measured sky brightness. We assume that the polarization components of the DGL, the ISL, and the EBL are negligible compared to the ZL, as discussed in Appendix B.2. The measured sky brightness of the polarized component, $I_{\rm sky,pol}$, can then be assumed as $I_{\rm sky,pol} = I_{\rm ZL,pol}$.

The mean sky brightness comprises

$$I_{\rm sky,mean}(\lambda) = I_{\rm ZL,mean}(\lambda) + I_{\rm DGL}(\lambda) + I_{\rm ISL}(\lambda) + I_{\rm EBL}(\lambda). \tag{2.1}$$

To derive $I_{\rm ZL,mean}$, the DGL, the ISL, and the EBL contributions need to be separated from the measured sky brightness (Matsuura et al., 2017). The DGL component, $I_{\rm DGL}(\lambda)$, is derived using its spatial distribution as traced by 100 μm emission on scales smaller than a degree (Arai et al., 2015). The ISL component, $I_{\rm ISL}(\lambda)$, is estimated by Monte-Carlo simulation of the star distribution in the FOV using the Two Micron All-Sky Survey (2MASS) catalog (Skrutskie et al., 2006), taking into account the limiting magnitude and the effective slit efficiency of the *LRS* (Arai et al., 2015). The EBL component, $I_{\rm EBL}(\lambda)$, can be assumed as identical in all the fields, but with a lot of indeterminacy. To derive the fiducial unpolarimetric spectral shape of ZL, we calculate the difference between two fields,

$$\begin{aligned} (I_{{\rm sky,mean},i}(\lambda) - I_{{\rm DGL},i}(\lambda) &- I_{{\rm ISL},i}(\lambda)) \\ -(I_{{\rm sky,mean},j}(\lambda) &- I_{{\rm DGL},j}(\lambda) - I_{{\rm ISL},j}(\lambda)) \\ = (I_{{\rm ZL,mean},i}(\lambda) + I_{{\rm EBL},i}(\lambda)) &- (I_{{\rm ZL,mean},j}(\lambda) + I_{{\rm EBL},j}(\lambda)) \\ = I_{{\rm ZL,mean},i}(\lambda) &- I_{{\rm ZL,mean},j}(\lambda) \end{aligned} \tag{2.2}$$

where i and j indicate different observation fields. We assume that the EBL component is identical in all the fields, so $I_{\rm EBL}(\lambda)$ is canceled in Equation 2.2. We also estimate the ZL brightness, $I_{\rm ZL_{model}}$, at 1.25 μm of each field from the *DIRBE/COBE*-based ZL model (Kelsall et al., 1998), which are summarized in Table 2.1, and normalize the differences of $I_{\rm ZL,mean}$ with $I_{\rm ZL_{model}}$ at 1.25 μm. Because of deep airglow contamination, only the NEP, Elat-30, and BOOTES-B fields are available to derive the fiducial unpolarimetric spectral shape of ZL with the polarization slit of the *LRS*. To improve the signal-to-noise ratio, we use not only the data with the polarization slit but also those with the center slit at the NEP and Elat-30 fields, and average these results. It is noteworthy that we could not use the data with center slit at the BOOTES-B field because the detector was not functioning properly. The airglow emission likely depends on atmospheric conditions and changes daily. The details of uncertainty of the airglow contamination are described in Appendix B.2.

Figure 2.4 presents the fiducial mean spectral shape of ZL during the third flight. The difference in the ZL spectral shape between the second and third flights may be due to the timing of the observations and the calibration accuracy. In deriving the ZL polarization spectrum, we only use the ZL spectral shape of the third flight in terms of the instrumental systematic uncertainties.

To derive $I_{\rm ZL,pol}$, we fit the measured sky spectrum, $I_{\rm sky}$, at all available wavelengths with Equation B.2 to separate the polarized and unpolarized components. In Figure 2.5, we show the measured $I_{\rm sky}(\theta)$ at 1.26 μm as a function of θ in the NEP field. The black curve presents the best fit by Equation B.2.

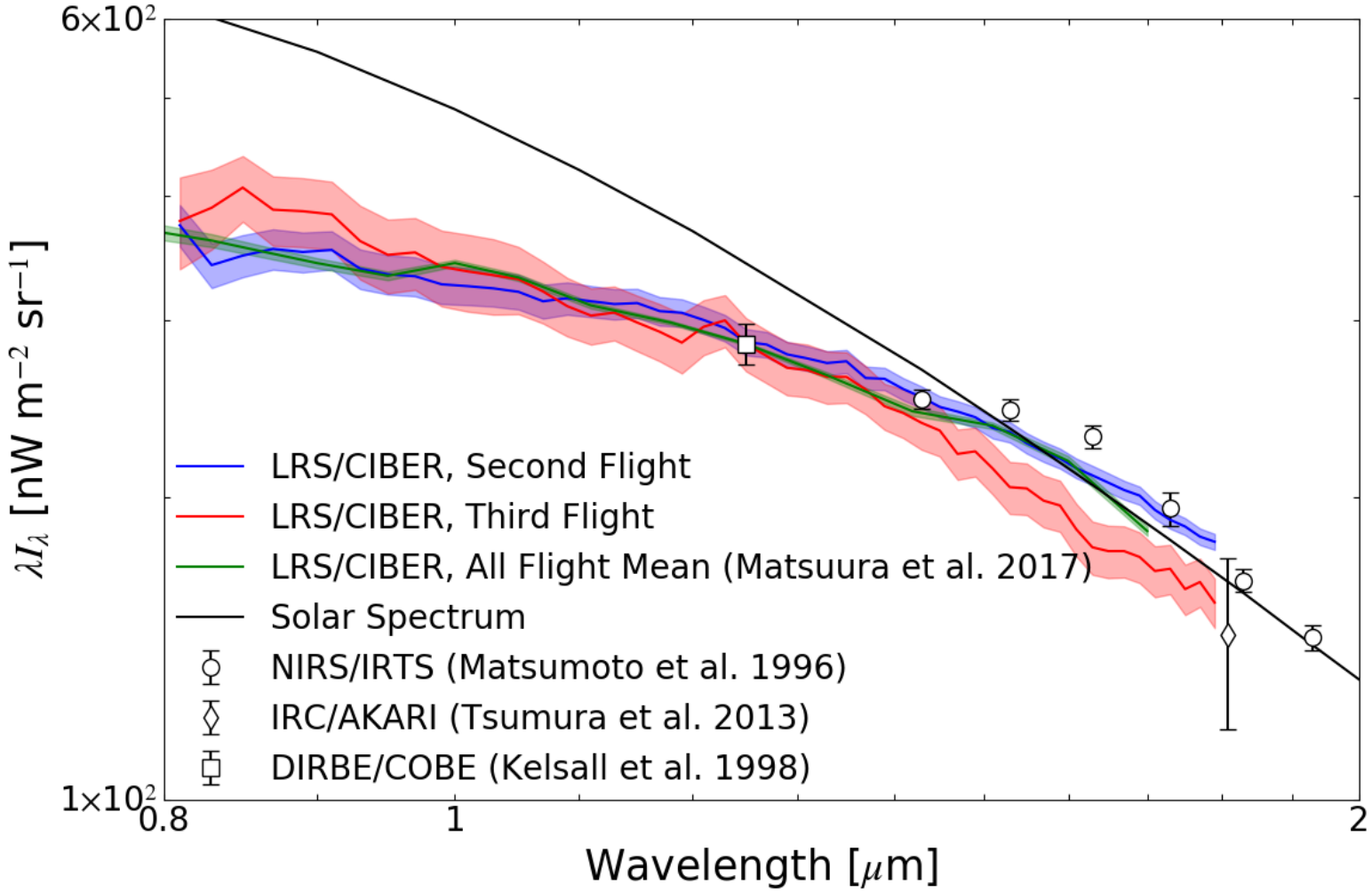

FIGURE 2.4: The ZL spectrum measured in the second flight (blue line) and the third flight (red line). The solid green line represents the mean ZL spectrum of all *CIBER* flights (Matsuura et al., 2017). The shaded regions indicate 1σ statistical uncertainties. The solid black line represents the solar spectrum (http://rredc.nrel.gov/solar/spectra/am0). The circles indicate the ZL spectrum measured using *NIRS/IRTS* (Matsumoto et al., 1996). The diamonds represent the ZL spectrum predicted by the IPD model derived from data from the Infrared Camera (*IRC*)/*AKARI* (Tsumura et al., 2013b). The square indicates the ZL brightness measured with *DIRBE/COBE* (Kelsall et al., 1998). Since the target fields of the *CIBER* observations are different from those of other studies, they are scaled to the brightness estimated from the 1.25 μm ZL model (Kelsall et al., 1998) at $(\lambda, \beta) = (335.^\circ 37, 89.^\circ 72)$.

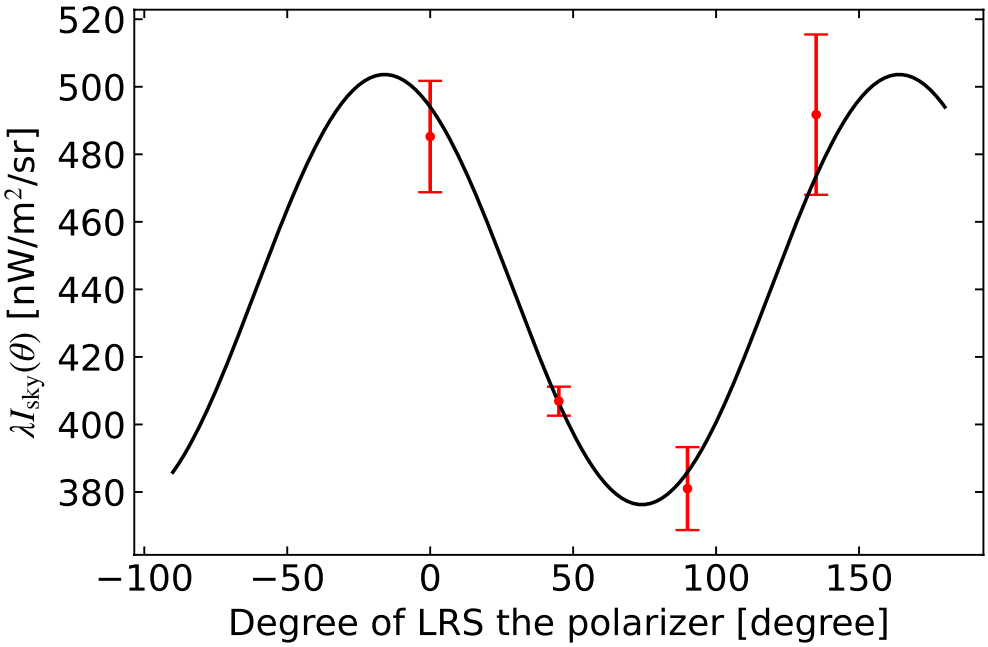

FIGURE 2.5: The red circles indicate the measured sky brightness, $I_{\rm sky}(\theta)$, at 1.26 μm through each polarization filter in the NEP field. The phase angles of the transmittance axis are labeled as $\theta = 0°, 45°, 90°$, and 135°. The error bars are dominated by the flat-field error (see Appendix B.2.1). The black line represents the best fit of Equation B.2. $\lambda I_{\rm sky,mean}$ is 439 ± 8 nW m^{-2} sr^{-1} and $\lambda I_{\rm sky,pol}$ is 63 ± 10 nW m^{-2} sr^{-1}.

TABLE 2.2: The Expected Phase Angle, $\phi_{0,exp}$, and the Measured Phase Angle, $\phi_{0,meas}$

Field Name	$\phi_{0,exp}$ (deg)	$\phi_{0,meas}$ (deg)
Lockman Hole	113±1	118±12
SWIRE/ELAIS-N1	73±3	68±4
North Ecliptic Pole (NEP)	120±1	119±2
Elat30 (β = 30°)	49±1	54±8
BOOTES-B	190±2	163±8

Because the *LRS* has a large FOV, $\phi_{0,exp}$ is different between the center and the edge of an image. The uncertainty of $\phi_{0,exp}$ indicates this difference. $\phi_{0,meas}$ is the average over all wavelengths. The uncertainty of $\phi_{0,meas}$ represents the standard deviation.

Finally, from Equation B.3, the ZL polarization spectrum, $P_{ZL}(\lambda)$, can be expressed as

$$P_{ZL}(\lambda) = \frac{I_{ZL,pol}(\lambda)}{I_{ZL,mean}(\lambda)} \tag{2.3}$$

2.4 RESULT

2.4.1 Validity of the Measured Polarization Angle

First of all, to validate our measurements, we compare an expected polarization angle, $\phi_{0,exp}$, with the measured polarization angle, $\phi_{0,meas}$. We show the geometric definition of the polarization angle in Figure 2.6 and 2.7. The angle of the plane-of-incidence, ν, toward the decl. is presented as

$$\nu = \tan^{-1} \frac{\sin(\beta)}{\tan(180^\circ - \lambda + \lambda_\odot)}. \tag{2.4}$$

Thus, ϕ_0 can be determined as

$$\phi_0 = \eta + \nu - 90^\circ, \tag{2.5}$$

where η indicates the rotational angle of the slit. We note that the scattered light by each IPD grain along the line of sight produces the same phase angle since it does not depend on the distance between the *LRS* and the IPD grains. We summarize these parameters to calculate the expected polarization angle in Table 2.2. The measured phase angle is generally consistent with expectation, which supports our polarimetric measurements.

2.4.2 Polarization Spectra

We show the ZL polarization spectrum, $P_{ZL}(\lambda)$, of the five fields measured in the third flight in Figure 2.8 and Table 2.3. This is the first measurement of the polarization ZL spectrum in the near-infrared. $P_{ZL}(\lambda)$ shows little wavelength dependence in all fields. On the other hand, $P_{ZL}(\lambda)$ clearly depends on the ecliptic coordinates and the solar elongation. $P_{ZL}(\lambda)$ peaks at the NEP field where the solar elongation is 90°. Details of systematic uncertainty are described in Appendix B.2.

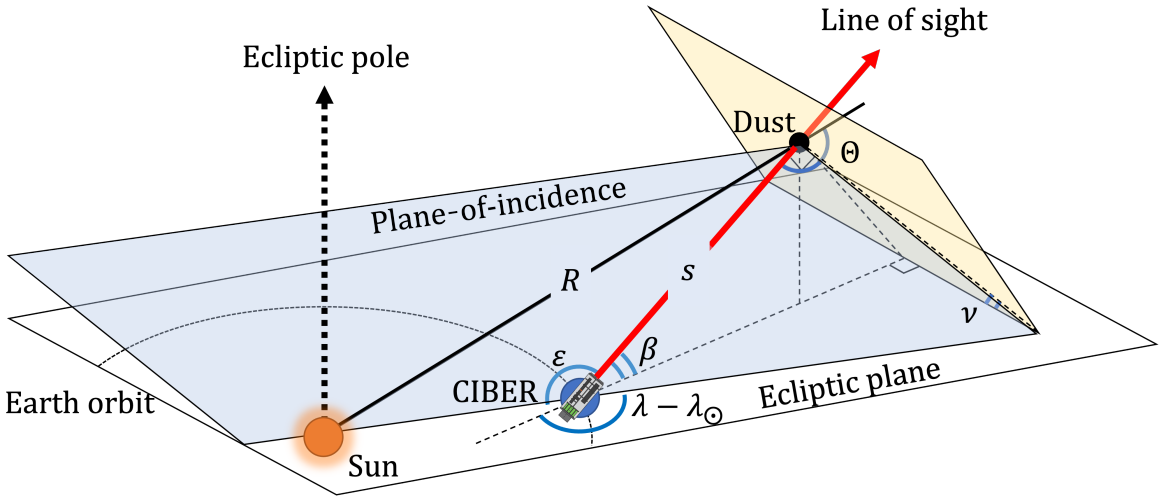

FIGURE 2.6: Geometric description of *CIBER* observation with respect to the ecliptic latitude, β, and the helio-ecliptic longitude, $(\lambda - \lambda_\odot)$, where λ is the ecliptic longitude and $\lambda_\odot$ is the ecliptic longitude of the Sun. The red arrow represents the line of sight from the *LRS*/*CIBER*, and s indicates the distance between the *LRS*/*CIBER* and a IPD grain. The observed ZL intensity corresponds to integrated light scattered by all IPD grains along the *LRS*/*CIBER* line of sight. The radial distance from the grain to the Sun is denoted by R, and the solar elongation is indicated by ϵ. The angle between the plane-of-incidence and the decl. axis is represented by ν. The scattering angle is denoted by Θ.

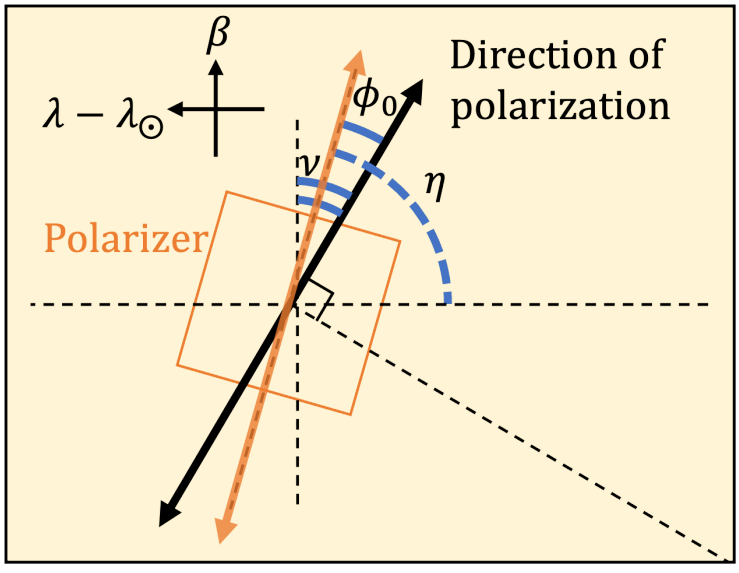

FIGURE 2.7: The orientation of the *LRS*/*CIBER* polarizer relative to the direction of the ZL polarization, as viewed from the *LRS* toward the line of sight. Helio-ecliptic coordinates are suitable to describe the ZL with the ecliptic latitude, β, and the helio-ecliptic longitude, $(\lambda - \lambda_\odot)$. The plane-of-incidence angle toward the decl. axis is represented by ν. The rotational angle of the polarizer toward the decl. axis is indicated by η. The angle of the direction of polarization toward the transmission axis is labeled as ϕ_0.

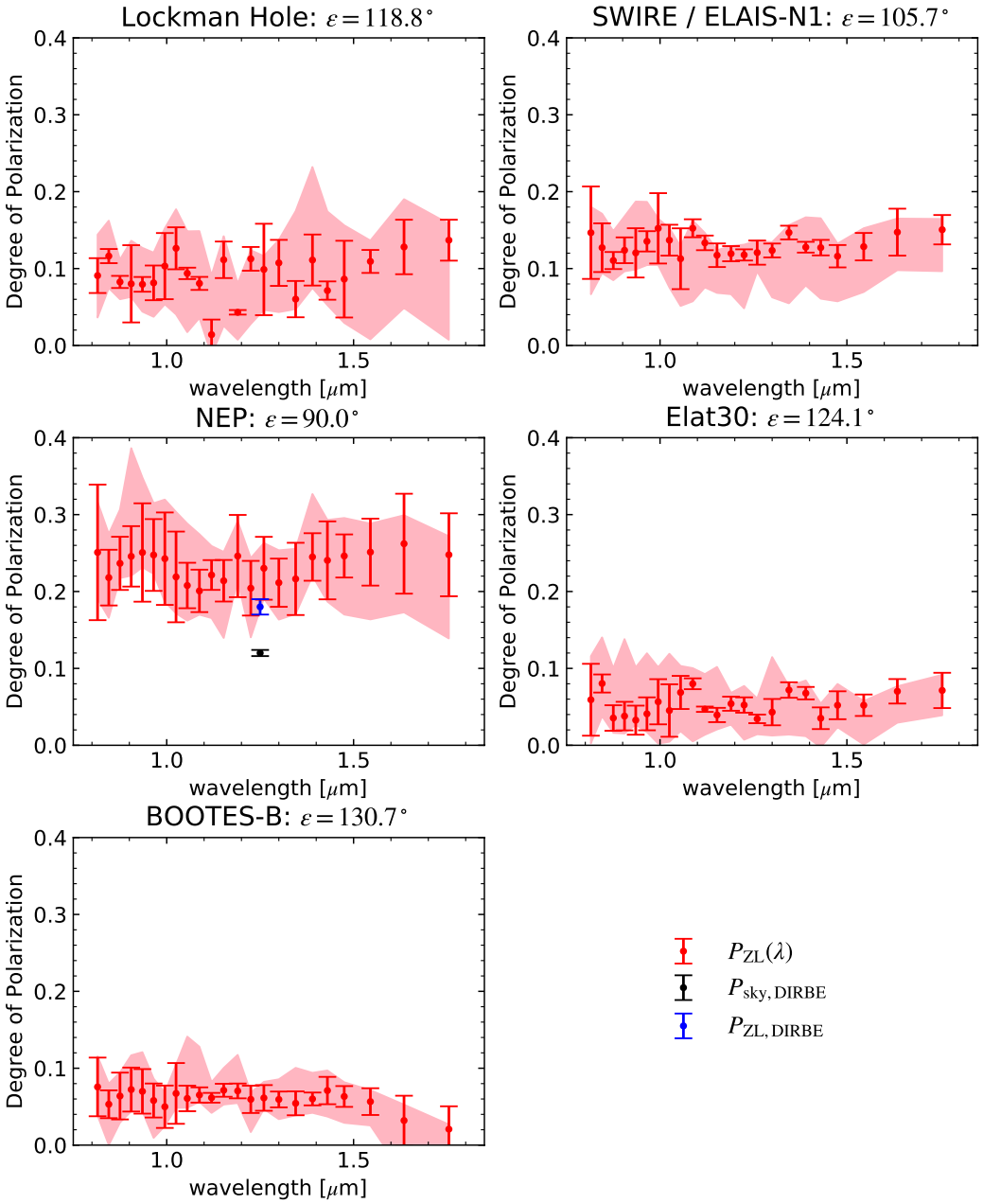

FIGURE 2.8: The ZL polarization spectrum, $P_{\rm ZL}(\lambda)$, measured in the third flight (red filled circles). The error bars represent the total uncertainty due to the fitting of Equation B.2 and the polarization calibration. The red shaded region indicates the total instrument and astronomical systematic uncertainty (Appendix B.2). The black circle is the original data of the degree of polarization, $P_{\rm sky,DIRBE}$, from Berriman et al. (1994), and the blue circle is the updated degree of polarization, $P_{\rm ZL,DIRBE}$, measured with *DIRBE/COBE* at $\lambda = 10°$ and $\beta = 0°$.

TABLE 2.3: The ZL polarization spectrum $P_{ZL}(\lambda)$ measured in the third flight

λ (μm)	$P_{ZL_{\text{Lockman Hole}}}$ (%)	$P_{ZL_{\text{SWIRE/ELAIS-N1}}}$ (%)	$P_{ZL_{\text{NEP}}}$ (%)	$P_{ZL_{\text{Elat30}}}$ (%)	$P_{ZL_{\text{BOOTES-B}}}$ (%)
0.815	$9.4 \pm 2.2 + 5.3/-5.5$	$15.2 \pm 6.1 + 3.4/-8.0$	$26.0 \pm 8.8 + 6.6/-6.0$	$6.1 \pm 4.8 + 3.4/-8.0$	$7.8 \pm 3.9 + 4.0/-3.7$
0.845	$13.1 \pm 0.5 + 4.6/-4.2$	$14.3 \pm 3.4 + 4.4/-3.3$	$24.5 \pm 3.7 + 5.7/-5.2$	$9.0 \pm 1.2 + 4.4/-3.3$	$6.0 \pm 2.0 + 2.7/-5.3$
0.875	$8.9 \pm 0.6 + 2.9/-2.3$	$11.9 \pm 0.9 + 3.8/-2.6$	$25.5 \pm 3.3 + 7.0/-1.9$	$3.8 \pm 1.8 + 3.8/-2.6$	$6.9 \pm 3.2 + 3.1/-3.5$
0.905	$8.6 \pm 5.4 + 5.6/-1.7$	$13.3 \pm 1.6 + 4.4/-2.7$	$26.3 \pm 3.8 + 14.1/-2.5$	$4.1 \pm 2.0 + 4.4/-2.7$	$7.7 \pm 3.0 + 4.5/-2.8$
0.935	$8.4 \pm 0.8 + 4.7/-3.5$	$12.7 \pm 3.2 + 6.7/-2.2$	$26.4 \pm 6.4 + 9.8/-1.9$	$3.4 \pm 2.0 + 6.7/-2.2$	$7.4 \pm 3.0 + 5.1/-2.6$
0.965	$8.5 \pm 2.3 + 3.9/-4.4$	$14.2 \pm 0.9 + 5.1/-3.1$	$25.9 \pm 4.5 + 6.7/-2.5$	$4.3 \pm 2.2 + 5.1/-3.1$	$6.1 \pm 2.3 + 2.8/-4.9$
0.995	$10.7 \pm 4.4 + 4.9/-5.0$	$15.8 \pm 4.6 + 1.3/-4.8$	$25.1 \pm 5.9 + 7.7/-5.6$	$5.9 \pm 3.0 + 1.3/-4.8$	$5.2 \pm 2.8 + 1.8/-2.5$
1.025	$13.0 \pm 2.6 + 5.1/-8.6$	$14.1 \pm 1.7 + 1.6/-6.1$	$22.5 \pm 5.8 + 8.5/-4.7$	$4.7 \pm 3.5 + 1.6/-6.1$	$6.9 \pm 4.0 + 3.7/-1.9$
1.055	$9.6 \pm 0.4 + 5.5/-7.6$	$11.6 \pm 4.0 + 1.6/-6.1$	$21.3 \pm 2.7 + 8.1/-4.6$	$7.0 \pm 2.2 + 1.6/-6.1$	$6.2 \pm 1.7 + 8.0/-1.2$
1.087	$8.0 \pm 0.7 + 6.8/-4.5$	$15.1 \pm 0.7 + 1.0/-9.5$	$20.0 \pm 2.5 + 7.4/-3.1$	$7.9 \pm 0.5 + 1.0/-9.5$	$6.5 \pm 0.9 + 6.3/-0.9$
1.120	$1.4 \pm 1.9 + 7.7/-2.6$	$13.1 \pm 0.6 + 1.3/-5.8$	$21.8 \pm 1.5 + 3.8/-5.6$	$4.6 \pm 0.2 + 1.3/-5.8$	$6.1 \pm 0.5 + 2.0/-2.0$
1.152	$10.8 \pm 2.2 + 3.1/-8.6$	$11.4 \pm 1.3 + 0.6/-4.9$	$20.7 \pm 2.3 + 3.8/-7.4$	$3.8 \pm 0.9 + 0.6/-4.9$	$6.9 \pm 0.7 + 2.9/-1.9$
1.190	$4.1 \pm 0.1 + 3.8/-3.6$	$11.3 \pm 0.6 + 1.0/-5.3$	$23.4 \pm 4.9 + 4.5/-3.2$	$5.1 \pm 0.8 + 1.0/-5.3$	$6.7 \pm 0.8 + 4.7/-1.6$
1.225	$11.4 \pm 1.4 + 1.1/-8.5$	$11.9 \pm 0.4 + 1.3/-7.0$	$20.7 \pm 3.4 + 3.9/-6.4$	$5.3 \pm 1.0 + 1.3/-7.0$	$6.0 \pm 1.8 + 0.9/-4.3$
1.260	$9.8 \pm 5.9 + 1.7/-5.3$	$12.0 \pm 1.4 + 1.5/-2.4$	$22.8 \pm 3.9 + 3.3/-3.9$	$3.4 \pm 0.5 + 1.5/-2.4$	$6.1 \pm 1.6 + 2.1/-1.4$
1.300	$10.5 \pm 2.9 + 3.0/-6.4$	$12.1 \pm 0.6 + 1.1/-6.1$	$20.7 \pm 2.9 + 4.2/-4.8$	$4.2 \pm 1.7 + 1.1/-6.1$	$5.8 \pm 1.0 + 2.6/-2.6$
1.345	$5.9 \pm 2.3 + 11.4/-1.3$	$14.3 \pm 0.4 + 1.0/-9.2$	$21.1 \pm 4.4 + 3.9/-4.6$	$7.0 \pm 0.9 + 1.0/-9.2$	$5.3 \pm 1.5 + 4.6/-1.6$
1.390	$10.6 \pm 3.1 + 12.1/-3.6$	$12.2 \pm 0.3 + 3.9/-5.0$	$23.4 \pm 2.7 + 8.2/-2.5$	$6.5 \pm 0.7 + 3.9/-5.0$	$5.7 \pm 0.8 + 3.4/-1.8$
1.430	$6.8 \pm 1.1 + 10.3/-1.9$	$12.1 \pm 0.7 + 3.8/-6.6$	$23.0 \pm 4.7 + 5.3/-5.4$	$3.4 \pm 1.3 + 3.8/-6.6$	$6.8 \pm 1.7 + 2.6/-3.4$
1.475	$8.0 \pm 4.6 + 7.0/-5.7$	$10.8 \pm 1.2 + 1.6/-5.9$	$22.9 \pm 2.3 + 4.9/-7.6$	$4.8 \pm 1.7 + 1.6/-5.9$	$5.9 \pm 1.2 + 1.9/-3.4$
1.545	$10.0 \pm 1.3 + 2.7/-10.1$	$11.8 \pm 1.5 + 2.4/-5.9$	$23.0 \pm 3.8 + 3.7/-8.8$	$4.8 \pm 1.2 + 2.4/-5.9$	$5.2 \pm 1.6 + 1.5/-3.1$
1.635	$11.2 \pm 3.0 + 6.2/-7.9$	$12.9 \pm 2.6 + 1.8/-4.9$	$22.9 \pm 5.5 + 3.7/-8.9$	$6.1 \pm 1.3 + 1.8/-4.9$	$2.8 \pm 2.8 + 2.1/-7.1$
1.755	$12.2 \pm 2.3 + 2.1/-13.0$	$13.4 \pm 1.5 + 1.4/-5.4$	$22.1 \pm 4.7 + 2.4/-10.9$	$6.4 \pm 2.0 + 1.4/-5.4$	$1.9 \pm 2.7 + 0.6/-10.3$

Mean value $\pm$ statistical uncertainty + systematic uncertainty (upper/lower).

TABLE 2.4: Corrected degree of polarization measured by *DIRBE/COBE* at $\lambda = 10^\circ$ and $\beta = 0^\circ$

Wavelength (μm)	$P_{\text{sky,DIRBE}}$ (%)	Detection Limit (Jy)	$I_{\text{ZL,mean}}$	I_{ISL}	I_{DGL}	I_{EBL}	$P_{\text{ZL,DIRBE}}$ (%)
			(nW m^{-2} sr^{-1})				
1.25	12.00 ± 0.4	15	831 ± 41	318 ± 15	10 ± 1	54 ± 17	18 ± 1
2.2	10.00 ± 0.5	15	302 ± 15	257 ± 13	5 ± 1	28 ± 7	19 ± 1

See Section 2.4 for details.

2.4.3 Solar Elongation Dependence

We show the mean of $P_{ZL}(\lambda)$ from 0.8 to 1.8 μm as a function of the solar elongation in Figure 2.9. We plot two results scaled to the ZL brightness estimated from the Kelsall et al. (1998) model (hereafter the Kelsall model) and the Wright (1998) model (hereafter the Wright model). The degree of polarization of the spherical IPD as a function of the scattering angle, Θ, in different scattering models is shown in Figure 2.10. The models we consider are empirical scattering, Rayleigh scattering, and Mie scattering with astronomical silicate, $Mg_{1.1}Fe_{0.9}SiO_4$, and with graphite (Bohren and Huffman, 1983). The empirical scattering refers to the empirical degree of polarization of IPD in the visible band, $P = 0.33 \sin^5 \Theta$ (Leinert, 1975), but this function does not cover a sufficient range of particle sizes and materials to replace the Mie calculation. For Mie scattering, we assume the mean complex refractive indices $m = 1.714 + 0.031i$ for astronomical silicate as a typical refractive material and $m = 2.995 + 1.590i$ for graphite as a typical absorptive material from 0.8 to 1.8 μm (Draine and Lee, 1984). The middle and bottom of Figure 2.10 show Mie scattering models using the complex refractive indexs of astronomical silicate and graphite, respectively. Small particles at $r = 0.1$ μm ($x \gg 1$) are approximated to Rayleigh scattering, while large particles at $r = 100$ μm ($x \ll 1$) are approximated to the geometric optics limit. The degree of polarization in each model is calculated by integrating along the line of sight in each field and assuming the IPD geometry of the Kelsall model (Figure 2.9). Since each observation field in *CIBER* is toward solar elongation $\epsilon > 90^\circ$, the degree of polarization with scattering angle $< 90^\circ$ is

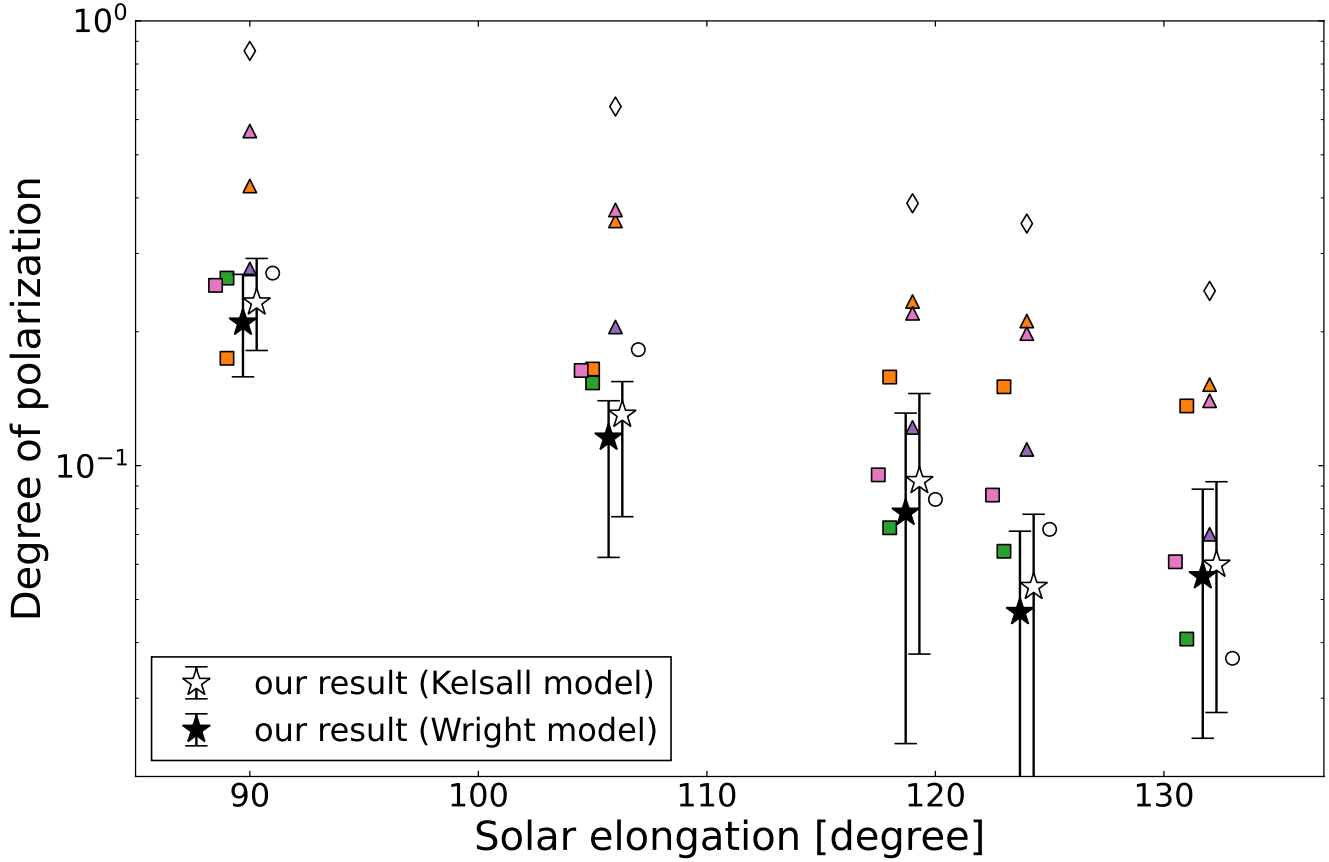

FIGURE 2.9: The degree of polarization, $P_{\rm ZL}(\lambda)$, as a function of the solar elongation. Open and closed stars are average $P_{\rm ZL}(\lambda)$ between 0.8 and 1.8 μm scaled to the brightness estimated from the Kelsall model and the Wright model. Error bars indicate the systematic uncertainties. Open circles indicate the $P_{\rm ZL}$ produced by the empirical scattering in the visible band (Leinert, 1975), and open diamonds represent that calculated by the Rayleigh scattering (Bohren and Huffman, 1983) along the line of sight. The triangles and the squares indicate the $P_{\rm ZL}$ calculated by the Mie scattering with astronomical silicate and graphite, respectively (Draine and Lee, 1984). The marker colors mean different particle radii (see Figure 2.10). Note that each marker has an offset in the x-axis so that they do not overlap with each other, even if they have the same solar elongation. The empirical model and the Mie model with graphite can clearly reproduce the measurements better than the other models.

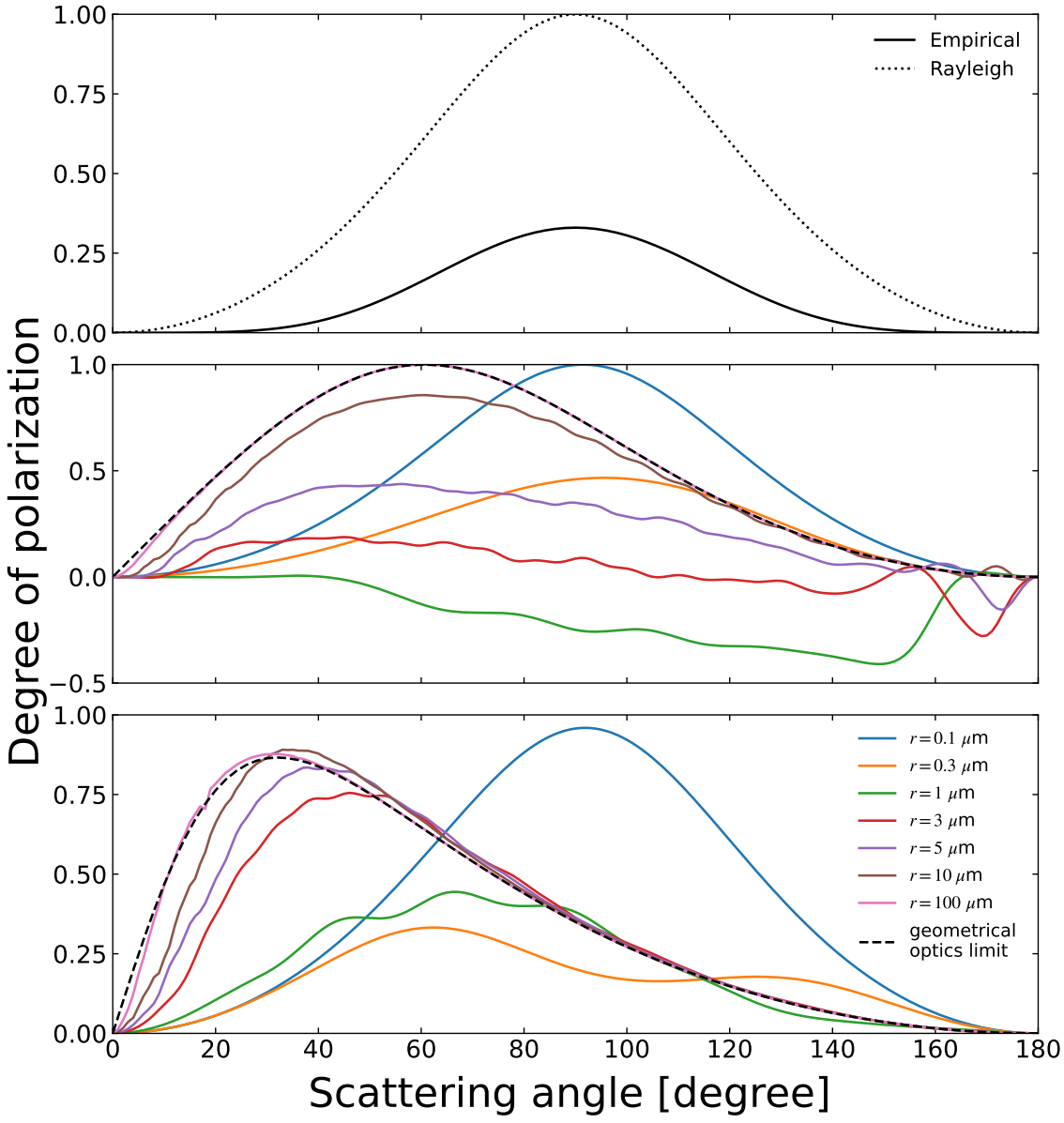

FIGURE 2.10: The degree of polarization as a function of the scattering angle, Θ. Top; the solid line indicates the empirical degree of polarization by the IPD in the visible band relative to Θ (Leinert, 1975). The dotted line indicates the Rayleigh scattering. Middle; the solid lines indicate the Mie scattering models using the complex refractive index of astronomical silicate. The particle radius, r, is varied from 0.1 to 100 μm, and each r is integrated over $r \pm 50\%$. The dashed line represent the geometric optics limit. Bottom; same as middle, but using the complex refractive index of graphite.

not included in the line-of-sight integration. Our results are consistent with the degree of polarization inferred from the scattering properties of the empirical model and the Mie scattering model with $r \geq 1$ μm graphite. The Rayleigh scattering and the Mie scattering with astronomical silicate can be rejected as the principal mechanism of the ZL polarization. If the order of the wavelength and particle radius is comparable, the Mie scattering model shows complex scattering characteristics due to interference, and there are cases where the degree of polarization is close to our results. The degree of polarization of the Mie scattering model with $r = 5$ μm astronomical silicate is similar to our results, but it does not make sense to explain the ZL polarization only by a certain dust size.

2.4.4 Comparison with the *DIRBE*/*COBE* data

To compare our result with the *DIRBE*/*COBE* data at 1.25 and 2.2 μm, we estimate the ZL polarization, $P_{\mathrm{ZL,DIRBE}}$, from the result presented in Berriman et al. (1994). Because Berriman et al. (1994) did not take into account the contributions of DGL, the ISL, and the EBL, they present the polarization of the sky brightness, $P_{\mathrm{sky,DIRBE}}$. In order to estimate $P_{\mathrm{ZL,DIRBE}}$, we estimate $I_{\mathrm{ZL,mean}}$, I_{ISL}, I_{DGL}, and I_{EBL}. We estimate $I_{\mathrm{sky,mean,DIRBE}}$ as the following:

$$I_{\mathrm{sky,mean,DIRBE}} = I_{\mathrm{ZL,mean}} + I_{\mathrm{ISL}} + I_{\mathrm{DGL}} + I_{\mathrm{EBL}}, \tag{2.6}$$

where $I_{\mathrm{ZL,mean}}$ is estimated from the Kelsall model. I_{ISL} is calculated by integrating stars fainter than the detection limit of the point sources of *DIRBE*, at 15 Jy (Arendt et al., 1998). We integrate starlight fainter than 15 Jy by using the 2MASS catalog (Skrutskie et al., 2006) and TRILEGAL, which is a population synthesis code for Monte-Carlo simulation of a star count in the Galaxy (Girardi et al., 2005). The uncertainty of I_{ISL} is estimated from the variance due to the Monte-Carlo simulation. I_{DGL} is estimated from Arai et al. (2015) and Tsumura et al. (2013a) at 1.25 and 2.2 μm. I_{EBL} is adopted from Cambrésy et al. (2001). These estimated components are summarized in Table 2.4. Since these sources can be assumed to be unpolarized, we calculate the surface brightness of the polarization component, $I_{\mathrm{ZL,pol,DIRBE}}$ as

$$I_{\mathrm{ZL,pol,DIRBE}} = P_{\mathrm{sky,DIRBE}} I_{\mathrm{sky,mean,DIRBE}}. \tag{2.7}$$

Finally, we infer $P_{\mathrm{ZL,DIRBE}}$ using the estimated $I_{\mathrm{ZL,mean}}$ and $I_{\mathrm{ZL,pol,DIRBE}}$:

$$P_{\mathrm{ZL,DIRBE}} = \frac{I_{\mathrm{ZL,pol,DIRBE}}}{I_{\mathrm{ZL,mean}}}. \tag{2.8}$$

The resultant $P_{\mathrm{ZL,DIRBE}}$ is summarized in Table 2.4. Although the original *DIRBE*/*COBE* data, $P_{\mathrm{sky,DIRBE}}$, indicates redder color than our data, $P_{\mathrm{ZL,DIRBE}}$ shows little wavelength dependence after we account for other diffuse sources. We show a comparison between $P_{\mathrm{sky,DIRBE}}$, $P_{\mathrm{ZL,DIRBE}}$, and $P_{\mathrm{ZL}}(\lambda)$ at the NEP field with the same solar elongation $\epsilon = 90^\circ$ in Figure 2.8. $P_{\mathrm{ZL,DIRBE}}$ is consistent with $P_{\mathrm{ZL}}(\lambda)$ at the NEP field.

Chapter 3

NEAR INFRARED POLARIMETRY OF THE ZODIACAL LIGHT OBSERVED WITH *DIRBE/COBE*

3.1 OVERVIEW OF *DIRBE/COBE*

3.1.1 The Experiment: Objectives and Approach

The *DIRBE*, one of three instruments aboard the *COBE* satellite, was designed to measure total intensity and two perpendicular components of linear polarization in its short wavelength bands at 1.25, 2.2, and 3.5 μm. The polarimetry was an important object to help distinguish the contribution to the infrared background from sunlight scattered by IPD and to help in modeling the spatial distribution of the IPD.

Since the *DIRBE* optical axis is oriented 30° from the spin axis of the *COBE* spacecraft, it views half the sky every day at solar elongation angles ranging from $\epsilon = 64°$ to 124° with many redundant scans (Figure 3.1, 3.2). Over the course of six months, all celestial directions were redundantly sampled at all possible elongation angles in this range. The *DIRBE* instrument operated at cryogenic temperatures for 10 months, from 1989 November 24 to 1990 September 21, mapping the full sky with high redundancy during the first six months, and covering most of the sky with similar redundancy during the final four months. After the cryogen ran out, the *DIRBE* continued to provide photometric and polarimetric data, at reduced sensitivity, in the near-infrared until the instrument was turned off in December 1993.

3.1.2 The *DIRBE* Instrument for Polarimetry

TABLE 3.1: Instrument characteristics

Telescope diameter (primary)	19 cm
Telescope type	Cryogenic off–axis folded Gregorian
Telescope effective focal length	14.24 cm
Instantaneous FOV	$0.°7 \times 0.°7$
Instrument type	absolute photometer and polarimeter
Photometric bands (μm)	1.25, 2.2, 3.5, 4.9, 12, 25, 60, 100, 140, 240
Polarimetric bands (μm)	1.25, 2.2, 3.5

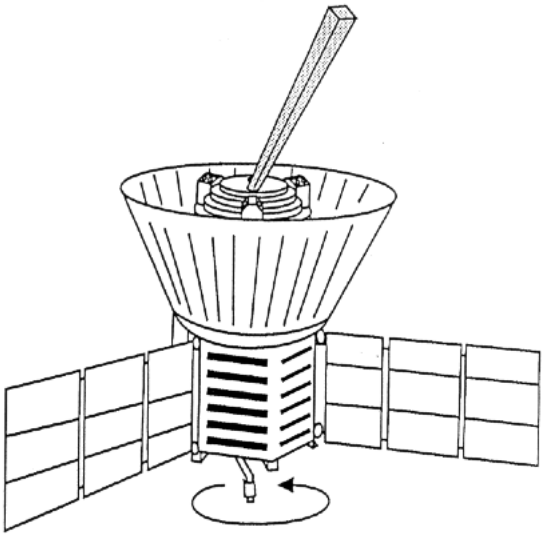

FIGURE 3.1: Schematic drawing of the viewing direction for the *DIRBE* instrument with respect to the spin axis of the spacecraft (COBE/DIRBE Collaboration, 1998).

TABLE 3.2: Detector and filter characteristics

Band	λ^a **(μm)**	$\Delta\nu_e^b$ **(Hz)**	**Detector Type**	**Filter Construction**[c]
1	1.25	5.95×10^{13}	InSb[d]	Coated Glass
2	2.2	2.24×10^{13}	InSb[d]	Coated Glass
3	3.5	2.20×10^{13}	InSb[d]	Coated Germanium

[a] Nominal wavelength of *DIRBE* band.
[b] Effective bandwidth assuming source spectrum νI_ν = constant.
[c] MLIF = multi–layer interference filter.
[d] Anti–reflection coated for the band center wavelength.

The *DIRBE* is a cryogenically–cooled ten band absolute photometer that measures the difference between the sky brightness and a zero–flux internal surface using a tuning–fork chopper running at 32 Hz. The synchronously demodulated signal is averaged for $\frac{1}{8}$th of a second before transmission to the ground. A cold shutter can be closed to block the sky signal to measure instrumental offsets. *DIRBE* uses celestial objects and internal thermal reference sources for monitoring response stability, and celestial sources for absolute response calibration. Table 3.1 summarizes the instrument characteristics.

Optics and Baffling

The *DIRBE* optics were designed to reject strong stray light (Magner, 1987). The configuration (Figure 3.3) includes re–imaging with both a secondary field stop and a Lyot stop, superpolished primary and secondary mirrors to further reduce scattered light, extensive internal baffling as well as a reflective forebaffle, and a complete light–tight enclosure within the *COBE* dewar to eliminate any optical cross–talk from the dewar or the other cryogenic instrument. Additional protection from the Earth and Sun are provided by the attitude control system and by the Sun–Earth

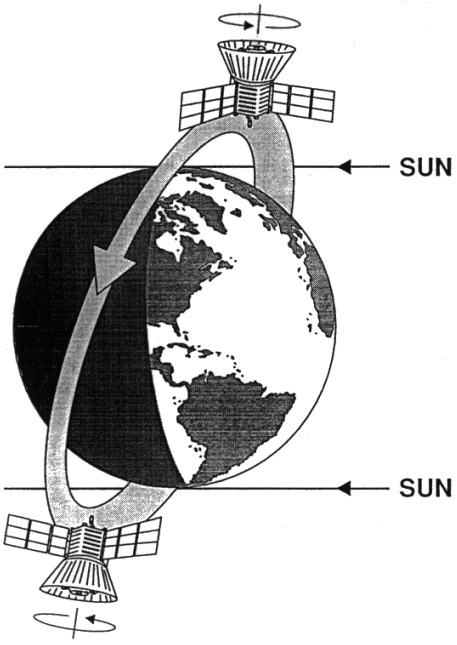

FIGURE 3.2: Schematic drawing of *COBE* in orbit (COBE/DIRBE Collaboration, 1998). *COBE* is shown in a high–inclination orbit with its axis of rotation always pointing away from the Earth and about 90° from the Sun.

shade surrounding the *COBE* dewar, which prevent any direct illumination of the dewar or instrument apertures from these omnipresent strong local sources.

The front end of *DIRBE* utilizes an off–axis folded Gregorian telescope with a 19 cm diameter off–axis segment of a parabolic mirror as the primary. There are no structural elements in the optical beam. Collimated incident light is imaged at the first field stop. An off–axis segment of an elliptical secondary forms an image of the primary at a pupil stop. This pupil stop (Lyot stop) is smaller than the image of the primary, blocking radiation diffracted from the primary mirror. The secondary mirror also images the first field stop at a second field stop. The second field stop is smaller than the first, blocking stray radiation scattered or diffracted at the first stop and setting the $0.^\circ7 \times 0.^\circ7$ instantaneous field of view. An ellipsoidal tertiary mirror imaged the pupil (Lyot stop) at a tuning fork chopper with mirrored blades. In the chopper open position sky light reaches the elliptical quaternary mirror, which images the pupil via a folding flat onto detector assembly 2. With the chopper closed, the aspheric mirror (M5) reimages the pupil onto detector assemblies 1 and 3.

In this optical arrangement, all detector assemblies are located at a pupil image. Since the required sensitivity could be achieved with modest etendue in the first 8 bands (1–100 μm), pupil division was employed to divide energy between bands, giving these bands an effective etendue of 0.0044 cm^{2}sr; the 140 and 240 μm bands used the entire entrance aperture and have an etendue of 0.044 cm^{2}sr.

All of the spectral bands view the same instantaneous $0.^\circ7 \times 0.^\circ7$ FOV simultaneously. Optical testing showed small misalignments of the beam centroids. Corrections for these small pointing offsets are applied in the ground data processing. With this configuration, each detector assembly received radiation chopped alternately between the sky and the cold beam stop. The cold beam stop was a black enclosure maintained below 3° K, producing no detectable signal at any *DIRBE*

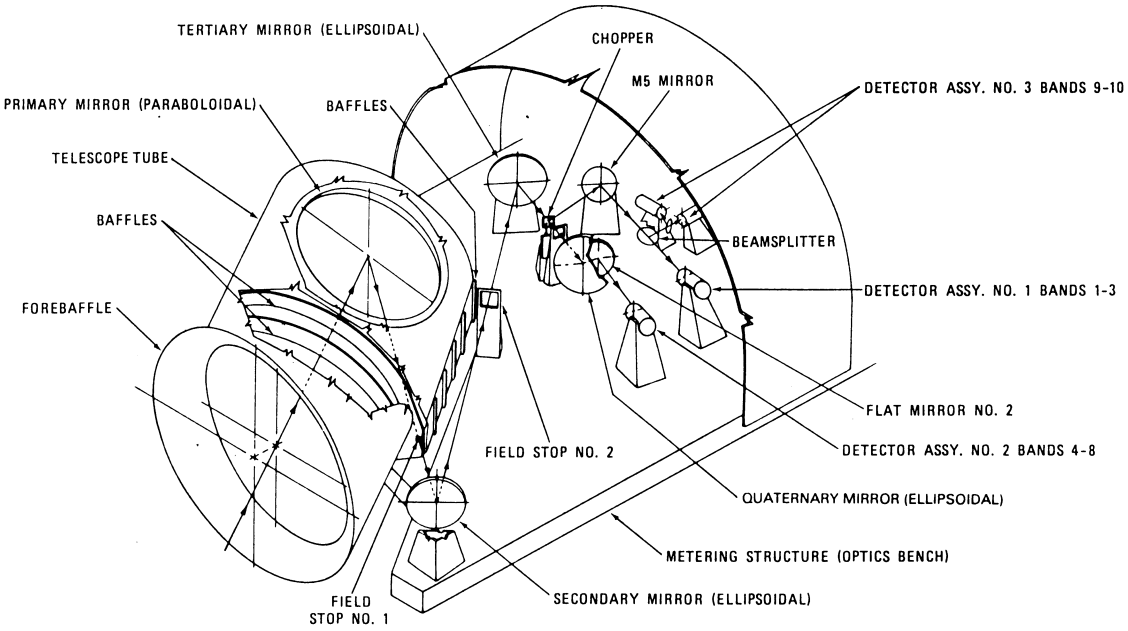

FIGURE 3.3: Optics diagram of *DIRBE* (COBE/DIRBE Collaboration, 1998). The full beam shutter (not shown) was located at field stop 1. The cold beam stop (not shown), viewed by all detectors when not exposed to the sky (or shutter), was located to the left of the chopper blades in this Figure.

wavelength. *DIRBE* sky measurements were thus continuously referenced to zero flux. Instrumental zero point offsets due to electronic pick–up or stray radiation could be measured by closing the full–beam cold shutter located at field stop 1.

Detector Assemblies

The detectors are arranged into three separate mechanical assemblies. Beamsplitters divide the light spectrally to direct the appropriate wavelengths to each detector assembly. The detector and filter characteristics and descriptions are shown in Table 3.2. Bands at 1.25, 2.2, and 3.5 μm are each equipped with three detectors, one measuring total intensity and two additional detectors, each of which has a linear polarizer in front of it. Each detector channel in an assembly included a detector element, Winston cone condensing element, spectrally–defining filter, and a cold Junction Field Effect Transistor (JFET) and load resistor for preamplification.

Each detector element (except the bolometers) was mounted on a low heat capacity substrate which was weakly coupled thermally to the mechanical structure. The substrate included a heater element which was used to set an optimal DC operating temperature for that detector, and, where necessary, to provide thermal annealing of detector response changes due to passage through the South Atlantic Anomaly.

The *DIRBE* detectors are listed by band in Table 3.2. All of the detectors were custom–made. The InSb detectors for 1.25 – 3.5 μm (bands 1 –3) were 1 mm diameter photodiodes obtained from Cincinnati Electronics.

Filters for the 1.25 – 3.5 μm bands consisted of multi–layer interference coatings on transparent substrates and were supplied by the AGA Corporation of Sweden (presently Spectrogon, AB). All of the filters were paralene encapsulated and

anti–reflection coated. The filter transmission and beamsplitter characteristics were measured at < 10 K using the Nicolet fourier transform infrared spectroscopy at Goddard Space Flight Center (Heaney et al., 1986).

Not counting the polarizers, there were two beamsplitters. One beamsplitter, consisting of a Cr/Au inductive mesh on a sapphire substrate, reflected long wavelengths and transmitted short wavelengths, and was used to separate the 1.1 – 4.0 μm bands (detector assembly 1; see Figure 3.3) from the 120 – 300 μm bands (assembly 3). The second beamsplitter, a mesh filter on a Si substrate, was used to separate the 140 and 240 μm bands.

The *DIRBE* passbands were formed by the convolution of filters, detector response functions, and dichroic beamsplitters. Out–of–band leaks were measured to 1 part in at least 10^4 (in some bands to a part in 10^8) and determined to satisfy the (to–be–provided) requirements.

In addition to the full intensity channels (designated 'A') in the 1.25, 2.2 and 3.5 μm bands, two detectors were used to make polarization measurements in each of these bands. Channels designated 'B' and 'C' contain polarizers whose transmission axes are orthogonal and fixed inside the *DIRBE* as well as band–defining spectral filters and detectors like those used in the corresponding A channels. The C channels have axes of maximum transmission aligned along the component of the *DIRBE* scan direction attributable to the spacecraft spin. The polarizing elements are 5000 line/mm aluminum grids etched on sapphire substrates.

Thermal Control

Temperatures inside the cryostat were maintained stable and below 1.6 K while the cryogen supply lasted except during occasional transient events. The external surfaces of the dewar and surrounding system were designed to minimize the dewar main shell temperature and, therefore, heat loads to the cryogen. A Sun–Earth shield protected the *DIRBE* and dewar apertures from direct solar radiation when the *DIRBE* line of sight was pointed more than 60° from the Sun, a constraint which was maintained throughout the mission.

3.2 *DIRBE* SKY COVERAGE

DIRBE's helical scans covered the sky nonuniformly. Portions of the sky that were observed at the solar elongation extrema ($\epsilon \sim 94° \pm 30°$) were scanned more frequently than regions that lay closer to the center of the viewing swath (at $\epsilon \sim 94°$). Furthermore, unlike directions within $\sim 30°$ of the ecliptic poles, which were observed year–round, sites along the ecliptic plane were in range for 2 months and then remained inaccessible for 4 months before coming back into view.

Figure 3.4 shows the depth of coverage attained during a typical week and for the entire cryogenic mission (10 months). In a week, a typical pixel was observed ∼10–15 times, and the most densely–surveyed pixels, which delineate two circumpolar annuli at ecliptic latitudes, $|\beta| \simeq 60°$, were observed ∼80–100 times. Over the course of the cryogenic mission, most pixels were observed approximately 200 times, those at $|\beta| \simeq 60°$ were observed ∼800–1000 times, and those at the ecliptic polar caps ($|\beta| > 60°$) were observed roughly 400–500 times. Because the cryogenic mission lasted for 10 months rather than a full year, coverage along the ecliptic equator is also uneven. The coverage was relatively sparse at ecliptic longitudes near 120° and 300°.

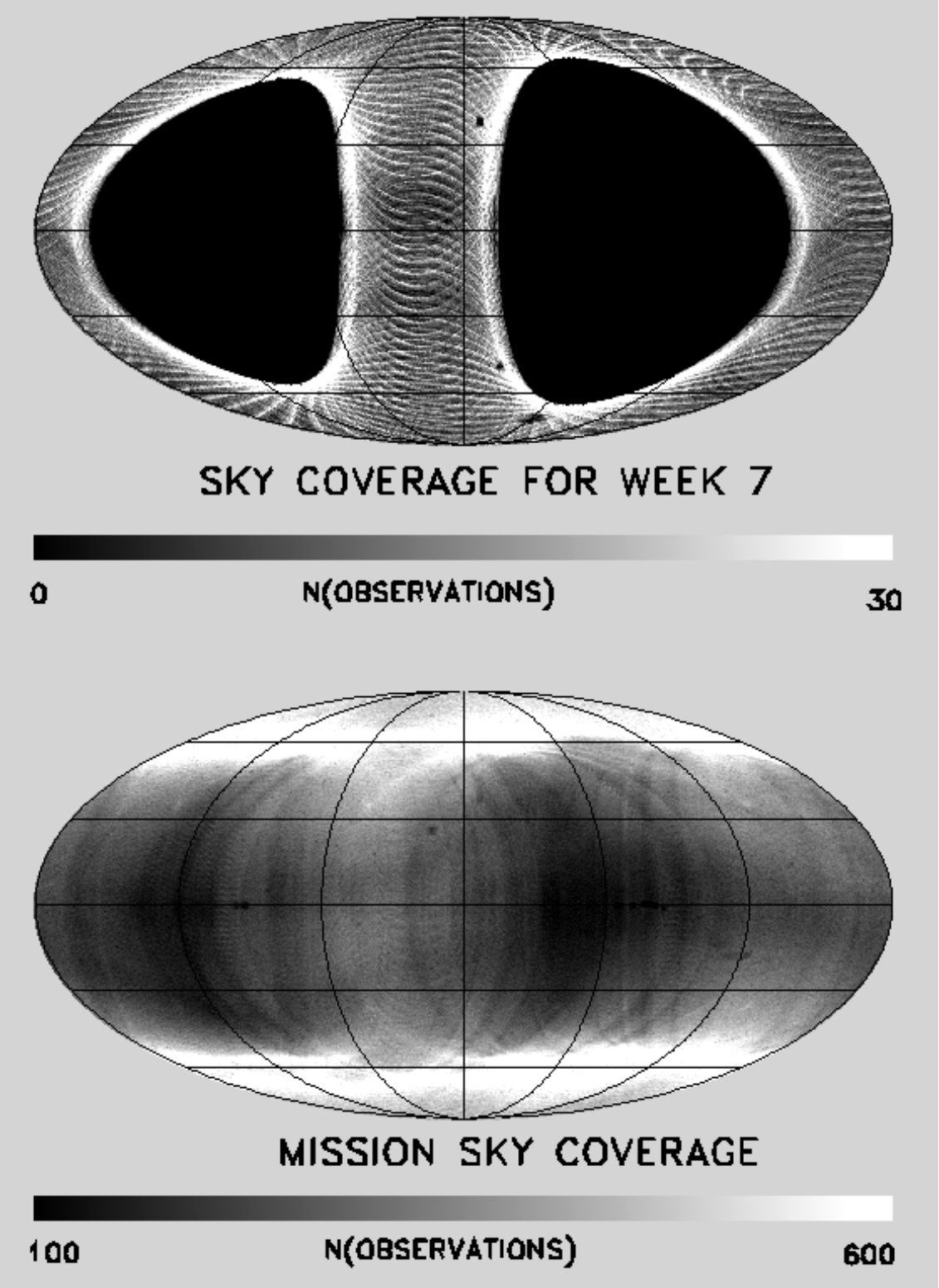

FIGURE 3.4: Depth of survey coverage in a typical week and for the whole cryogenic mission (COBE/DIRBE Collaboration, 1998). Number of observations per pixel for week 7 *(upper)* and the entire *(lower)* cryogenic mission. The maps are ecliptic coordinate projections.

TABLE 3.3: Weekly sky coverage

File	Week	Time interval (yyddd)	Elongation range (°)	Ecliptic longitude range (°)	
				Ascending	Descending
1	4	89345 – 89351	63 – 125	323 – 29	201 – 132
2	5	89352 – 89358	63 – 128	329 – 38	209 – 138
3	6	89359 – 89365	65 – 124	338 – 44	216 – 149
4	7	90001 – 90007	65 – 124	346 – 50	223 – 156
5	8	90008 – 90014	65 – 124	353 – 59	230 – 163
6	9	90015 – 90021	65 – 128	0 – 68	237 – 170
7	10	90022 – 90028	65 – 124	7 – 73	244 – 178
8	11	90029 – 90035	65 – 124	14 – 80	251 – 185
9	12	90036 – 90042	65 – 124	21 – 87	258 – 192
10	13	90043 – 90049	65 – 128	28 – 98	265 – 199
11	14	90050 – 90056	65 – 124	35 – 101	272 – 206
12	15	90057 – 90063	65 – 124	42 – 109	277 – 213
13	16	90064 – 90070	65 – 124	49 – 116	286 – 220
14	17	90071 – 90077	65 – 126	56 – 124	292 – 227
15	18	90078 – 90084	65 – 124	63 – 129	295 – 234
16	19	90085 – 90091	62 – 124	69 – 136	305 – 241
17	20	90092 – 90098	65 – 124	77 – 143	314 – 248
18	21	90099 – 90105	65 – 124	84 – 150	321 – 255
19	22	90106 – 90112	63 – 128	94 – 156	330 – 259
20	23	90113 – 90119	63 – 122	99 – 161	337 – 271
21	24	90120 – 90126[a]	62 – 122	102 – 168	344 – 278
22	25	90127 – 90133	62 – 122	109 – 175	350 – 286
23	26	90134 – 90140	62 – 128	116 – 183	356 – 286
24	27	90141 – 90147	64 – 123	124 – 189	2 – 297
25	28	90148 – 90154	63 – 122	132 – 194	10 – 303
26	29	90155 – 90161	63 – 122	136 – 202	17 – 311
27	30	90162 – 90168	63 – 122	143 – 208	23 – 318
28	31	90169 – 90175	63 – 122	149 – 215	30 – 324
29	32	90176 – 90182	63 – 124	156 – 223	37 – 329
30	33	90183 – 90189	63 – 122	163 – 228	44 – 338
31	34	90190 – 90196	63 – 122	169 – 235	50 – 344
32	35	90197 – 90203	63 – 126	176 – 246	57 – 351
33	36	90204 – 90210	63 – 122	183 – 249	64 – 358
34	37	90211 – 90217	63 – 124	190 – 257	67 – 6
35	38	90218 – 90224	65 – 124	198 – 264	76 – 7
36	39	90225 – 90231[a]	65 – 124	205 – 271	82 – 14
37	40	90232 – 90238[a]	65 – 129	212 – 278	89 – 23
38	41	90239 – 90245	65 – 128	218 – 285	95 – 29
39	42	90246 – 90252	65 – 129	225 – 294	102 – 35
40	43	90253 – 90259	65 – 127	232 – 300	109 – 43
41	44	90260 – 90264	65 – 129	239 – 305	113 – 50

[a] coverage reduced due to JFET–off test.

Table 3.3 lists a range of solar elongation angles and two ranges of ecliptic longitudes spanned by the *DIRBE* scan path at the ecliptic equator for each week of the cryogenic mission. Two ecliptic longitude ranges are given. Those denoted "Ascending" refer to ecliptic plane crossings from South to North; "Descending" scans cross the ecliptic plane from North to South. To first order, the elongation range was constant ($64^\circ \leq \epsilon \leq 124^\circ$). However, small perturbations in elongation coverage were introduced during the eclipse season and during roll maneuvers, and the coverage was extremely sparse during JFET–off test periods.

3.3 DATA PRODUCT: WEEKLY SKY MAPS

Telemetry data from the *DIRBE* instrument were calibrated and converted to some data products via the sequentially executed set of programs. The Weekly Sky Maps give weekly–averaged intensity values for the 10 *DIRBE* photometric bands, plus the Stokes Q and U parameters at 1.25, 2.2 and 3.5 μm. There are 41 Weekly Sky Map files, one per week of optimized operation in the cryogenic mission (see Table 3.3). This section briefly describes the processing steps that led to the creation of the Weekly Sky Maps data product.

3.3.1 Initial Pipeline Processing Stages

The unprocessed *DIRBE* science data consisted of consecutive $\frac{1}{8}$–second sampled observations of the sky brightness. At the survey scan rate, point sources were visible in the field of view for 0.3 s, during which time 2.4 samples were obtained. The attitude solution used to determine the line–of–sight for each sample was based upon data from the spacecraft Sun and Earth sensors and gyros, with fine corrections based upon the locations of isolated bright stars detected in the *DIRBE* 2.2 μm band. The rms accuracy of the attitude solution is approximately $1.5'$. Sky observations were routinely interrupted when the *COBE* spacecraft passed through the South Atlantic Anomaly (SAA) or when the instrument calibration stability was checked. The time–ordered sky observations had instrument offset signals removed and were calibrated photometrically relative to the *DIRBE* Internal Reference Source. They were then made into daily sky maps by associating each sample with a pixel on the sky. Pixel area and location were determined according to the adopted map projection, the *COBE* Quadrilaterilized Spherical Cube (CSC) in ecliptic J2000 coordinates. On average, in that half of the sky covered, each pixel in a daily sky map was observed about 2.4 times, but the sampling was much denser for pixels near the edges of the viewing swath (solar elongation angles near 64° and 124°) than for those near the middle.

3.3.2 Creation of Weekly Sky Maps

The *DIRBE* daily sky maps were averaged to make Weekly Sky Maps as follows. First, long–term gain stabilization corrections based upon repeated observations of stable celestial sources were applied, and the data were converted from instrumental units to calibrated specific intensities in MJy/sr. Data collected when the *COBE* spacecraft was in the SAA or when the *DIRBE* line–of–sight was close to the Moon, Mars, Jupiter, Saturn, Neptune, Uranus, or a bright comet or asteroid were excluded. Consequently, there are small holes in the *DIRBE* Weekly Sky Maps corresponding to these times. The remaining observations were then averaged to derive the quoted intensity at each pixel and wavelength; a robust averaging technique was employed

TABLE 3.4: Polarization coefficients and beam solid angles

λ (μm)	$K_{\lambda,B}$	$\sigma^a_{K_{\lambda,B}}$	$K_{\lambda,C}$	$\sigma^a_{K_{\lambda,C}}$	$\Omega_{\lambda,A}$ (10^{-4} sr)	$\sigma_{\Omega_{\lambda,A}}$ (%)	$\Omega_{\lambda,B}$ (10^{-4} sr)	$\sigma_{\Omega_{\lambda,B}}$ (%)	$\Omega_{\lambda,C}$ (10^{-4} sr)	$\sigma_{\Omega_{\lambda,C}}$ (%)
1.25	0.784	0.002	0.630	0.002	1.198	0.28	1.174	0.56	1.331	0.26
2.2	0.359	0.002	0.303	0.002	1.420	0.27	1.324	0.35	1.323	0.34
3.5	0.317	0.002	0.279	0.002	1.285	0.25	1.291	0.22	1.282	0.35

[a] standard deviation of the mean

to reduce the effects of outliers. The polarization channel intensities were converted to Stokes Parameters, Q and U. The mean time of observation and the mean solar elongation angle for each pixel were also recorded in the Weekly Sky Maps.

The intensities in the polarization and photometry channels are all independently celestially stabilized in the same fashion. To preserve the values of the ratios of the intensities in the 'B' and 'C' channels relative to the photometric ('A') channels, the absolute calibration applied to the polarization data is handled differently than that of the photometry: the calibration factors and beam solid angles are fixed to the same values used for the corresponding photometric channels.

To calculate the polarizations in the 'B' and 'C' channels, the measured intensities in each channel are iteratively fitted to an expression of the form:

$$P_{\lambda,B \text{ or } C} = Q \cos 2\Theta + U \sin 2\Theta \tag{3.1}$$

where

$$P_{\lambda,B} = 1 - \frac{(I_{\lambda,B}/I_{\lambda,A})\,(\Omega_{\lambda,A}/\Omega_{\lambda,B})}{K_{\lambda,B}},$$

$$P_{\lambda,C} = \frac{(I_{\lambda,C}/I_{\lambda,A})\,(\Omega_{\lambda,A}/\Omega_{\lambda,C})}{K_{\lambda,C}} - 1,$$

$K_{\lambda,B}$ and $K_{\lambda,C}$ are the polarization coefficients, and Ω is the beam solid angle (see Table 3.4).

The quantity $P_{\lambda,B \text{ or } C}$ is the fractional signal in the 'B' or 'C' channel relative to 'A', after both channels are placed on the same relative photometric scale via the scaling factors $K_{\lambda,B \text{ or } C}(\Omega_{\lambda,B \text{ or } C}/\Omega_{\lambda,A})$. The polarization coefficients, K, are derived from observations of unpolarized point sources corrected for channel–to–channel differences in detector responsivity. The solid angle ratio $(\Omega_{\lambda,B \text{ or } C}/\Omega_{\lambda,A})$ compensates for variations in the beam profile.

To compute the Stokes parameters Q and U from the 'B' and 'C' channel intensities, the orientations of the polarizers, Θ, must be known. By *DIRBE* convention, Θ is defined as the angle between the polarizer axes and the local meridian (*i.e.*, a great circle drawn through the spacecraft and the North and South ecliptic poles). Noting that the transmission axes of the 'C' channel polarizers are aligned with the direction of scan motion, Θ can be calculated as follows:

1. Compute the ecliptic longitude and latitude, (λ, β), in radians, from the pixel number

2. Calculate

$$\texttt{att\_x} = \texttt{AttackV}(1)\cos(\lambda) + \texttt{AttackV}(2)\sin(\lambda),$$

$$\texttt{att\_y} = \texttt{AttackV}(2)\cos(\lambda) - \texttt{AttackV}(1)\sin(\lambda),$$

$$\texttt{colatitude} = \frac{\pi}{2} - \beta,$$

and

$$x' = \texttt{att\_x}\cos\left(\texttt{colatitude}\right) - \texttt{AttackV}(3)\sin\left(\texttt{colatitude}\right),$$

where AttackV is the Attack Vector whose three components specify the rate of change of the *DIRBE* boresight unit vector. The Attack Vector is computed from the cross product of the spacecraft angular velocity vector (which includes both orbital and spin components) and the boresight. The Attack Vector points in the *DIRBE* scan direction across the sky, and is normal to the leading edge of the field of view.

3. Finally, calculate

$$\Theta = \arctan\left(\texttt{atty}/x'\right),$$

such that Θ is in the range $[-90^\circ, +90^\circ]$.

Close to the solar elongation extrema, $\epsilon = 64^\circ$ and 124°, the 'C' channel transmission axis is nearly aligned with the local meridian, and $\Theta \simeq 0$. When $\epsilon \sim 94^\circ$, the scan direction is perpendicular to the local meridian and $\Theta \simeq \pm 90^\circ$.

Further information about the *DIRBE* polarization algorithm can be found in Berriman et al., 1994.

3.4 ANALYSIS AND RESULT

3.4.1 Initial Data Separation and Calculation of Polarization

The first step is to download the 41 Weekly Sky Map files from the *BIRBE* homepage (www.lambda.gsfc.nasa.gov). All file extensions are in FITS format. A quadrilateralized spherical projection and a quad–tree pixelization scheme were adopted for all *COBE* sky maps, including the *DIRBE* maps. The so–called "*COBE* Quadrilateralized Spherical Cube" (CSC) is an approximately equal–area projection (to within a few percent) in which the celestial sphere is projected onto an inscribed cube. An advantage of the CSC over the Aitoff, Mollweide and Global–Sinusoidal projections is that polar singularities are avoided. A disadvantage is that there is no standard way to present data in the quad–cube projection in a FITS file. Figure 3.5 depicts the CSC projection. The coordinate system is Geocentric Ecliptic J2000. The ecliptic plane runs horizontally through the middle of the unfolded cube. The North Ecliptic Pole is centered on "face 0" and the South Ecliptic Pole is centered on "face 5". The *DIRBE* convention is to divide each cube face into 256×256 pixels; thus, all–sky maps have $256^2 \times 6 = 393216$ pixels. Each pixel is approximately 0.32° on a side. Figure 3.6 illustrates the pixel numbering scheme.

An ancillary information file called DIRBE_SKYMAP_INFO.FITS explains the quad–tree scheme that relates CSC pixel numbers to (x,y) positions within the quad–sphere cube faces and tabulates the ecliptic J2000, Galactic (l, b) and equatorial J2000 coordinates corresponding to the *DIRBE* pixel centers. This file may be obtained from the *DIRBE* ANCILLARY DATA PRODUCTS page (www.lambda.gsfc.nasa.gov).

After running the program to convert pixel numbers to ecliptic, galactic, and equatorial coordinates, the following similar process is applied to each map.

1. Extract only the data in the high Galactic latitude region ($|b| > 30^\circ$) , because the data in the Galactic plane are not suitable for studying ZL polarization.

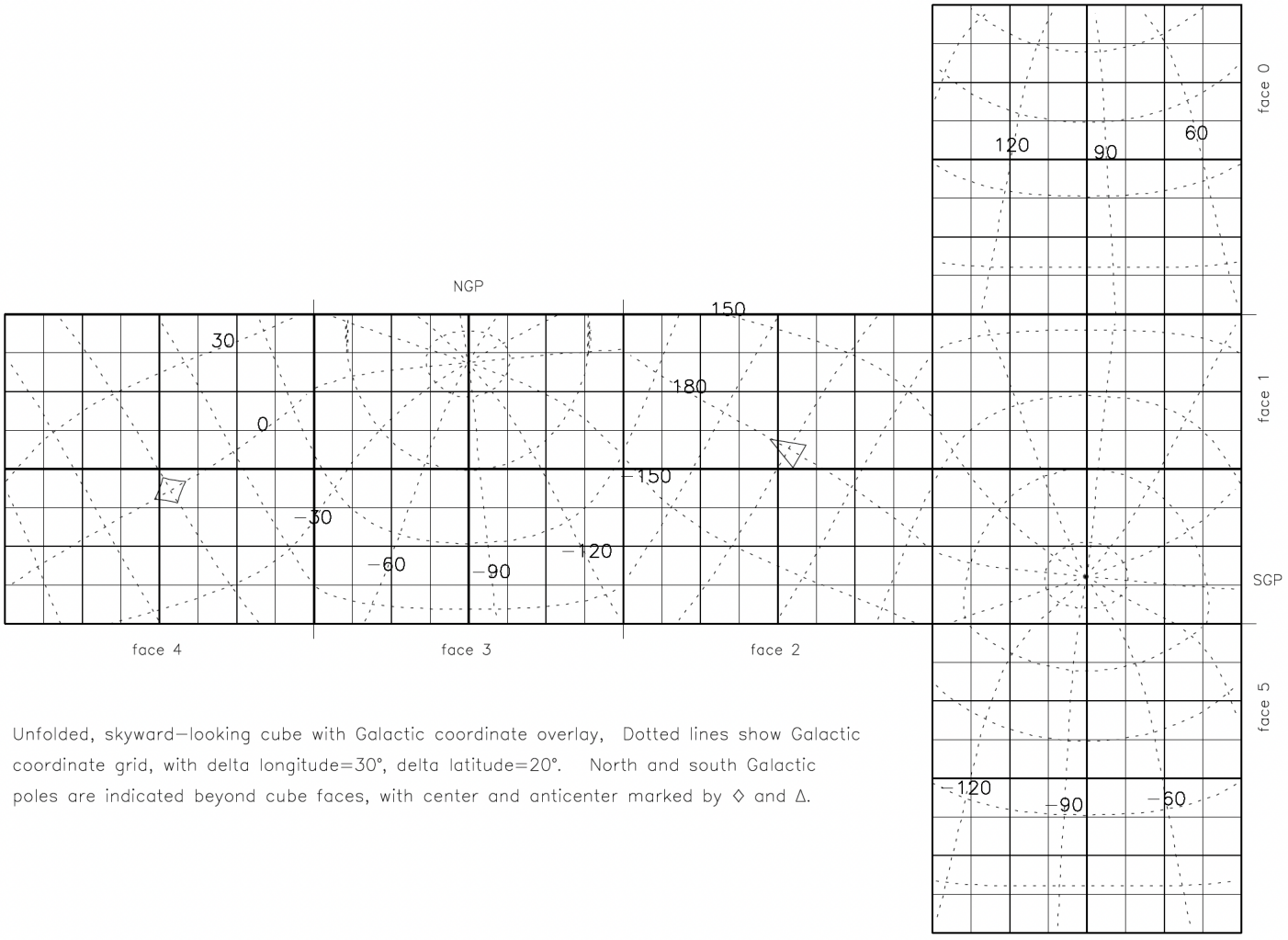

FIGURE 3.5: Internal storage of data using the CSC (COBE/DIRBE Collaboration, 1998). Unfolded, skyward–looking cube in ecliptic coordinates with Galactic coordinate overlay.

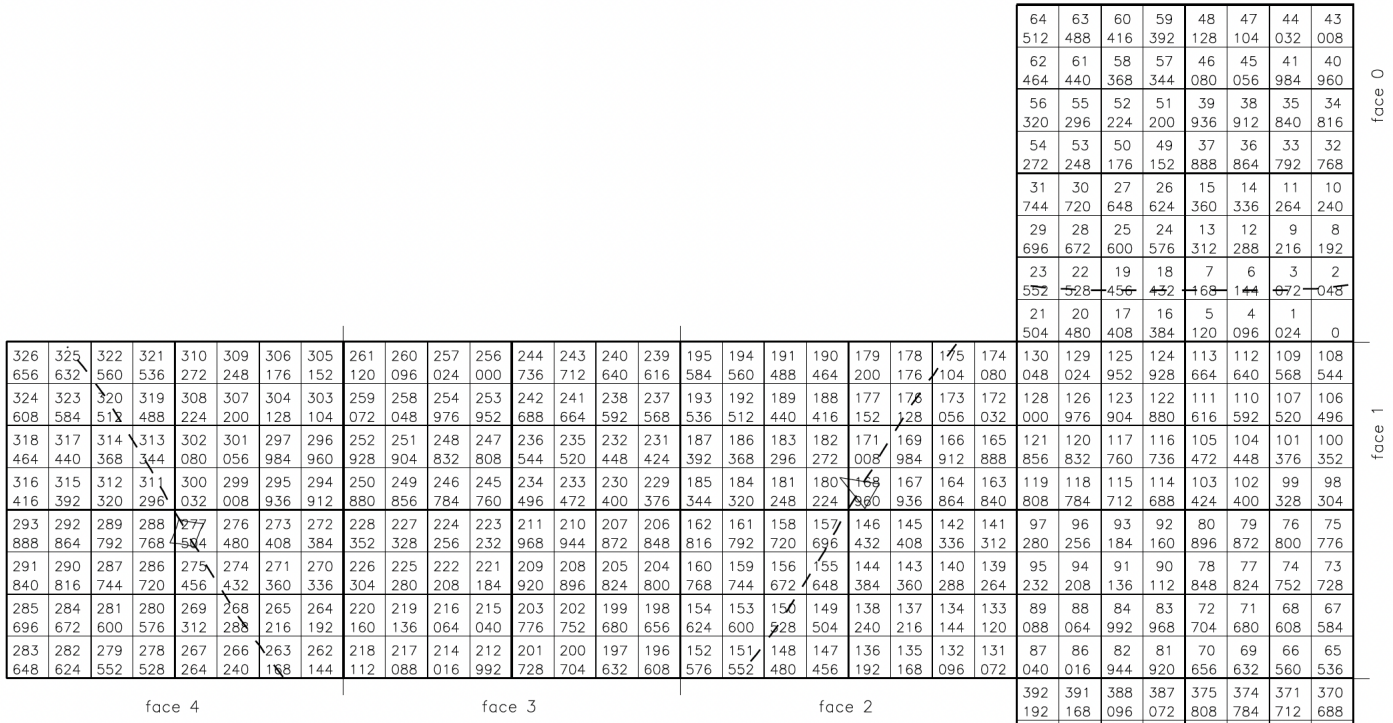

Unfolded DIRBE skycube with pixel numbering indicated. The number in each box is the number in the lower right corner of that portion of the cube face; top row gives hundred thousands, ten thousands, thousands and bottom gives hundreds, tens, units. Each face has 256 by 256 pixels. The dashed line shows Galactic plane, ◇ marks Galactic center and Δ marks anticenter.

FIGURE 3.6: The *DIRBE* pixel numbering scheme in the quadrilateralized spherical cube projection (COBE/DIRBE Collaboration, 1998).

2. Divide the data in the map region into ten parts according to the ecliptic latitude as follows,

$$\text{Region 0}: \ 0^\circ < |\beta| < 5^\circ, \ \text{Region 1}: \ 0^\circ < \beta < 10^\circ, \ \text{Region 2}: \ 10^\circ < \beta < 20^\circ,$$

$$\text{Region 3}: \ 20^\circ < \beta < 30^\circ, \text{Region 4}: \ 30^\circ < \beta < 40^\circ, \ \text{Region 5}: \ 40^\circ < \beta < 50^\circ,$$

$$\text{Region 6}: \ 50^\circ < \beta < 60^\circ, \text{Region 7}: \ 60^\circ < \beta < 70^\circ, \ \text{Region 8}: \ 70^\circ < \beta < 80^\circ,$$

$$\text{Region 9}: \ 80^\circ < \beta < 90^\circ.$$

3. Calculate the orientations of the polarizers Θ in the range $[-90^\circ, +90^\circ]$. `AttackV` used to calculate Θ is stored in the Calibrated Individual Observations (CIO) files. At this time, the observation time contained in the CIO file can be extracted at the same time to calculate more clearly where the *COBE* was observing from.

4. Replace the sentinel value with Not a Number (NaN). When there is no effective polarization ratio to form Stokes Q or U, the sentinel value (-16394) is set instead of the polarization ratio.

5. Calculate the polarization P_λ from Stokes Q_λ and U_λ.

$$P_\lambda = Q_\lambda \cos 2\Theta + U_\lambda \sin 2\Theta \ \ (\text{if } Q_\lambda \neq \text{NaN and } U_\lambda \neq \text{NaN}),$$

$$P_\lambda = \text{NaN} \ \ (\text{if } Q_\lambda = \text{NaN and } U_\lambda = \text{NaN}),$$
$$P_\lambda = Q_\lambda / \cos 2\Theta \ \ (\text{if } Q_\lambda \neq \text{NaN and } U_\lambda = \text{NaN}),$$
$$P_\lambda = U_\lambda / \sin 2\Theta \ \ (\text{if } Q_\lambda = \text{NaN and } U_\lambda \neq \text{NaN}).$$

The standard deviation of the mean of the Stokes parameters $\sigma_{Q \text{ or } U}$ is reconstructed by:

$$\sigma_{Q \text{ or } U} \leq 10^{-4} \ \ (\text{if } B = 0),$$
$$\sigma_{Q \text{ or } U} = 10^{\frac{2B-1}{127}-4} \ \ (\text{if } 1 \leq B \leq 254),$$
$$\sigma_{Q \text{ or } U} \geq 1 \ \ (\text{if } B = 255).$$

which B is given on a uniform logarithmic, and the maximum error on the reconstructed value is 1.8%. Then, σ_P can be derived as follows,

$$\sigma_P = P\sqrt{\frac{\sigma_Q}{Q} + \frac{\sigma_U}{U}} \ \ (\text{if } Q \neq \text{NaN and } U \neq \text{NaN}),$$

$$\sigma_P = \text{NaN} \ \ (\text{if } Q = \text{NaN and } U = \text{NaN}),$$
$$\sigma_P = P\frac{\sigma_Q}{Q} \ \ (\text{if } Q \neq \text{NaN and } U = \text{NaN}),$$
$$\sigma_P = P\frac{\sigma_U}{U} \ \ (\text{if } Q = \text{NaN and } U \neq \text{NaN}).$$

6. Divide P_λ without NaN into 15 parts according to solar elongation ϵ as follows,

$$\text{SE 66}: \ 64^\circ < \epsilon \leq 68^\circ, \ \text{SE 70}: \ 68^\circ < \epsilon \leq 72^\circ, \ \text{SE 74}: \ 72^\circ < \epsilon \leq 76^\circ,$$

$$\text{SE 78}: \ 76^\circ < \epsilon \leq 80^\circ, \ \text{SE 82}: \ 80^\circ < \epsilon \leq 84^\circ, \ \text{SE 86}: \ 84^\circ < \epsilon \leq 88^\circ,$$

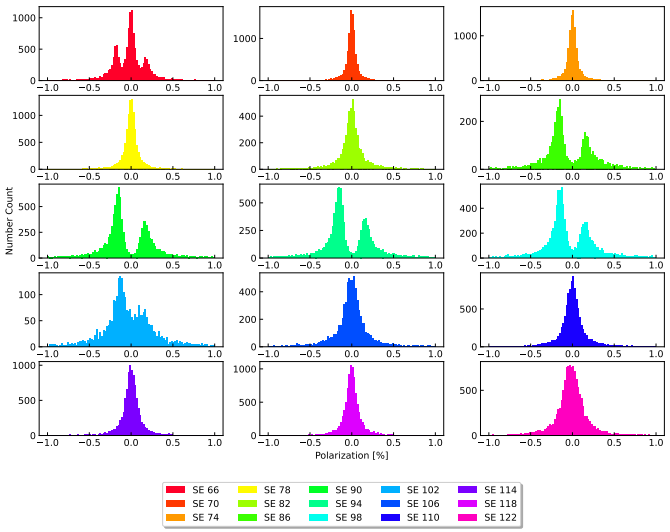

(A) Band1

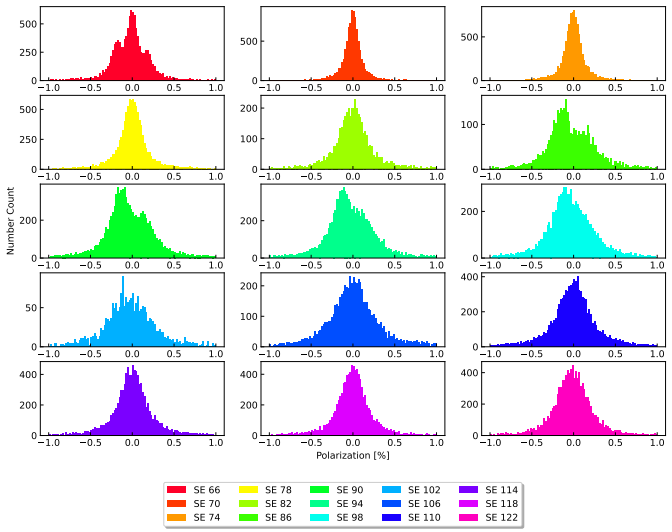

(B) Band2

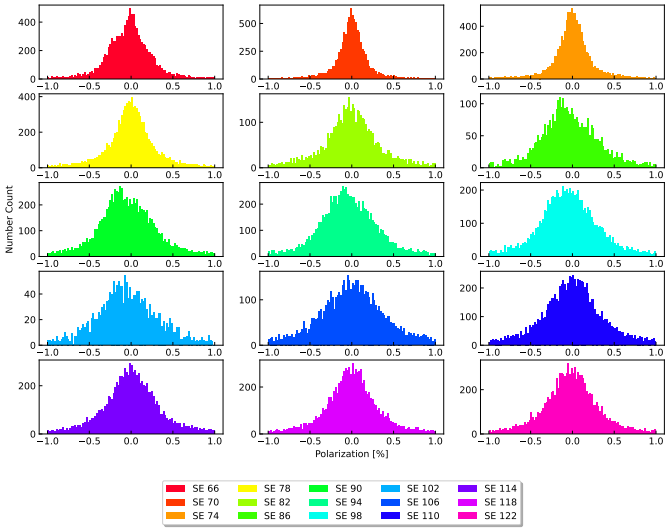

(C) Band3

FIGURE 3.7: Histogram of polarization $P_{\lambda,\,\mathrm{ZL}}$ in Region 0.

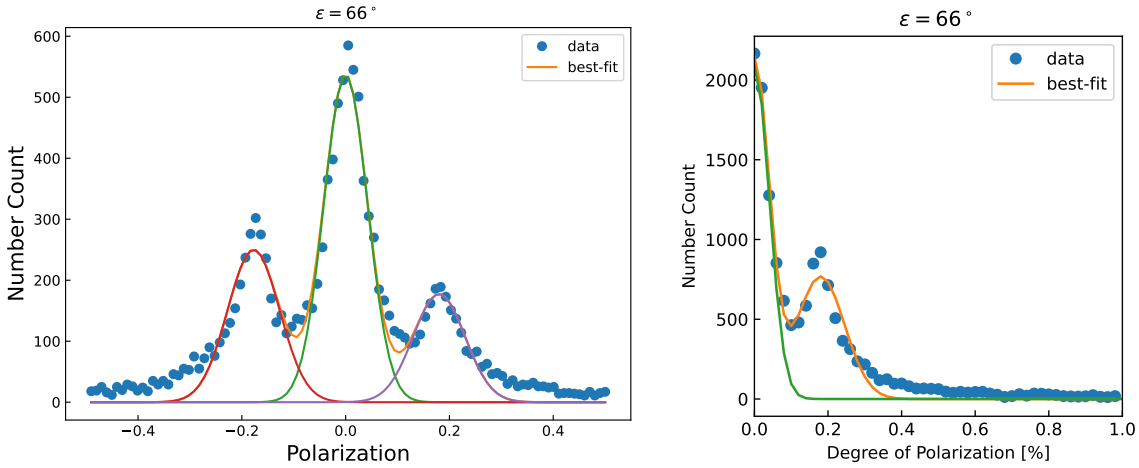

(A) $P_{\text{Band1, ZL}}$ (B) $|P_{\text{Band1, ZL}}|$

FIGURE 3.8: Histogram of polarization $P_{\text{Band1, ZL}}$ and degree of polarization $|P_{\text{Band1, ZL}}|$ at SE 66 in Region 0. There are three polarization peaks (red and purple), and the polarization near zero may come from low quality data (green). The orange line is the best fitting curve with triple Gaussian function for the data points.

$$\text{SE } 90: \ 88^\circ < \epsilon \leq 92^\circ, \ \text{SE } 94: \ 92^\circ < \epsilon \leq 96^\circ, \ \text{SE } 98: \ 96^\circ < \epsilon \leq 100^\circ,$$
$$\text{SE } 102: \ 100^\circ < \epsilon \leq 104^\circ, \ \text{SE } 106: \ 104^\circ < \epsilon \leq 108^\circ, \ \text{SE } 110: \ 108^\circ < \epsilon \leq 112^\circ,$$
$$\text{SE } 114: \ 112^\circ < \epsilon \leq 116^\circ, \ \text{SE } 118: \ 116^\circ < \epsilon \leq 120^\circ, \ \text{SE } 122: \ 120^\circ < \epsilon \leq 124^\circ.$$

7. Finally, correct P using the ZL intensity for each condition calculated from the Kelsall model. The corrected polarization $P_{\lambda,\text{ZL}}$ is expressed as:

$$P_{\lambda,\text{ZL}} = P_\lambda \frac{I_{\lambda,\text{ZL}}}{I_{\lambda,A}}.$$

Figure 3.7 shows the histograms of polarization $P_{\lambda,\text{ZL}}$ for each Band in Region 0. Figures for other regions are shown in Appendix D.1.

3.4.2 Solar Elongation Dependence

Figure 3.7(A) shows that there are two peaks at $\pm P_{\text{Band1, ZL}} \neq 0$ in the degree of polarization from SE 86 to SE 102, while three peaks including $P_{\text{Band1, ZL}} \simeq 0$ are found at SE 66. Polarization near 0 looks low observational accuracy and a large standard deviation, which may be able to removed by placing constraints on the $P_{\lambda,\text{ZL}}/\sigma_P$, only the values with high confidence are extracted from the polarization data (see Appendix C). In this subsection, I attempt to determine the degree of polarization at SE 66 by separating the polarization near 0 from the other two polarizations and extracting the polarization with the two non-zero peaks. Figure 3.8 shows the histogram of polarization $P_{\text{Band1, ZL}}$ and degree of polarization $|P_{\text{Band1, ZL}}|$ at SE 66 in Region 0. After subtracting the green curve from the data points, the representative values of $|P_{\text{Band1, ZL}}|$ at SE 66 are determined in three patterns: mean, median, and center of Gaussian fit. Figure 3.9 shows the results of determination of representative values $|P_{\text{Band1, ZL}}|$ in Region 0. The results of determination of representative

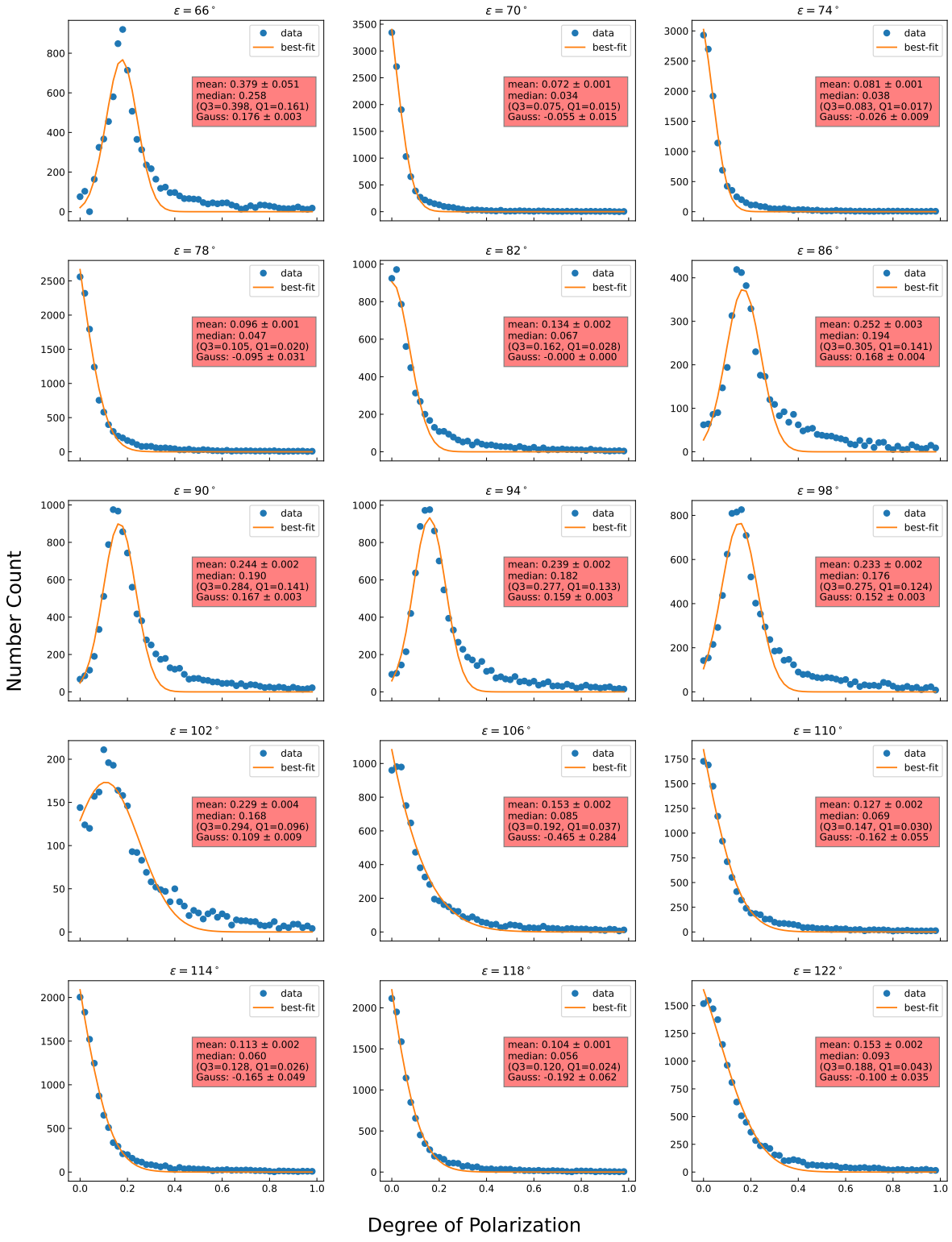

FIGURE 3.9: Histogram of degree of polarization $|P_{\text{Band1, ZL}}|$ in Region 0. The orange line is the best fitting curve with single Gaussian function for the data points. The standard error is applied to the error relative to the mean. The error relative to the center of the Gaussian fit indicates the standard error relative to the center value. The values of Q1 and Q3 for the median are shown.

TABLE 3.5: Parameters of the size distribution models

	Maximum Model		
Region	I	II	III
s[cm]	$7.96 \times 10^{-7} \sim 1.59 \times 10^{-5}$	$1.59 \times 10^{-5} \sim 2.88 \times 10^{-3}$	$2.88 \times 10^{-3} \sim 3.39 \times 10^{-2}$
c	6.95×10^{-23}	1.79×10^{-19}	2.21×10^{-25}
k	2.7	2.0	4.33
n_0[cm^{-3}]	9.49×10^{-13}	1.12×10^{-14}	1.91×10^{-17}
	Minimum Model		
Region	I	II	III
s[cm]	$7.96 \times 10^{-7} \sim 3.98 \times 10^{-5}$	$3.98 \times 10^{-5} \sim 2.14 \times 10^{-3}$	$2.14 \times 10^{-3} \sim 3.39 \times 10^{-2}$
c	1.27×10^{-23}	7.51×10^{-22}	5.03×10^{-26}
k	2.7	2.5	4.33
n_0[cm^{-3}]	1.75×10^{-13}	1.99×10^{-15}	1.17×10^{-17}

values $|P_{\text{Band2, ZL}}|$ and $|P_{\text{Band3, ZL}}|$ in Region 0 are shown in Appendix D.2. The degree of polarization varies greatly depending on the method used to determine the representative value. The standard error is applied to the error relative to the mean. The error relative to the center of the Gaussian fit indicates the standard error relative to the center value. By the limit theorem on the median, the error of the median is defined as

$$\frac{1}{4nf(\mu_{\text{median}})},$$

where μ is the sample median, n is the number of data, and $f(x)$ is the probability density function. Figure 3.10 shows the degree of polarizaton $P_{\text{Band1, ZL}}$ as a function of the solar elongation in Region 0. I plot the three results along with some models. The degree of polarization in each model is calculated by integrating along the line of sight in each field and assuming the IPD geometry of the Kelsall model. In addition to the scattering model already described in the Subsection 2.4.3, the degree of polarization from the Mie scattering model simulated using two size distribution models (Giese et al., 1978) of IPD particles is also shown. Figure 3.11 shows differential size distribution of IPD particles near 1 AU: the maximum model prefers a number density close to the upper limit of observation, while the minimum model approximates the lower boundary. Approximation of $f(s)ds$ by power laws dn in three size regimes i=I, II and III leads to the model parameters summarized in Table 3.5. The result of this work, as determined by the Gaussian fit, is consistent with the degree of polarization inferred from the scattering properties of the empirical model. The Rayleigh scattering and the Mie scattering by graphite with size distribution taken into account can be rejected as the principal mechanism of the ZL polarization. The degree of polarization of the geometric optics scattering model with graphite is similar to the result of this work determined by the median, and it can be explained by large dust size particles. Since there are in fact IPD particles of various sizes, the result of this work can be reproduced if the size distribution is dominated by a large dust contribution.

3.4.3 Wavelength Dependence

I plot the representative values of the ZL polarization spectra determined from each of the three analysis methods. Figure 3.12(A) shows the wavelength dependence of

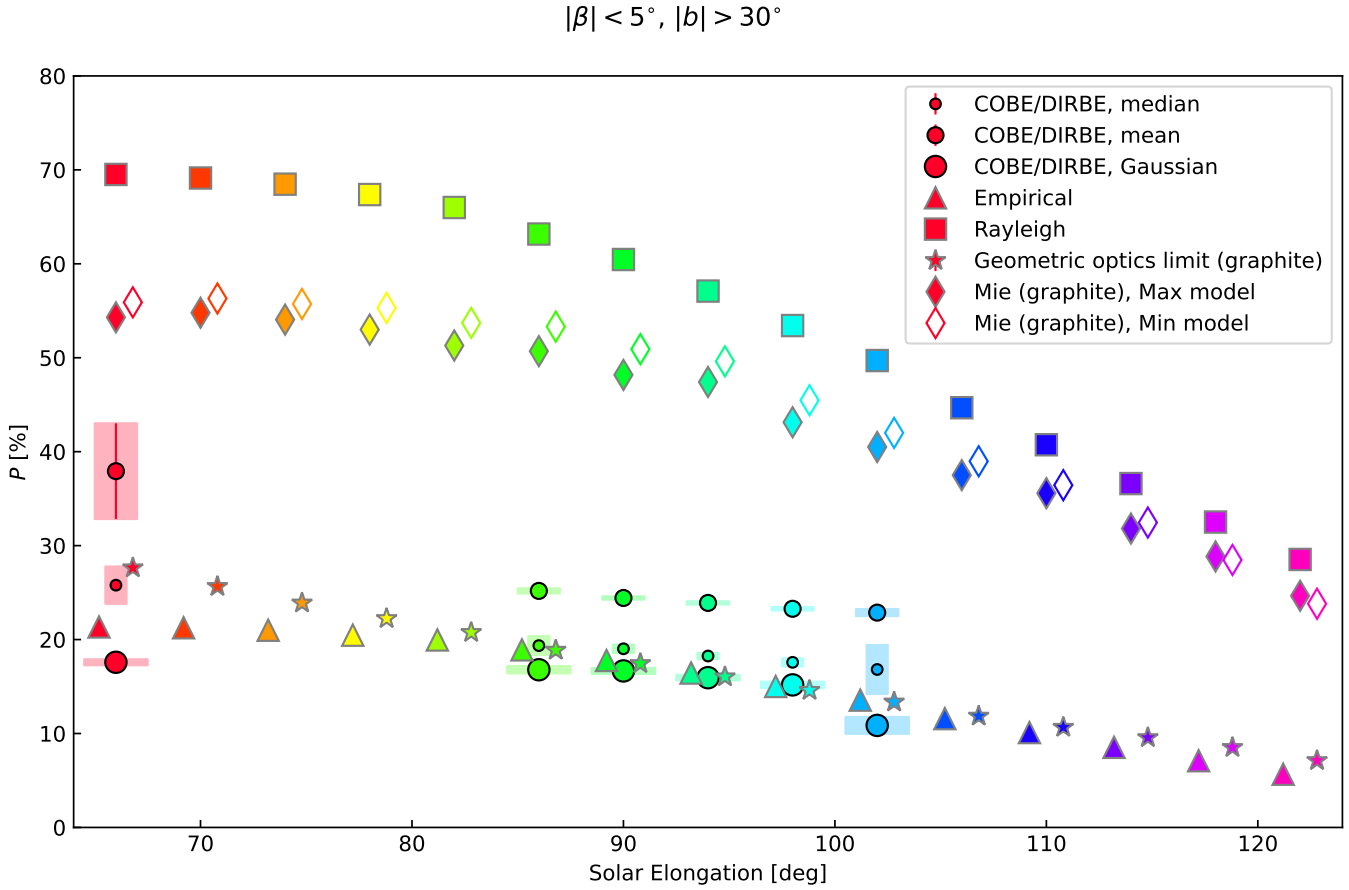

FIGURE 3.10: The degree of polarizaton $|P_{\mathrm{Band1,\,ZL}}|$ as a function of the solar elongation in Region 0. The small, medium, and large circles are the median, mean, and center of the Gaussian fit, respectively, of the results of this work. Thin, medium, and thick shades indicate the standard error relative to the median, the standard error relative to the mean, and the standard error relative to the center value, respectively. The triangles indicate the degree of polarization produced by the empirical scattering in the visible band (Leinert, 1975), and the squares present that calculated by the Rayleigh scattering (Bohren and Huffman, 1983) along the line of sight. The stars indicates the degree of polarization produced by the geometric optics scattering with graphite (Draine and Lee, 1984). The diamonds indicate the P_{ZL} produced by the Mie scattering considering the size distribution of the maximum and minimum model with graphite (Giese et al., 1978).

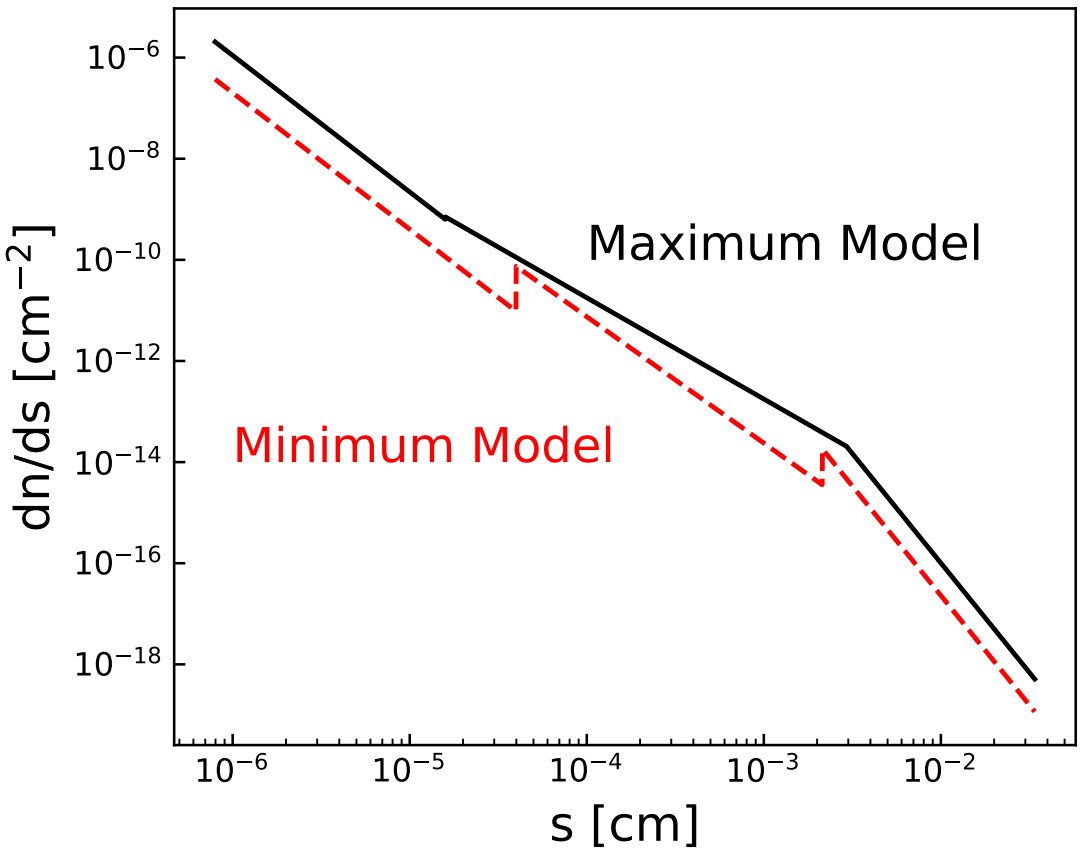

FIGURE 3.11: Differential size distribution of IPD particles near 1 AU (Giese et al., 1978). Maximum Model prefers a number density close to the upper limit of observation, while Minimum Model approximates the lower boundary. Approximations by power laws $dn = c_i s^{-ki} ds$; s[cm] particle radius; n[cm^{-3}] number density.

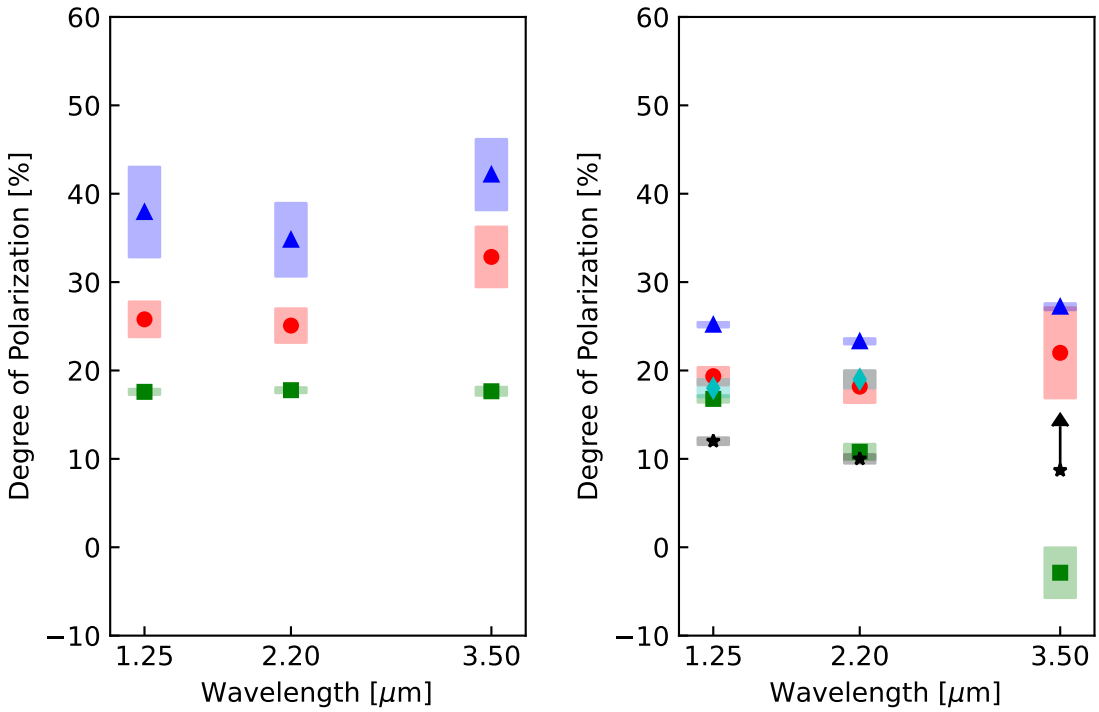

(A) $P_{\lambda,\,\mathrm{ZL}}$ at SE 66 (B) $P_{\lambda,\,\mathrm{ZL}}$ at SE 90

FIGURE 3.12: The wavelength dependence of $P_{\lambda,\,\mathrm{ZL}}$ at SE 66 and SE 90 in Region 0. The red circles, blue triangles, and green squares are the median, mean, and center of the Gaussian fit, respectively, of the results of this work. Each shades indicate the standard error relative to the median, the standard error relative to the mean, and the standard error relative to the center value, respectively. The degree of polarization calculated by Berriman et al. (1994) is shown as a black stars (1.25 and 2.2 μm) and arrow (limits at 3.5 μm). The cyan diamonds are the corrected degree of polarization $P_{\mathrm{ZL,DIRBE}}$ measured with *DIRBE/COBE* at $\lambda = 10^{\circ}$ and $\beta = 0^{\circ}$ (see Table 2.4).

$P_{\lambda,\,\mathrm{ZL}}$ at SE 66 in Region 0. The ZL polarization spectra are flat and weakly wavelength dependent for all the representative values. Figure 3.12(B) shows the wavelength dependence of $P_{\lambda,\,\mathrm{ZL}}$ at SE 90 in Region 0. Compared to the average value $P_{\mathrm{sky,DIRBE}}$ calculated by Berriman et al. (1994) using the same observation data, my mean calculation result shows more than twice the degree of polarization. On the other hand, the corrected degree of polarization $P_{\mathrm{ZL,DIRBE}}$ is consistent with the median of this work.

3.4.4 Ecliptic Latitude Dependence

Figure 3.13 shows the histogram of degree of polarization $|P_{\mathrm{Band1,\,ZL}}|$ at SE 90. The peak of the histogram of $|P_{\mathrm{Band1,\,ZL}}|$ is found near 20% for all ecliptic latitudes. Figure 3.14 shows the degree of polarizaton $P_{\mathrm{Band1,\,ZL}}$ as a function of the ecliptic latitude at SE 90. The degree of polarization varies greatly depending on the method used to determine the representative value, but the tendency for the degree of polarization to increase at higher ecliptic latitudes is the same. This tendency is also consistent with the degree of polarization observed from Earth at a wavelength of 500 nm. In addition, the two models compared in Figure 3.10, which are consistent with the results of this work, also show the same ecliptic latitude dependence, and the degree of polarization is consistent with the value obtained from the median.

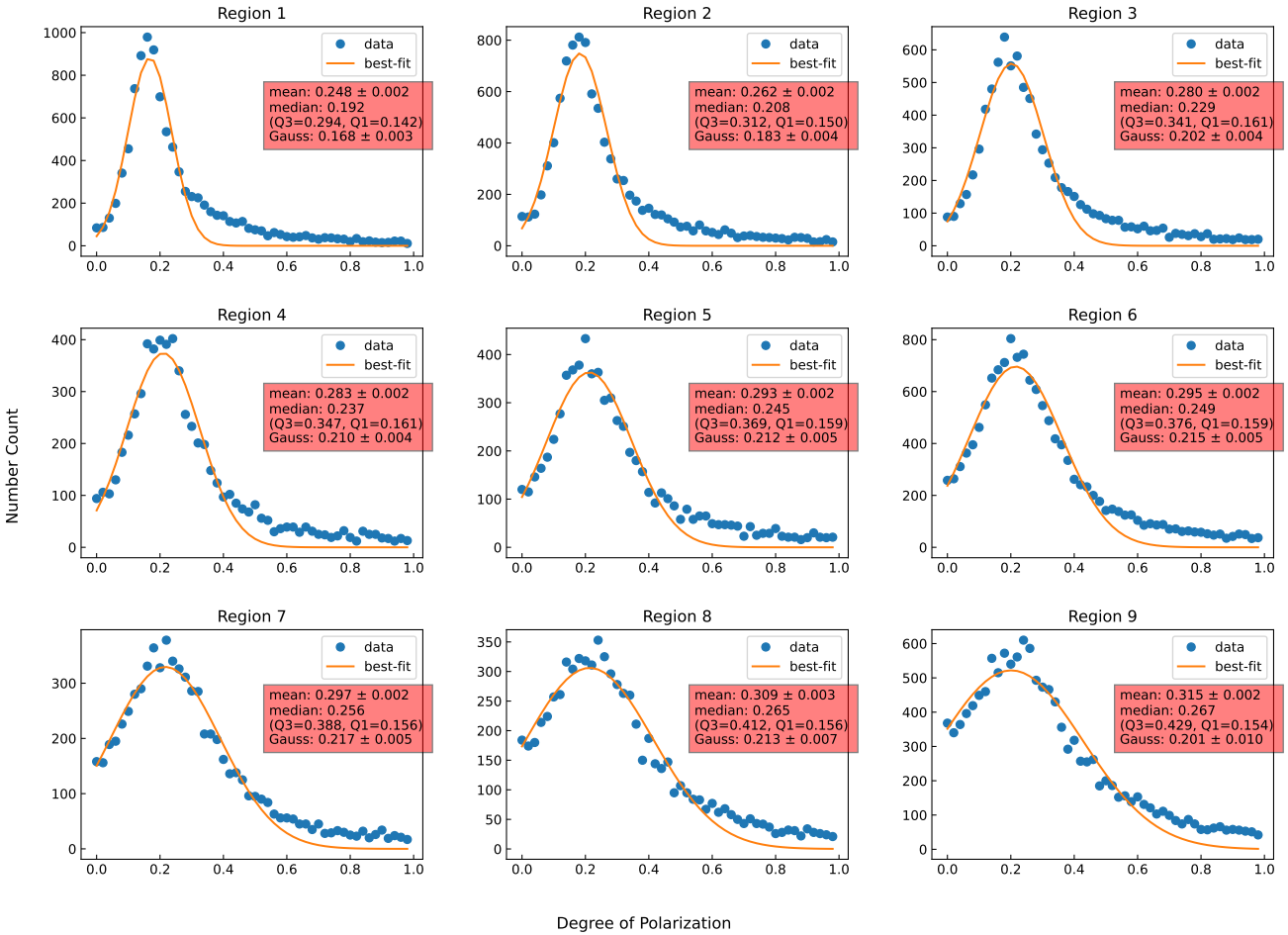

FIGURE 3.13: Histogram of degree of polarization $|P_{\text{Band1, ZL}}|$ at SE 90. The orange line is the best fitting curve with single Gaussian function for the data points. The standard error is applied to the error relative to the mean. The error relative to the center of the Gaussian fit indicates the standard error relative to the center value. The values of Q1 and Q3 for the median are shown.

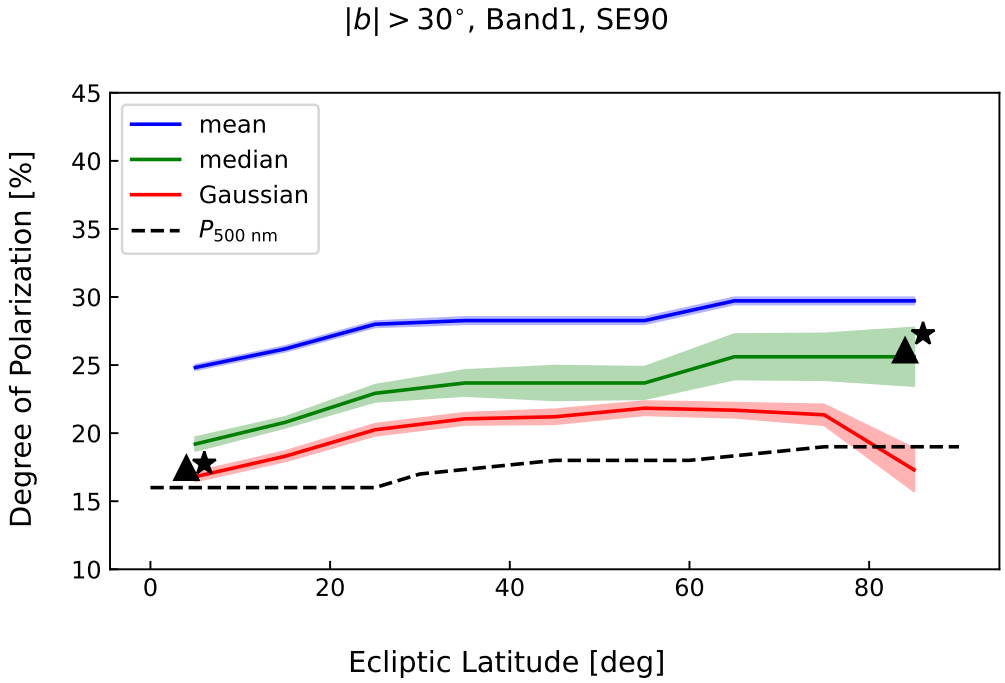

FIGURE 3.14: The ecliptic latitude dependence of $|P_{\text{Band1, ZL}}|$ at SE 90. The solid lines are the mean (blue), the median (green), and center of the Gaussian fit (red), respectively, of the results of this work. The shaded regions indicate the standard error relative to the mean, the standard error relative to the median, and the standard error relative to the center value, respectively. The black dashed line represents the ZL polarization at 500 nm (same data as Figure 1.6). The triangles indicate the P_{ZL} produced by the empirical scattering in the visible band (Leinert, 1975), and the stars indicates the P_{ZL} produced by the geometric optics scattering with graphite (Draine and Lee, 1984).

Chapter 4

DISCUSSION

4.1 SIZE OF INTERPLANETARY DUST

Figure 4.1 shows the comparison between the ZL polarization spectrum, the ZL polarization of five Mie models, and the comet polarization. In Figure 4.1, the ZL polarization has little wavelength dependence from visible to infrared. The similar scattering properties at different wavelengths suggest that large IPD grains contribute to the ZL polarization. This suggestion is supported by the fact that our observations are consistant with the ZL polarization calculated by the empirical scattering model in the visible band. The similar scattering properties at different wavelengths suggest that large IPD grains contribute to the ZL polarization. We provide another test for the IPD size by comparing the ZL polarization spectrum with the polarization of Mie scattering theories. We used five models with different particle radii (r=0.3, 0.5, 1, 3, and 10 μm) with a constant complex refractive index independent of wavelength, referring to $m = 2.98 + 1.6i$ for graphite, a typical absorber. The wavelength dependence of the ZL polarization from visible to infrared is consistent with the Mie scattering model for large particles ($r > 1$ μm). The observed degree of polarization is also roughly consistent with the Mie scattering model for large particles within the systematic uncertainty. In addition, the particle size of the IPD can be constrained in terms of the ZL intensity. In Figure 4.2 and Figure 4.3, The ZL brightness dependence on ecliptic latitude and solar elongation can be explained by the calculations with large size dust ($x \gg 1$).

As shown in Figure 2.9, our results can also be reproduced by the Mie scattering with graphite, suggesting that the IPD is dominated by large particles ($r >$ 1 μm). However, graphite is not a significant component of the IPD complex and could be a better analog for the very evolved organics detected in meteorites and comets (Hadamcik et al., 2020). The observed ZL polarization is not consistent with the Rayleigh scattering, which would favor a small IPD grain size ($x \ll 1$). The Rayleigh scattering implies that the amount of scattering is inversely proportional to the fourth power of the wavelength. However, the ZL polarization spectrum shows little wavelength dependence, therefore disfavoring the Rayleigh explanation. In fact, the IPD is composed of several of these components, suggesting that the larger particles contribute more to ZL polarization than the smaller ones. We have used the spherical IPD model as a comparison, but more complex shapes, such as aggregates and spheroids, have been considered in recent ZL scattering models (Lasue et al., 2007; Kimura et al., 2016). Our comparison results explain that IPD particles are not small spheres.

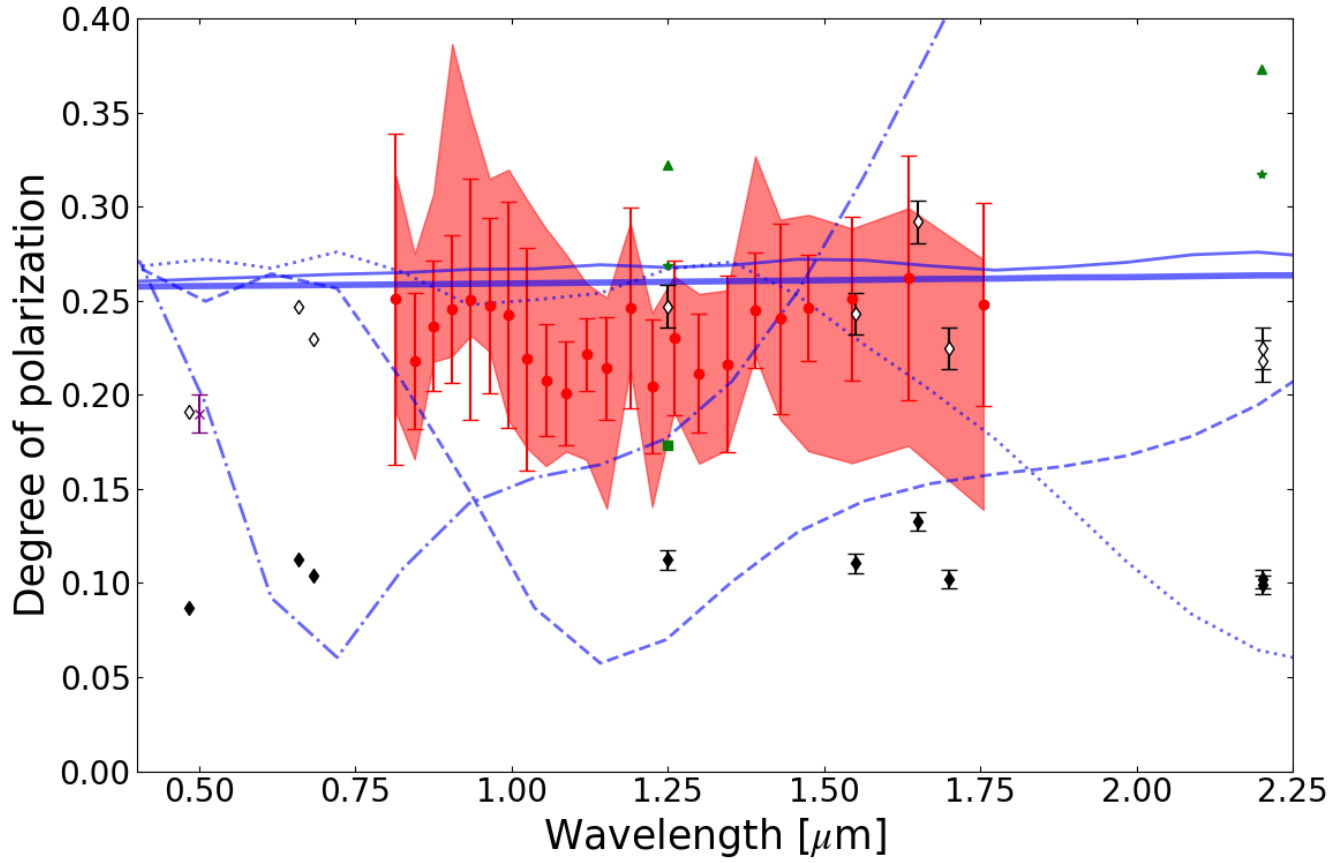

FIGURE 4.1: Comparison between the ZL polarization spectrum, the ZL polarization of five Mie models, and the comet polarization. The red filled circles indicate the ZL polarization spectrum, $P_{\rm ZL}(\lambda)$, at the NEP field. The error bars represent the total uncertainty from fitting of Equation B.2 and the polarization calibration. The red shaded region indicates the total systematic uncertainty. The green plots are the degree of polarization measured with DIRBE/COBE at $\lambda = 10^\circ$, $\beta = 0^\circ$, and SE 90. Triangles: the mean. Squares: center of the Gaussian fit. Stars: the median. The purple asterisk is the ZL polarization at 0.5 μm in the NEP field (Levasseur-Regourd and Dumont, 1980). The black diamonds are the polarization of comet Hale-Bopp extrapolated to 40° phase angle; the white diamonds are the same data, scaled by the purple asterisk (Kelley et al., 2004). The blue lines indicate the ZL polarization of five Mie scattering (spherical particle) models. Thick solid line: $r = 10$ μm. Thin solid line: $r = 3$ μm. Dotted line: $r = 1$ μm. Dashed line: $r = 0.5$ μm. Dashed-dotted: $r = 0.3$ μm.

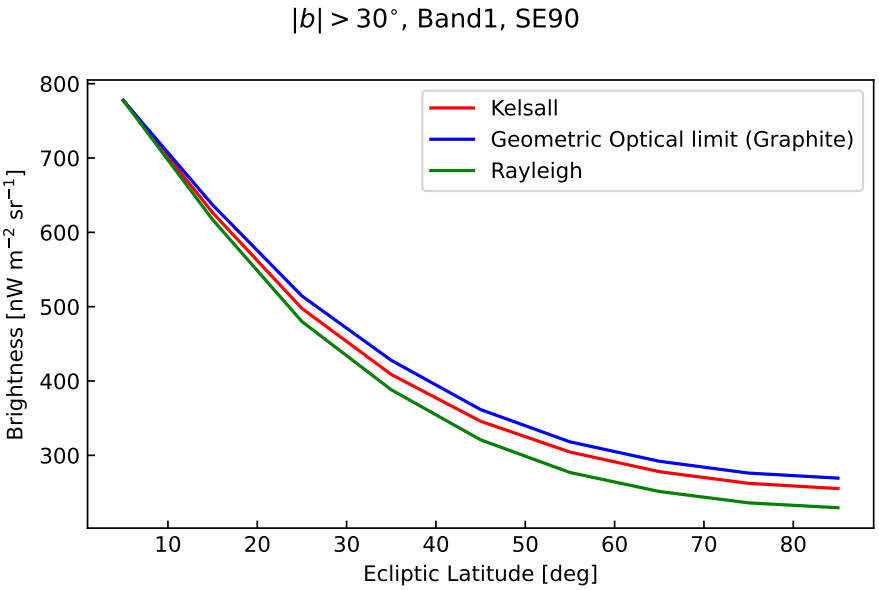

FIGURE 4.2: The ecliptic latitude dependence of the ZL brightness at SE 90 in Band 1. The red line indicates the ZL brightness calculated by Kelsall model based on *DIRBE/COBE* measurement. The blue line and the green line indicate the ZL brightness calculated from the geometric optics theory for $x \gg 1$ and Rayleigh theory for $x \ll 1$, respectively, and scaled by the ZL brightness in the ecliptic plane of the Kelsall model.

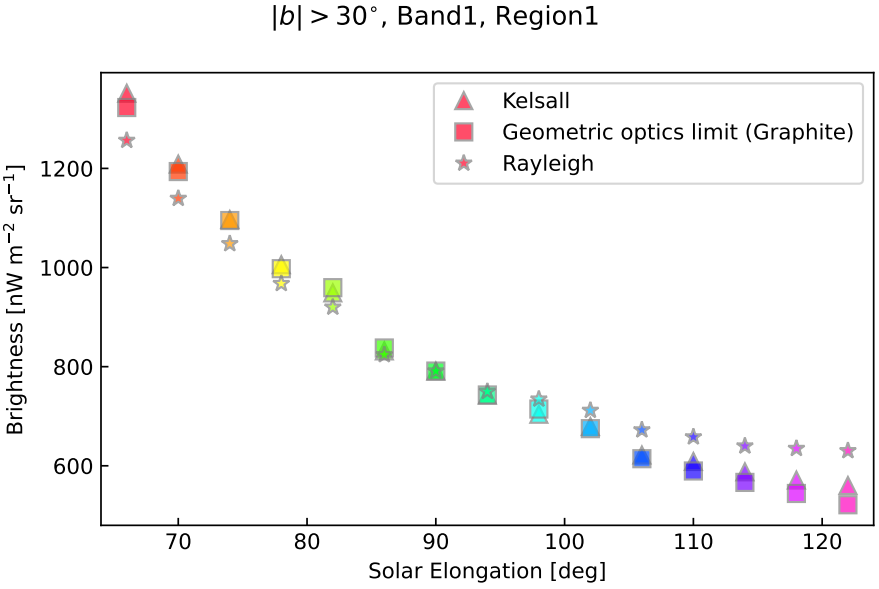

FIGURE 4.3: The solar elongation dependence of the ZL brightness at Band 1 in Region 1. The triangles indicate the ZL brightness calculated by Kelsall model based on *DIRBE/COBE* measurement. The squares and the stars indicate the ZL brightness calculated from the geometric optics theory for $x \gg 1$ and Rayleigh theory for $x \ll 1$, respectively, and scaled by the ZL brightness of the Kelsall model at $\epsilon = 90^\circ$.

4.2 COMPARISON WITH COMETARY DUST

In Figure 4.1, we also consider the polarization of the cometary dust of comet Hale-Bopp extrapolated to 40° phase angle. The polarization of cometary dust also has little wavelength dependence. This is consistent with our observed polarization and that of large absorbing materials. However, cometary dust also contains silicate. As reported by Ootsubo et al. (2009), the ZL spectrum exhibits crystalline silicate features at 9.3 and 11.35 μm. Silicate emission bands similar to comets were also detected in the ZL spectrum (Reach et al., 2003). Hanner (1999) also reported Mg-rich silicate features at 9.3 and 11.3 μm. Zubko et al. (2014) reproduced the polarization measurement in comet C/1975 V1 (West) in the visible band by modeling a mixture of weakly and highly absorptive particles with complex refractive indices $m = 1.5 + 0i$ or $1.6 + 0.0005i$ and $2.43 + 0.59i$. This mixture corresponds to Mg-rich silicates and amorphous carbon. Crystalline silicate features have been observed in the dust inner of the coma of comet C/1995 O1 Hale-Bopp (Wooden et al., 1999; Wooden et al., 2000). Lasue et al. (2009) also found evidence of a similar mixture comprising nonabsorbing silicate-type and absorbing organic-type materials in the cometary dust of comets C/1995 O1 Hale-Bopp and 1P/Halley.

Several lines of evidence based on different arguments make a compelling case to link the properties of the IPD particles to those of cometary dust particles. The dust density distribution models and related dynamics indicate that the majority of dust particles within 1 au from the Sun probably originate in major part from the activity of short period comets. This observation is also consistent with some of the properties detected for the meteoroids population impacting the Earth, almost all meteor showers have been linked with cometary parent bodies (Jenniskens and Jenniskens, 2006). The properties of IPD particles collected in the stratosphere of the Earth by airplanes are also consistent with primitive material and represent a family of samples that are chemically unlike the extraterrestrial matter represented by the meteorites originating from asteroids (Flynn, Nittler, and Engrand, 2016; Koschny et al., 2019). A population of micrometeorites with very high carbon content (from 48% to 85%) has also been studied, and their D/H ratios are more than one order of magnitude larger than the terrestrial values, strongly suggesting a cometary origin (Duprat et al., 2010).

4.3 FUTURE WORK

We cannot conclusively determine the origin of the IPD from our data alone. Future work is necessary to better constrain the properties of the IPD particles scattering the ZL. Further observation of comets and asteroids as well as theoretical modeling of the IPD scattering are required to reveal the origin of the IPD. Investigating the polarization properties of asteroidal dust is one of the most important goals of future works. In future model simulations, careful consideration of the variation of the complex refractive index of the astronomical material with wavelength will provide a better understanding of the structural and physical properties of the IPD (Dorschner et al., 1995). In addition, more detailed incorporation of complex particle shapes and size distributions into the model would allow us to reproduce the observed ZL polarization spectrum.

We will extend the ZL observation to shorter wavelengths using the second *CIBER* experiment, *CIBER*-2 (Takimoto et al., 2020). *CIBER*-2 was successfully

launched in mid-2021 and its data will provide a ZL spectrum at 0.5-2.5 μm. Future observations of ZL polarization spectra in the visible and near-infrared will help us understand the structural and physical properties of IPD. At the same time, the heliocentric IPD distribution will be observed by ZL observation from outside the Earth's orbit (0.7-1.5 au) by the *Hayabusa*-2 extended mission (Hirabayashi et al., 2021). These missions will allow us to better probe the origins of IPD. For future work, the sky regions that should be observed for near-infrared ZL polarization are near the Gegenschein region ($\lambda - \lambda_\odot \approx 180^\circ,\ \beta \approx 0^\circ$) and regions with small solar elongation ($\epsilon < 60^\circ$).

Chapter 5

SUMMARY

To determine the size and composition of the IPD, we observed the linear polarization spectrum of the ZL at the near-infrared wavelengths from 0.8 - 1.8 μm with the spectro-polarimetric function of the $LRS/CIBER$ instrument. We subtracted the contributions of the ISL, the DGL, and the EBL from the total sky brightness to derive the ZL polarization spectrum. The ZL polarization spectrum shows little wavelength dependence, and the degree of polarization shows clear dependence on the ecliptic coordinates and the solar elongation. I also analyzed the ZL polarization map data in the near-infrared wavelength bands of 1.25, 2.2, and 3.5 μm observed by the $DIRBE/COBE$ instrument. The measured degree of polarization and its solar elongation dependence are reproduced by an empirical scattering model in the visible band and also by a scattering model for large absorptive particles, while small particles cannot reproduce ($r < 1$ μm). The ZL brightness is also explained by large absorbing particles. All of our results suggest that the IPD is dominated by large particles. The wavelength dependence of the ZL polarization in a wide wavelength range including the visible band is similar to that of comet Hale-Bopp, although further data are needed to constrain the compositions. Additional work is needed for a better constrain on the particles' properties.

Appendix A

ZODIACAL LIGHT MODELS

A.1 KELSALL ZL MODEL

In order to quantify the ZL contribution at infrared wavelengths, the Kelsall ZL model employs a parameterized physical model that includes the three-dimensional density distribution and the physical properties of the IPD based on $DIRBE$ observations. The model for the IPD foreground computes the ZL intensity $Z_\lambda(p,t)$ $(= I_{\mathrm{ZL}})$ observed at wavelength λ for eachpixel p at time t as the integral along the line of sight of scattered and thermal emission contributions, summed over each density component c:

$$Z_\lambda(p,t) = \sum_c \int n_c(X,Y,Z)[A_{c,\lambda}F_\lambda^\odot \Phi_\lambda(\Theta) + (1-A_{c,\lambda})E_{c,\lambda}B_\lambda(T)K_\lambda(T)]ds$$

where $n_c(X,Y,Z)$ is the three-dimensional density for each of the components, $A_{c,\lambda}$ is the albedo for component c at wavelength λ, $F_\lambda^\odot$ is the solar flux, $\Phi_\lambda(\Theta)$ is the phase function at scattering angle Θ, $E_{c,\lambda}$ is an emissivity modification factor that measures deviation from the blackbody thermal radiance functon $B_\lambda(T)$, and $K_\lambda(T)$ is the $DIRBE$ color correction factor appropriate for $B_\lambda(T)$. The dust grain temperature T is assumed to vary with distance from the Sun as $T(R) = T_0 R^{-\delta}$. The derived model value of $\delta = 0.467$ is very close to the theoretical value of 0.5 for large gray grains in radiative equilibrium. The Kelsall ZL model assumes that the IPD consists of three components c: smooth cloud, dust bands, and circumsolar ring, which refer to the origin of JFCs (short-period comets from the Edgeworth-Kuiper belt with aphelion near Jupiter's orbit), asteroids, and the ring-shaped components in the Earth's orbit, respectively. Figure A.1 shows the density distribution of each IPD component determined by this method.

In the Kelsall ZL model, the density distribution of the smooth cloud is assumed to be separable into radial and vertical terms (Giese, Kneissel, and Rittich, 1986):

$$n_c(X,Y,Z) = n_0 {R_c}^{-\alpha} f(|Z_c/R_c|),$$

where n_0 is the IPD density at $R = 1$ au, R_c and Z_c denote the radial and vertical distance from the symmetric plane of the smooth cloud, α is the radial power law motivated by the radial distribution expected for particles under the influence of Poynting-Robertson drag. The vertical distribution $f(|Z_c/R_c|)$ was written in a form representing a widened, modified fan model:

$$f(|Z_c/R_c|) = e^{-\beta g^\gamma},$$

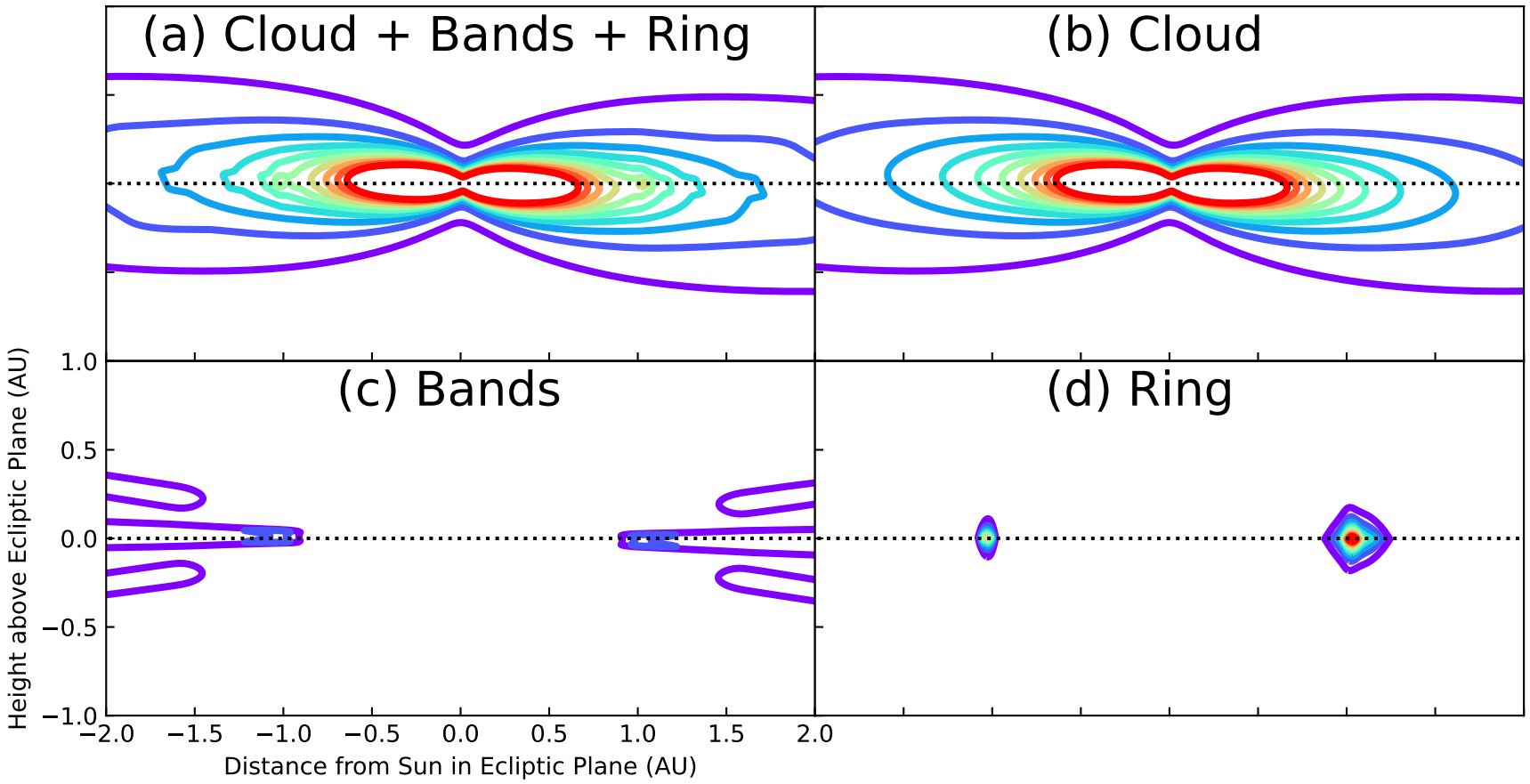

FIGURE A.1: Three-dimensional density of the IPD components. Isodensity contours of the IPD model components, shown for a cross-sectional slice perpendicular to the ecliptic plane: (a) all components combined; (b) smooth cloud; (c) dust bands; (d) circumsolar ring. Contour levels used for (c) and (d) are a factor of 8 smaller.

where

$$g = \begin{cases} (Z_c/R_c)^2/2\mu & \text{for } |Z_c/R_c| < \mu, \\ |Z_c/R_c| - \mu/2 & \text{for } |Z_c/R_c| \geq \mu, \end{cases}$$

and β, γ, μ are free parameters. The density distribution of dust bands consists of three band pairs, at ecliptic latitudes around $\pm 1.^\circ 4$ (Themis and Koronis families), $\pm 10^\circ$ (Eos asteroid family), and $\pm 15^\circ$ (Mario/Io family), respectively. All band pairs are at the center of the Sun, and the density distribution is

$$n_{Bi}(X,Y,Z) = \frac{3n_{3Bi}}{R}\exp\left[-\left(\frac{Z_{Bi}/R_c}{\delta_{|Z_{Bi}/R_c|}}\right)^6\right]\left[v_{Bi} + \left(\frac{Z_{Bi}/R_c}{\delta_{|Z_{Bi}/R_c|}}\right)^{p_{Bi}}\right]$$

$$\times\left\{1 - \exp\left[-\left(\frac{R}{\delta_{R_{Bi}}}\right)^{20}\right]\right\},$$

where n_{3Bi} is the density at 3 AU of band i, $\delta_{|Z_{Bi}/R_c|}$, v_{Bi}, and p_{Bi} are adjustable shape parameters. The parameter $\delta_{R_{Bi}}$ determines the distance to which band i migrates in toward the Sun. The circumsolar ring is the dust component bound by the Earth's gravity to a temporarily resonant orbit. The circumsolar ring also contains trailing blobs, which are dust components that follow the Earth's orbit in a steady state. The three-dimensional ring dust density distribution is modeled as

$$n_R(X,Y,Z) = n_{\mathrm{SR}}\exp\left[-\frac{(R-R_{\mathrm{SR}})^2}{2\sigma_{r\mathrm{SR}}^2} - \frac{|Z_R|}{\sigma_{z\mathrm{SR}}}\right]$$

$$+n_{\mathrm{TB}}\exp\left[-\frac{(R-R_{\mathrm{TB}})^2}{2\sigma_{r\mathrm{TB}}^2} - \frac{|Z_R|}{\sigma_{z\mathrm{TB}}} - \frac{(\theta-\theta_{TB})^2}{2\sigma_{\theta\mathrm{TB}}^2}\right],$$

where the subscript SR stand for the circumsolar ring and TB stands for the trailing blob. The σ values are free parameters for scale lengths in the R, Z_R, and θ coordinates. Also free are the radial locations of the peak density of the ring (R_{SR}) and blob (R_{TB}) and the peak densities n_{SR} and n_{TB}. See Kelsall et al. (1998) for further details and value of each parameter.

A.2 WRIGHT ZL MODEL

The Wright ZL model is that integrate a volume emissivity along the the line of sight specified by unit vector $\hat{n}$:

$$I_i(\hat{n},t) = \int \rho[r(s)][\kappa_i D_i(T(R)) + \sigma_i \Phi(\mu) D_i(T_\odot) R^{-2}]ds,$$

where $R = |r|$, and κ_i is a coefficient giving the efficiency in the i $DIRBE$ band of the IPD grains for thermal emission, while σ_i gives their scattering efficiency. The phase function is $\Phi(\mu)$ for scattering in terms of μ, the cosine of the scattering angle. $D_i(T)$ is the integral of the Planck function through the $DIRBE$ filter response functions. The position vector r is given by

$$r(s) = x_\oplus(t) + \hat{n}s,$$

where $x_\oplus(t)$ is the position of the Earth in its orbit around the Sun. $\rho(r)$ and $T(R)$ are the density and temperature of the IPD cloud, respectively. κ_i and σ_i are scaled

values of the grain efficiency factors. See Wright (1998) for further details and value of each parameter.

Appendix B

SUPPLEMENTARY INFORMATION ON *LRS/CIBER*

B.1 INSTRUMENTAL CALIBRATION FOR POLARIMETRY WITH *LRS/CIBER*

We describe the wavelength calibration, surface brightness calibration, and flat-field correction, and polarization calibration in this section. The wavelength calibration, surface brightness calibration, and flat-field correction are similar to Arai et al. (2015).

B.1.1 Wavelength Calibration

We conduct the wavelength calibration, which measures the relationship between the incident monochromatic light and a position on the detector array. For spectral calibration in the laboratory, we use two different light sources consisting of the SIRCUS (spectral irradiance and radiance responsivity calibrations using uniform sources) laser facility and a standard quartz-tungsten-halogen lamp coupled to a monochrometer. To illuminate the *LRS*, both light sources are coupled via fiber to an integrating sphere 20 cm in diameter. After exposure to a monochromatic light source, the detected signal is fitted with a Gaussian function. The accuracy of the wavelength calibration is calculated to be ± 1 nm by combining the center of this Gaussian function with the externally determined wavelength of the incident light.

B.1.2 Surface Brightness Calibration

The *LRS* sensitivity requirement is $\sim$ 10 nW m^{-2} sr^{-1}, corresponding to a 4% level of the sky brightness. To find the conversion between the photocurrent and the surface brightness, we use two different light sources consisting of the SIRCUS laser facility and a super-continuum laser (SCL). Both light sources coupled to a 20 cm diameter integrating sphere through a fiber illuminating the *LRS* aperture. The setup for surface brightness calibration is basically the same as for polarization calibration shown in Figure B.1, but without the external polarizer (polarization holder). The calibration factor is calculated from the measurement results of both light sources. The statistical uncertainty of 1 σ is estimated to be less than 0.1% from the variance over all pixels of the detector array. The measured calibration factor is consistent within a 3% rms variation.

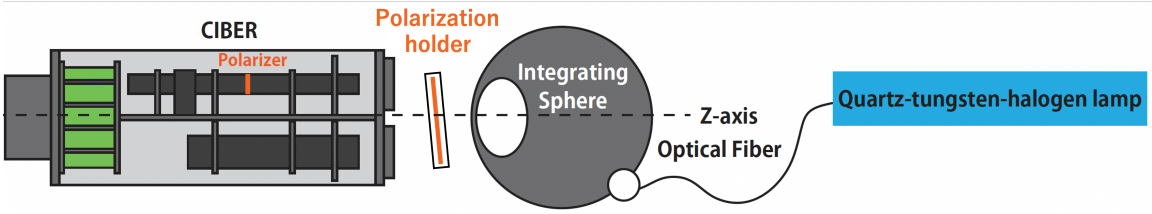

FIGURE B.1: Schematic view of the setup for the polarization calibration.

B.1.3 Flat-field Correction

In order to correct for the spatial fluctuations generated by the detector's nonuniform response, we use laboratory measurements to construct the flat field. We use three different light sources consisting of the SIRCUS laser facility, a SCL, and a standard quartz-tungsten-halogen lamp with a solar-like filter. All light sources are coupled via fiber to an integrating sphere with a diameter of 10 or 20 cm, which then illuminates the aperture of the *LRS*. By combining various light sources and integrating spheres, we can quantify the systematic uncertainty of the flat-field correction. The illumination patterns of the spheres are uniform with an accuracy of less than 1%.

B.1.4 Polarization Calibration

In order to characterize the polarization measurement, we conduct the polarization calibration in the laboratory. This polarization calibration determined the transmittance, the extinction ratio, and the relative angle of the *LRS* polarizer in the laboratory. The extinction ratio quantifies the performance of the polarizer and is expressed as

$$r_e = \frac{P_{\rm pol}}{P_{\rm unpol}}, \tag{B.1}$$

where $P_{\rm pol}$ is the polarization degree of the light passing through the polarizer, and $P_{\rm unpol}$ is the degree of the unpolarization $P_{\rm unpol} = 1 - P_{\rm pol}$. The extinction ratio of the polarizer for parallel light was known as > 1000 in advance, but not for convergent light. The *LRS* polarizer operates with converging rays, so its extinction ratio needs to be measured in the laboratory before the flight.

A schematic view of the setup for the polarization calibration is shown in Figure B.1. A standard quartz-tungsten-halogen lamp is used as the light source and is coupled to an integrating sphere through a fiber illuminating the *LRS* aperture. A 100 mm diameter wire-grid polarizing film is settled between the *LRS* aperture and the integrating sphere , which is installed on a rotational polarization holder. The polarization holder is rotated around the optical axis of the *LRS* by 10° steps.

In Figure B.2, we show the normalized photocurrent measured with the *LRS* as a function of the angle of the polarization holder, ϕ, at a the wavelength H band of 1.00 μm. To quantify the degree of polarization and the extinction ratio, we fit the following equation with the Levenberg-Marquardt algorithm:

$$I(\phi, \lambda) = I_{\rm pol}(\lambda) \sin 2(\phi - \phi_0(\lambda)) + I_{\rm mean}(\lambda), \tag{B.2}$$

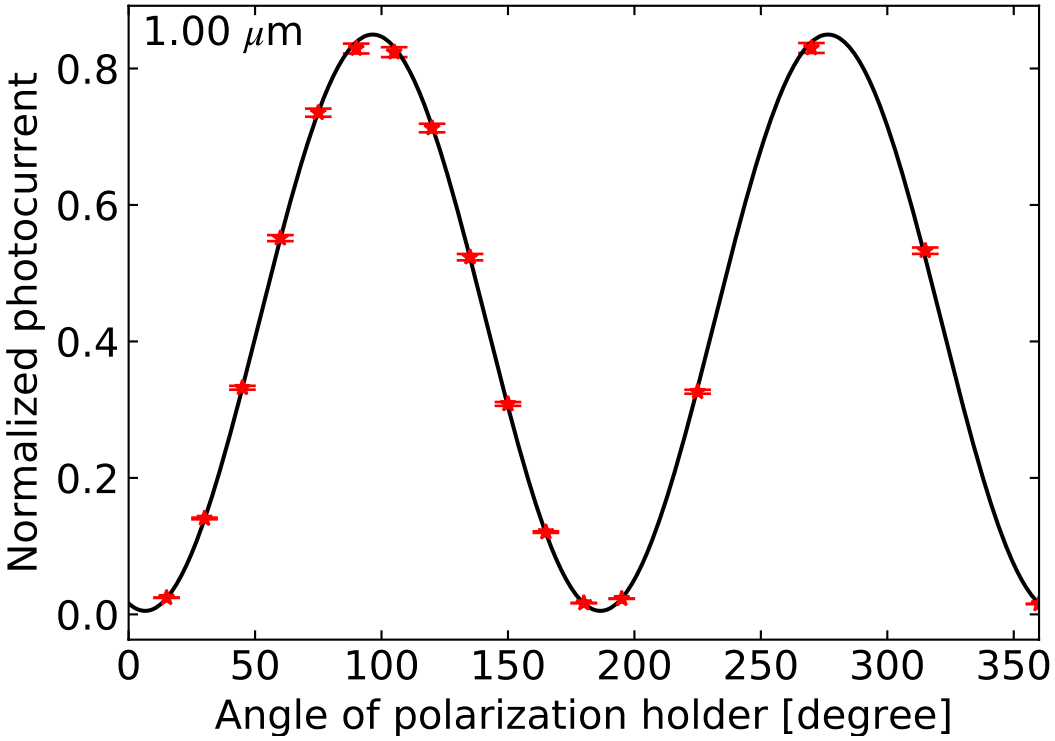

FIGURE B.2: Measured photocurrent through a polarization filter of $\theta = 0°$ as a function of the angle of polarization holder ϕ at 1.00 μm. Because the power of the light source is not stable, the y-axis is normalized by the photocurrent of the center slit. The red asterisks indicate measured data. The black curve indicates best-fit by Equation B.2 with the two variables $I_{\rm pol}$ and $I_{\rm mean}$.

where $I_{\rm pol}$ is the brightness of the polarized component, $I_{\rm mean}$ indicates the mean brightness of the light source, and $\phi_0(\lambda)$ represents the phase angle of polarization. The degree of polarization, $P_{\rm pol}$ is calculated by the following equation:

$$P_{\rm pol} = \frac{I(\phi_0 + 45°) - I(\phi_0 - 45°)}{I(\phi_0 + 45°) + I(\phi_0 - 45°)} = \frac{I_{\rm pol}}{I_{\rm mean}}. \tag{B.3}$$

We show the $P_{\rm pol}$ and $P_{\rm unpol}$ in Figure B.3. Although the $P_{\rm pol}$ for parallel light was larger than 0.999, and $P_{\rm unpol}$ is then less than 0.001, the $P_{\rm pol}$ measured in the experiment is ≈ 0.99. This is due to the oblique incident light at the position where the polarization film is installed in the *LRS*. However, $P_{\rm pol}$ is acceptably small to measure the polarization of ZL, and we regard the unpolarized component of 0.01 offset as a systematic uncertainty in the *LRS* data.

B.2 SYSTEMATIC UNCERTAINTY

Fig B.4 contains the same data as Fig 2.8, but overplotted with the instrumental and astronomical systematic uncertainties. The systematic uncertainties include the instrumental calibrations, the contributions from airglow emission, and the diffuse brightness estimation. The total systematic uncertainty is the upper limit because we assume maximum polarization of residual faint stars, and the DGL.

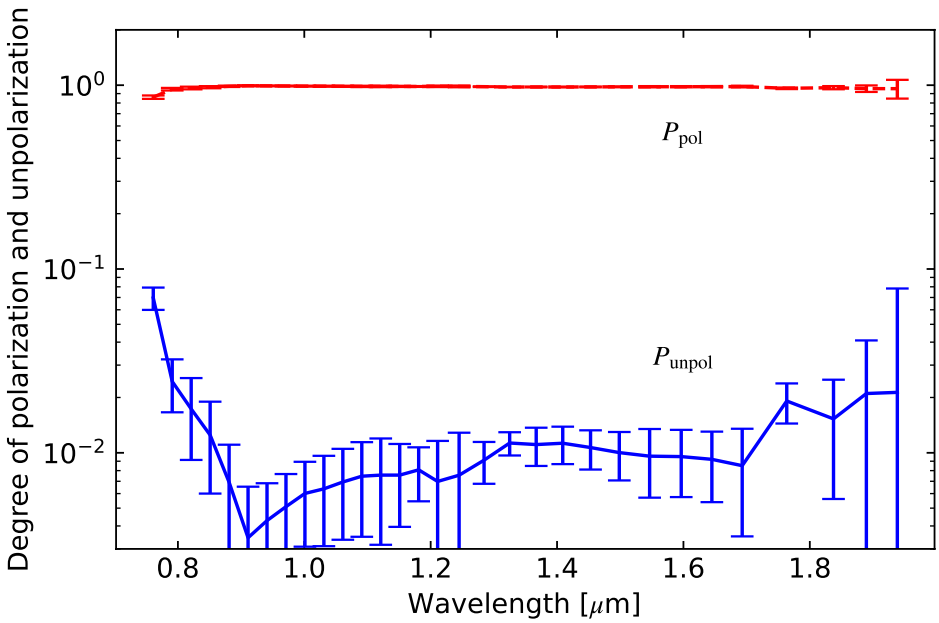

FIGURE B.3: The degree of polarization, $P_{\rm pol}$, and the degree of unpolarization, $P_{\rm unpol}$, of the *LRS* measured in the laboratory. The red dashed line indicates the degree of polarization defined by Equation B.3. The blue solid line indicates the degree of unpolarization. Each error bar represents the total uncertainty due to the fitting of Equation B.2 and polarization calibration.

B.2.1 Instrumental Systematic Uncertainty

Since the accuracy of the wavelength calibration is ± 1 nm, to quantify how the wavelength uncertainty propagates into the ZL polarization spectrum, we shift the wavelength by ± 1 nm, then recompute the ZL polarization spectrum with the shifted wavelength in each case. The uncertainty due to the wavelength calibration is then captured by the difference between the $+1$ and -1 shifted ZL spectra. As shown in Figure B.4, the propagated uncertainty is negligible.

We estimated the bias introduced by the flat-field correction by differencing the flat-field measurements from various integrating spheres. We used two integrating spheres with 10 and 20 cm exit port diameters as described in Arai et al. (2015). We then derive two ZL spectra for these two flat fields, and take their difference as the uncertainty of ZL polarization due to the flat field. The flat-field systematic uncertainty is $< 6\%$, which is acceptably small. To check the systematic uncertainty from the dark-current subtraction, we closed a cold shutter and measured the dark-current images twice, on the rail and during the flight. The flight-rail difference makes a ~ 0.03 e- s^{-1} systematic offset corresponding to ~ 0.7 nW m^{-2} sr^{-1} at 1.25 μm. We subtracted these dark-current images from the each sky image and then calculated the difference between the rail and flight cases, which gives us the bias from dark-current subtraction. The systematic uncertainty in the dark-current subtraction does not significantly affect the final results.

In general, the absolute brightness calibration uncertainty is canceled because the calibration is common between the polarization and the brightness channels. However, since we estimate the ZL brightness using a ZL model, a bias arises when comparing our data with the ZL model brightness. As described in Arai et al. (2015),

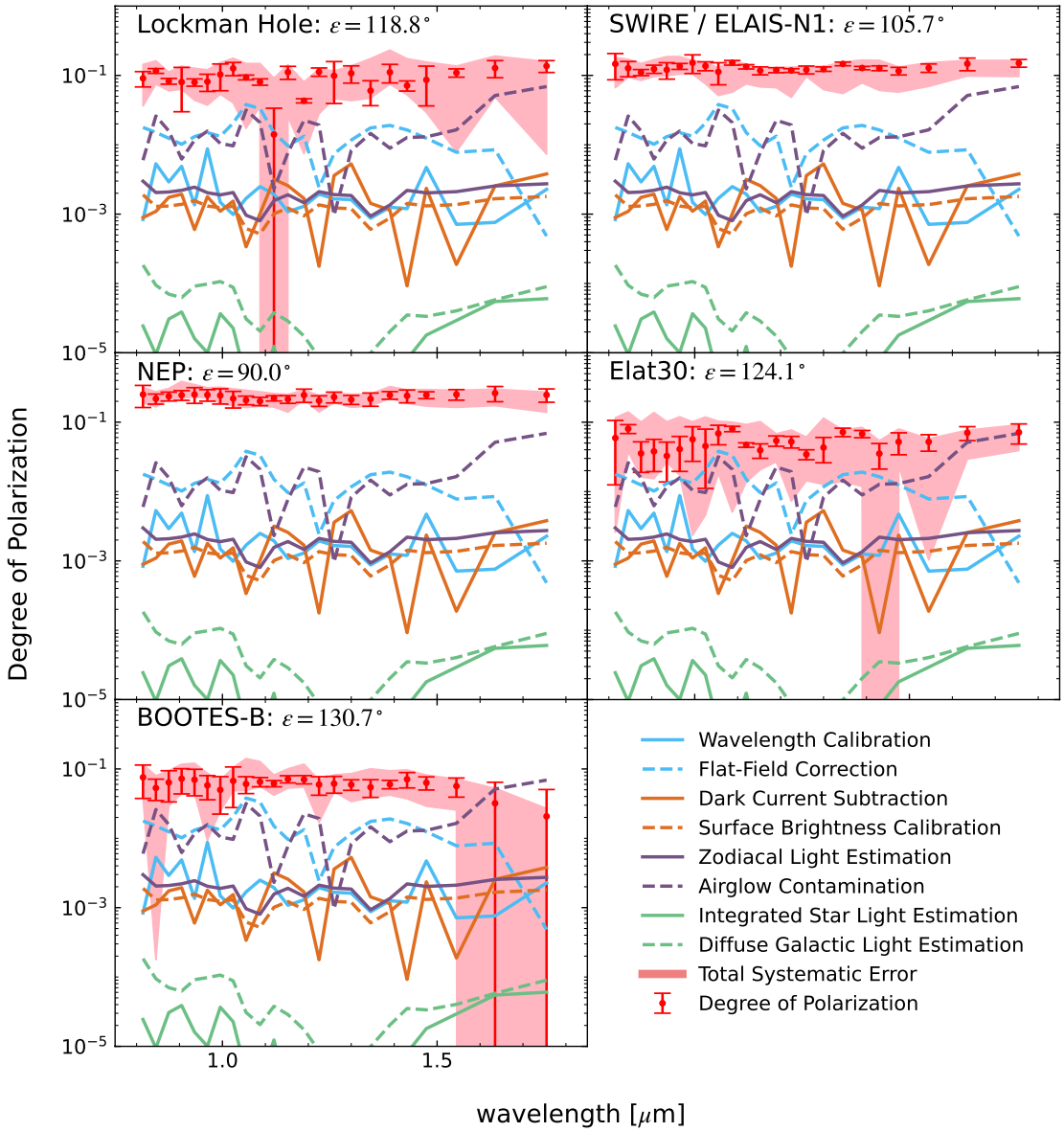

FIGURE B.4: The ZL polarization spectrum, $P_{\rm ZL}(\lambda)$, measured in the third flight (red filled circles). The instrumental systematic uncertainties associated with the wavelength calibration (aqua solid line), the flat-field (aqua dashed line), the dark-current subtraction (orange solid line), and the surface brightness calibration (orange dashed line) are indicated. The systematic uncertainties from the astronomical foreground composed by ZL (purple solid line), the airglow contamination (purple dashed line), the ISL (light green solid line), and the DGL (light green dashed line) are also presented. The red shaded region indicates the total instrument and astronomical systematic uncertainty that is the quadrature sum of the systematic uncertainties.

we conducted the absolute brightness calibration with several different setups in the laboratory. The measured calibration factors are consistent to within a 3% rms variation, which sets the uncertainty of the absolute brightness calibration.

To quantify the bias of the polarization measurement, we investigate the *LRS* polarization calibration data described in Section B.1. Although the extinction ratio of the wire-grid polarization film is higher than 1000, the measured extinction ratio of the *LRS* is 100. The opening angle of incidence at the polarization film in the *LRS* is large, so some incident light leaks and decreases the extinction ratio of the *LRS*. This means that the polarization measurement has a 0.01 offset. We regard this offset as the systematic uncertainty of the polarization measurement by the *LRS*.

B.2.2 Airglow Contamination

We attribute a time and a rocket-altitude dependence to the airglow emission, so the observed brightness is written as

$$I_{obs}(t,h) = I_{sky} + I_{air}(t,h), \tag{B.4}$$

where I_{air} indicates the brightness of the airglow emission, t is the time from the launch, and h is the altitude of the rocket. To estimate the contamination from airglow, we separate the sky image into a first- and a second-half integrations and derive the ZL polarization spectrum from each half. If there is difference between the ZL polarization spectra derived from the first- and the second-half images, this difference should be due to the airglow contamination. We calculate this difference as the bias from the airglow. The measured bias from the airglow contamination is $\sim$ 20% at the Lockman and Elat30 fields, $\sim$ 10% at the BOOTES-B field, $\sim$ 5% at the SWIRE field, and $\sim$ 2% at the NEP field. From these results, we confirm that the airglow contamination decays with time and the altitude of the rocket, because the amount of the airglow contamination in the first half is higher than that in the second half. Because the integration time of Elat30 is shorter than other fields, the large airglow contamination can also be due to noise. As shown in Figure B.4, the airglow contamination is not negligible but is acceptably small.

B.2.3 Astronomical Systematic Uncertainty

Starlight is known to be linearly polarized due to interstellar dust grains aligned by the magnetic field of the Galaxy (Heiles, 2000). The maximum polarization is 0.03 at $\tau_V = 1$, where τ_V is optical depth in the V band (Serkowski, 1973). If the brightness of residual faint stars is $\sim$ 15% of the ZL brightness at the NEP field, the maximum starlight polarization is 0.0045. Because stars are randomly distributed and the *LRS* FOV is large, the starlight polarization should be lower than this estimation. The starlight polarization is then only a few percent of the ZL polarization, which is negligible.

Because the DGL polarization has never been measured, we adopt the polarization of molecular clouds and reflection nebulae to quantify the DGL polarization. Hashimoto et al. (2007) measured the linear polarization of the Orion molecular clouds and reported that the maximum polarization is 0.10 and 0.19 at the J band and H band, respectively. Nagata et al. (1987) reported that the polarization of the extended reflection nebulae around GGD27 IRS and W75N IRS is $\sim$ 0.2 at 2.2 μm. From these results, we assume that the DGL polarization is $\sim$ 0.2. Because the DGL brightness is $\sim$ 10% of the ZL brightness at the NEP field, the contamination by the DGL polarization is 0.02.

Appendix C

Additional verification of *DIRBE* data

C.1 Improving the Quality of Polarization Data

By placing constraints on the $P_{\lambda,\mathrm{ZL}}/\sigma_P$, only the values with high confidence are extracted from the polarization data. Figure C.1 shows the polarization histograms for $P_{\mathrm{Band1,\ ZL}}/\sigma_P > k$ $(k = 1,2,3,4,5)$ in Region1. Figure D.1(A) is equivalent to $P_{\mathrm{Band1,\ ZL}}/\sigma_P > 0$.

C.2 Determination of Representative Values

Using the polarization data in each Region and each Band, determine the representative value of polarization in each solar elongation. Three values are candidates as representative values of polarization: the mean, the median, and the central value obtained by Gaussian fitting. The results of the Gaussian fitting of the histogram of absolute value of polarization, $|P_{\lambda,\ \mathrm{ZL}}|$, in each Region are shown in Appendix D.3. $P_{\lambda,\ \mathrm{ZL}}$ and the number of data, N, in each region and each solar elongation for three different representative values with the condition that $P_{\lambda,\ \mathrm{ZL}}/\sigma_P > k$ are also shown in Appendix D.4.

Comparing the three types of representative values, the most appropriate way to select a representative value for Band 1 seems to be the method using the median under the condition of $k \sim 3$. Figure C.1(A) shows that there are two peaks at $\pm P_{\mathrm{Band1,\ ZL}} \neq 0$ in the degree of polarization from SE 86 to SE 102, while three peaks including $P_{\mathrm{Band1,\ ZL}} \simeq 0$ are found at SE 66. Polarization near 0 has low observational accuracy and a large standard deviation, which can be removed by constraining by k. Therefore, it is possible to extract two peaks with high confidence in solar elongations that appear to have only one peak, such as SE 70 and SE 122. However, $k \sim 3$ appears to be the most plausible, since a strong constraint on k will reduce the number of remaining data and make it impossible to find the exact peak position. The most plausible representative value based on the remaining data is the median one, so in future discussions, the polarization at Band 1 will be calculated using the median of $k = 3$, unless otherwise noted. Figure C.1(B) also shows that SE 66 has three peaks. However, the standard deviation in Band 2 is more scattered than in Band 1, and the distribution is biased toward larger values, so the data cannot be separated based on the standard deviation. Similarly for Band 3, the good quality data is buried in the poor quality data and they cannot be separated, hence the median of $k = 0$ for Band 2 and Band 3 is defined as the lower limit value of polarization in future discussions. If there are exceptions, annotations will be given.

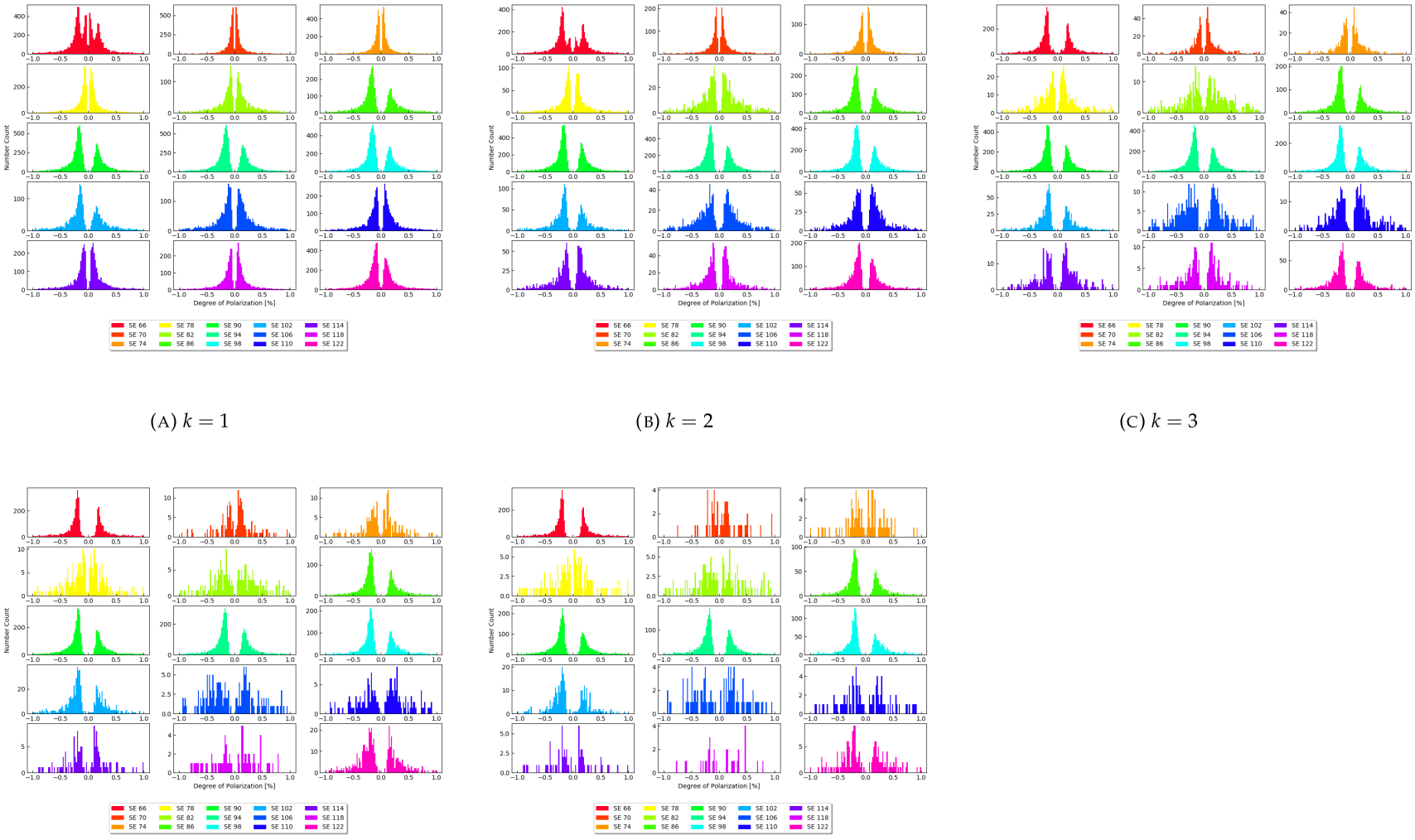

(A) $k = 1$ (B) $k = 2$ (C) $k = 3$

(D) $k = 4$ (E) $k = 5$

FIGURE C.1: Histogram of polarization for $P_{\text{Band1, ZL}}/\sigma_P > k$ in Region 1.

C.3 The Wavelength Dependence of Polarization

The wavelength dependence of $P_{\lambda,\,\mathrm{ZL}}$ in each Region and each solar elongation under the condition that $P_{\lambda,\,\mathrm{ZL}}/\sigma_P > k$ are shown in Appendix D.5. The wavelength dependence of polarization determined in Appendix C.2 is shown in Figure C.2. The wavelength dependence of polarization is weak in any Region. Considering that Band 2 and Band 3 are the lower limits of polarization, the wavelength dependence should be even weaker.

C.4 The Solar Elongation Dependence and the Ecliptic Latitude Dependence of Polarization

The solar elongation dependence and the ecliptic latitude dependence of $P_{\lambda,\,\mathrm{ZL}}$ under the condition that $P_{\lambda,\,\mathrm{ZL}}/\sigma_P > k$ are shown in Appendix D.6. The solar elongation dependence and the ecliptic latitude dependence of polarization determined in Appendix C.2 is shown in Figure C.3. In the region of high ecliptic latitude, the polarization is large and the degree of polarization of the ecliptic pole is about twice that of the ecliptic plane. On the other hand, the dependence of polarization on solar elongation is weak, and the dependence does not change at different ecliptic latitudes.

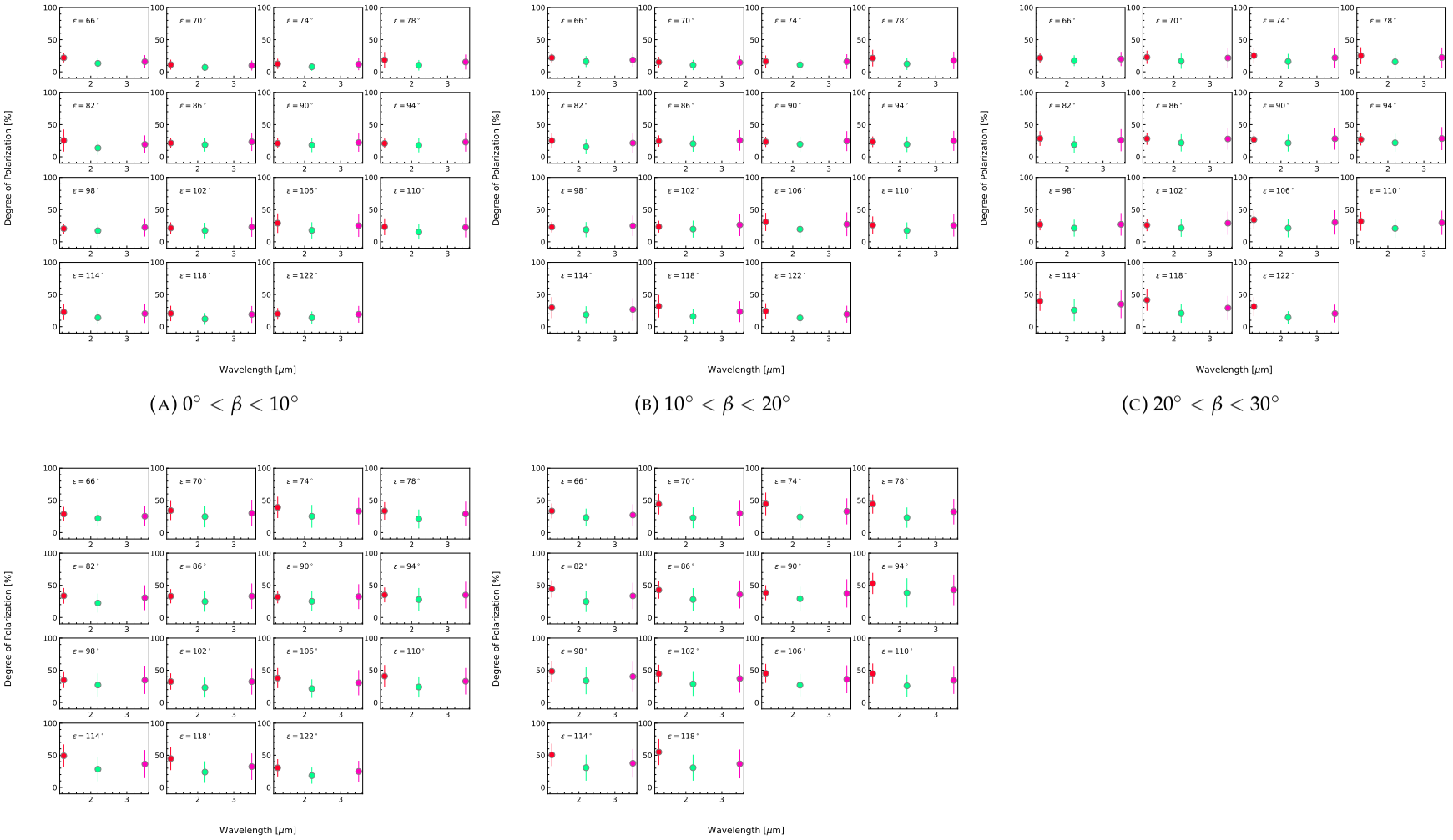

(A) $0° < \beta < 10°$ (B) $10° < \beta < 20°$ (C) $20° < \beta < 30°$

(D) $30° < \beta < 60°$ (E) $60° < \beta < 90°$

FIGURE C.2: The wavelength dependence of $P_{\lambda,\,\mathrm{ZL}}$ in each Region. Error bars indicate Quartile deviation relative to the median.

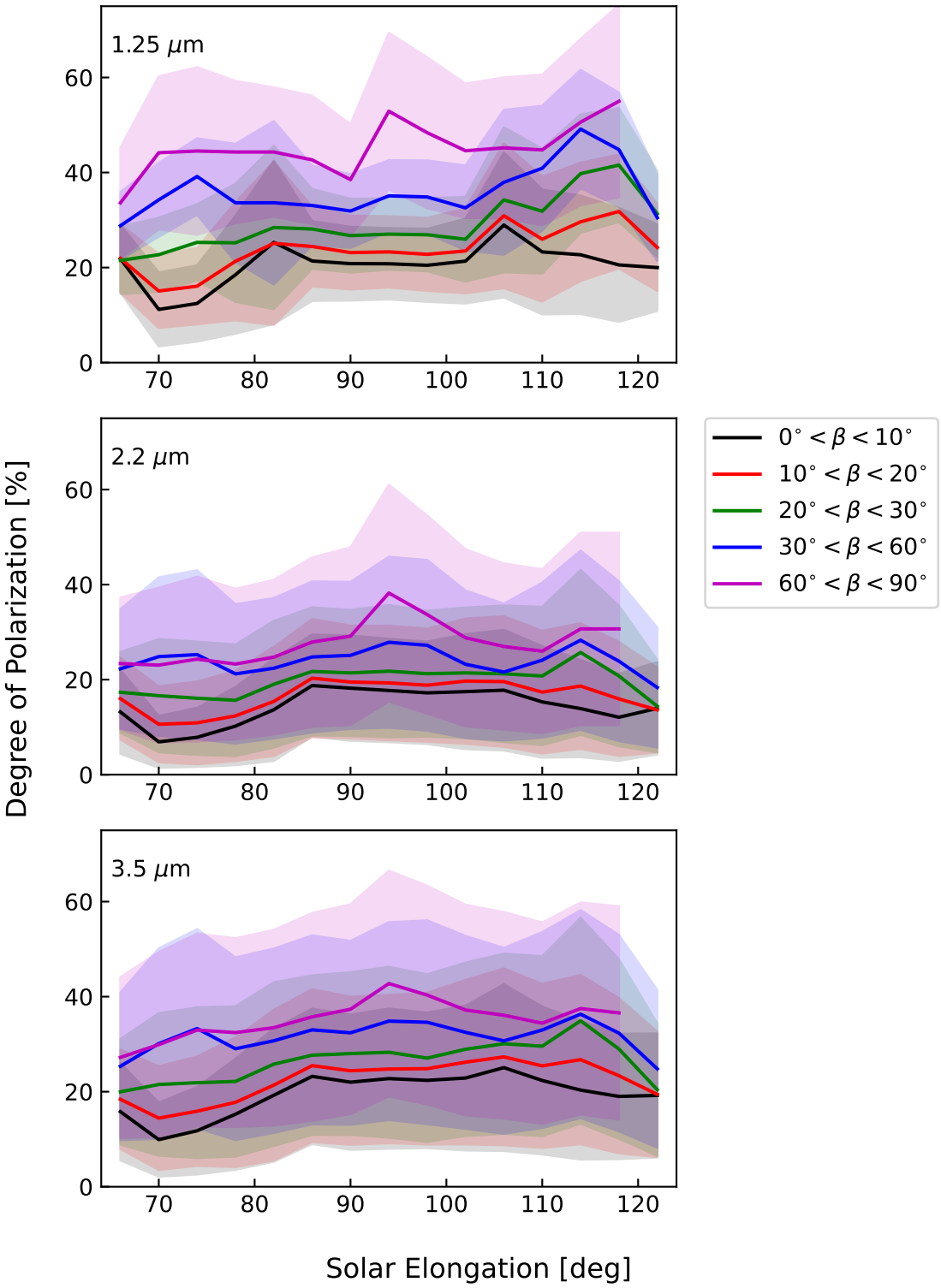

FIGURE C.3: The solar elongation dependence and the ecliptic latitude dependence of $P_{\lambda,\,\mathrm{ZL}}$ in each Region and each solar elongation. The shaded regions indicate Quartile deviation relative to the median.

Appendix D

EXTRA FIGURES

D.1 HISTOGRAM OF POLARIZATION IN EACH REGION

(Figure D.1, D.2, D.3, D.4, and D.5)

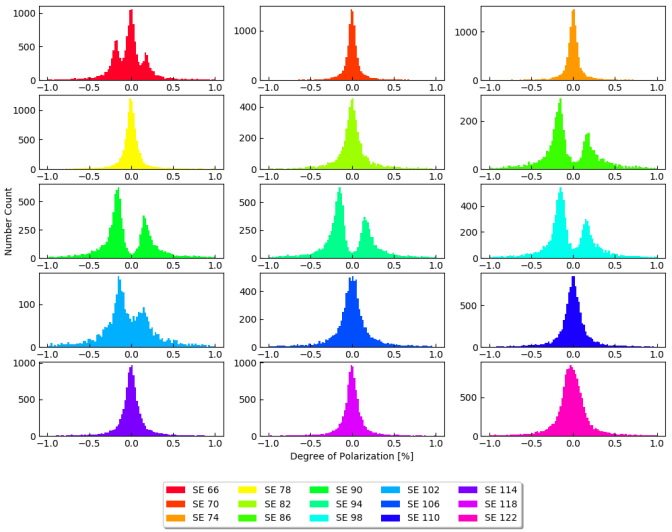

(A) Band1

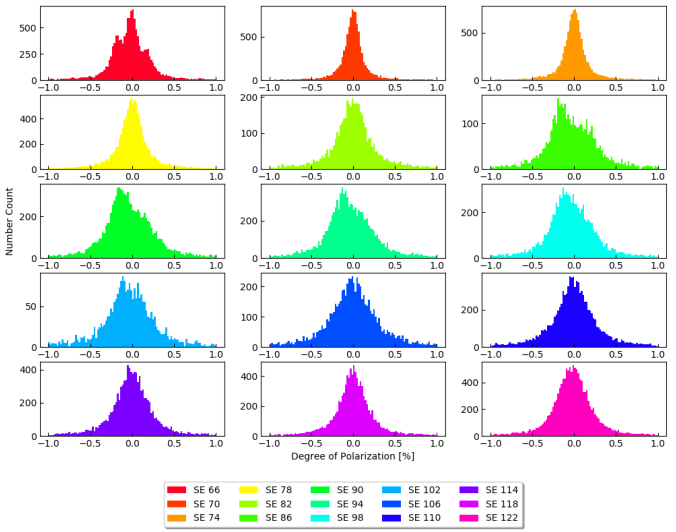

(B) Band2

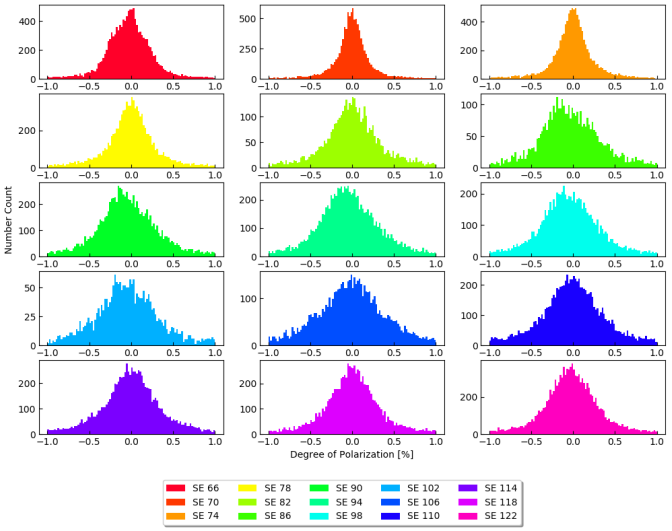

(C) Band3

FIGURE D.1: Histogram of polarization $P_{\lambda,\,\mathrm{ZL}}$ in Region 1.

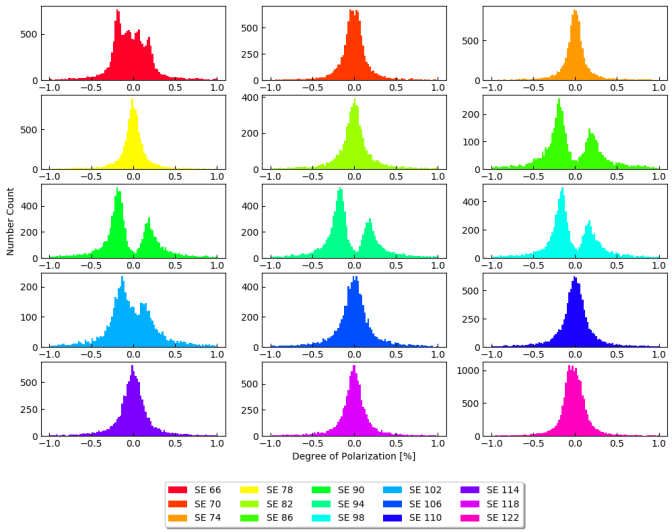

(A) Band1

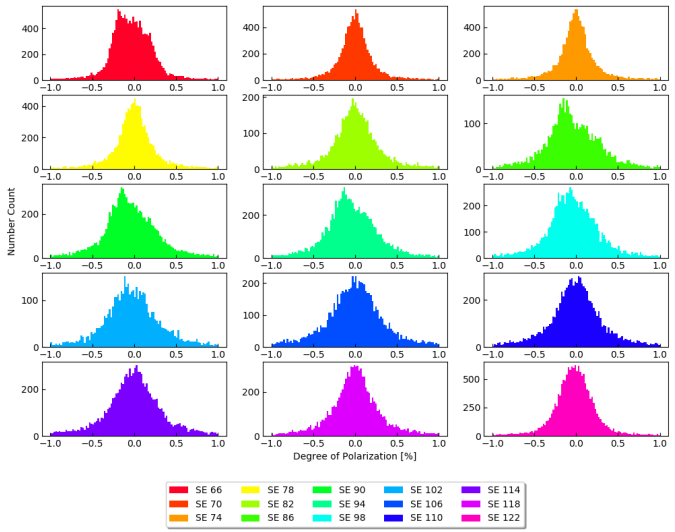

(B) Band2

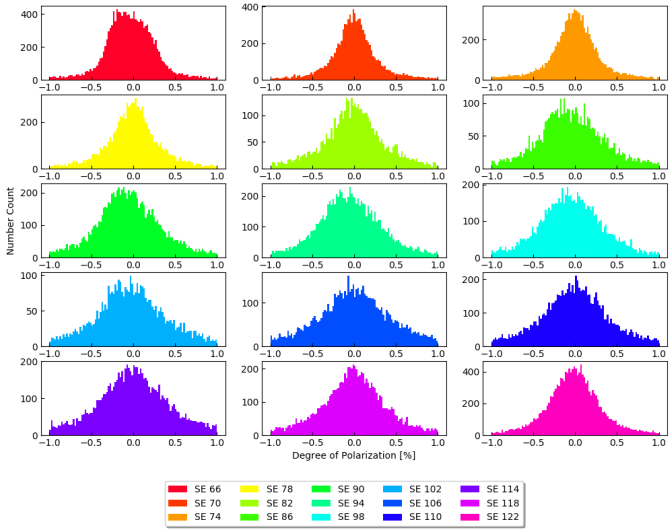

(C) Band3

FIGURE D.2: Histogram of polarization $P_{\lambda,\,\mathrm{ZL}}$ in Region 2.

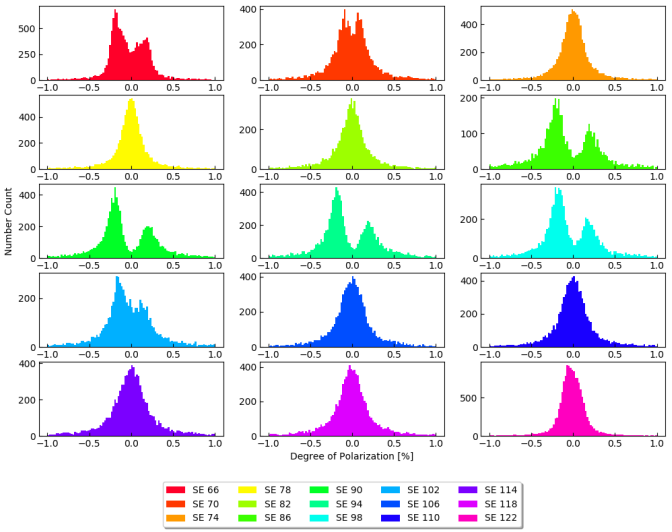

(A) Band1

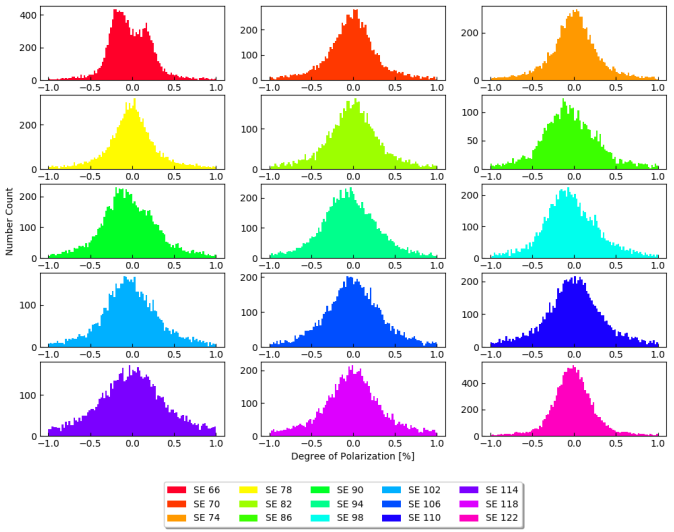

(B) Band2

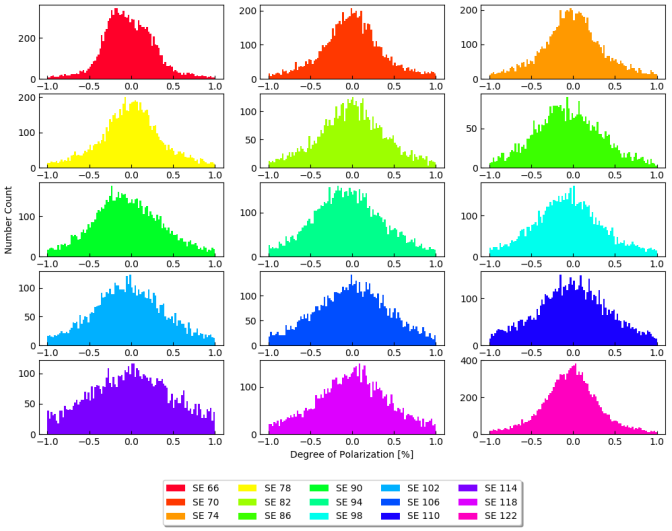

(C) Band3

FIGURE D.3: Histogram of polarization $P_{\lambda,\,\mathrm{ZL}}$ in Region 3.

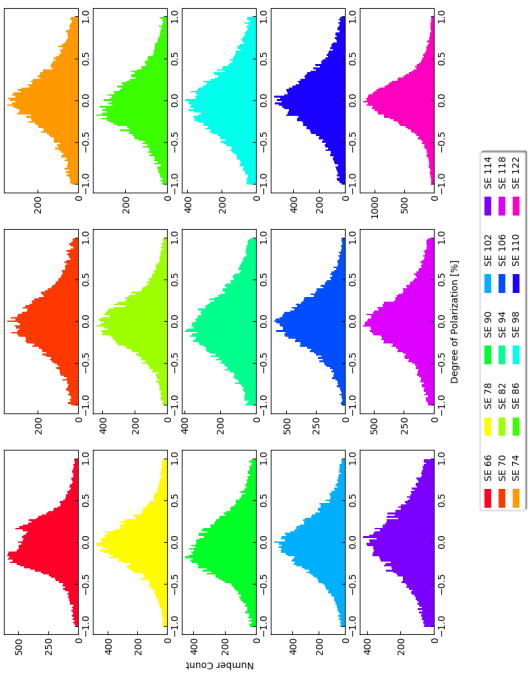

(B) Band2

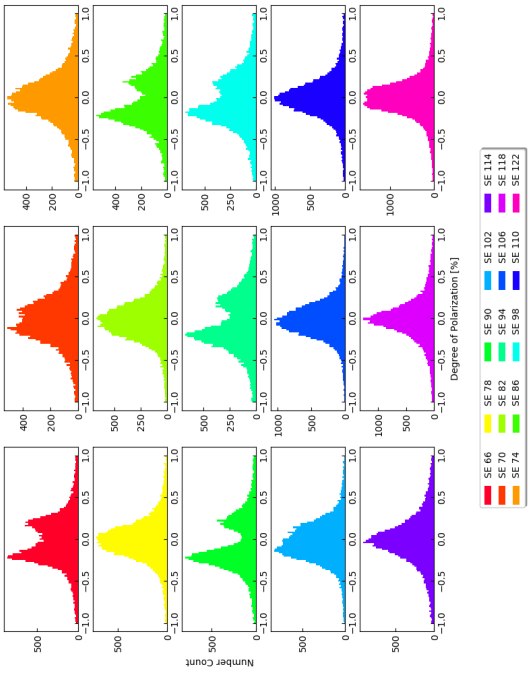

(A) Band1

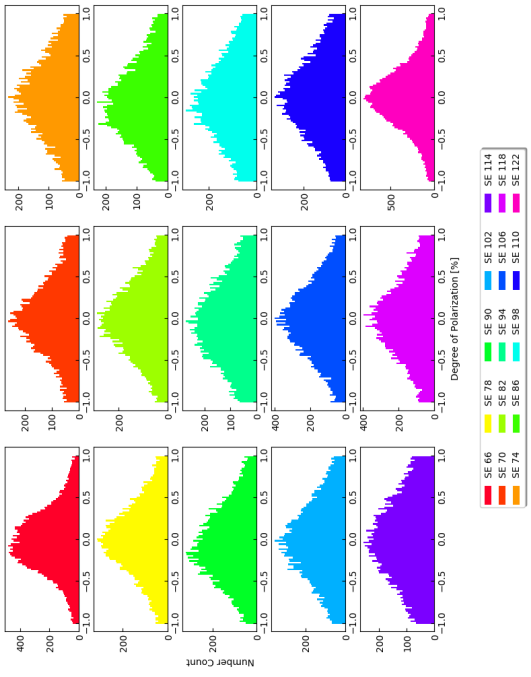

(C) Band3

FIGURE D.4: Histogram of polarization $P_{\lambda,\,\mathrm{ZL}}$ summed over Region 4, 5, and 6.

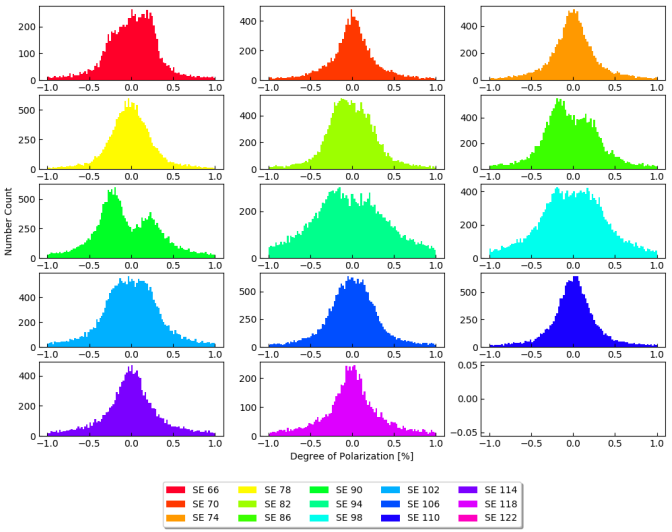

(A) Band1

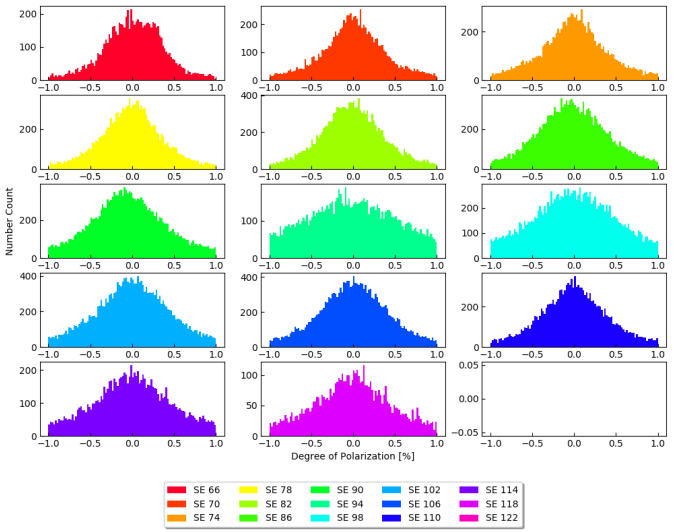

(B) Band2

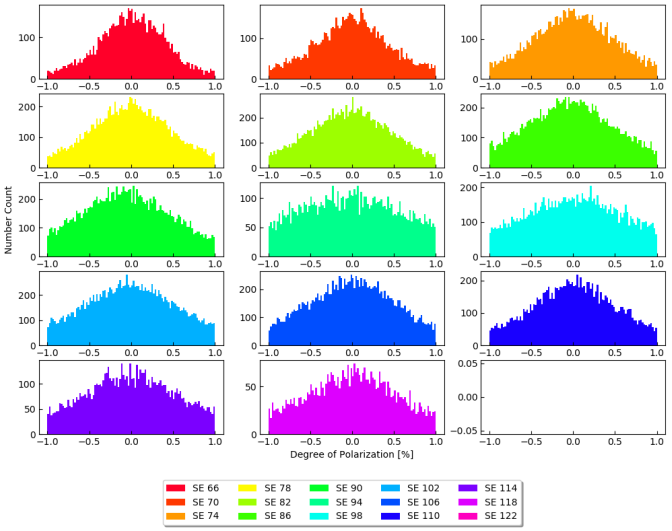

(C) Band3

FIGURE D.5: Histogram of polarization $P_{\lambda,\,\mathrm{ZL}}$ summed over Region 7, 8, and 9.

D.2 RESULTS OF GAUSSIAN FITTING FOR A HISTOGRAM OF POLARIZATION IN REGION 0

(Figure D.6 and D.7)

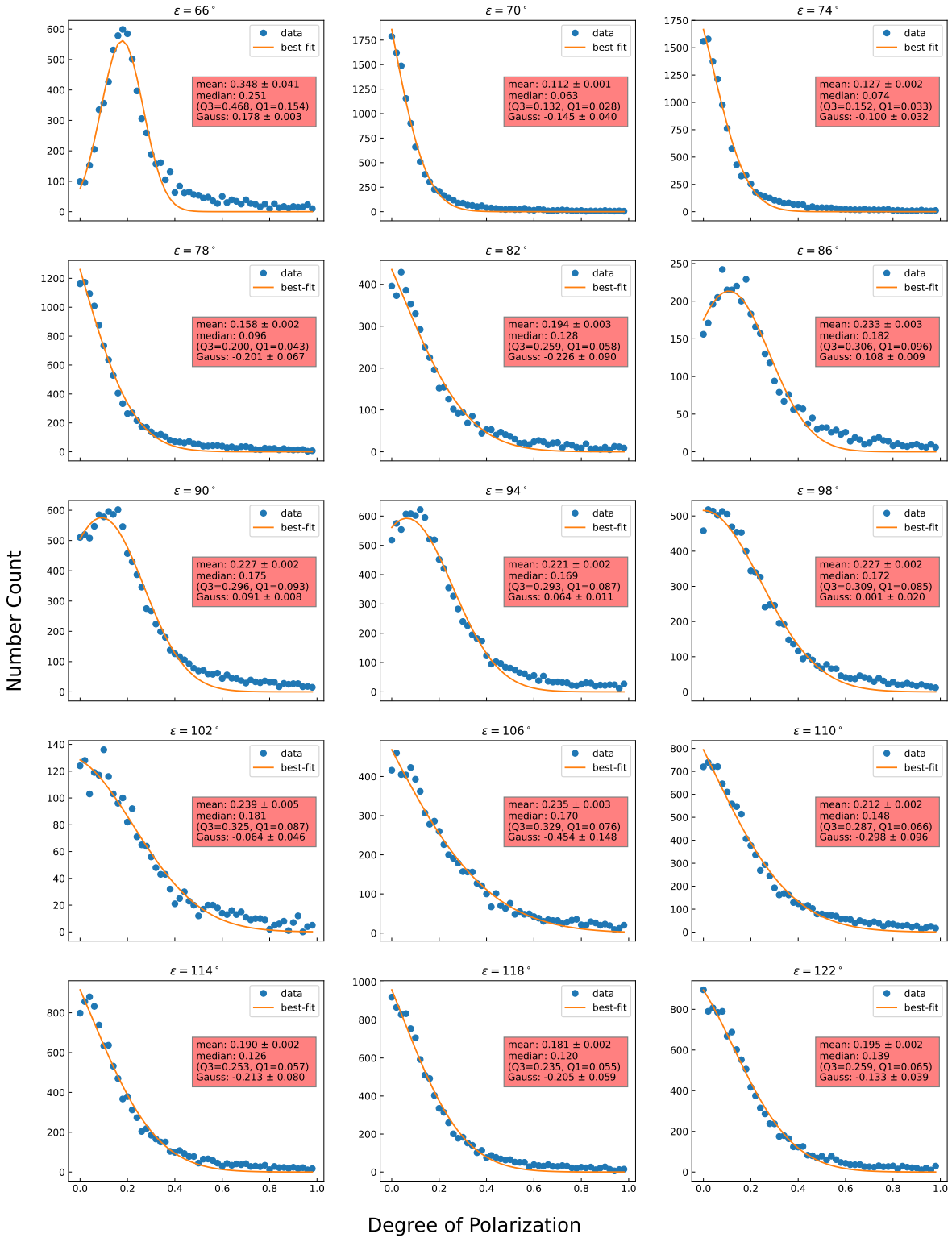

FIGURE D.6: Histogram of degree of polarization $|P_{\text{Band2, ZL}}|$ in Region 0. The orange line is the best fitting curve with single Gaussian function for the data points. The standard error is applied to the error relative to the mean. The error relative to the center of the Gaussian fit indicates the standard error relative to the center value. The values of Q1 and Q3 for the median are shown.

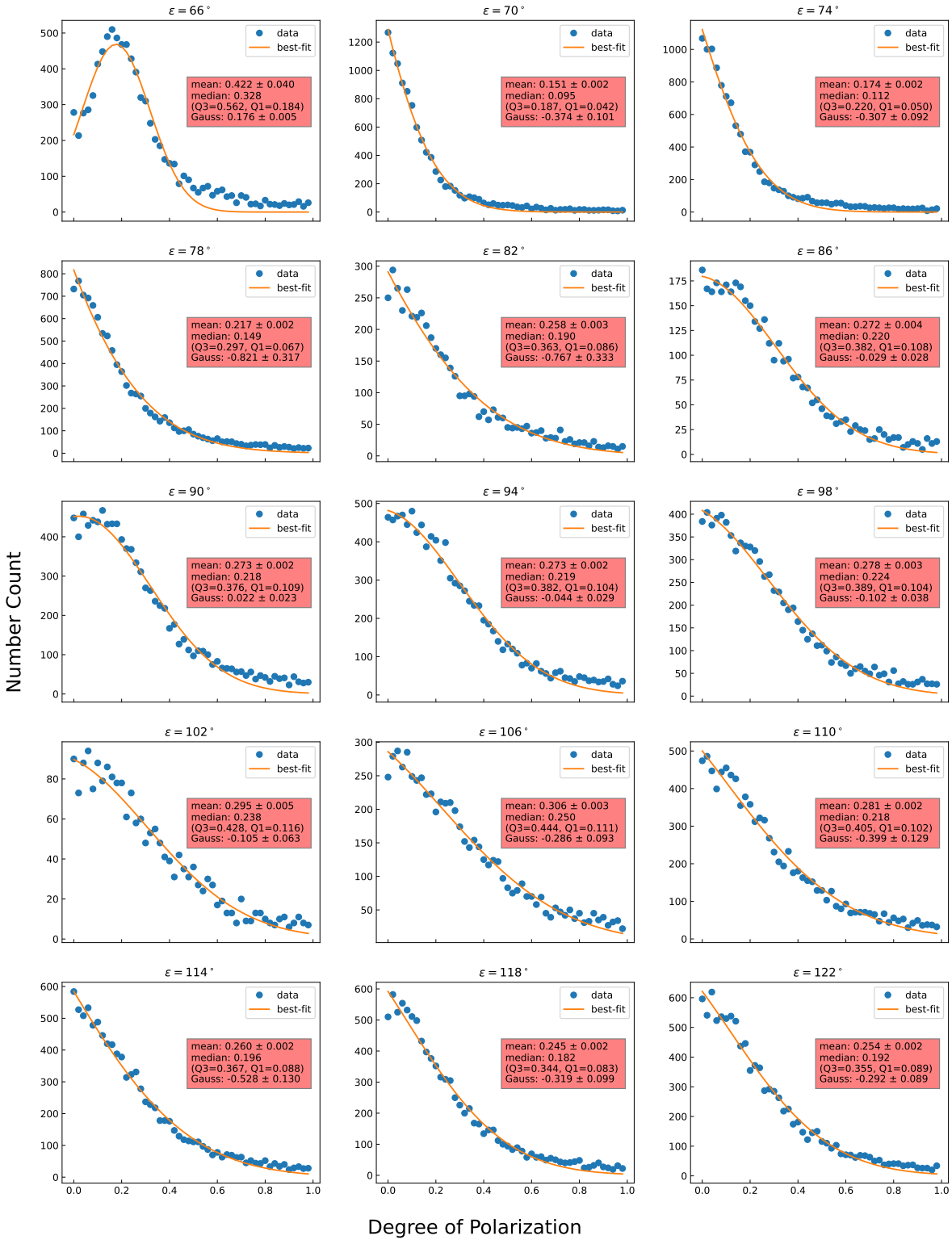

FIGURE D.7: Histogram of degree of polarization $|P_{\text{Band3, ZL}}|$ in Region 0. The orange line is the best fitting curve with single Gaussian function for the data points. The standard error is applied to the error relative to the mean. The error relative to the center of the Gaussian fit indicates the standard error relative to the center value. The values of Q1 and Q3 for the median are shown.

D.3 RESULTS OF GAUSSIAN FITTING FOR A HISTOGRAM OF POLARIZATION

(Figure D.8, D.9, D.10, D.11, D.12, D.13, D.14, D.15, D.16, D.17, D.18, D.19, D.20, D.21, D.22, D.23, D.24, D.25, D.26, D.27, D.28, D.29, D.30, D.31, D.32, D.33, D.34, D.35, D.36, and D.37)

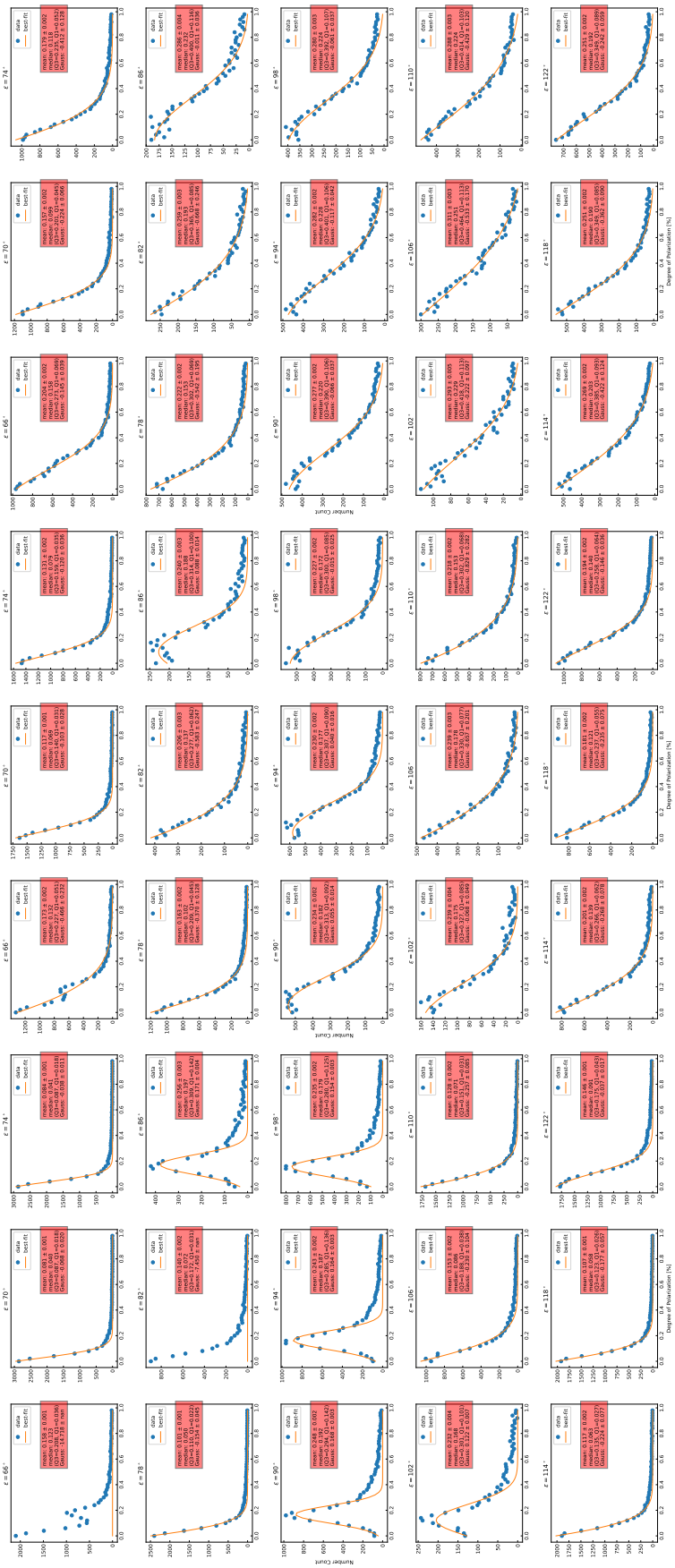

(A) Band1 (B) Band2 (C) Band3

FIGURE D.8: Histogram of $|P_{\lambda,\,\mathrm{ZL}}|$ for $P_{\lambda,\,\mathrm{ZL}}/\sigma_P > 0$ in Region 1.

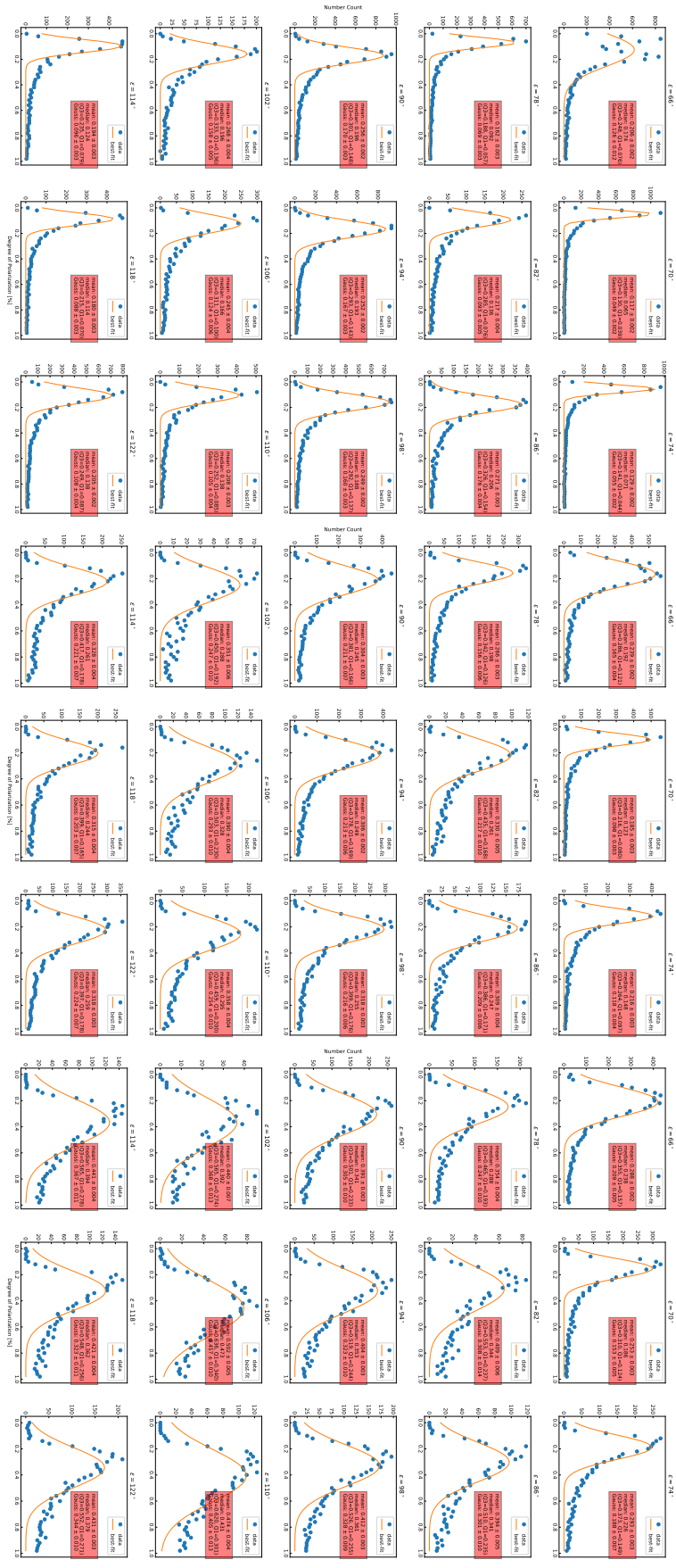

(A) Band1 (B) Band2 (C) Band3

FIGURE D.9: Histogram of $|P_{\lambda,\,\mathrm{ZL}}|$ for $P_{\lambda,\,\mathrm{ZL}}/\sigma_P > 1$ in Region 1.

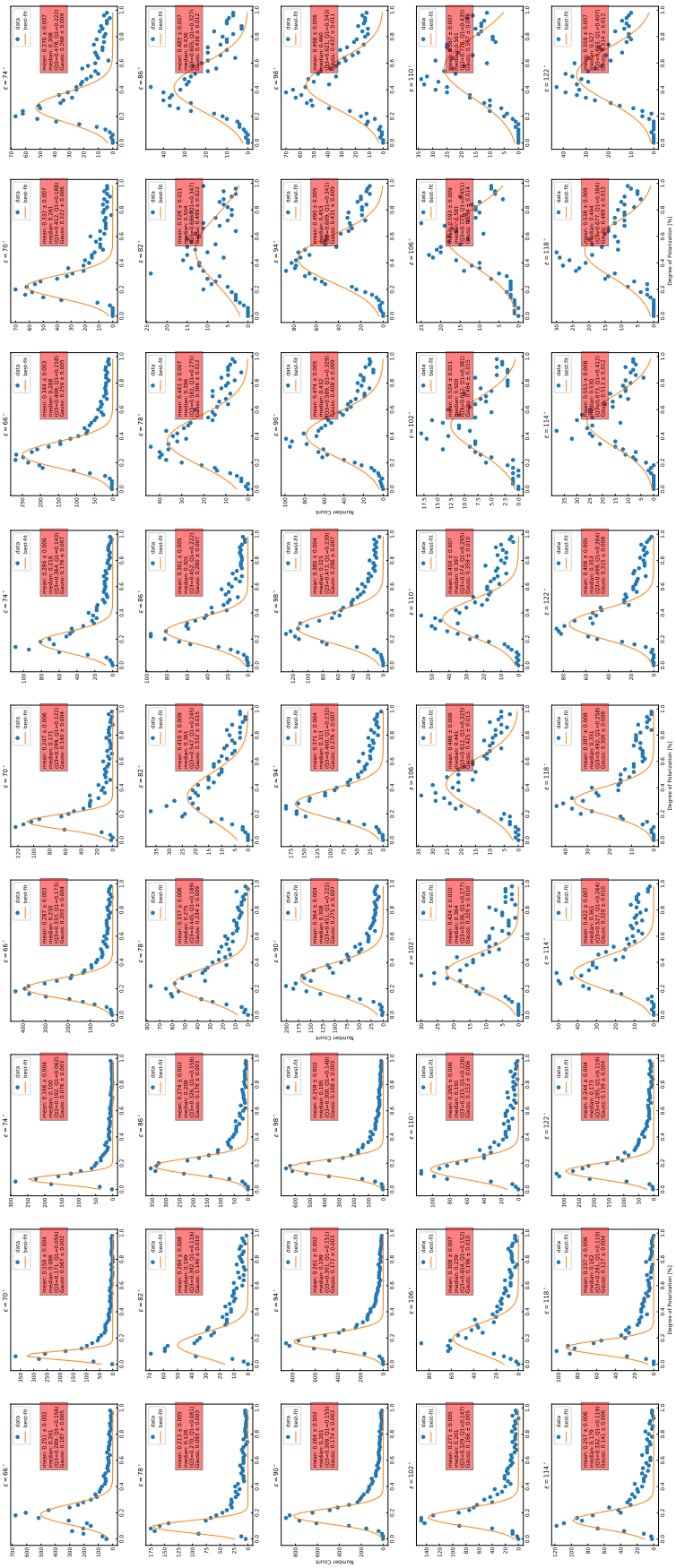

(A) Band1 (B) Band2 (C) Band3

FIGURE D.10: Histogram of $|P_{\lambda,\,\mathrm{ZL}}|$ for $P_{\lambda,\,\mathrm{ZL}}/\sigma_P > 2$ in Region 1.

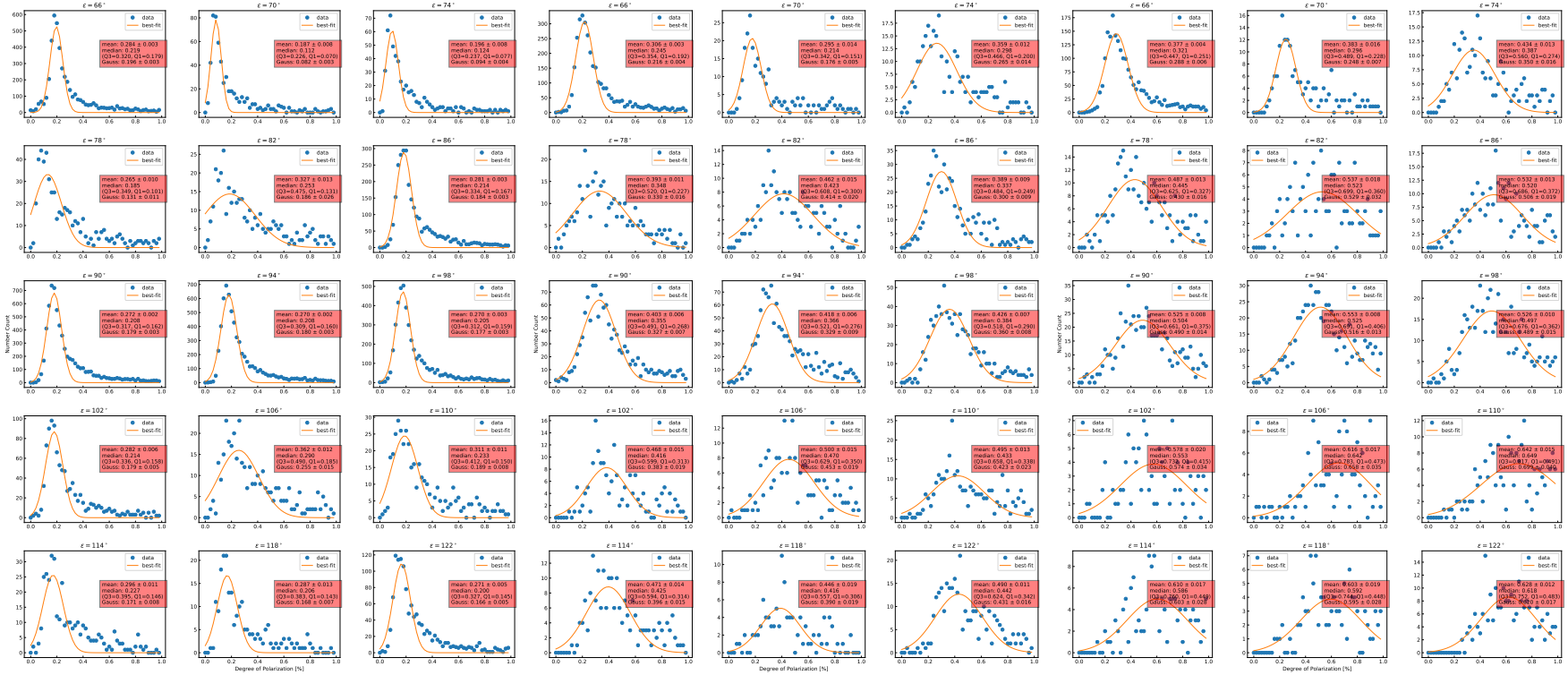

(A) Band1 (B) Band2 (C) Band3

FIGURE D.11: Histogram of $|P_{\lambda,\,\mathrm{ZL}}|$ for $P_{\lambda,\,\mathrm{ZL}}/\sigma_P > 3$ in Region 1.

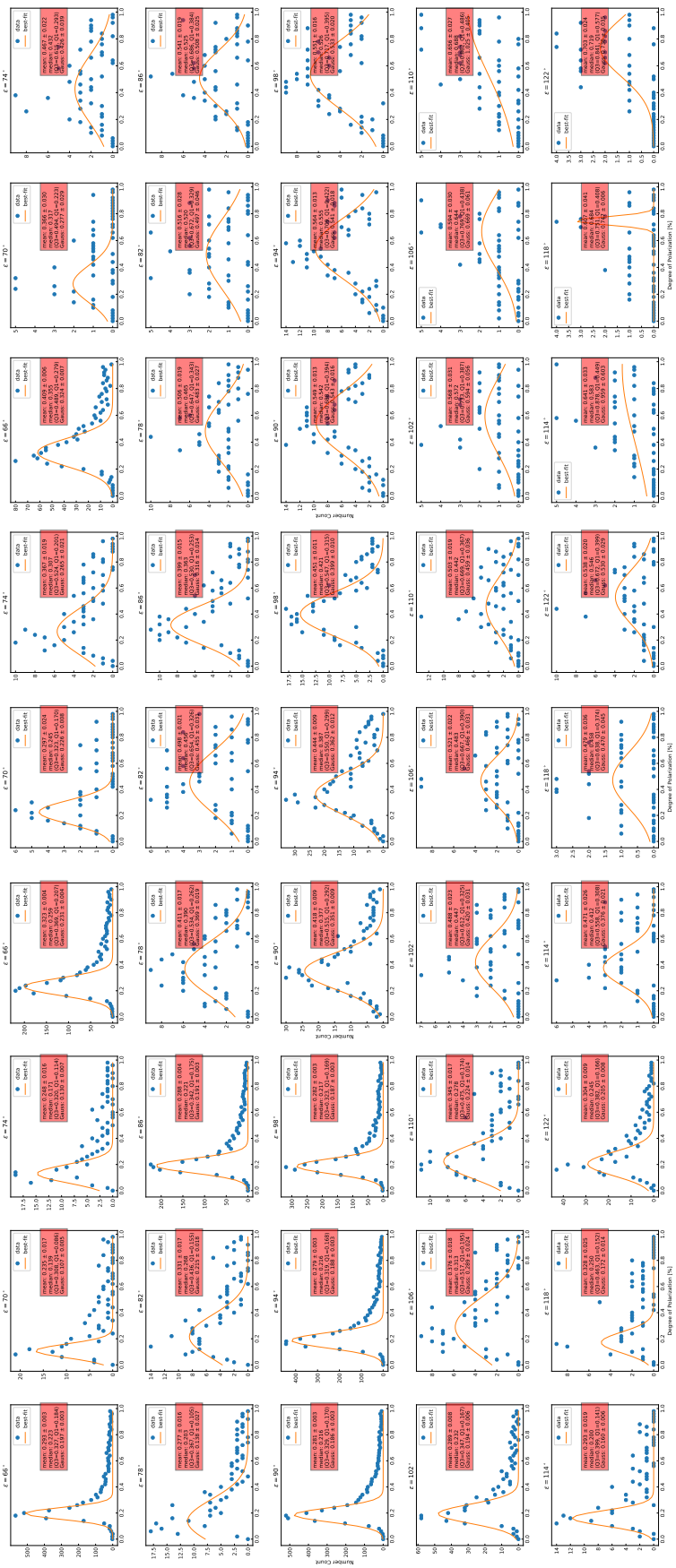

(A) Band1 (B) Band2 (C) Band3

FIGURE D.12: Histogram of $|P_{\lambda,\,\mathrm{ZL}}/\sigma_P| > 4$ in Region 1.

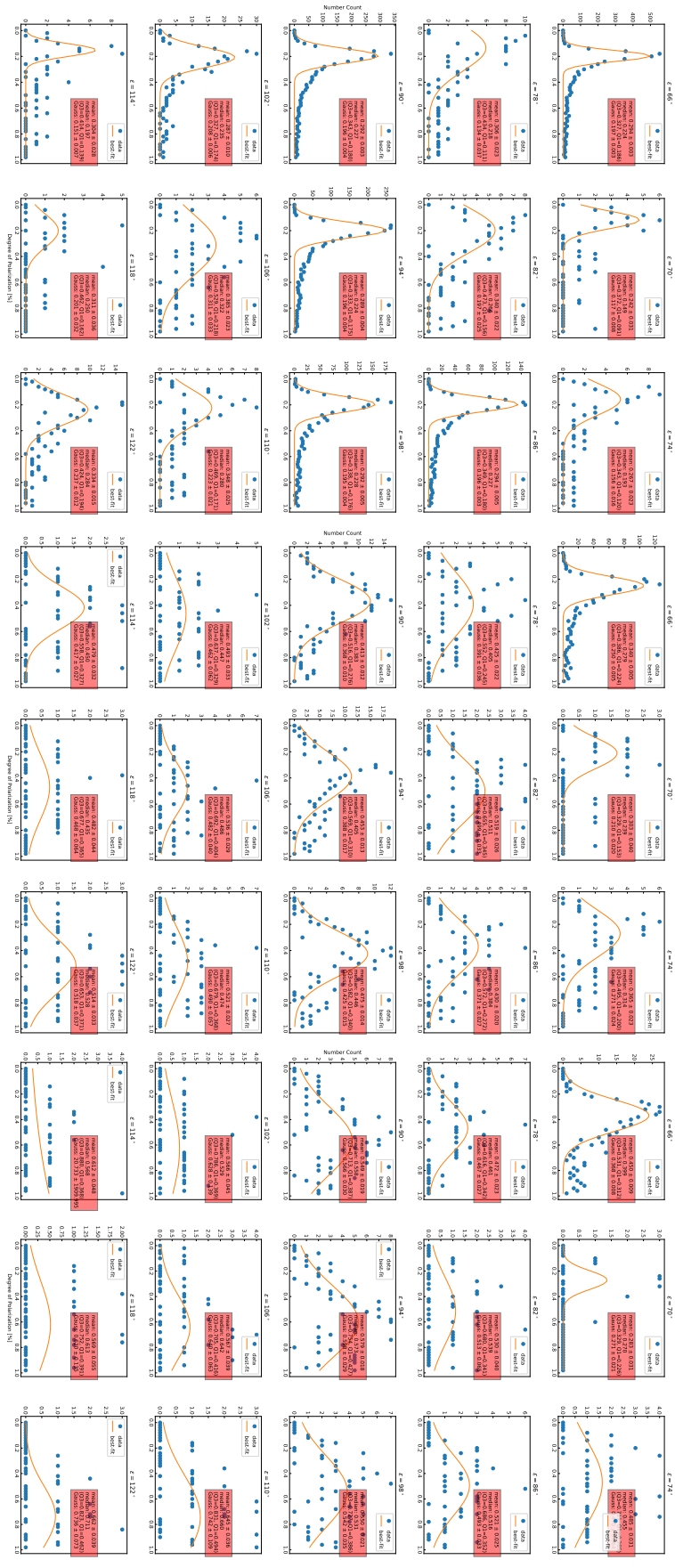

(A) Band1 (B) Band2 (C) Band3

FIGURE D.13: Histogram of $|P_{\lambda,\,\mathrm{ZL}}|$ for $P_{\lambda,\,\mathrm{ZL}}/\sigma_P > 5$ in Region 1.

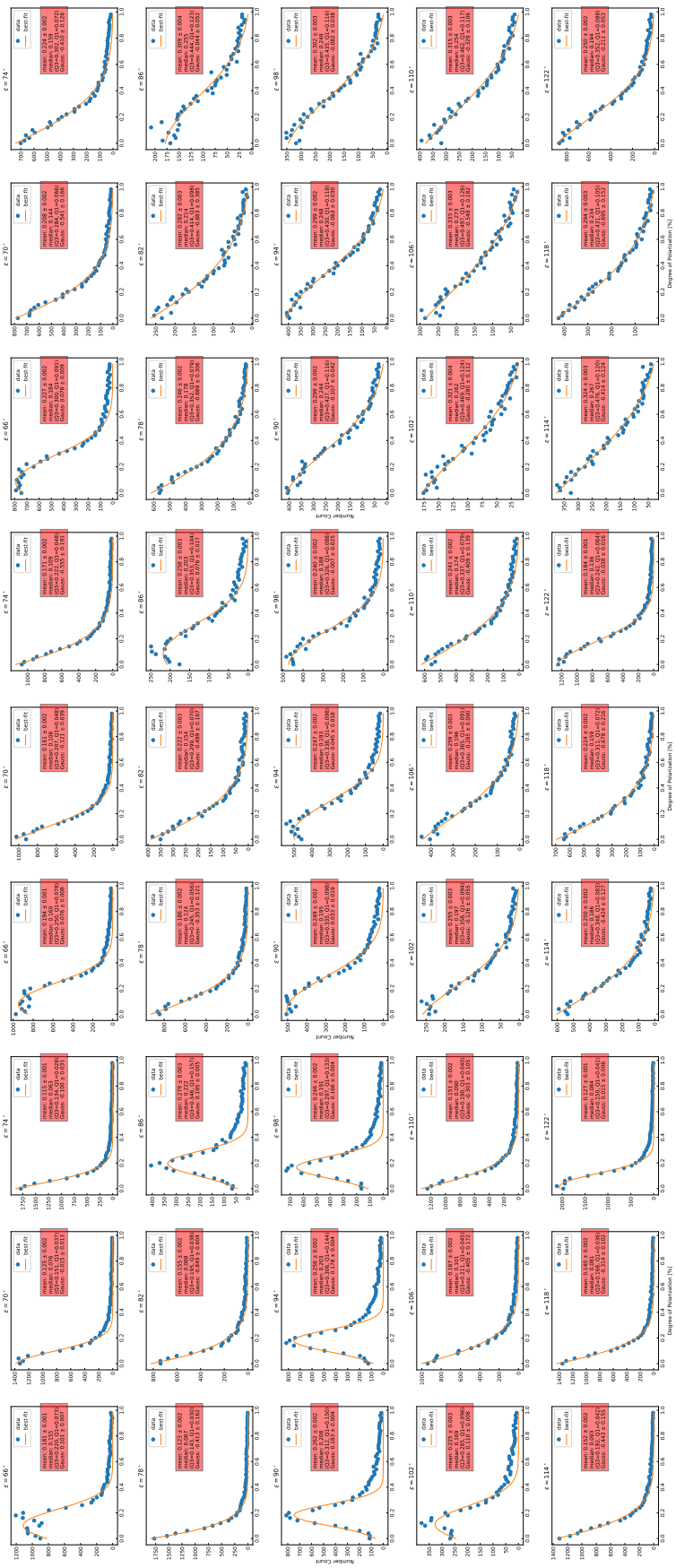

(A) Band1 (B) Band2 (C) Band3

FIGURE D.14: Histogram of $|P_{\lambda,\,\mathrm{ZL}}/\sigma_P > 0$ in Region 2.

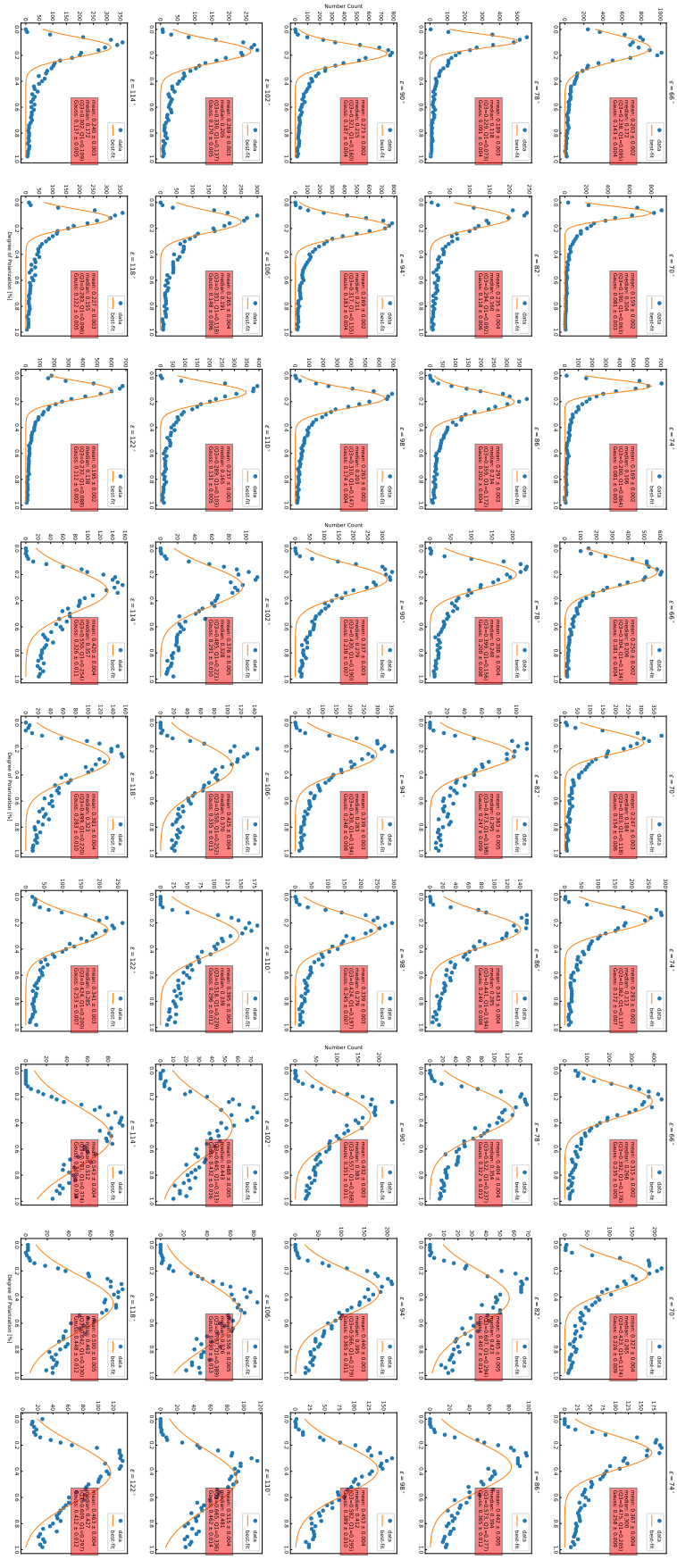

(A) Band1 (B) Band2 (C) Band3

FIGURE D.15: Histogram of $|P_{\lambda,\,\mathrm{ZL}}|$ for $P_{\lambda,\,\mathrm{ZL}}/\sigma_P > 1$ in Region 2.

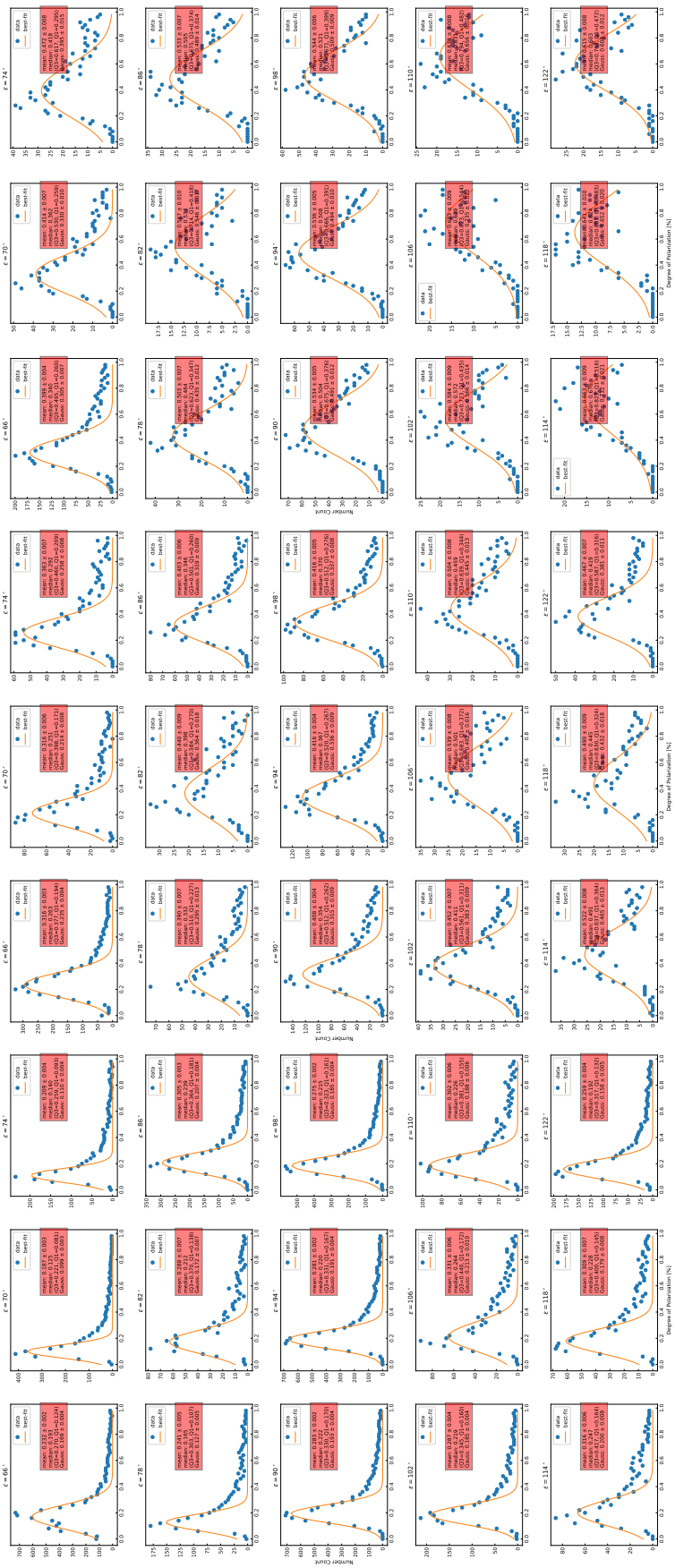

(A) Band1 (B) Band2 (C) Band3

FIGURE D.16: Histogram of $|P_{\lambda,\,\mathrm{ZL}}|$ for $P_{\lambda,\,\mathrm{ZL}}/\sigma_P > 2$ in Region 2.

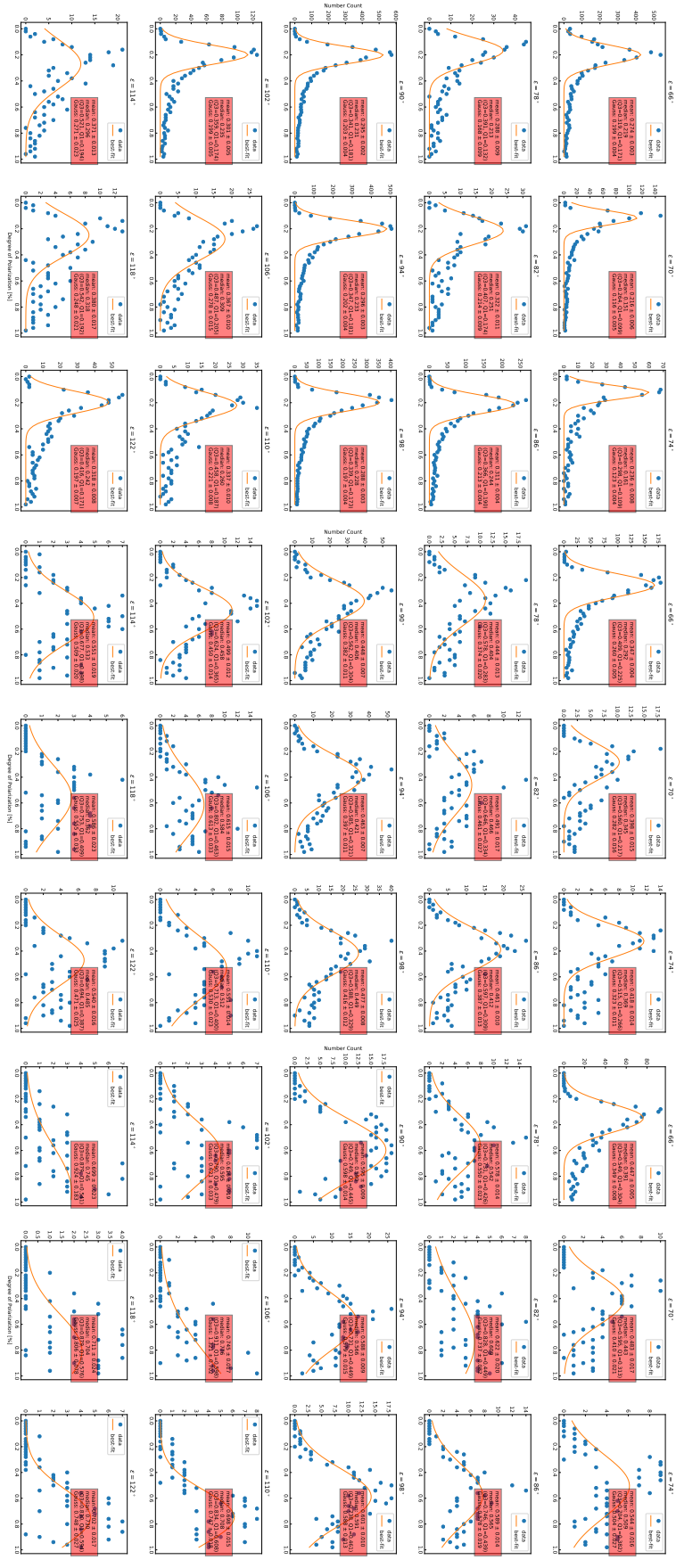

(A) Band1 (B) Band2 (C) Band3

FIGURE D.17: Histogram of $|P_{\lambda,\,\mathrm{ZL}}|$ for $P_{\lambda,\,\mathrm{ZL}}/\sigma_P > 3$ in Region 2.

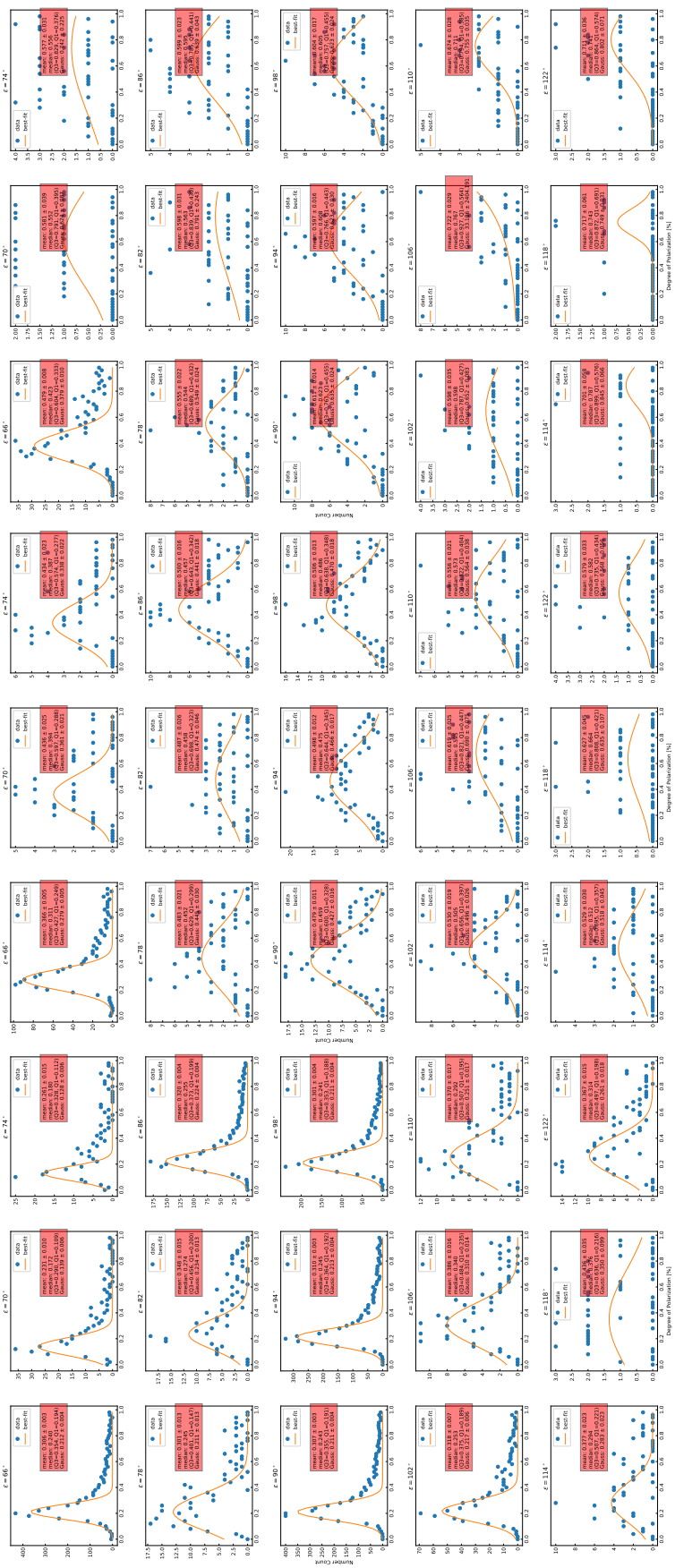

(A) Band1 (B) Band2 (C) Band3

FIGURE D.18: Histogram of $|P_{\lambda,\,\mathrm{ZL}}|$ for $P_{\lambda,\,\mathrm{ZL}}/\sigma_P > 4$ in Region 2.

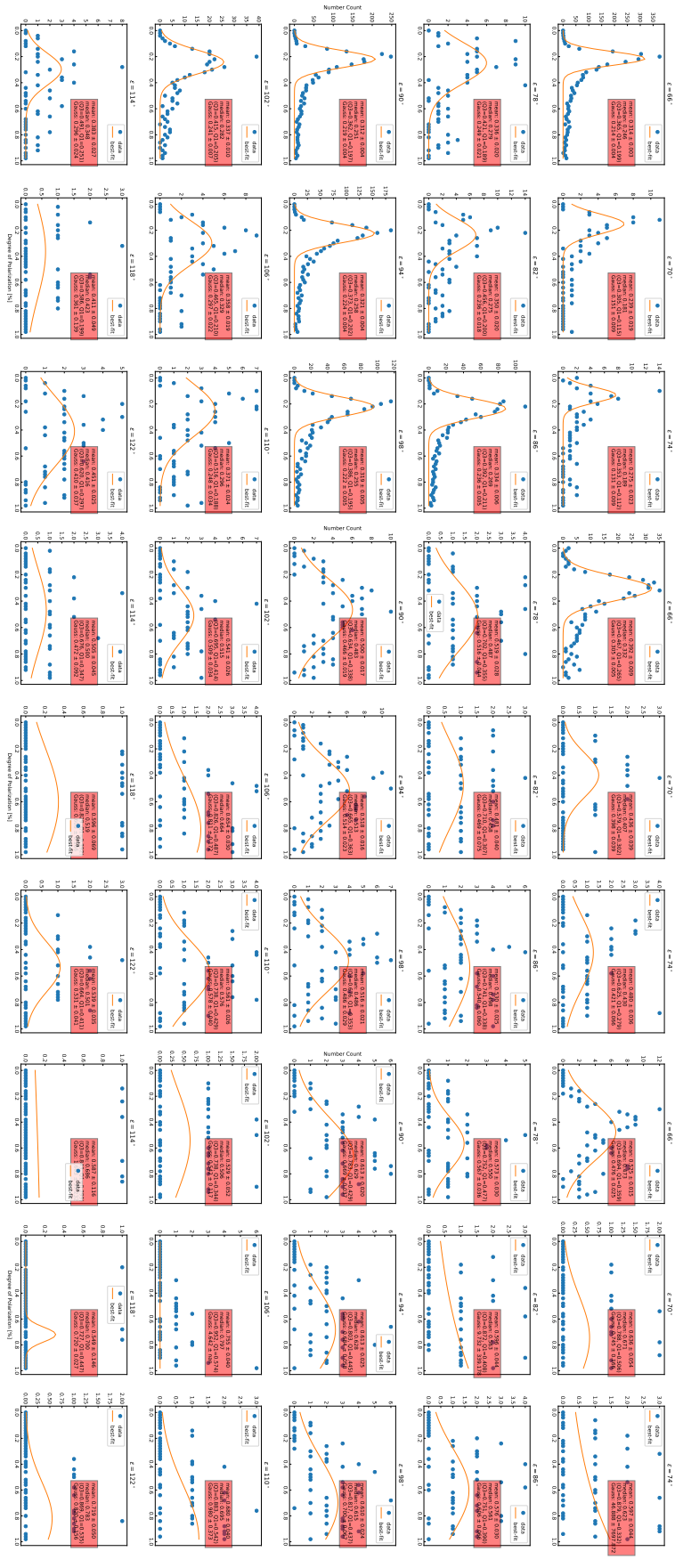

(A) Band1 (B) Band2 (C) Band3

FIGURE D.19: Histogram of $|P_{\lambda,\,\mathrm{ZL}}|$ for $P_{\lambda,\,\mathrm{ZL}}/\sigma_P > 5$ in Region 2.

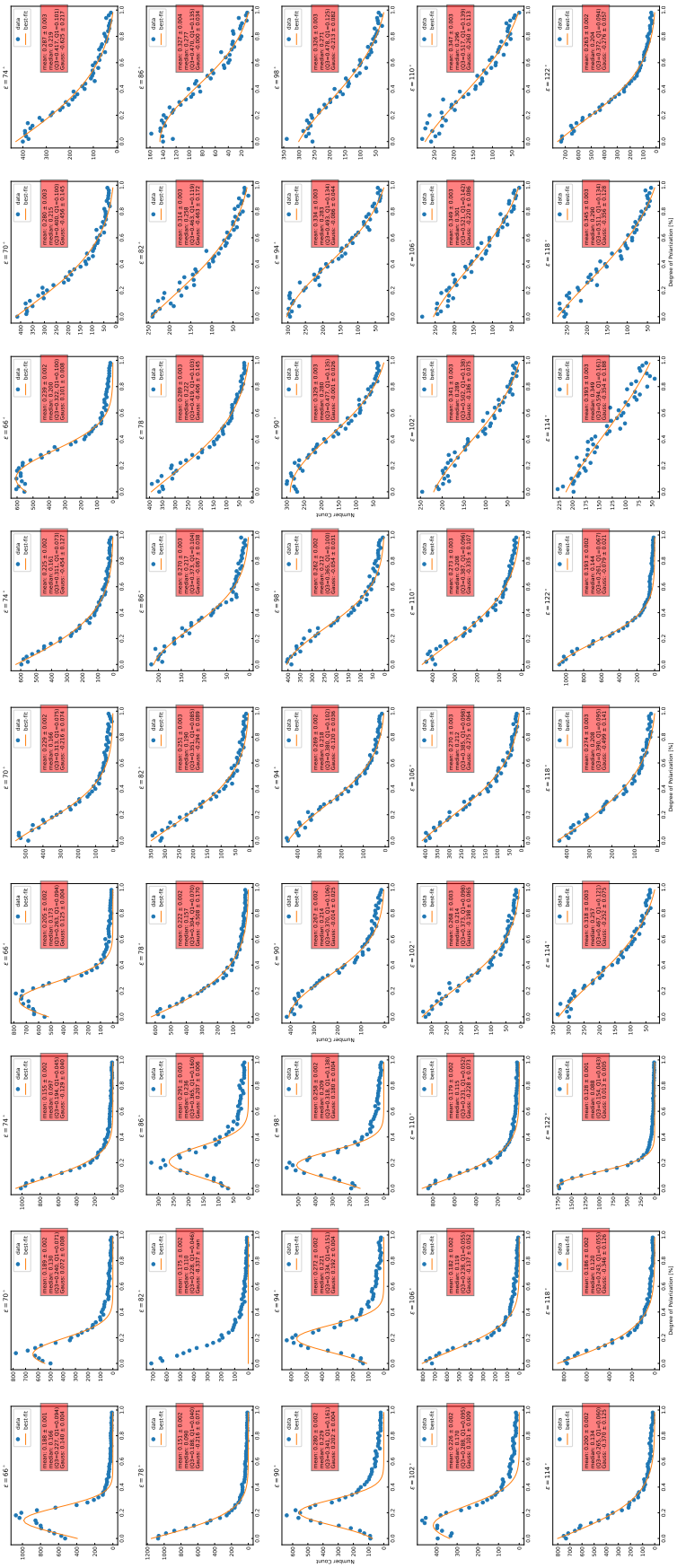

(A) Band1 (B) Band2 (C) Band3

FIGURE D.20: Histogram of $|P_{\lambda,\,\mathrm{ZL}}|$ for $P_{\lambda,\,\mathrm{ZL}}/\sigma_P > 0$ in Region 3.

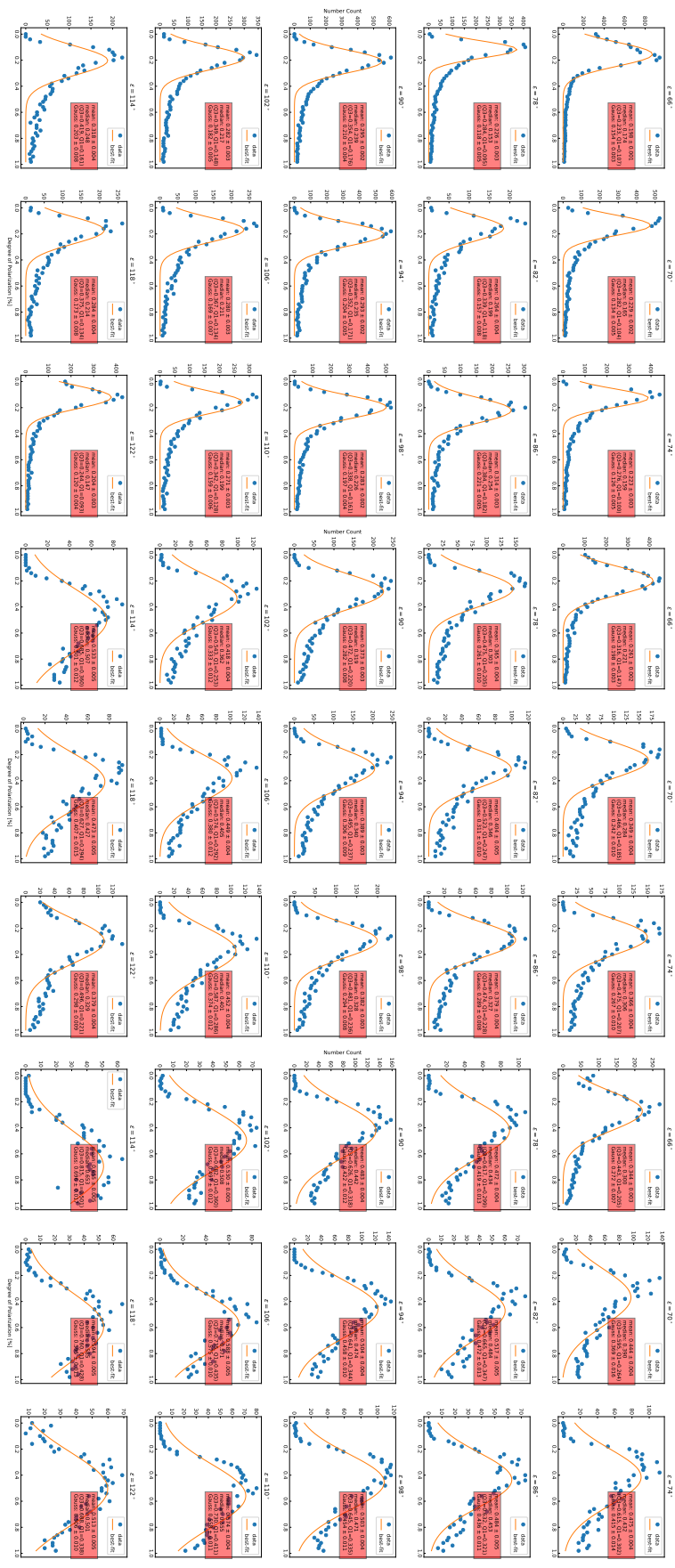

(A) Band1 (B) Band2 (C) Band3

FIGURE D.21: Histogram of $|P_{\lambda,\,\mathrm{ZL}}|$ for $P_{\lambda,\,\mathrm{ZL}}/\sigma_P > 1$ in Region 3.

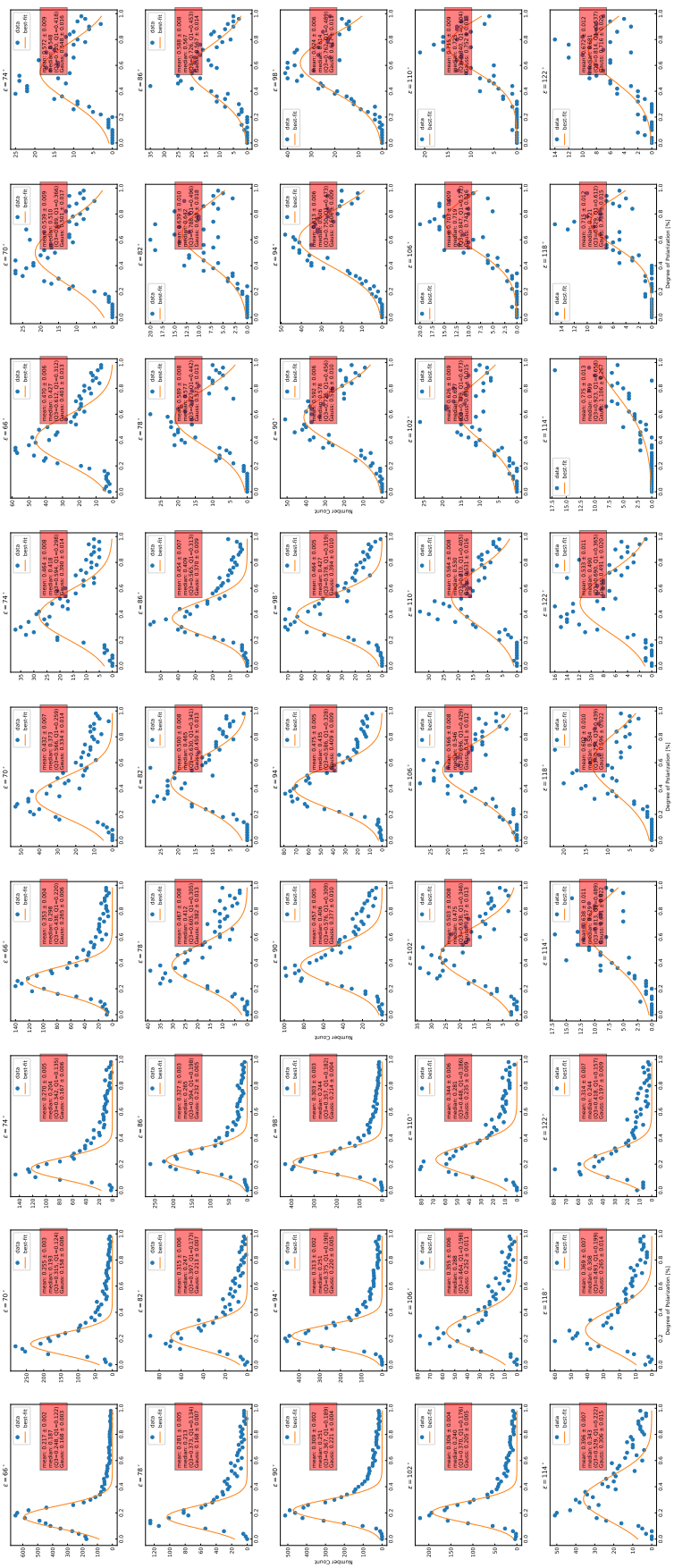

(A) Band1 (B) Band2 (C) Band3

FIGURE D.22: Histogram of $|P_{\lambda,\,\mathrm{ZL}}|$ for $P_{\lambda,\,\mathrm{ZL}}/\sigma_P > 2$ in Region 3.

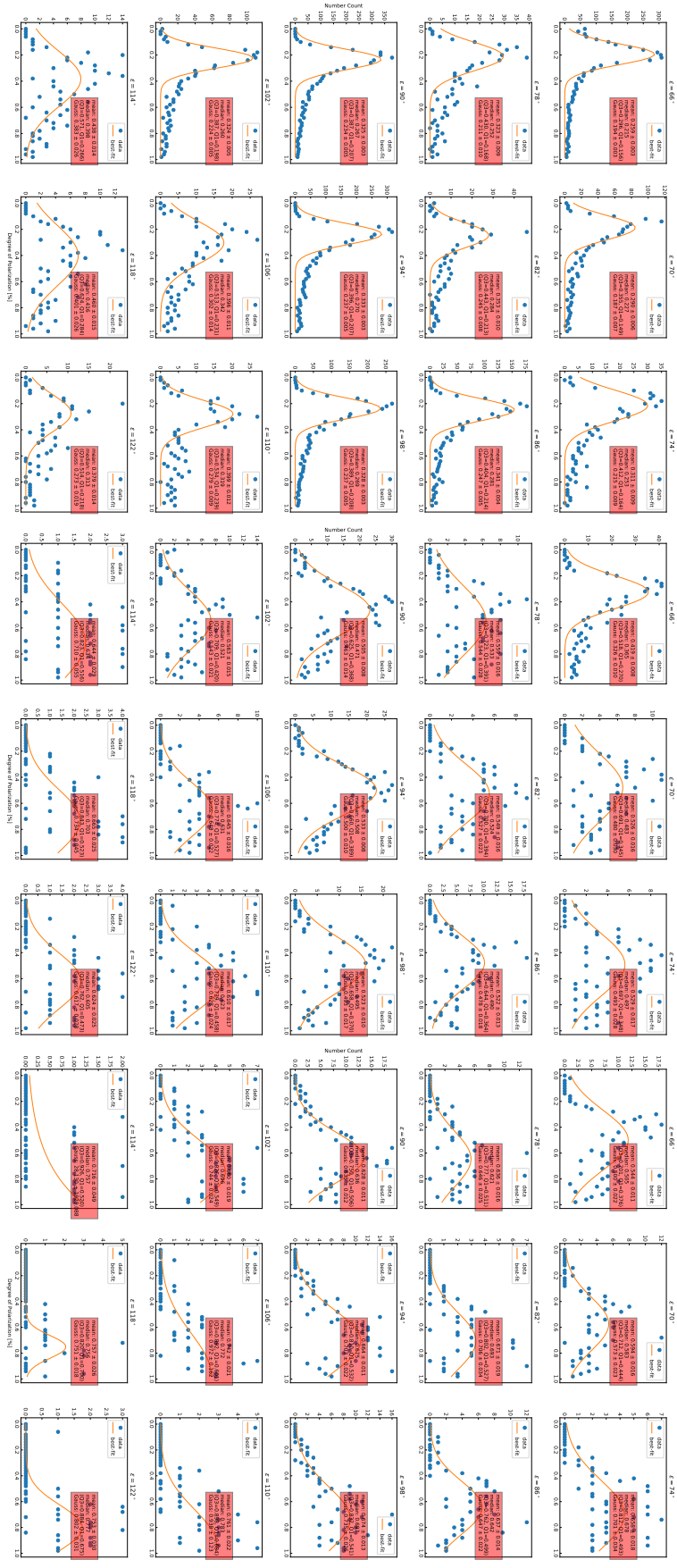

(A) Band1 (B) Band2 (C) Band3

FIGURE D.23: Histogram of $|P_{\lambda,\,\mathrm{ZL}}|$ for $P_{\lambda,\,\mathrm{ZL}}/\sigma_P > 3$ in Region 3.

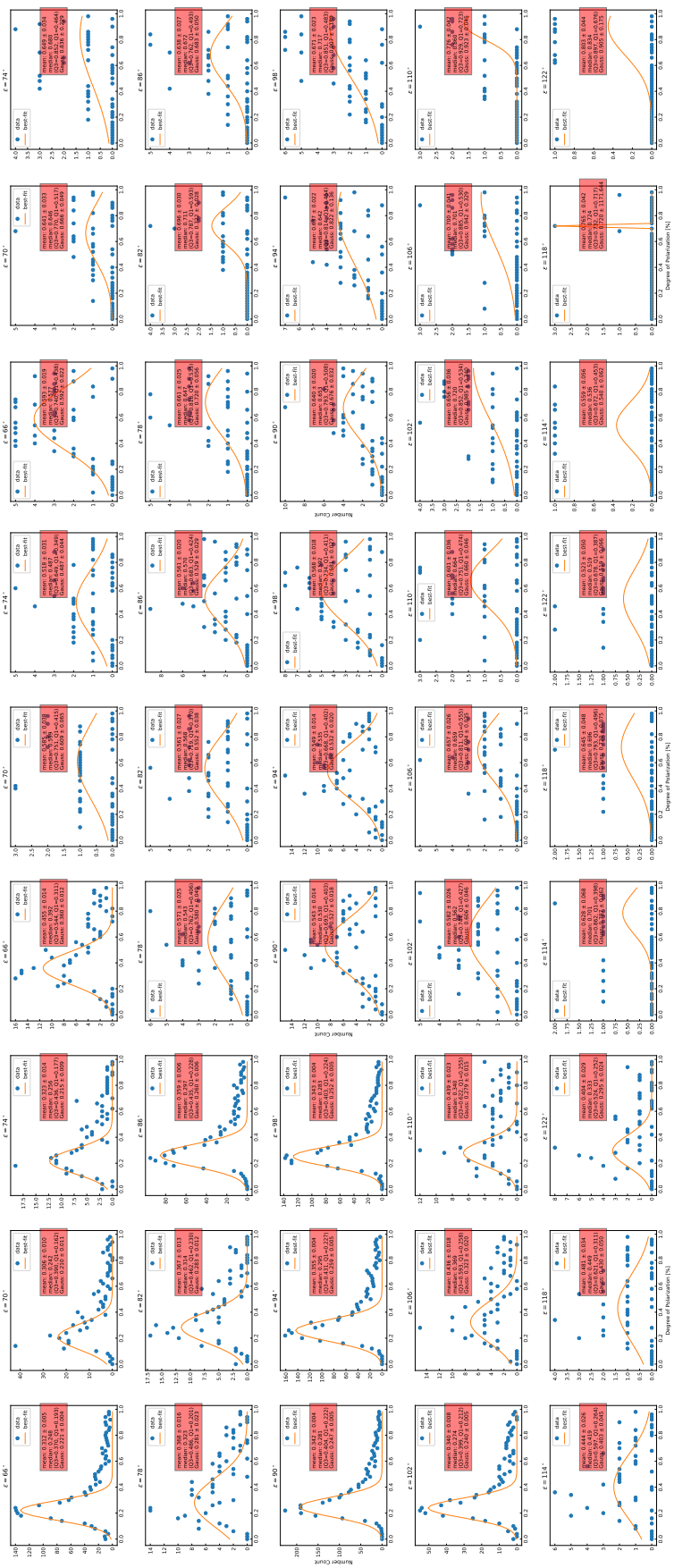

(A) Band1 (B) Band2 (C) Band3

FIGURE D.24: Histogram of $|P_{\lambda,\,\mathrm{ZL}}|$ for $P_{\lambda,\,\mathrm{ZL}}/\sigma_P > 4$ in Region 3.

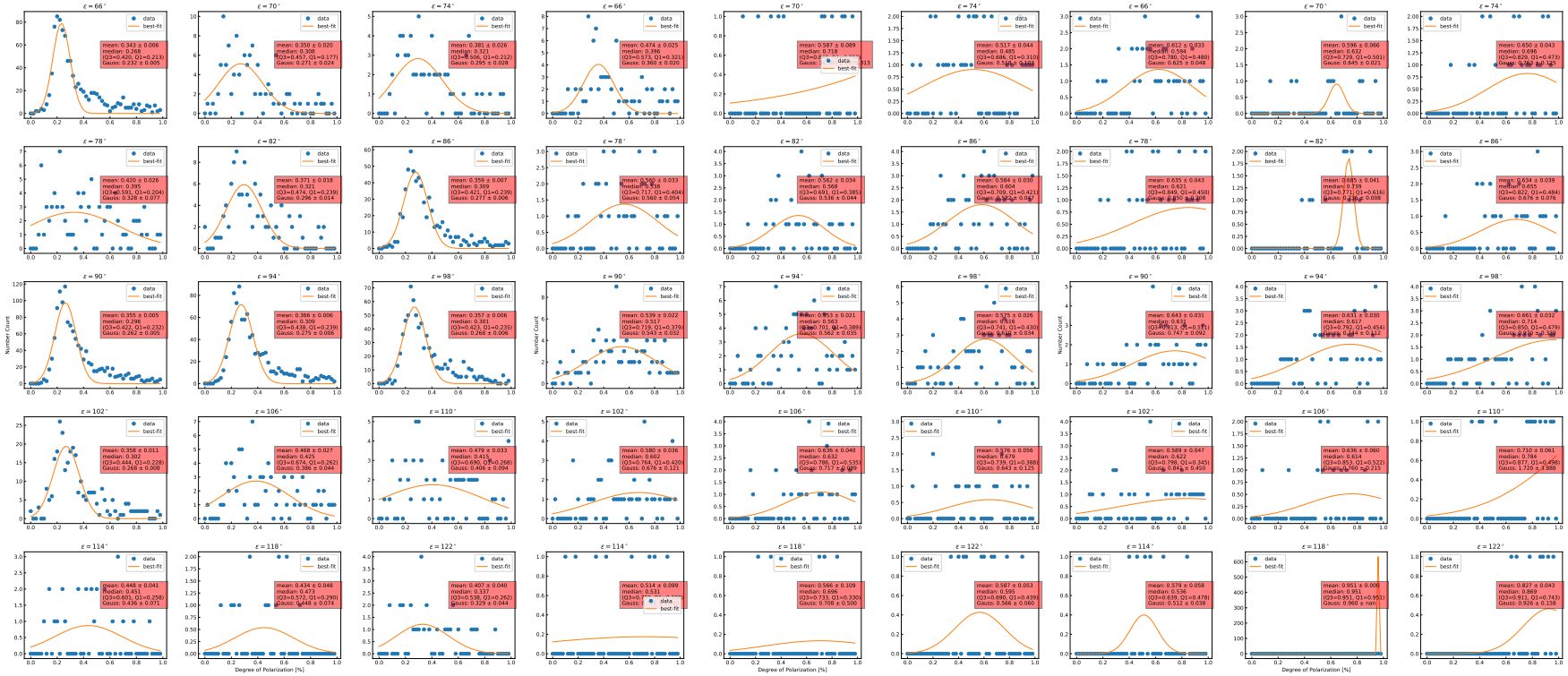

(A) Band1 (B) Band2 (C) Band3

FIGURE D.25: Histogram of $|P_{\lambda,\,\mathrm{ZL}}|$ for $P_{\lambda,\,\mathrm{ZL}}/\sigma_P > 5$ in Region 3.

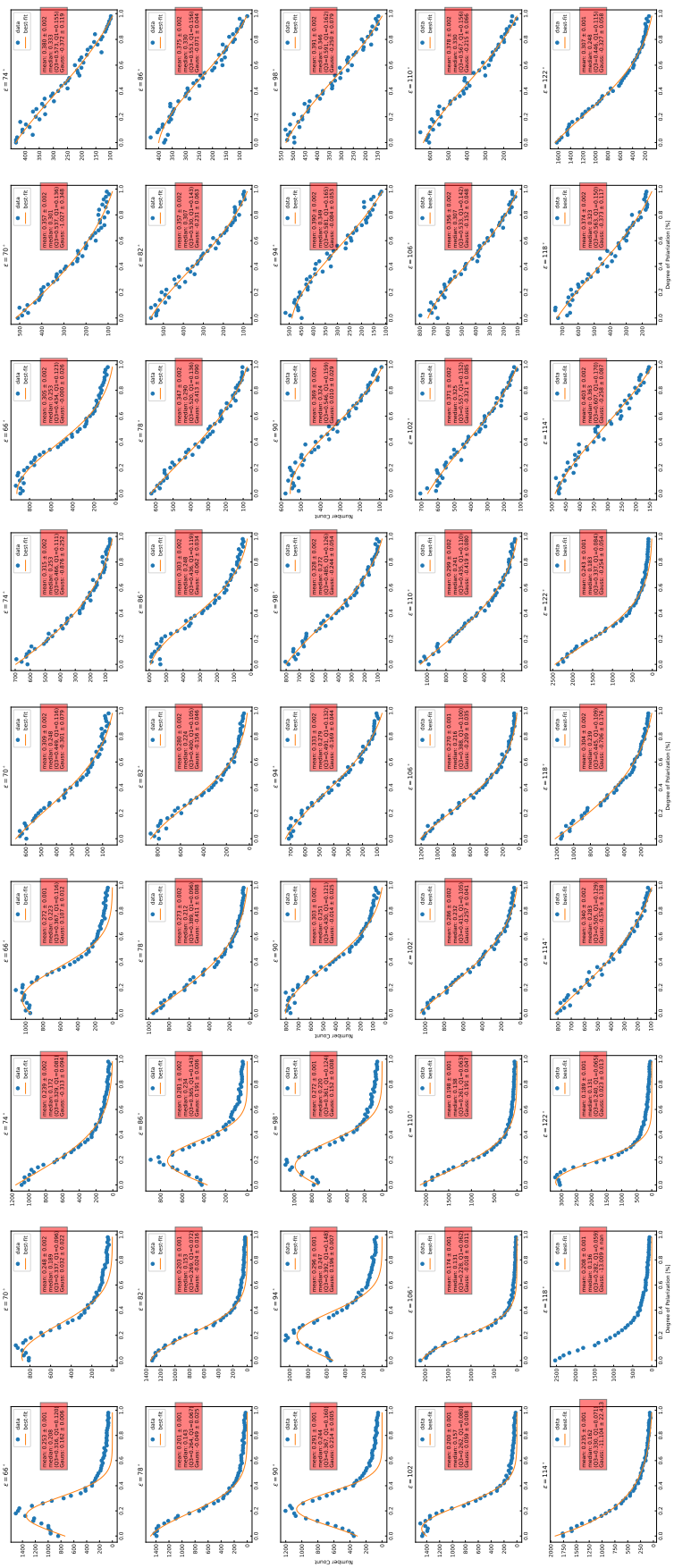

(A) Band1 (B) Band2 (C) Band3

FIGURE D.26: Histogram of $|P_{\lambda,\,\mathrm{ZL}}|$ for $P_{\lambda,\,\mathrm{ZL}}/\sigma_P > 0$ summed over Region 4, 5, and 6.

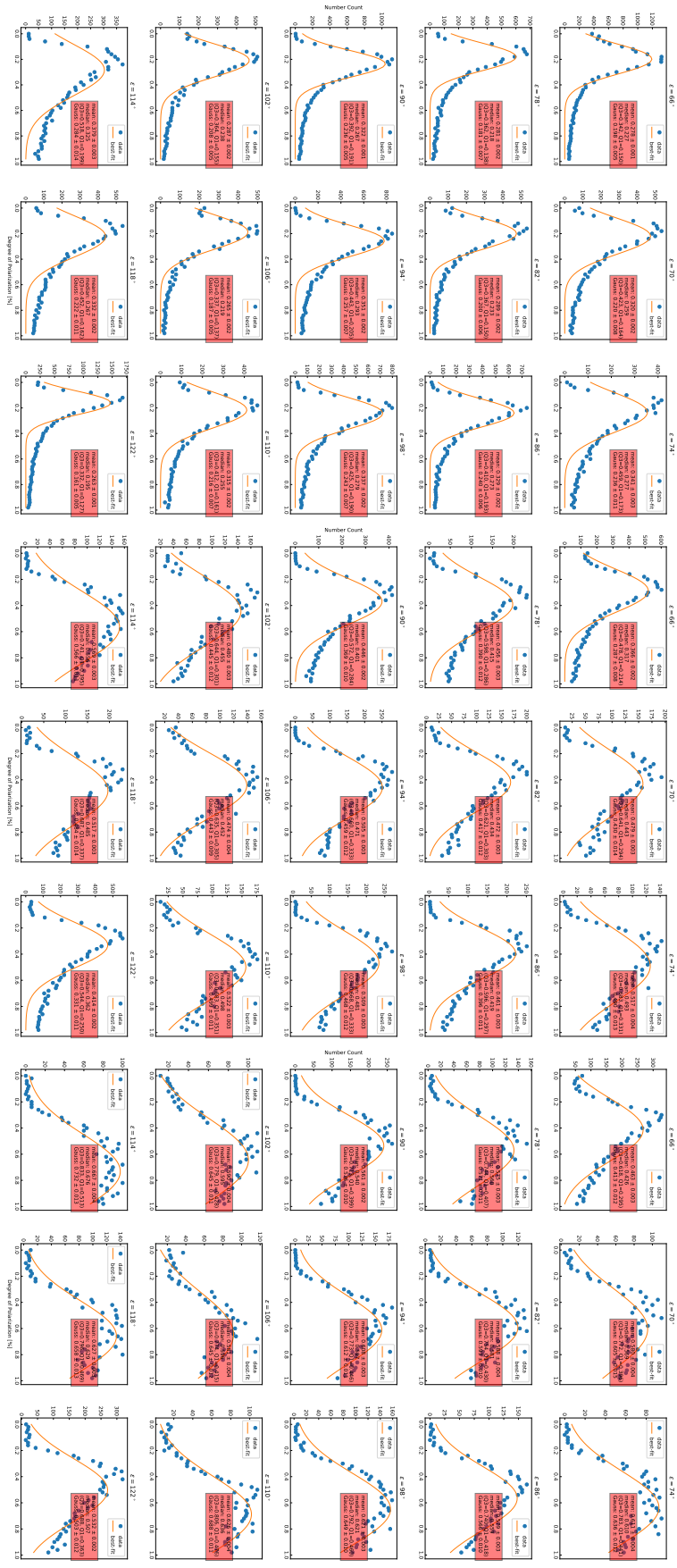

(A) Band1 (B) Band2 (C) Band3

FIGURE D.27: Histogram of $|P_{\lambda,\,\mathrm{ZL}}|$ for $P_{\lambda,\,\mathrm{ZL}}/\sigma_P > 1$ summed over Region 4, 5, and 6.

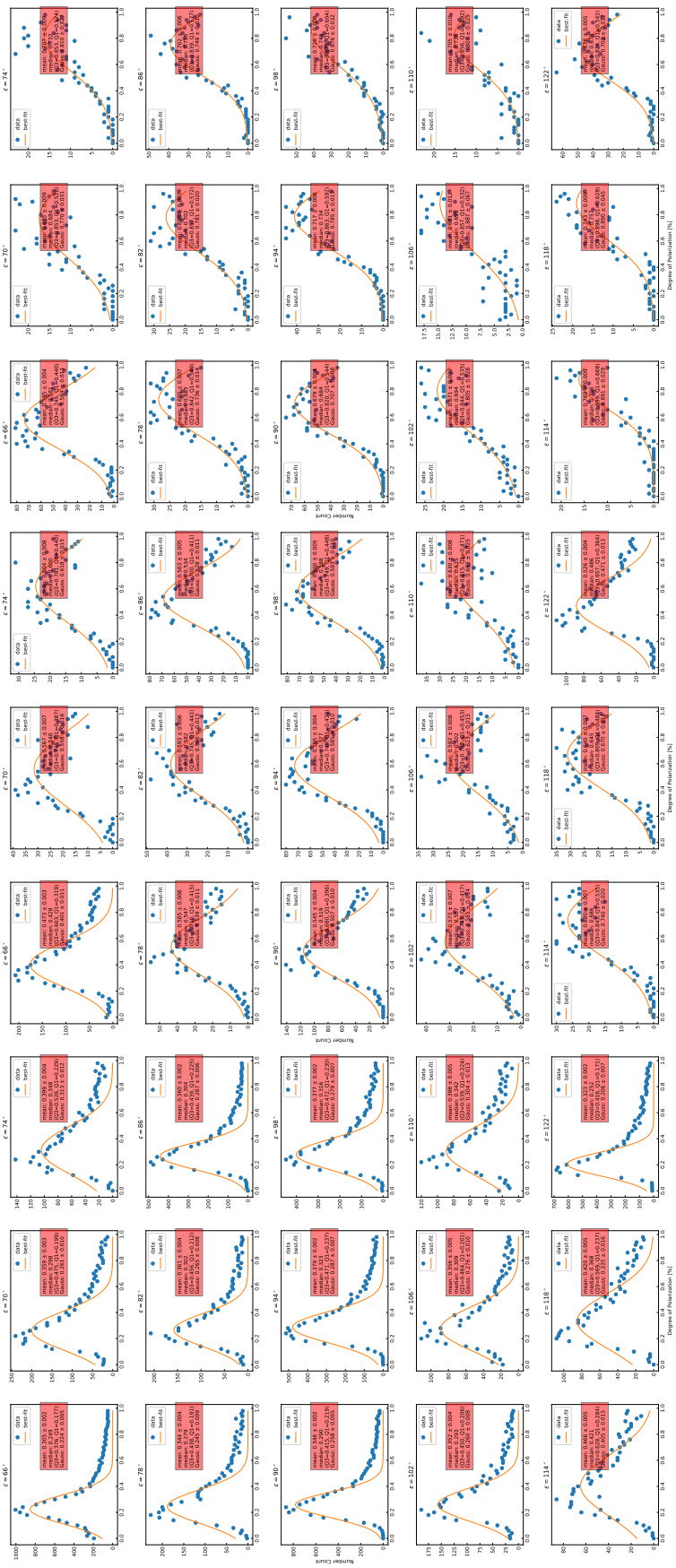

(A) Band1 (B) Band2 (C) Band3

FIGURE D.28: Histogram of $|P_{\lambda,\,\mathrm{ZL}}|$ for $P_{\lambda,\,\mathrm{ZL}}/\sigma_P > 2$ summed over Region 4, 5, and 6.

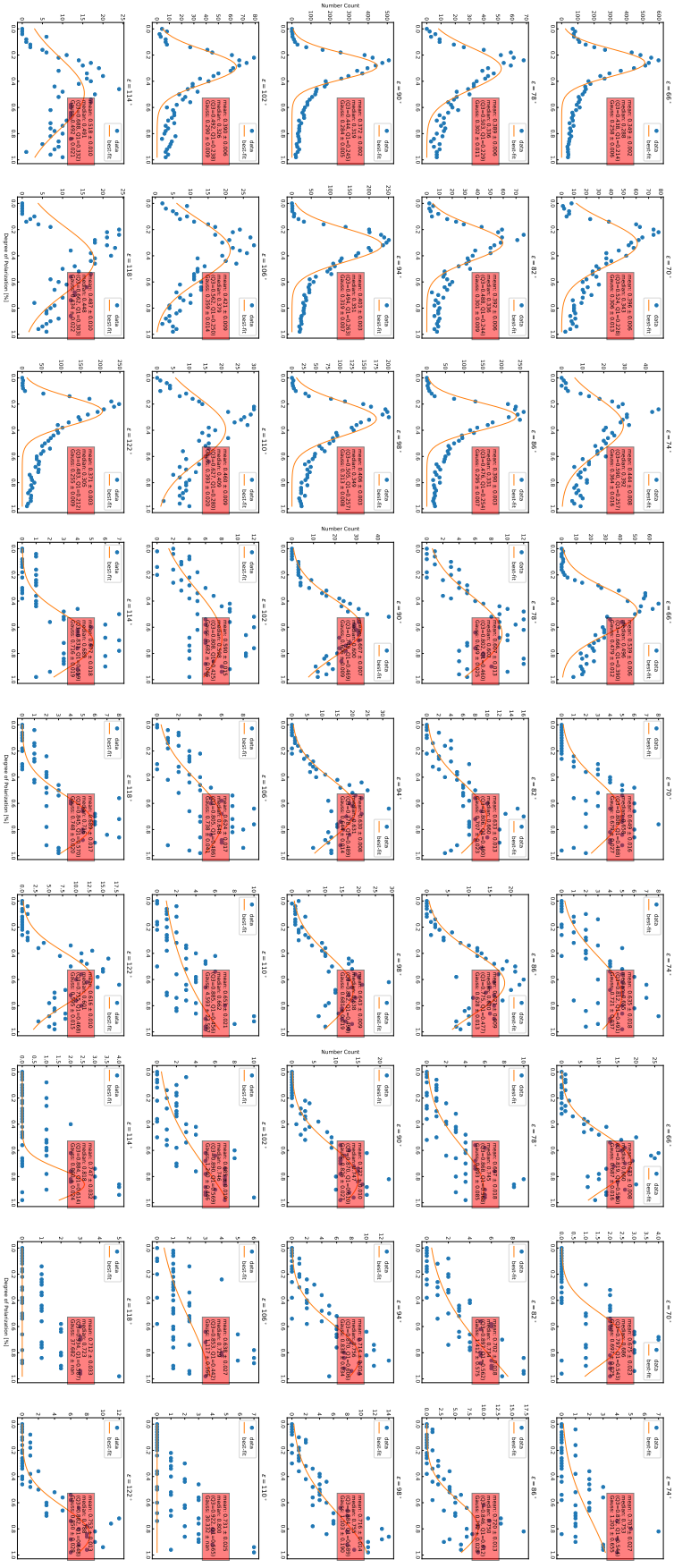

(A) Band1 (B) Band2 (C) Band3

FIGURE D.29: Histogram of $|P_{\lambda,\,\mathrm{ZL}}|$ for $P_{\lambda,\,\mathrm{ZL}}/\sigma_P > 3$ summed over Region 4, 5, and 6.

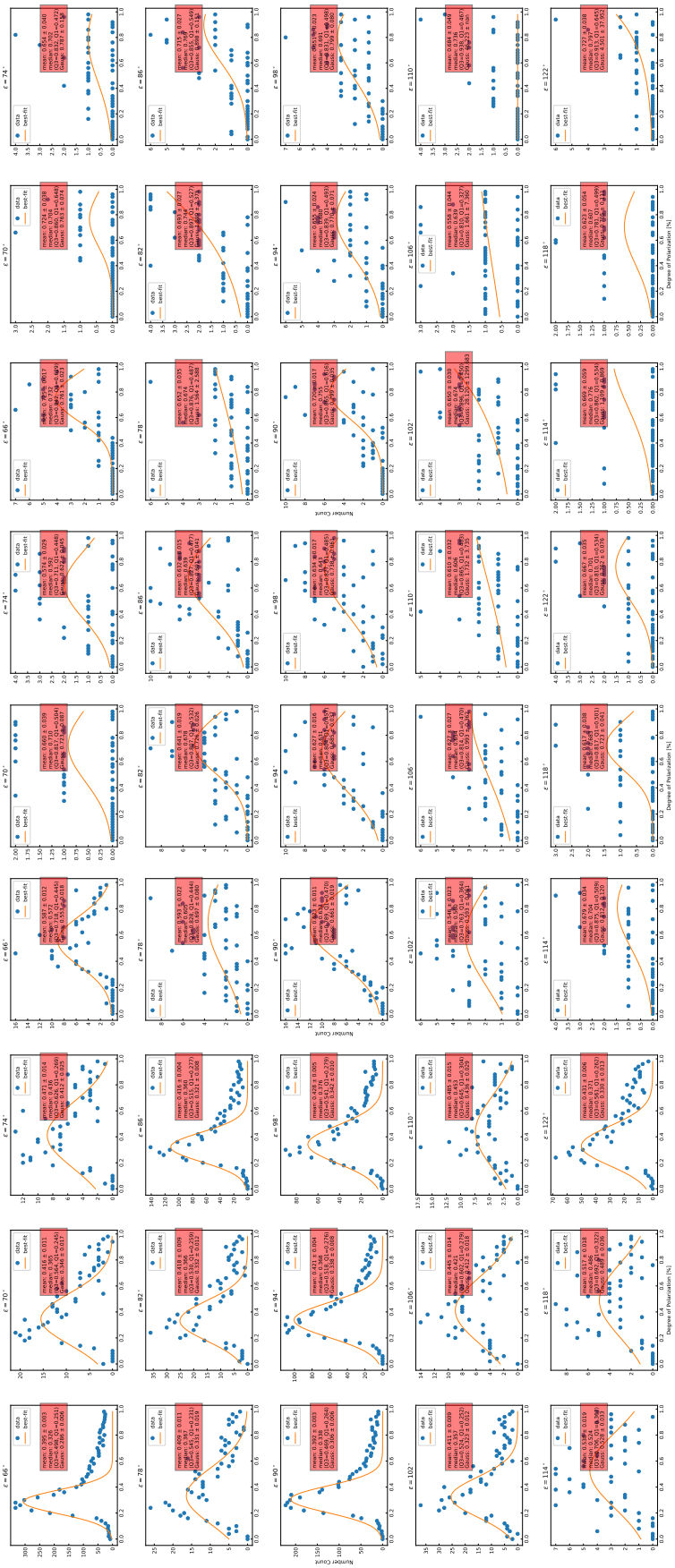

(A) Band1 (B) Band2 (C) Band3

FIGURE D.30: Histogram of $|P_{\lambda,\,\mathrm{ZL}}|$ for $P_{\lambda,\,\mathrm{ZL}}/\sigma_P > 4$ summed over Region 4, 5, and 6.

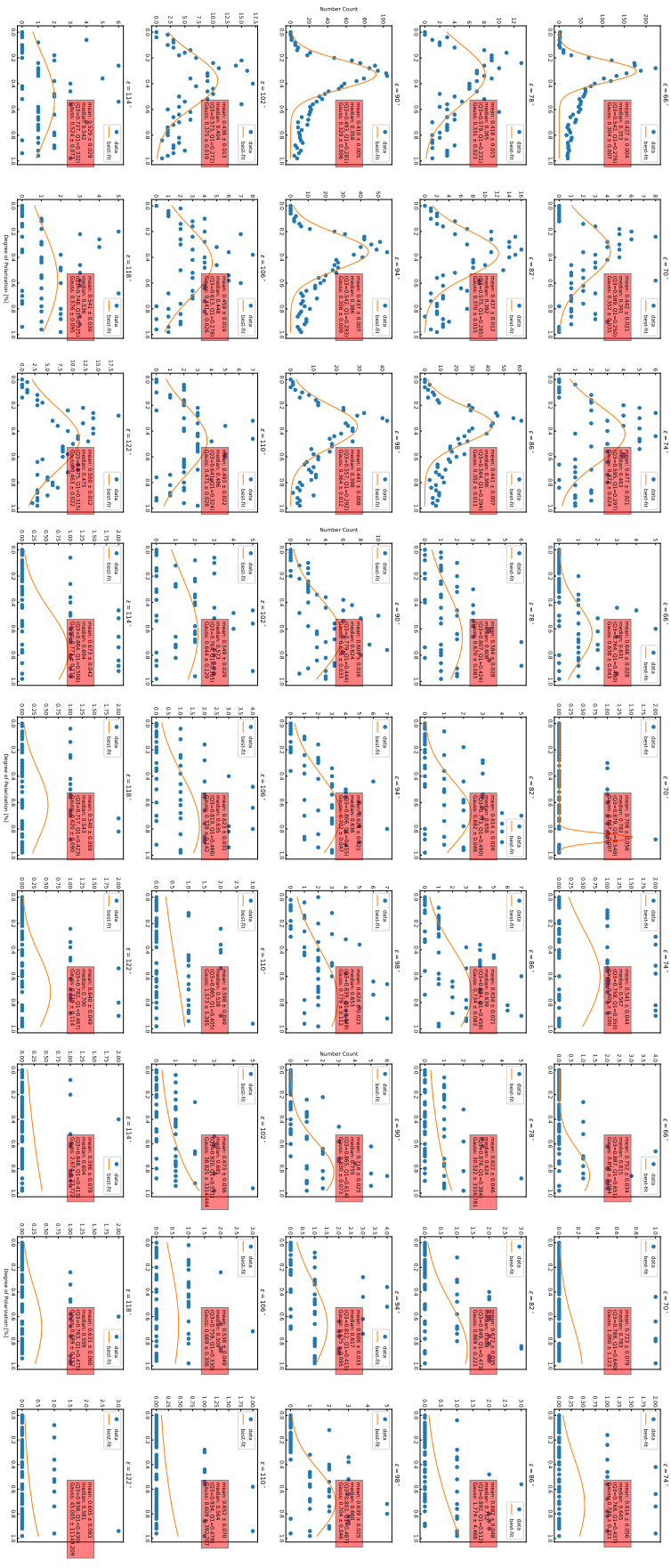

(A) Band1 (B) Band2 (C) Band3

FIGURE D.31: Histogram of $|P_{\lambda,\,\mathrm{ZL}}|$ for $P_{\lambda,\,\mathrm{ZL}}/\sigma_P > 5$ summed over Region 4, 5, and 6.

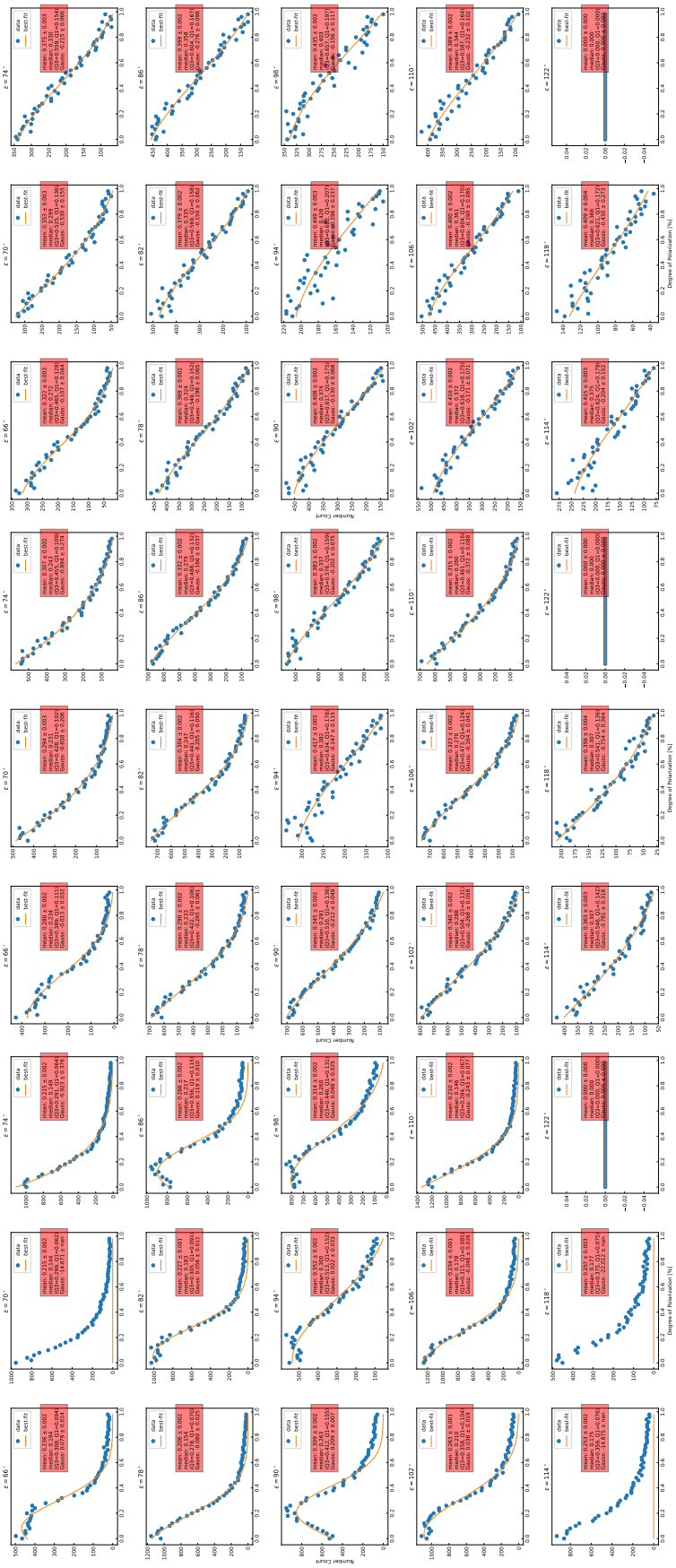

(A) Band1 (B) Band2 (C) Band3

FIGURE D.32: Histogram of $|P_{\lambda,\,\mathrm{ZL}}|$ for $P_{\lambda,\,\mathrm{ZL}}/\sigma_P > 0$ summed over Region 7, 8, and 9.

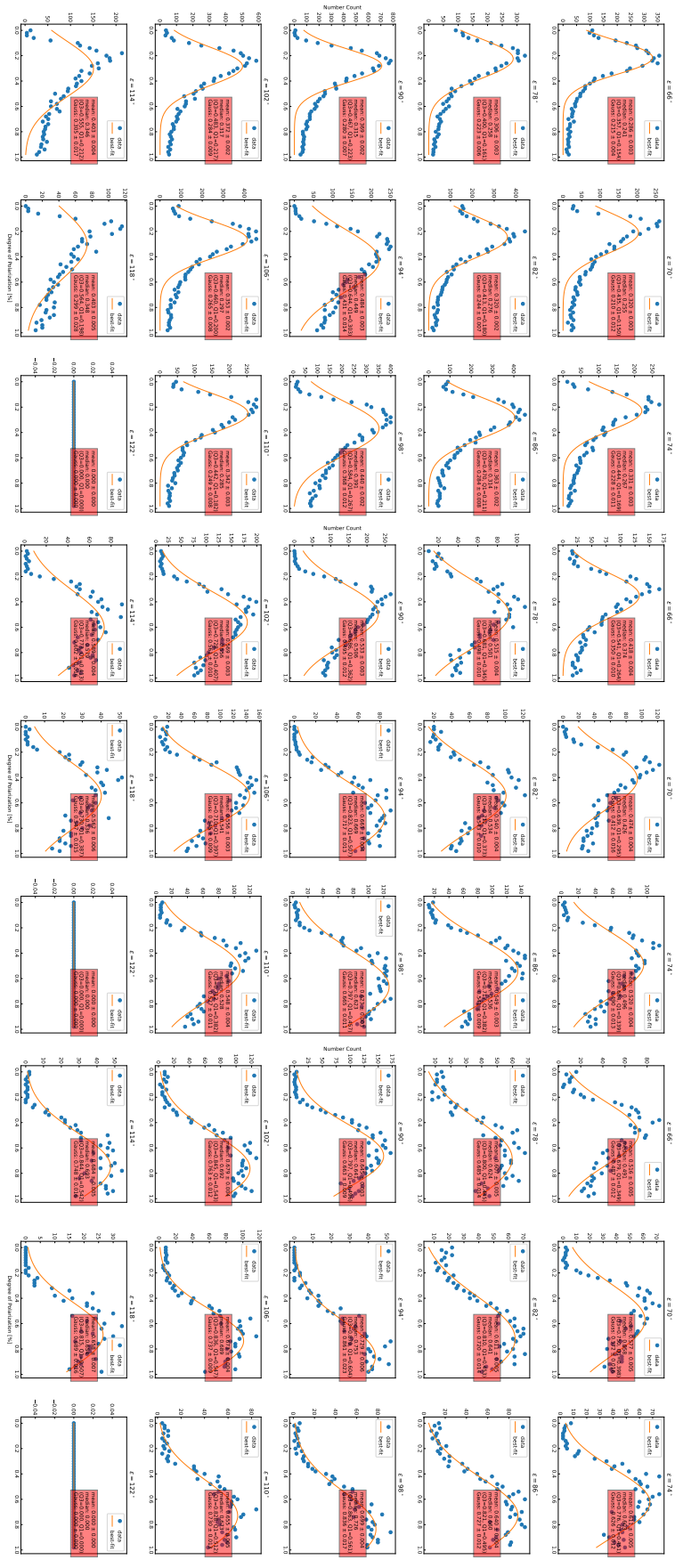

(A) Band1 (B) Band2 (C) Band3

FIGURE D.33: Histogram of $|P_{\lambda,\,\mathrm{ZL}}|$ for $P_{\lambda,\,\mathrm{ZL}}/\sigma_P > 1$ summed over Region 7, 8, and 9.

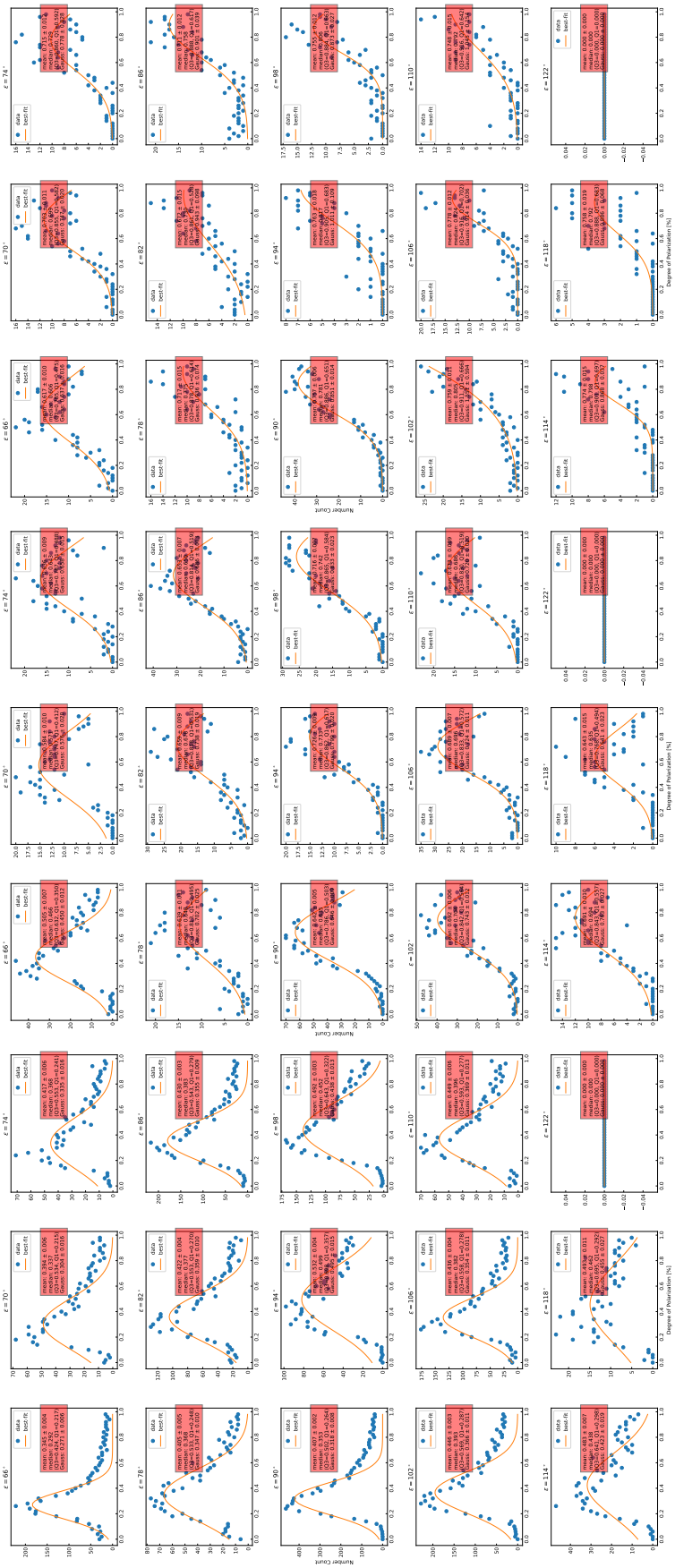

(A) Band1 (B) Band2 (C) Band3

FIGURE D.34: Histogram of $|P_{\lambda,\,\mathrm{ZL}}|$ for $P_{\lambda,\,\mathrm{ZL}}/\sigma_P > 2$ summed over Region 7, 8, and 9.

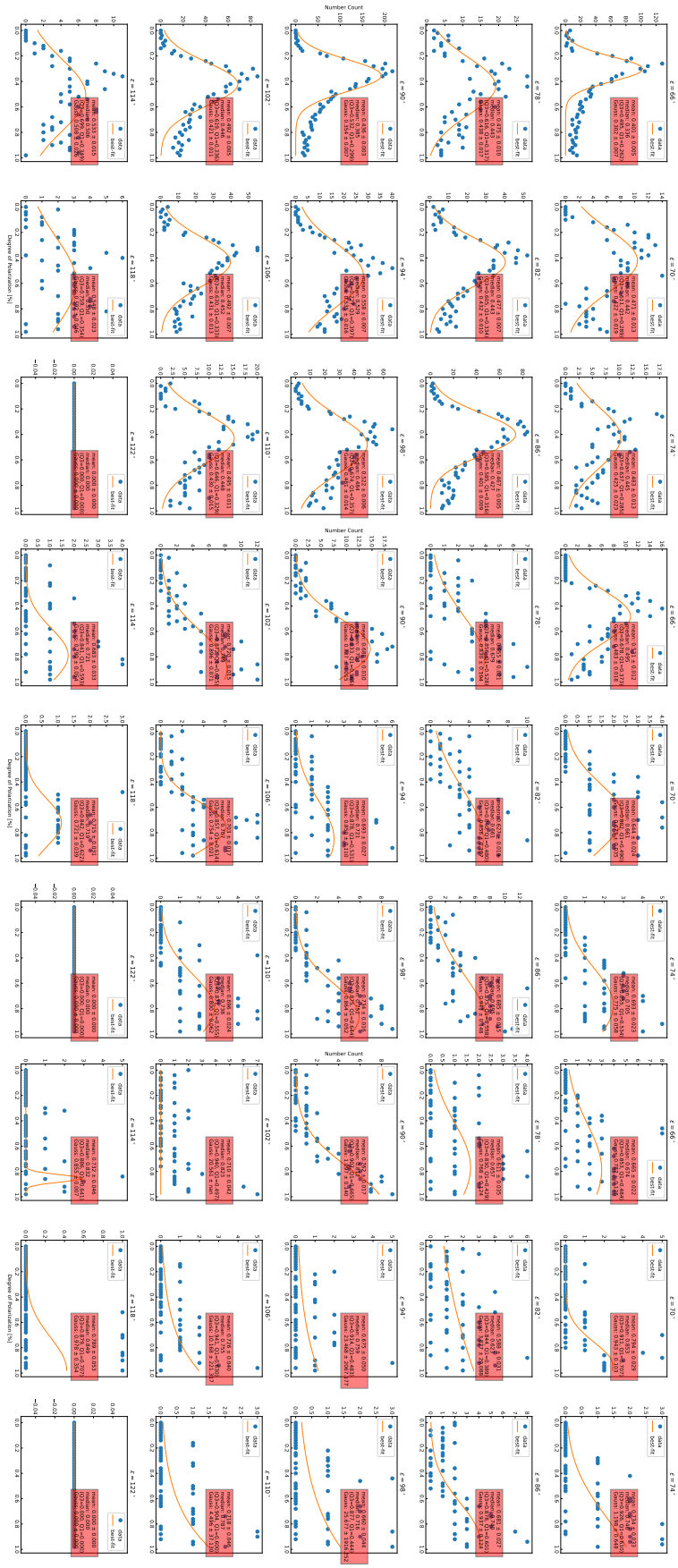

(A) Band1 (B) Band2 (C) Band3

FIGURE D.35: Histogram of $|P_{\lambda,\,\mathrm{ZL}}|$ for $P_{\lambda,\,\mathrm{ZL}}/\sigma_P > 3$ summed over Region 7, 8, and 9.

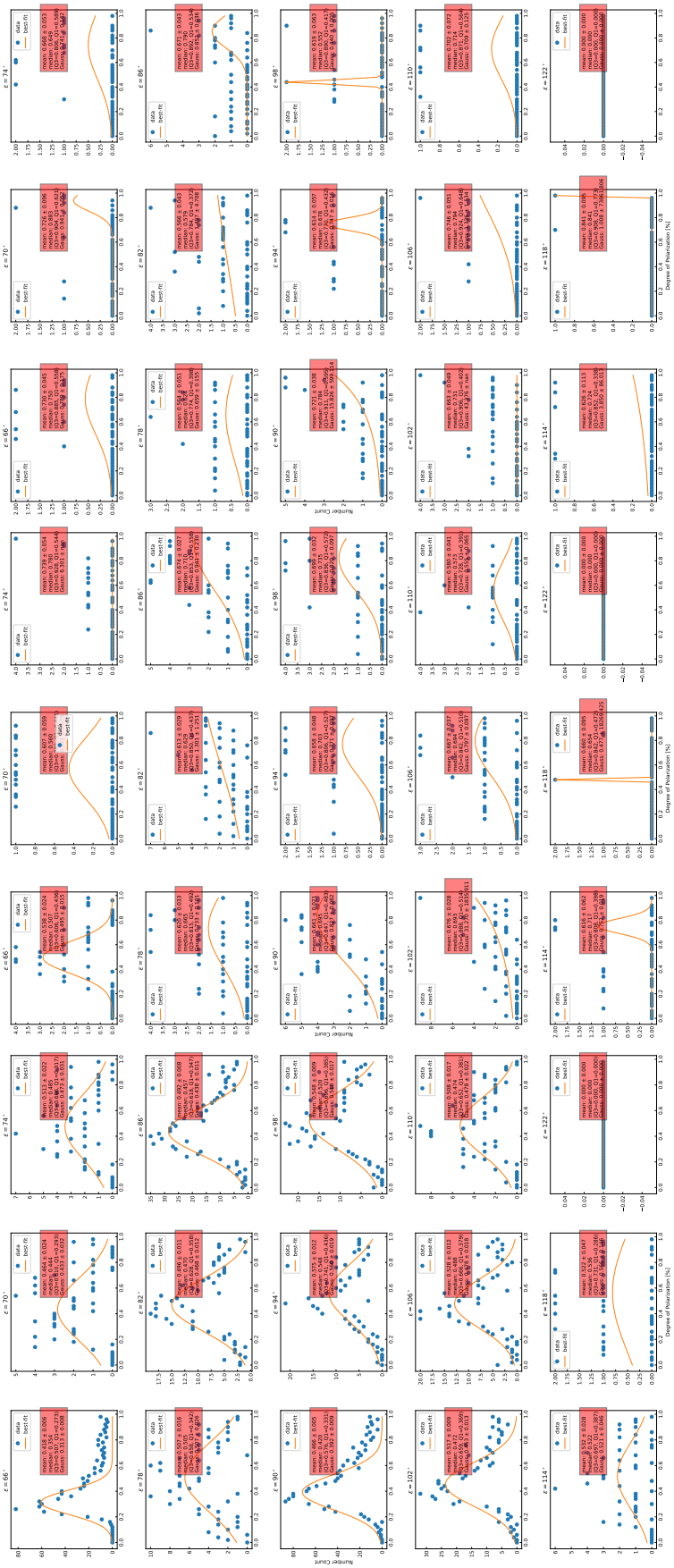

(A) Band1 (B) Band2 (C) Band3

FIGURE D.36: Histogram of $|P_{\lambda,\,\mathrm{ZL}}|$ for $P_{\lambda,\,\mathrm{ZL}}/\sigma_P > 4$ summed over Region 7, 8, and 9.

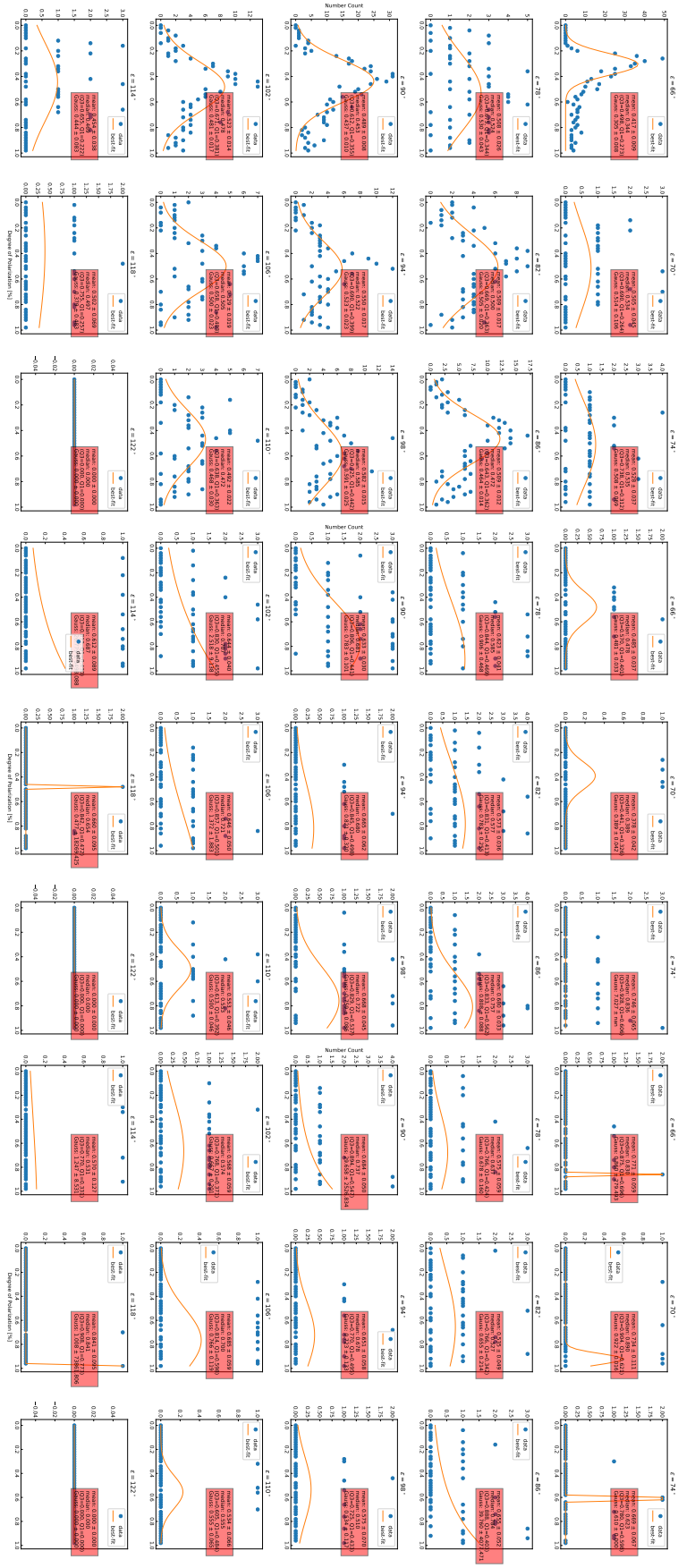

(A) Band1 (B) Band2 (C) Band3

FIGURE D.37: Histogram of $|P_{\lambda,\,\mathrm{ZL}}|$ for $P_{\lambda,\,\mathrm{ZL}}/\sigma_P > 5$ summed over Region 7, 8, and 9.

D.4 $P_{\lambda,\,\mathrm{ZL}}$ AND N IN EACH REGION AND EACH SOLAR ELONGATION FOR REPRESENTATIVE VALUES WITH THE CONDITION THAT $P_{\lambda,\,\mathrm{ZL}}/\sigma_P > k$

(Figure D.38, D.39, D.40, D.41, D.42, D.43, D.44, D.45, D.46, D.47, D.48, D.49, D.50, D.51, and D.52)

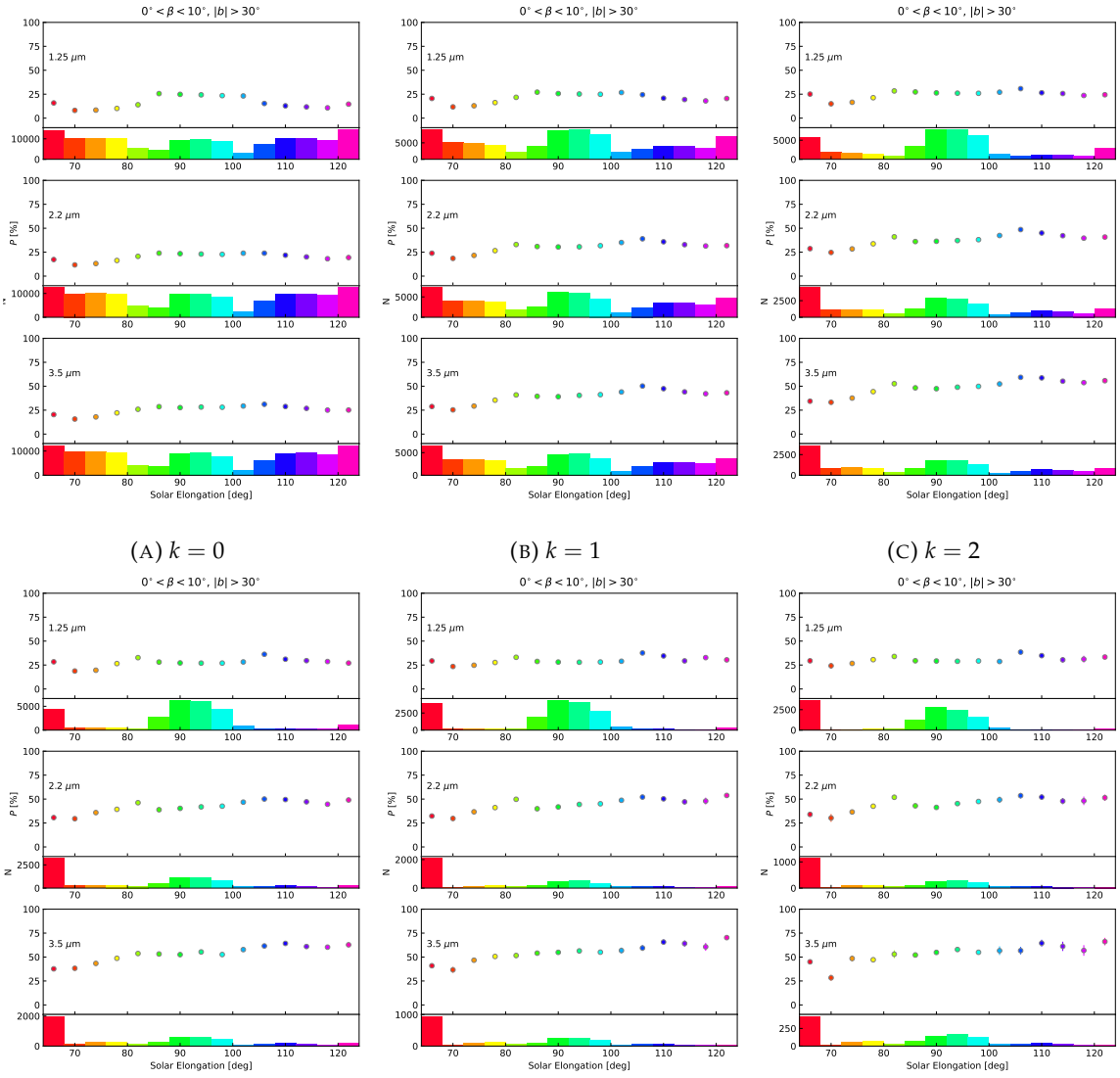

(A) $k = 0$ (B) $k = 1$ (C) $k = 2$

(D) $k = 3$ (E) $k = 4$ (F) $k = 5$

FIGURE D.38: The solar elongation dependence of $P_{\lambda,\,\mathrm{ZL}}$ and N in Region 1 when the representative value is taken as the mean value under the condition that $P_{\lambda,\,\mathrm{ZL}}/\sigma_P > k$. Error bars indicate the standard error relative to the mean.

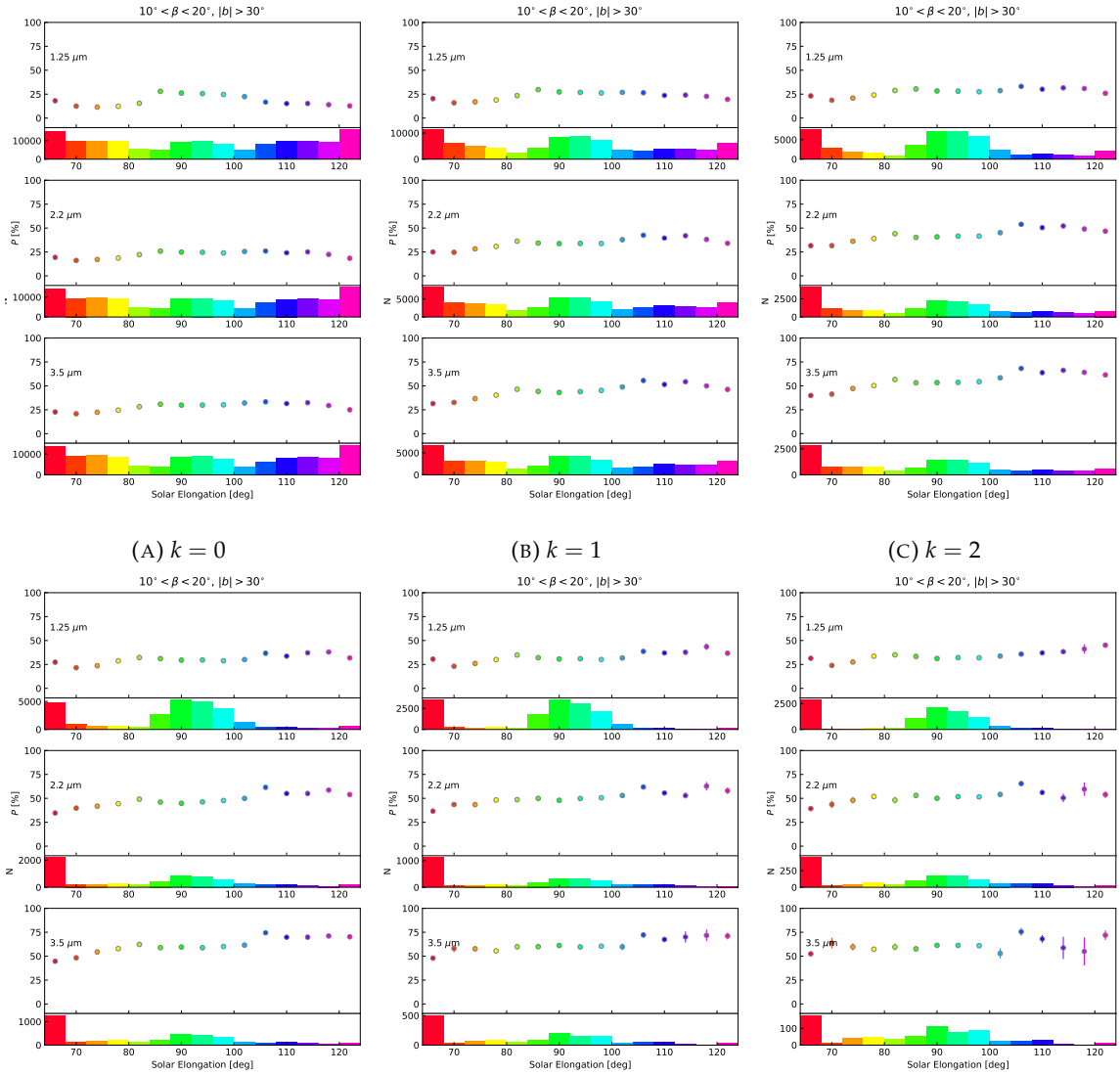

(A) $k = 0$ (B) $k = 1$ (C) $k = 2$

(D) $k = 3$ (E) $k = 4$ (F) $k = 5$

FIGURE D.39: The solar elongation dependence of $P_{\lambda,\,\mathrm{ZL}}$ and N in Region 2 when the representative value is taken as the mean value under the condition that $P_{\lambda,\,\mathrm{ZL}}/\sigma_P > k$. Error bars indicate the standard error relative to the mean.

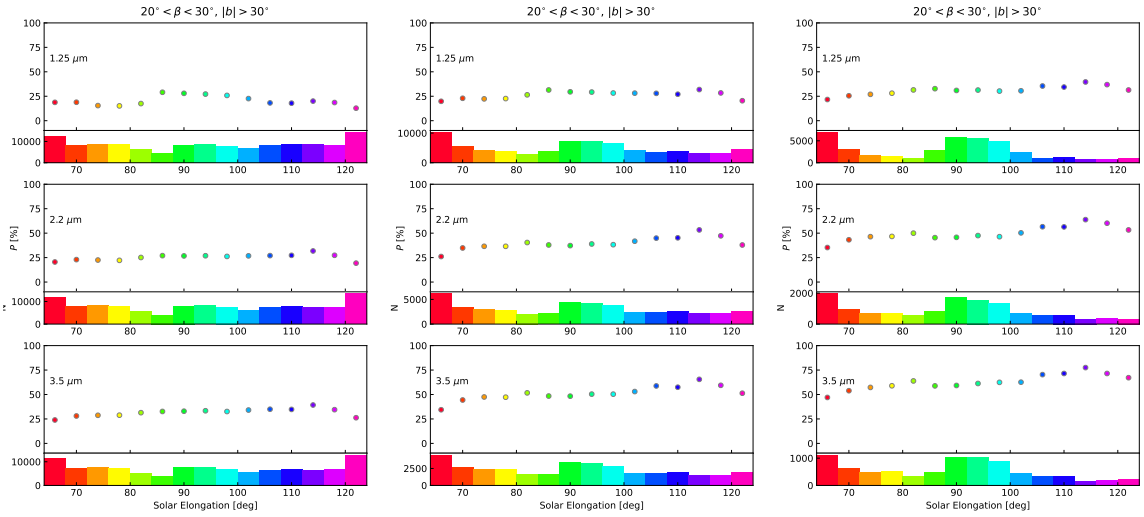

(A) $k = 0$ (B) $k = 1$ (C) $k = 2$

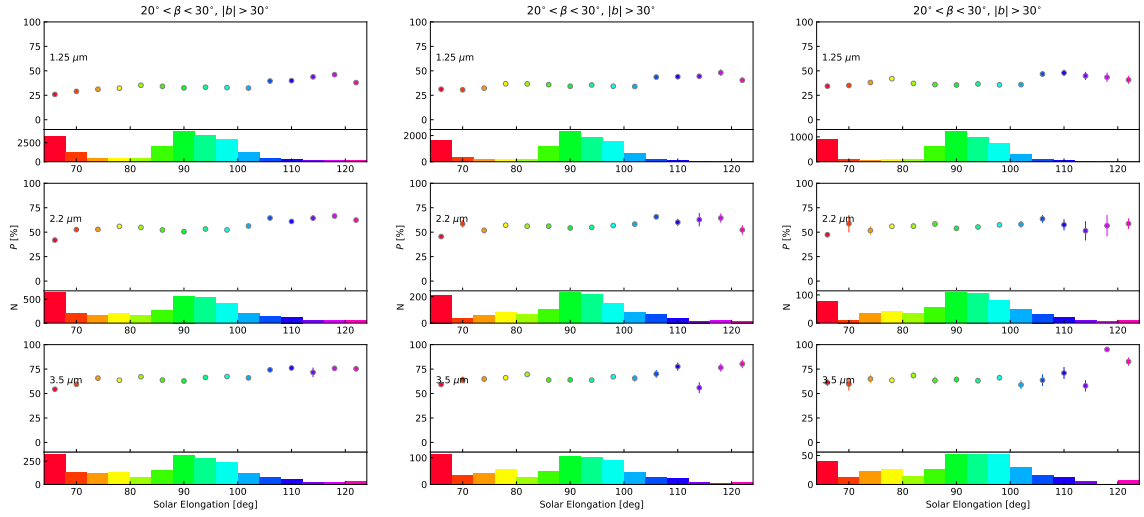

(D) $k = 3$ (E) $k = 4$ (F) $k = 5$

FIGURE D.40: The solar elongation dependence of $P_{\lambda,\,\mathrm{ZL}}$ and N in Region 3 when the representative value is taken as the mean value under the condition that $P_{\lambda,\,\mathrm{ZL}}/\sigma_P > k$. Error bars indicate the standard error relative to the mean.

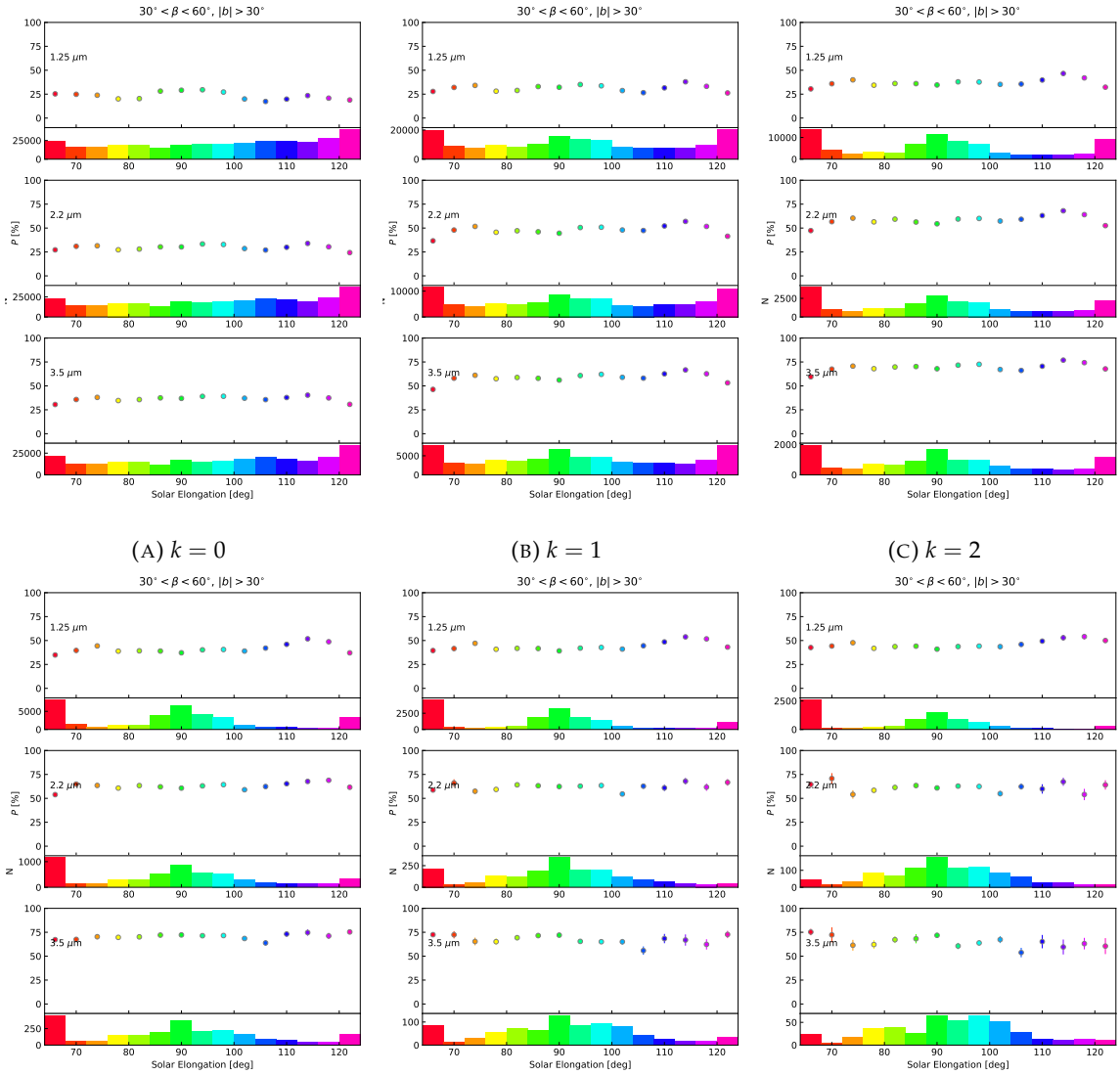

(A) $k = 0$ (B) $k = 1$ (C) $k = 2$

(D) $k = 3$ (E) $k = 4$ (F) $k = 5$

FIGURE D.41: The solar elongation dependence of $P_{\lambda,\,\mathrm{ZL}}$ and N summed over Region 4, 5, and 6 when the representative value is taken as the mean value under the condition that $P_{\lambda,\,\mathrm{ZL}}/\sigma_P > k$. Error bars indicate the standard error relative to the mean.

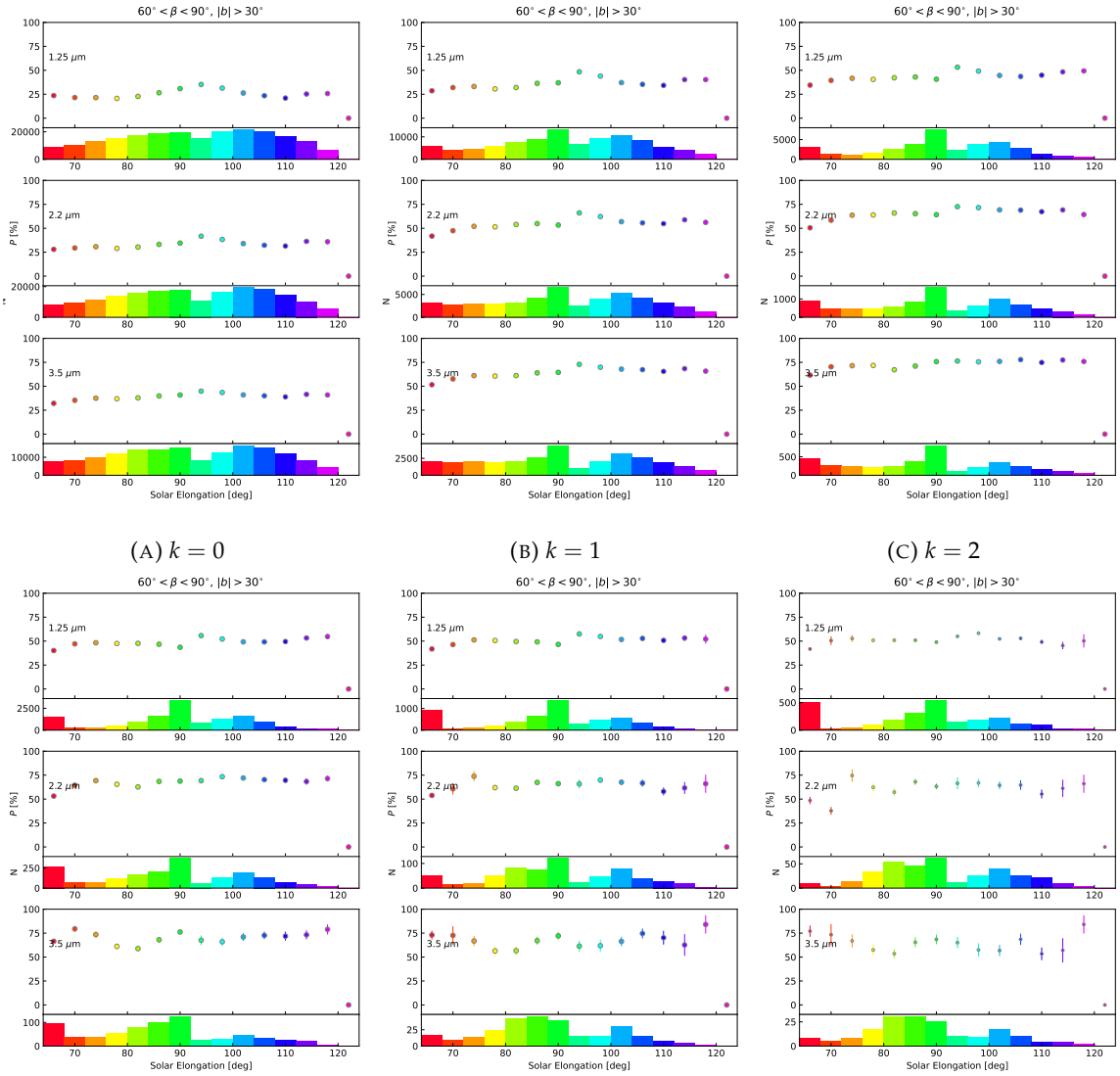

(A) $k = 0$ (B) $k = 1$ (C) $k = 2$

(D) $k = 3$ (E) $k = 4$ (F) $k = 5$

FIGURE D.42: The solar elongation dependence of $P_{\lambda,\,\mathrm{ZL}}$ and N summed over Region 7, 8, and 9 when the representative value is taken as the mean value under the condition that $P_{\lambda,\,\mathrm{ZL}}/\sigma_P > k$. Error bars indicate the standard error relative to the mean.

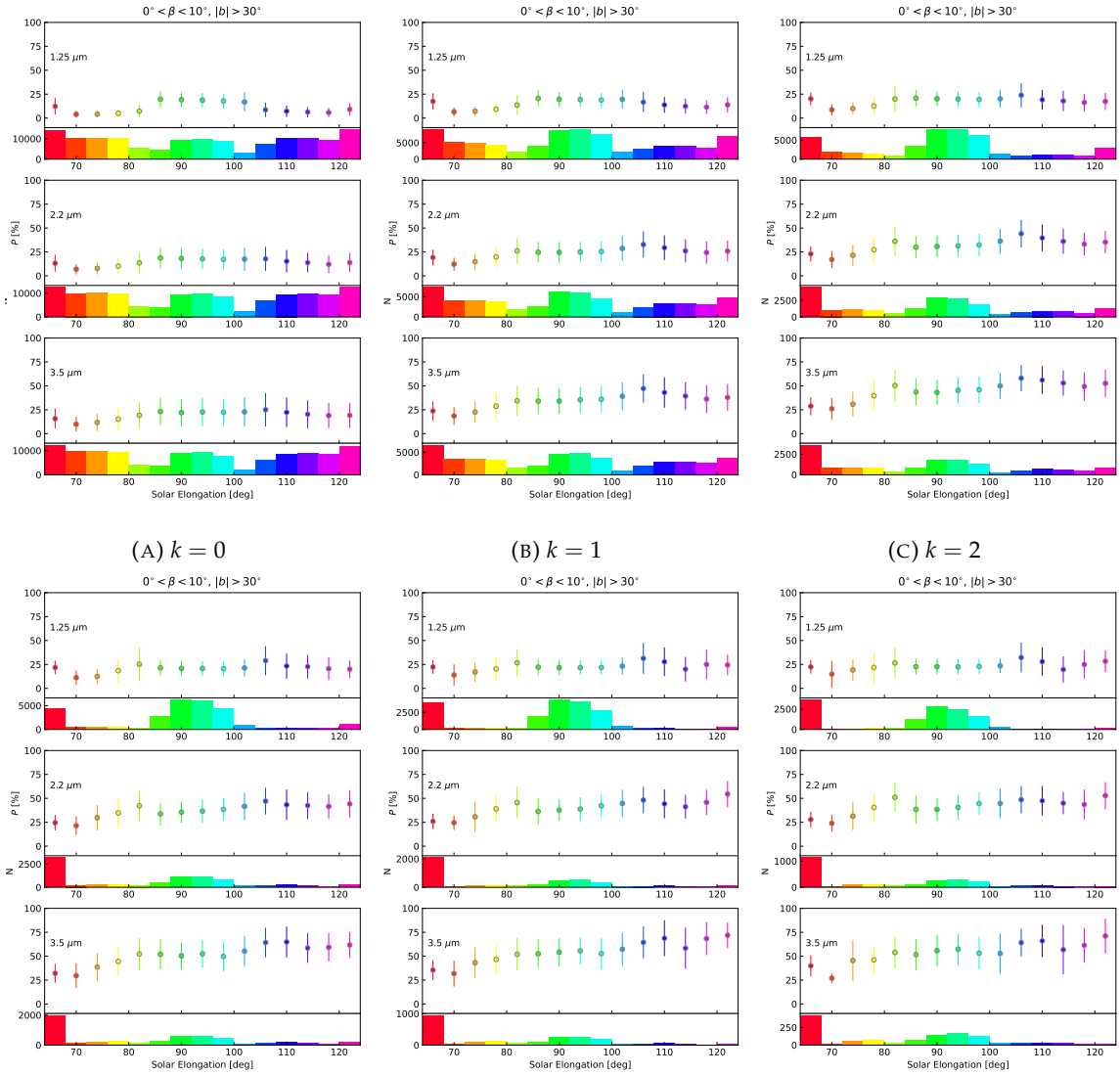

(A) $k = 0$ (B) $k = 1$ (C) $k = 2$

(D) $k = 3$ (E) $k = 4$ (F) $k = 5$

FIGURE D.43: The solar elongation dependence of $P_{\lambda,\,\mathrm{ZL}}$ and N in Region 1 when the representative value is taken as the median value under the condition that $P_{\lambda,\,\mathrm{ZL}}/\sigma_P > k$. Error bars indicate Quartile deviation relative to the median.

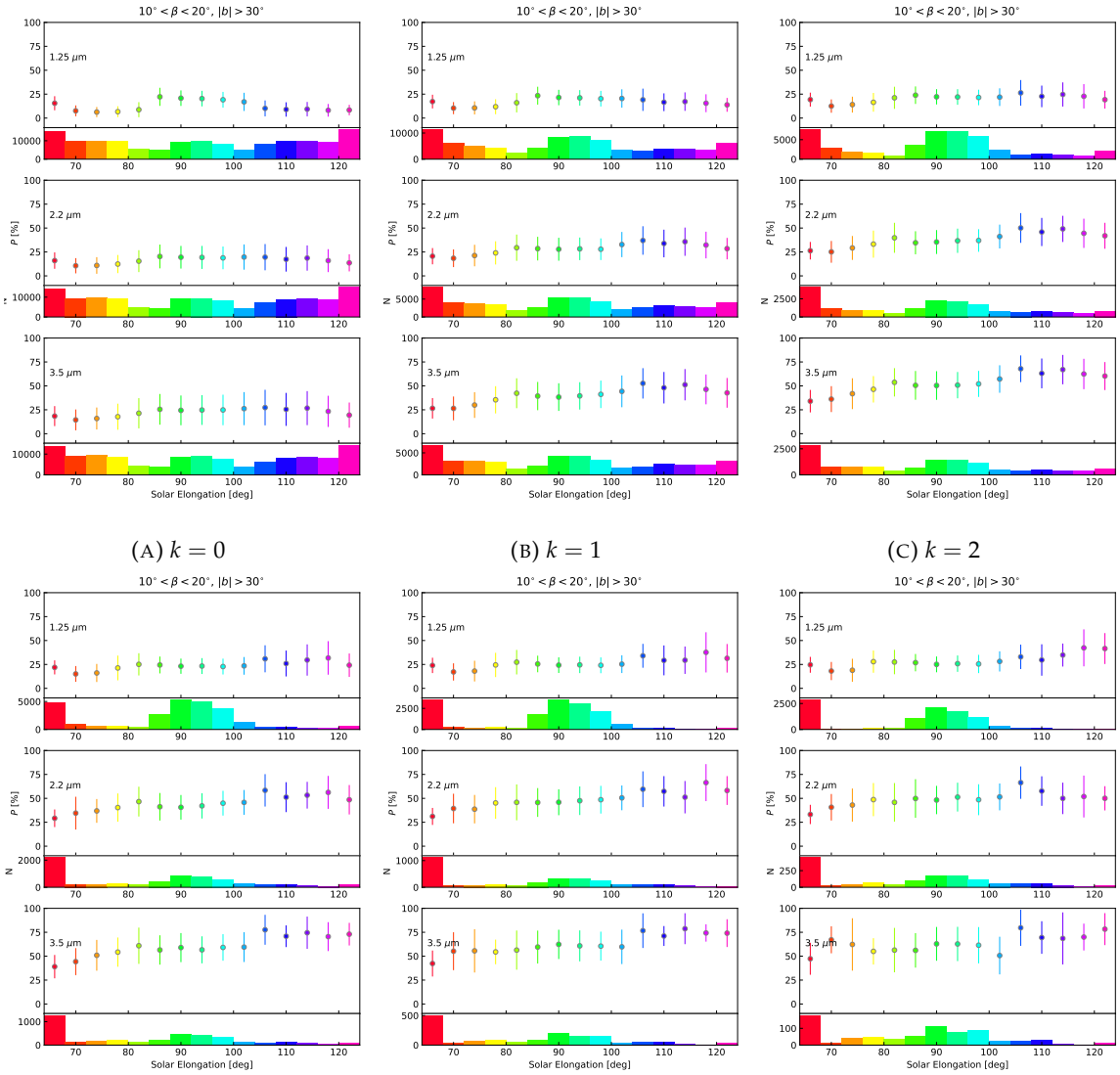

(A) $k = 0$ (B) $k = 1$ (C) $k = 2$

(D) $k = 3$ (E) $k = 4$ (F) $k = 5$

FIGURE D.44: The solar elongation dependence of $P_{\lambda,\,\mathrm{ZL}}$ and N in Region 2 when the representative value is taken as the median value under the condition that $P_{\lambda,\,\mathrm{ZL}}/\sigma_P > k$. Error bars indicate Quartile deviation relative to the median.

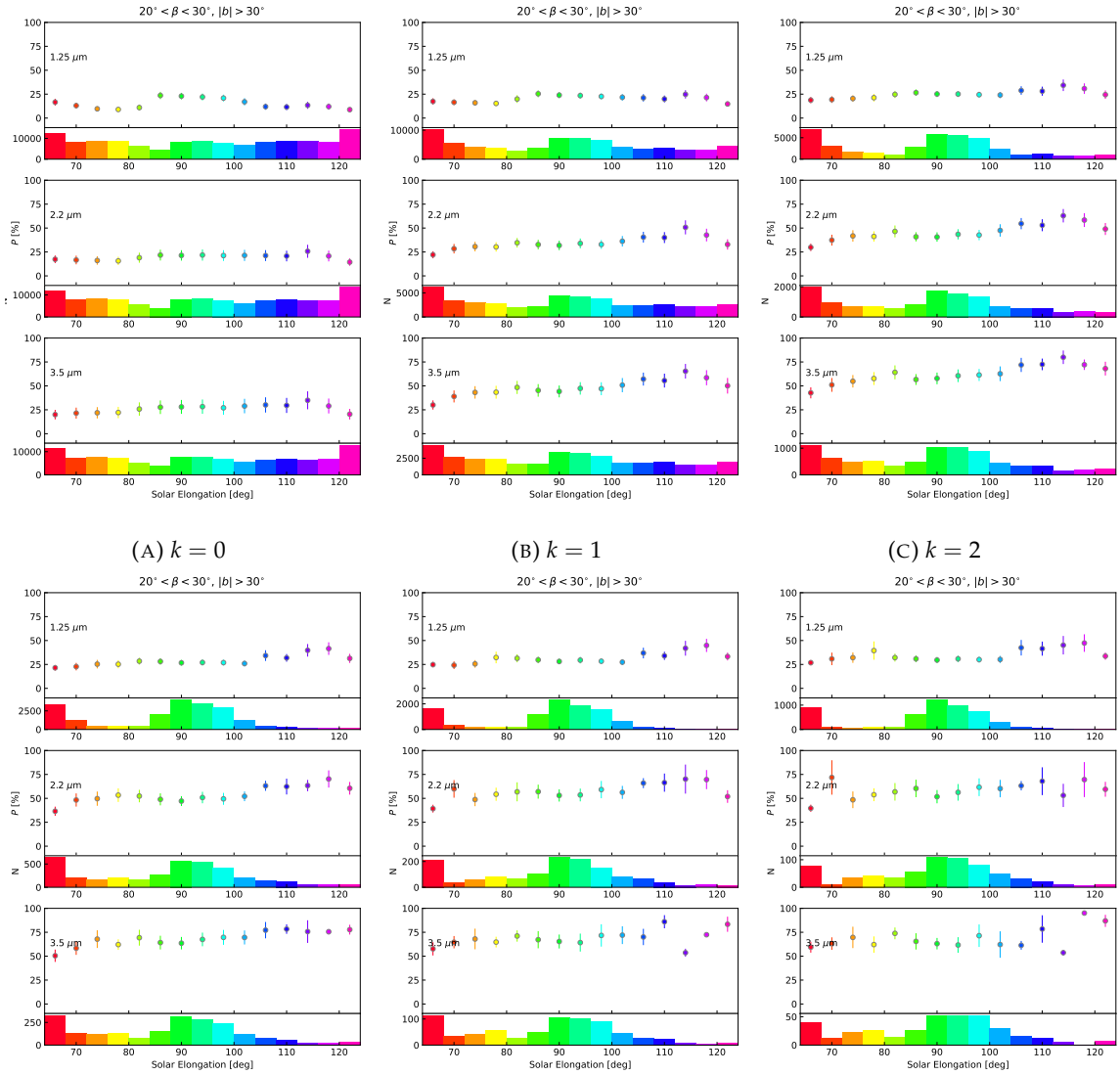

(A) $k = 0$ (B) $k = 1$ (C) $k = 2$

(D) $k = 3$ (E) $k = 4$ (F) $k = 5$

FIGURE D.45: The solar elongation dependence of $P_{\lambda,\,\mathrm{ZL}}$ and N in Region 3 when the representative value is taken as the median value under the condition that $P_{\lambda,\,\mathrm{ZL}}/\sigma_P > k$. Error bars indicate Quartile deviation relative to the median.

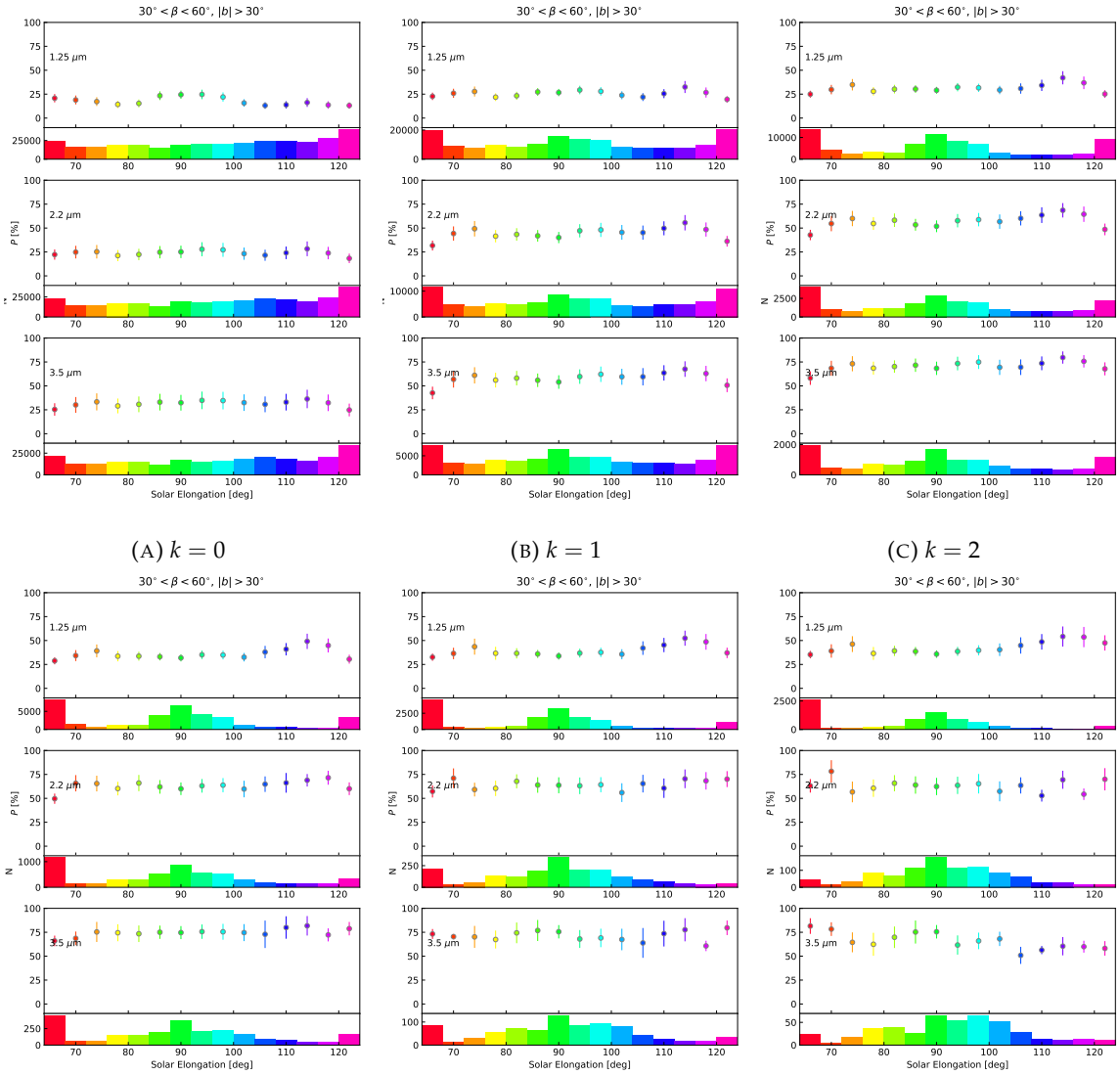

(A) $k = 0$ (B) $k = 1$ (C) $k = 2$

(D) $k = 3$ (E) $k = 4$ (F) $k = 5$

FIGURE D.46: The solar elongation dependence of $P_{\lambda,\,\mathrm{ZL}}$ and N summed over Region 4, 5, and 6 when the representative value is taken as the median value under the condition that $P_{\lambda,\,\mathrm{ZL}}/\sigma_P > k$. Error bars indicate Quartile deviation relative to the median.

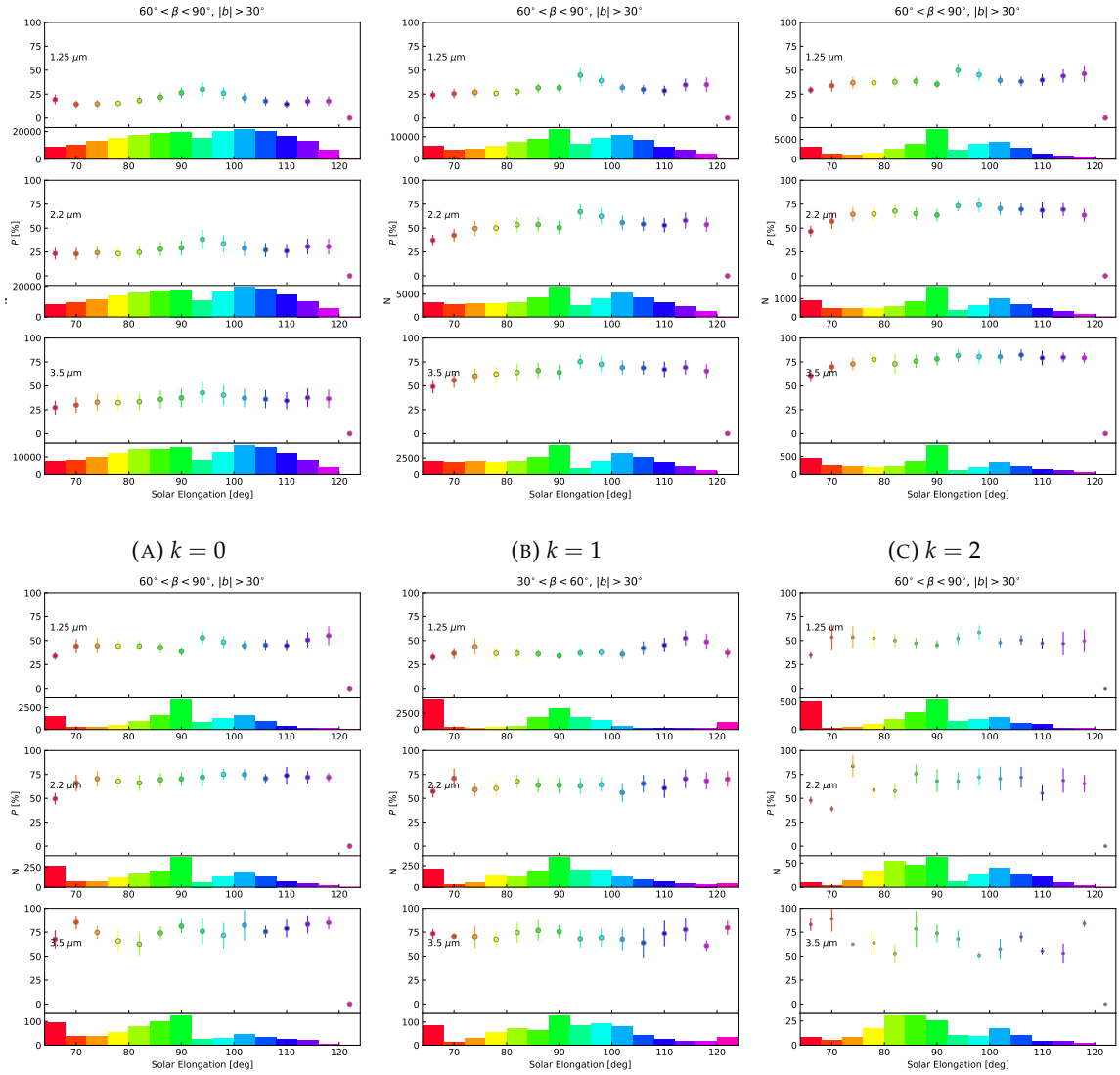

(A) $k = 0$ (B) $k = 1$ (C) $k = 2$

(D) $k = 3$ (E) $k = 4$ (F) $k = 5$

FIGURE D.47: The solar elongation dependence of $P_{\lambda,\,\mathrm{ZL}}$ and N summed over Region 7, 8, and 9 when the representative value is taken as the median value under the condition that $P_{\lambda,\,\mathrm{ZL}}/\sigma_P > k$. Error bars indicate Quartile deviation relative to the median.

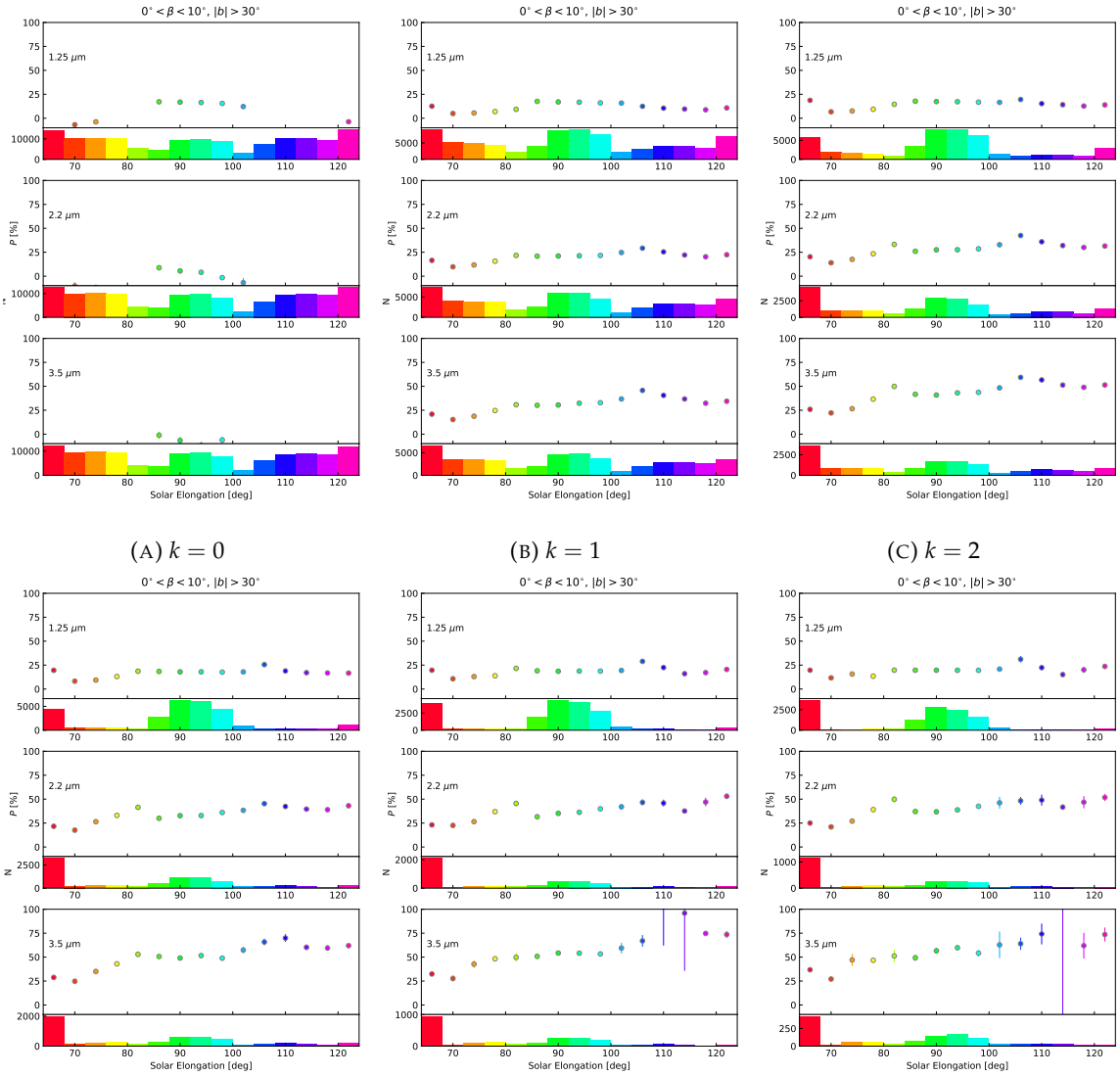

(A) $k = 0$ (B) $k = 1$ (C) $k = 2$

(D) $k = 3$ (E) $k = 4$ (F) $k = 5$

FIGURE D.48: The solar elongation dependence of $P_{\lambda,\,\mathrm{ZL}}$ and N in Region 1 when the representative value is taken as the central value obtained by Gaussian fitting under the condition that $P_{\lambda,\,\mathrm{ZL}}/\sigma_P > k$. Error bars indicate the standard error relative to the central value obtained by Gaussian fitting.

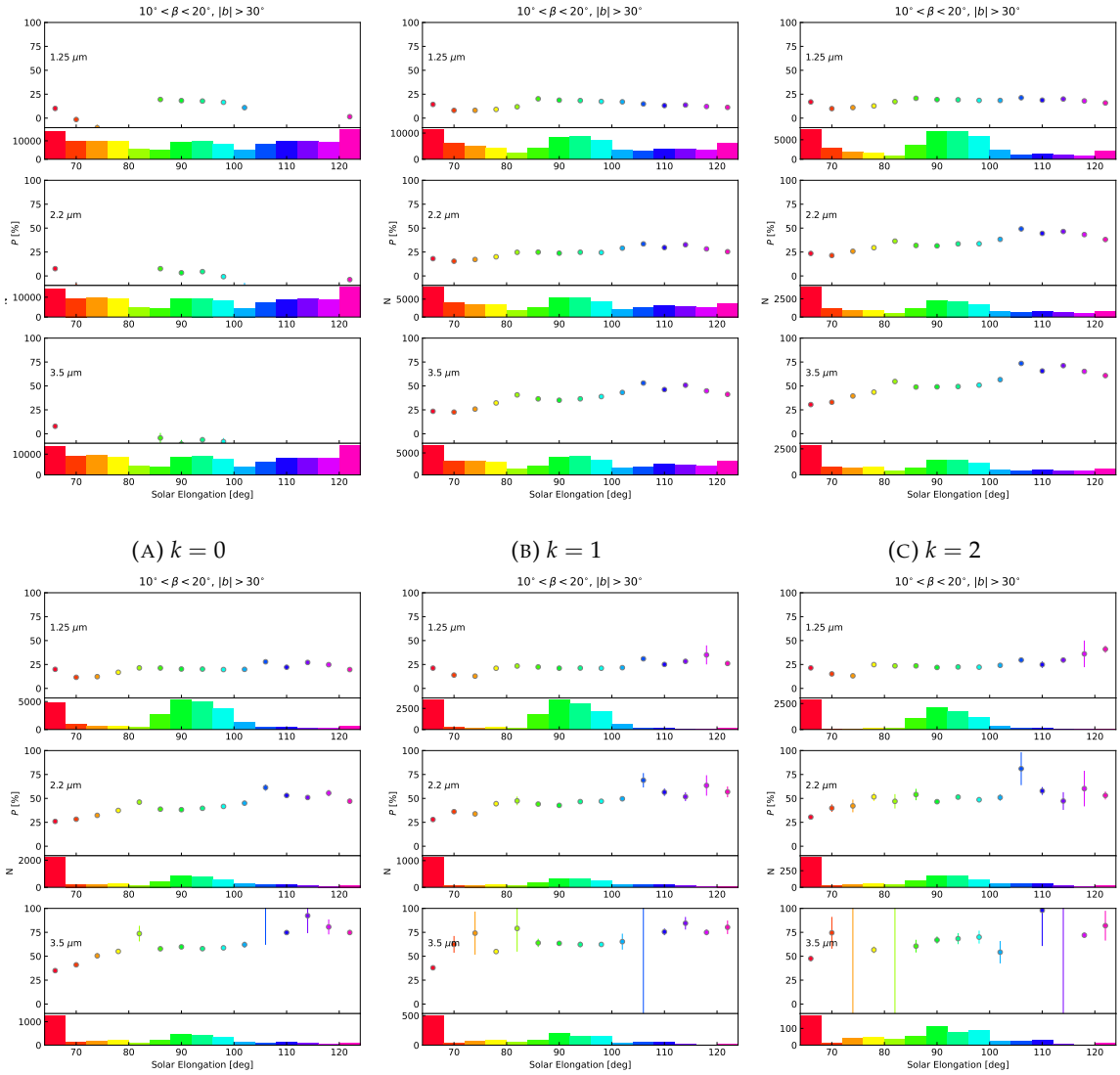

(A) $k = 0$ (B) $k = 1$ (C) $k = 2$

(D) $k = 3$ (E) $k = 4$ (F) $k = 5$

FIGURE D.49: The solar elongation dependence of $P_{\lambda,\,\mathrm{ZL}}$ and N in Region 2 when the representative value is taken as the central value obtained by Gaussian fitting under the condition that $P_{\lambda,\,\mathrm{ZL}}/\sigma_P > k$. Error bars indicate the standard error relative to the central value obtained by Gaussian fitting.

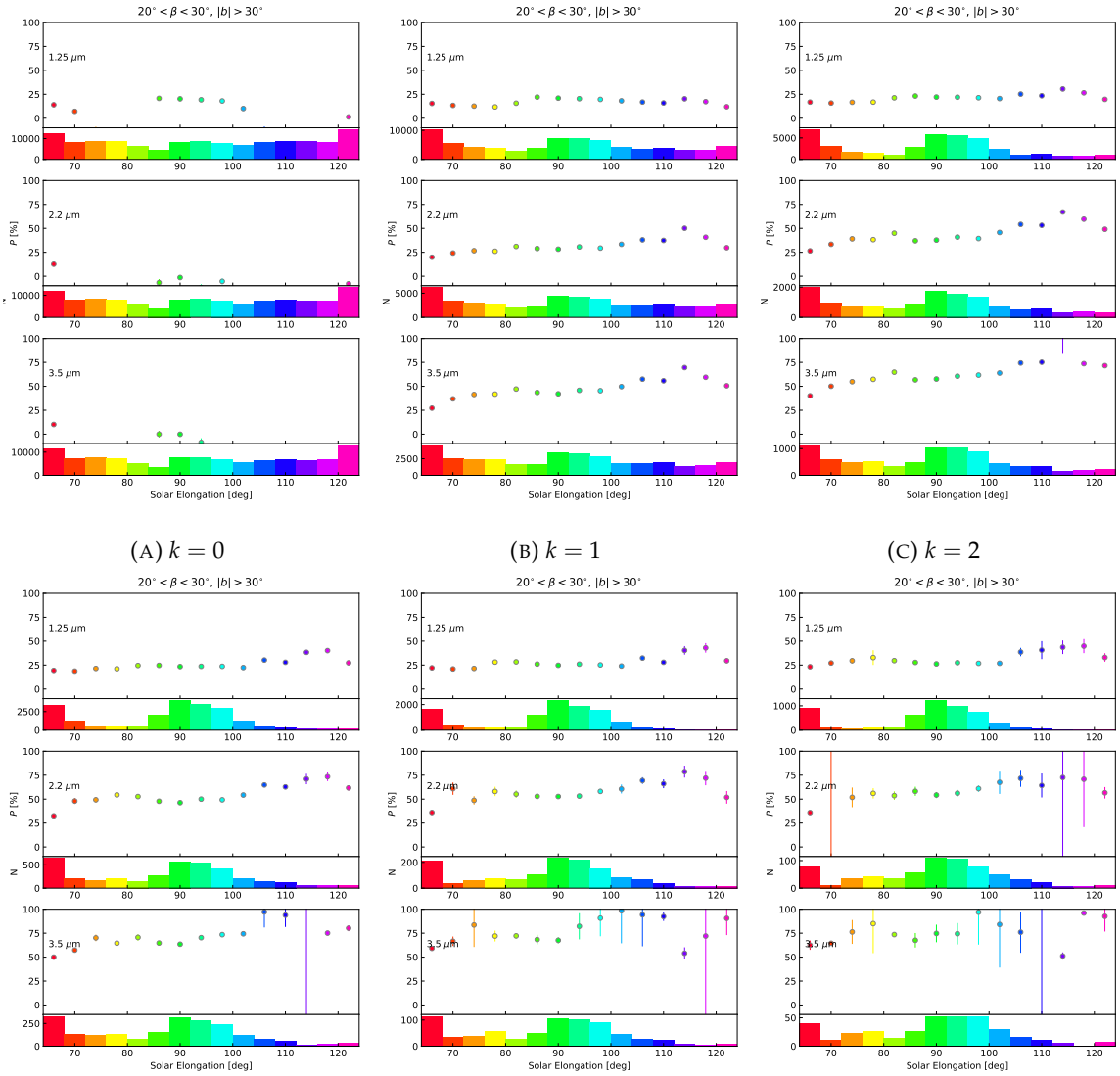

(A) $k = 0$ (B) $k = 1$ (C) $k = 2$

(D) $k = 3$ (E) $k = 4$ (F) $k = 5$

FIGURE D.50: The solar elongation dependence of $P_{\lambda,\,\mathrm{ZL}}$ and N in Region 3 when the representative value is taken as the central value obtained by Gaussian fitting under the condition that $P_{\lambda,\,\mathrm{ZL}}/\sigma_P > k$. Error bars indicate the standard error relative to the central value obtained by Gaussian fitting.

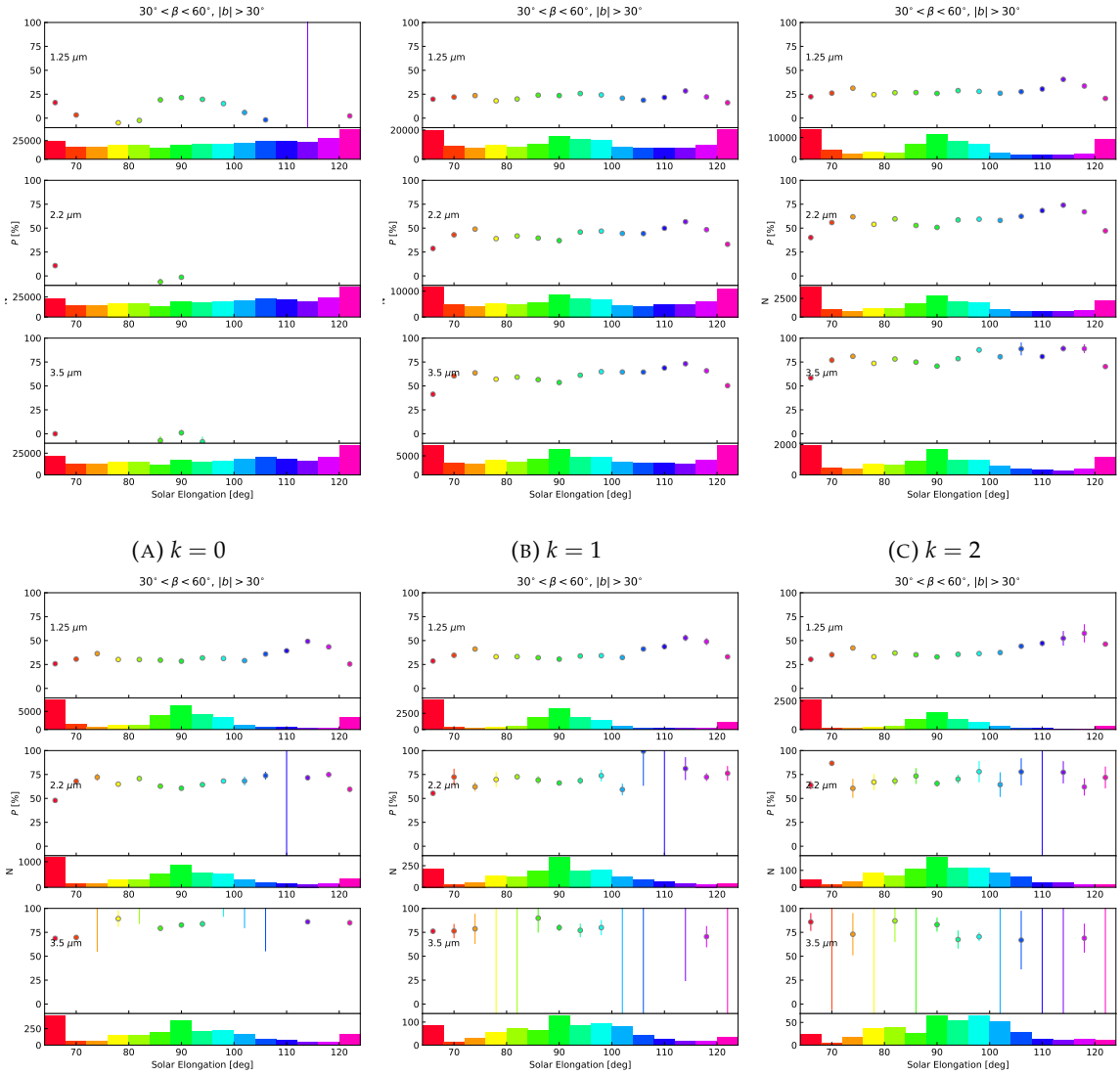

(A) $k = 0$ (B) $k = 1$ (C) $k = 2$

(D) $k = 3$ (E) $k = 4$ (F) $k = 5$

FIGURE D.51: The solar elongation dependence of $P_{\lambda,\,\mathrm{ZL}}$ and N summed over Region 4, 5, and 6 when the representative value is taken as the central value obtained by Gaussian fitting under the condition that $P_{\lambda,\,\mathrm{ZL}}/\sigma_P > k$. Error bars indicate the standard error relative to the central value obtained by Gaussian fitting.

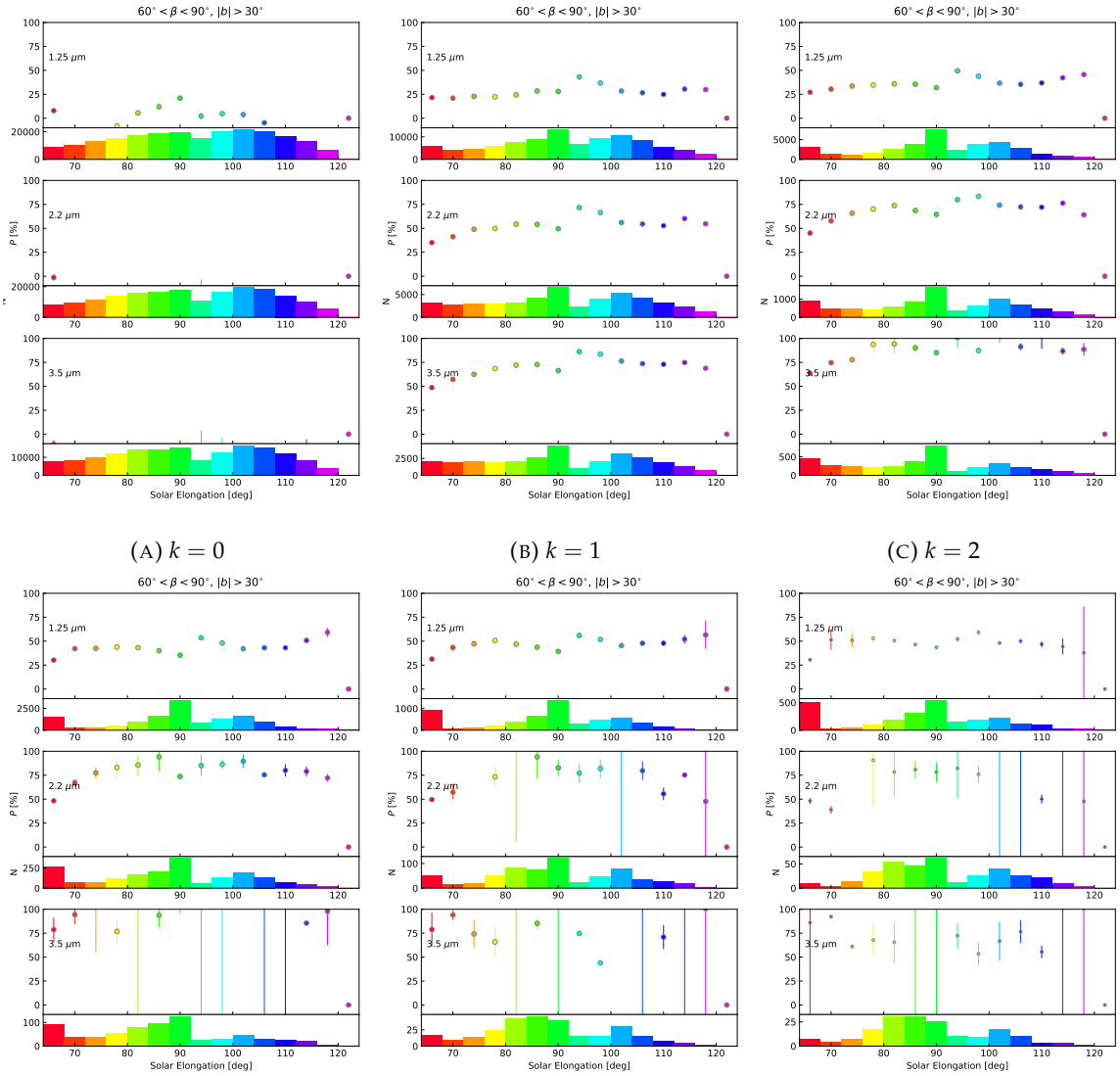

(A) $k = 0$ (B) $k = 1$ (C) $k = 2$

(D) $k = 3$ (E) $k = 4$ (F) $k = 5$

FIGURE D.52: The solar elongation dependence of $P_{\lambda,\,\mathrm{ZL}}$ and N summed over Region 7, 8, and 9 when the representative value is taken as the central value obtained by Gaussian fitting under the condition that $P_{\lambda,\,\mathrm{ZL}}/\sigma_P > k$. Error bars indicate the standard error relative to the central value obtained by Gaussian fitting.

D.5 IN EACH REGION AND EACH SOLAR ELONGATION UNDER THE CONDITION THAT $P_{\lambda,\,\mathrm{ZL}}$ IN EACH REGION AND EACH SOLAR ELONGATION UNDER THE CONDITION THAT $P_{\lambda,\,\mathrm{ZL}}/\sigma_P > k$

(Figure D.53, D.54, D.55, D.56, and D.57)

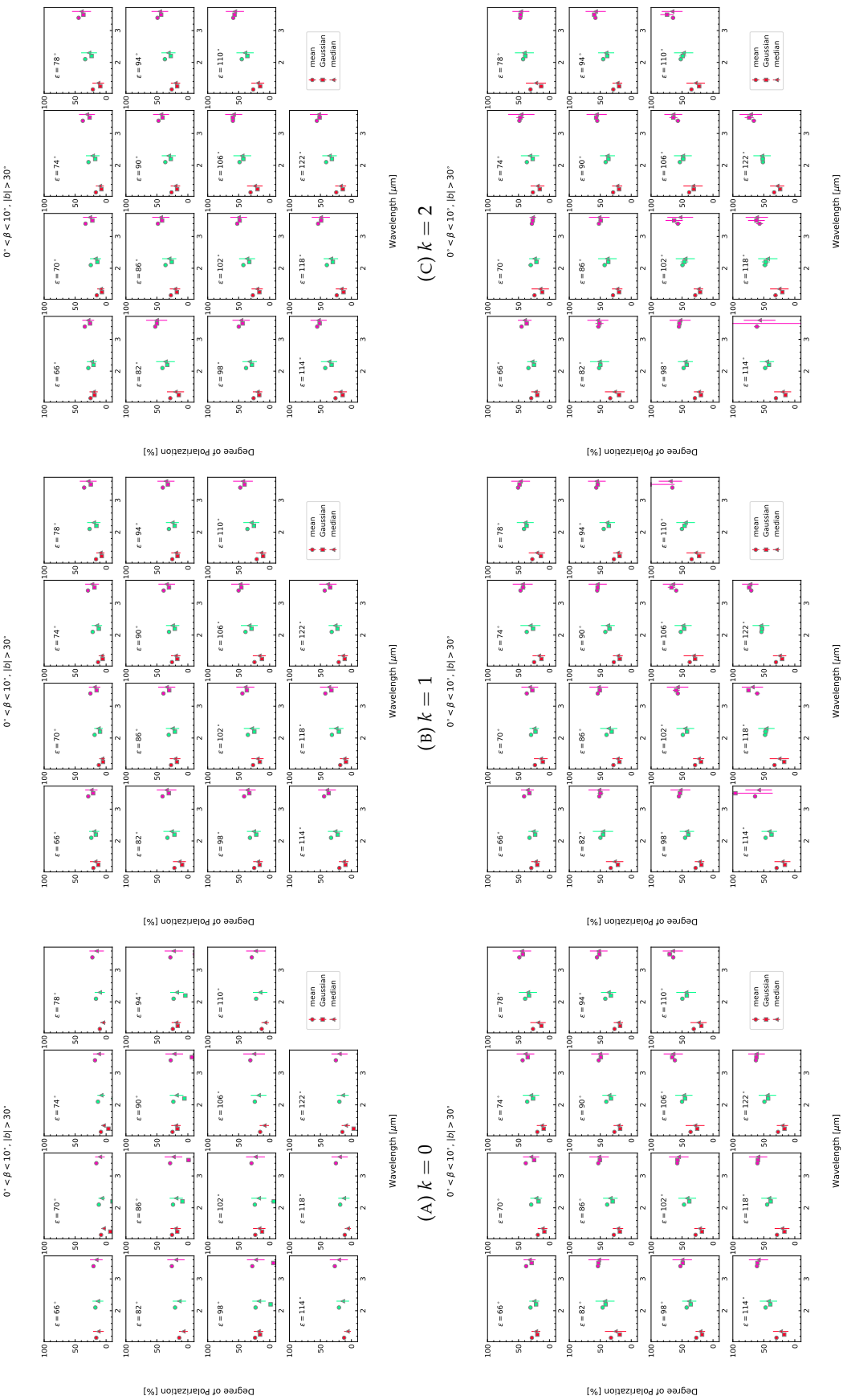

FIGURE D.53: The wavelength dependence of $P_{\lambda,\,\mathrm{ZL}}$ in Region 1 under the condition that $P_{\lambda,\,\mathrm{ZL}}/\sigma_P > k$.

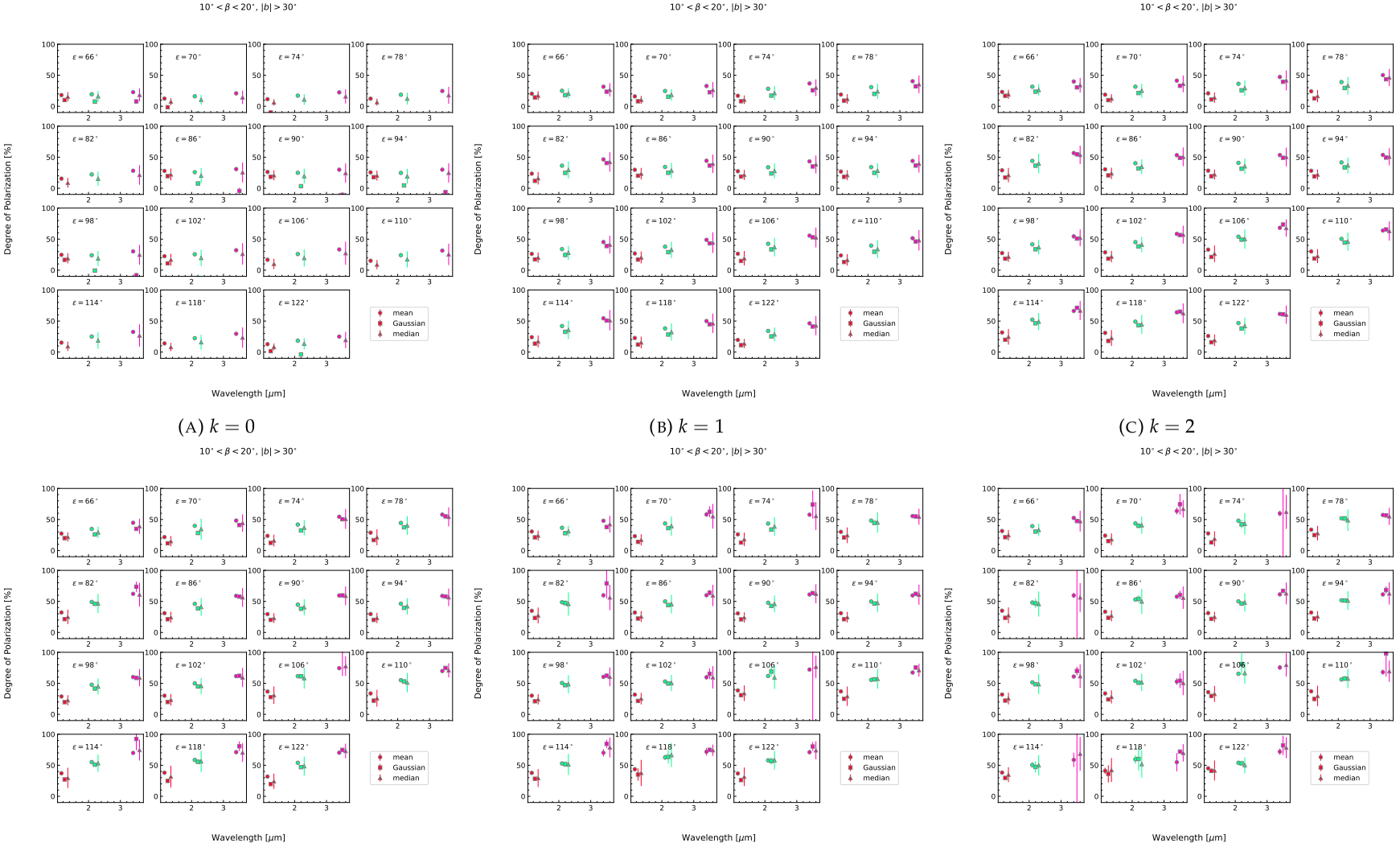

(A) $k = 0$ (B) $k = 1$ (C) $k = 2$

(D) $k = 3$ (E) $k = 4$ (F) $k = 5$

FIGURE D.54: The wavelength dependence of $P_{\lambda,\,\mathrm{ZL}}$ in Region 2 under the condition that $P_{\lambda,\,\mathrm{ZL}}/\sigma_P > k$.

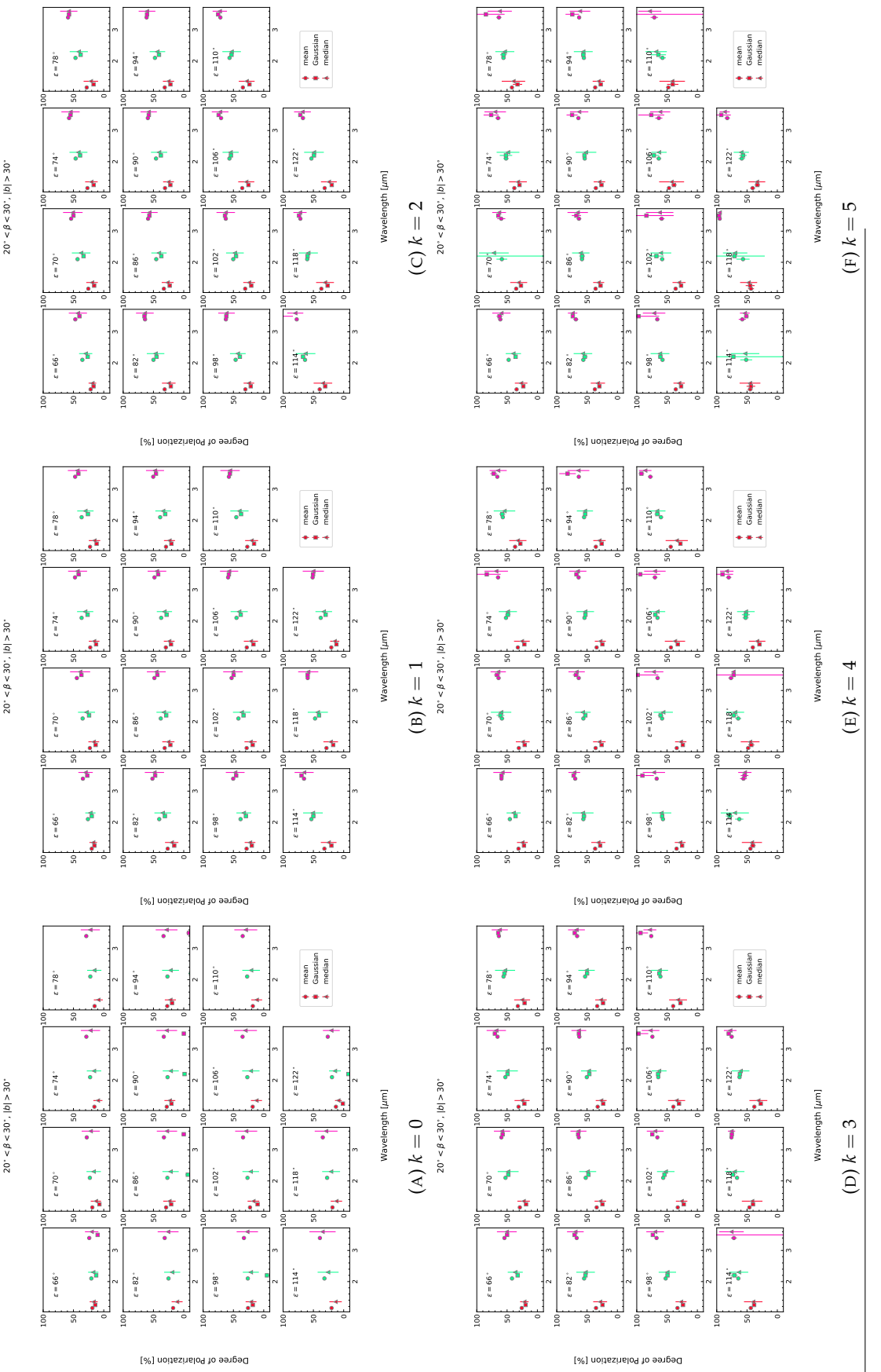

FIGURE D.55: The wavelength dependence of $P_{\lambda,\,\mathrm{ZL}}$ in Region 2 under the condition that $P_{\lambda,\,\mathrm{ZL}}/\sigma_P > k$.

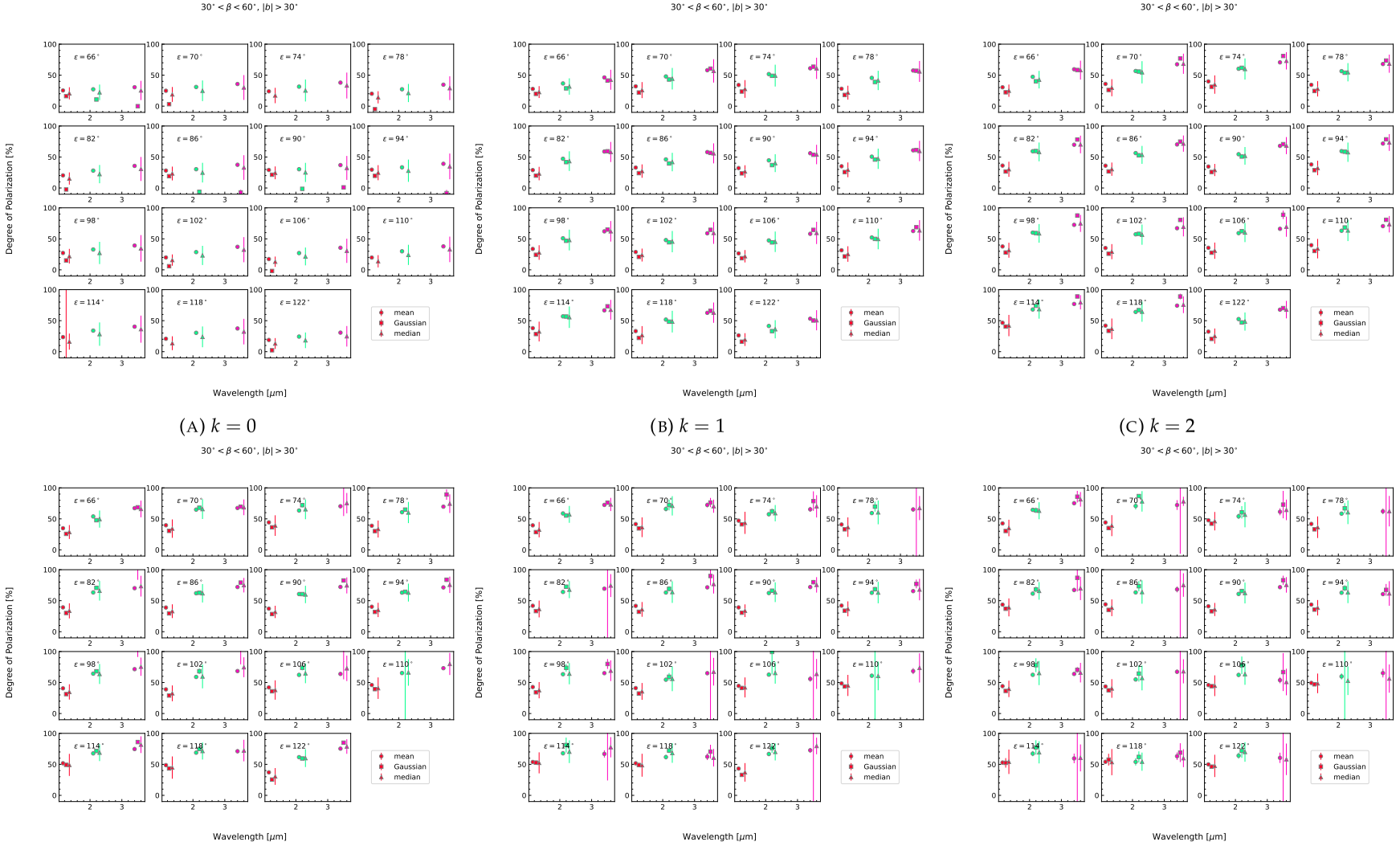

(A) $k = 0$ (B) $k = 1$ (C) $k = 2$

(D) $k = 3$ (E) $k = 4$ (F) $k = 5$

FIGURE D.56: The wavelength dependence of $P_{\lambda,\,\mathrm{ZL}}$ summed over Region 4, 5, and 6 under the condition that $P_{\lambda,\,\mathrm{ZL}}/\sigma_P > k$.

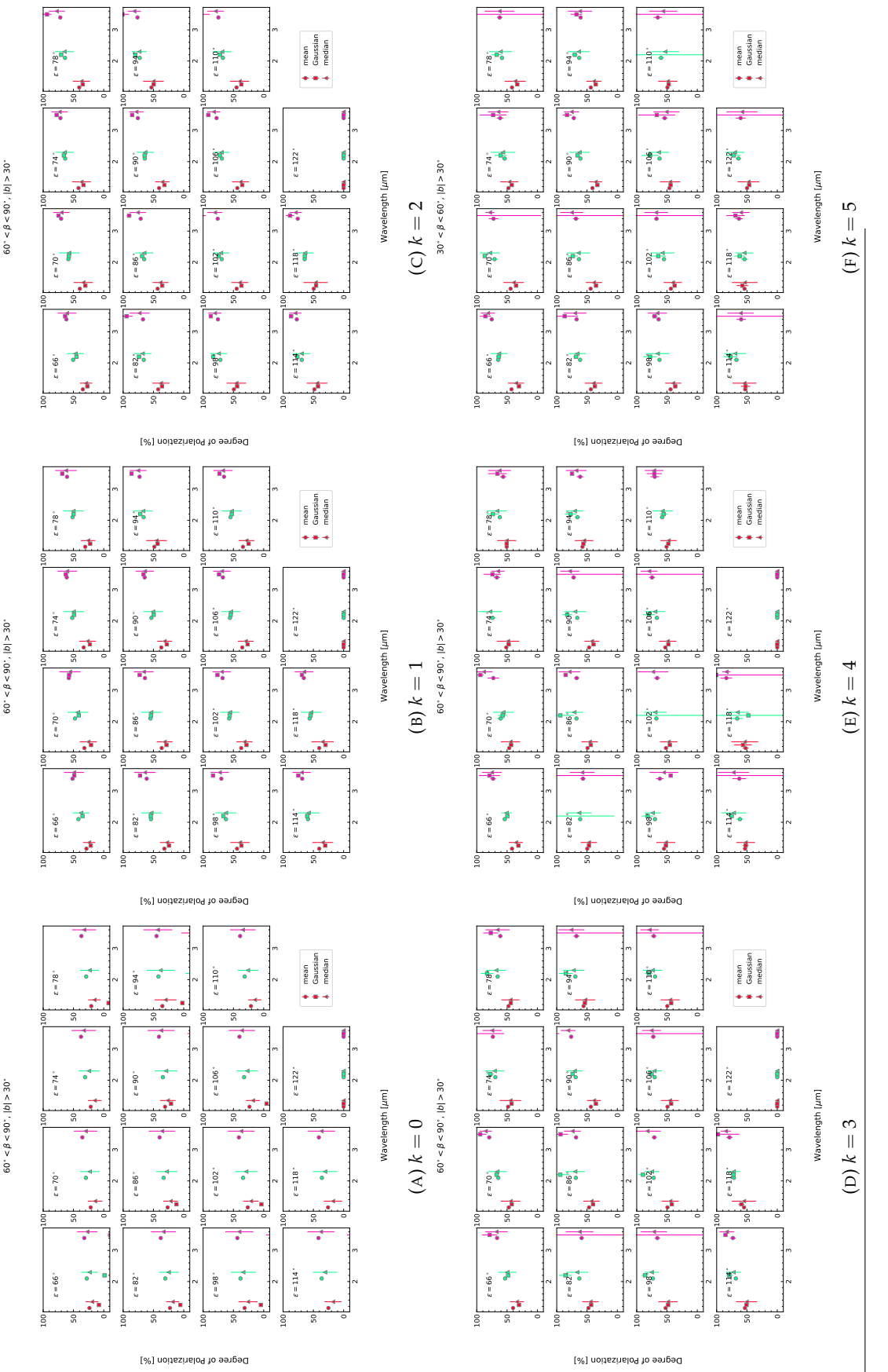

FIGURE D.57: The wavelength dependence of $P_{\lambda,\,\mathrm{ZL}}$ summed over Region 7, 8, and 9 under the condition that $P_{\lambda,\,\mathrm{ZL}}/\sigma_P > k$.

D.6 THE SOLAR ELONGATION DEPENDENCE AND THE ECLIPTIC LATITUDE DEPENDENCE OF $P_{\lambda,\,\mathrm{ZL}}$ UNDER THE CONDITION THAT $P_{\lambda,\,\mathrm{ZL}}/\sigma_P > k$

(Figure D.58, D.59, and D.60)

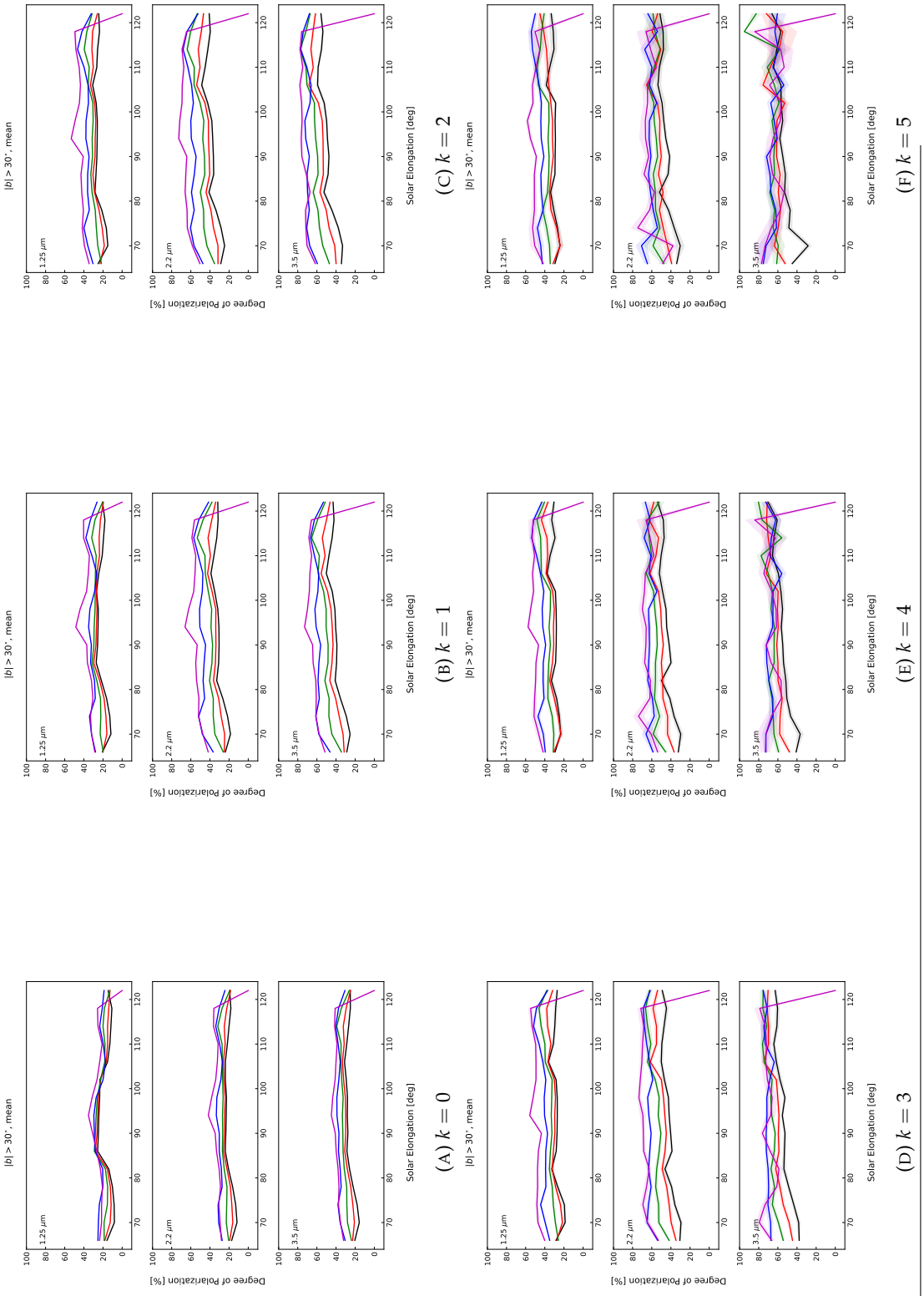

FIGURE D.58: The solar elongation dependence and the ecliptic latitude dependence of $P_{\lambda,\,\mathrm{ZL}}$ in each Region and each solar elongation when the representative value is taken as the mean value under the condition that $P_{\lambda,\,\mathrm{ZL}}/\sigma_P > k$ The shaded regions indicate the standard error relative to the mean.

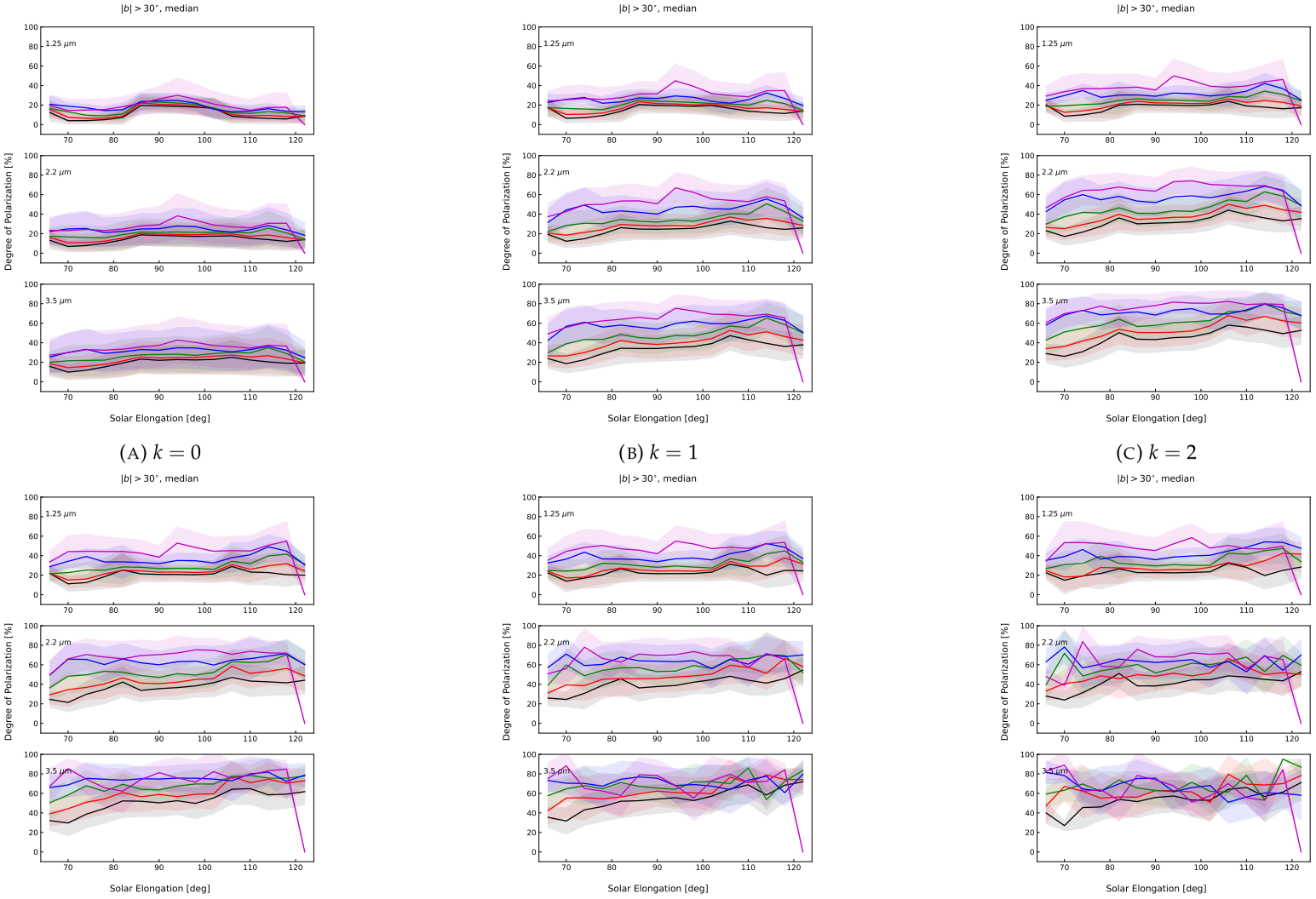

(A) $k = 0$ (B) $k = 1$ (C) $k = 2$

(D) $k = 3$ (E) $k = 4$ (F) $k = 5$

FIGURE D.59: The solar elongation dependence and the ecliptic latitude dependence of $P_{\lambda,\,\mathrm{ZL}}$ in each Region and each solar elongation when the representative value is taken as the median value under the condition that $P_{\lambda,\,\mathrm{ZL}}/\sigma_P > k$. The shaded regions indicate Quartile deviation relative to the median.

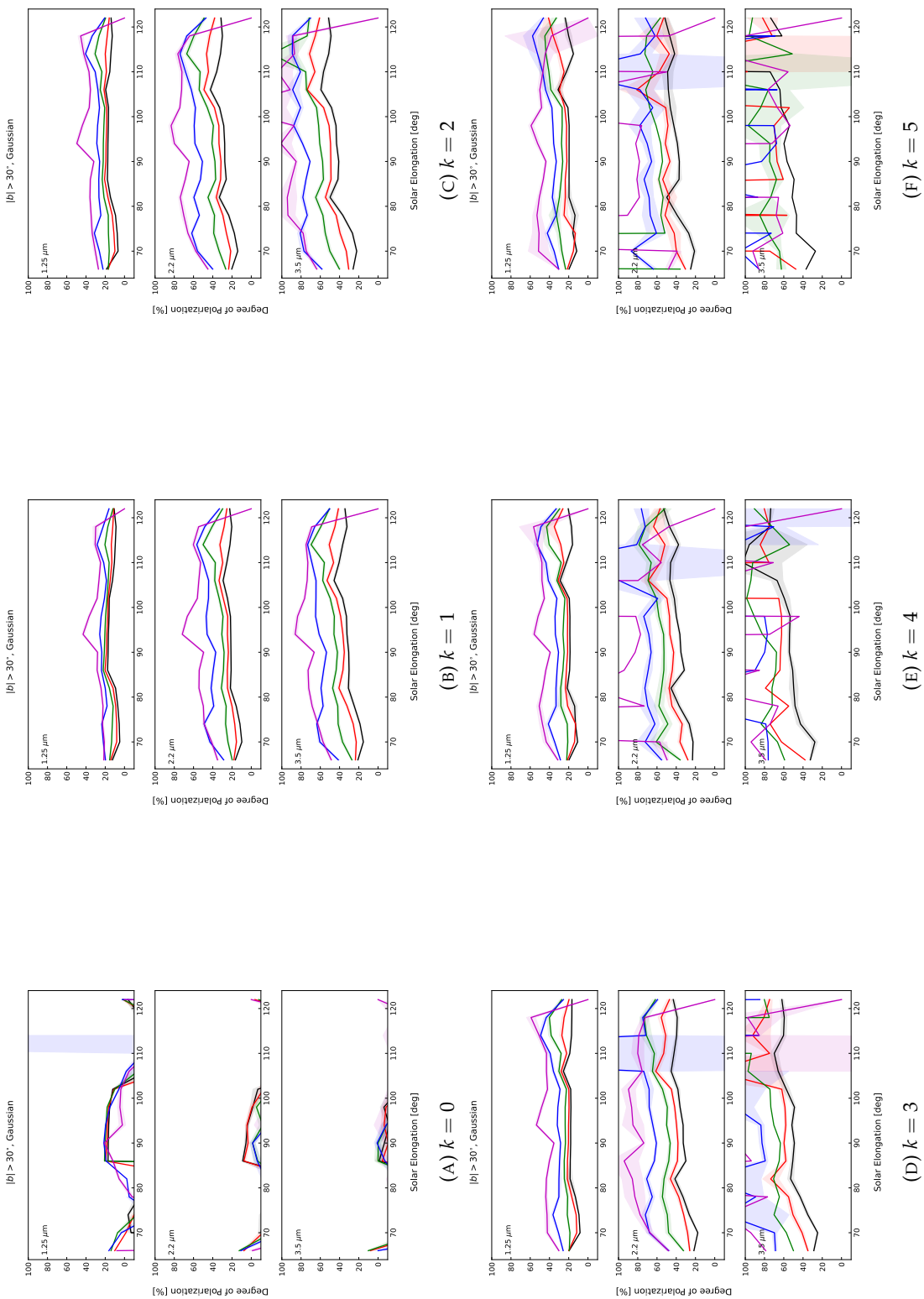

FIGURE D.60: The solar elongation dependence and the ecliptic latitude dependence of $P_{\lambda,\,\mathrm{ZL}}$ in each Region and each solar elongation when the representative value is taken as the central value obtained by Gaussian fitting under the condition that $P_{\lambda,\,\mathrm{ZL}}/\sigma_P > k$. The shaded regions indicate the standard error relative to the central value obtained by Gaussian fitting.

Bibliography

Arai, Toshiaki et al. (2015). "Measurements of the mean diffuse galactic light spectrum in the 0.95–1.65 μm band from CIBER". In: *The Astrophysical Journal* 806.1, p. 69.

Arendt, R. G. et al. (Nov. 1998). "The COBE Diffuse Infrared Background Experiment Search for the Cosmic Infrared Background. III. Separation of Galactic Emission from the Infrared Sky Brightness". In: 508, pp. 74–105. DOI: 10.1086/306381. eprint: astro-ph/9805323.

Berriman, G. B. et al. (Aug. 1994). "COBE DIRBE near-infrared polarimetry of the zodiacal light: Initial results". In: 431, pp. L63–L66. DOI: 10.1086/187473.

Bock, J. et al. (Aug. 2013). "The Cosmic Infrared Background Experiment (CIBER): The Wide-field Imagers". In: 207, 32, p. 32. DOI: 10.1088/0067-0049/207/2/32. arXiv: 1206.4702 [astro-ph.IM].

Bohren, C. F. and D. R. Huffman (1983). *Absorption and scattering of light by small particles*.

Burns, Joseph A, Philippe L Lamy, and Steven Soter (1979). "Radiation forces on small particles in the solar system". In: *Icarus* 40.1, pp. 1–48.

Cambrésy, L. et al. (July 2001). "The Cosmic Infrared Background at 1.25 and 2.2 Microns Using DIRBE and 2MASS: A Contribution Not Due to Galaxies?" In: 555, pp. 563–571. DOI: 10.1086/321470. eprint: astro-ph/0103078.

Cassini, Giovanni Domenico (1685). "Découverte de la lumière celeste qui paroist dans le zodiaque". In: *Découverte de la lumière celeste qui paroist dans le zodiaque*.

Caulet, A, RN Hook, and RAE Fosbury (1994). "Measurements of the sky background using the HST Faint Object Camera." In: *Astronomy and Astrophysics Supplement Series* 108, pp. 271–278.

COBE/DIRBE Collaboration (1998). "COBE Diffuse Infrared Background Experiment (DIRBE) Explanatory Supplement". In: v2.3.

Desert, F-X, F Boulanger, and J-L Puget (1990). "Interstellar dust models for extinction and emission". In: *Astronomy and Astrophysics* 237, pp. 215–236.

Désert, F-X et al. (1996). "Limits on the far infrared CIBR from DIRBE, FIRAS and HI surveys". In: *AIP Conference Proceedings*. Vol. 348. 1. American Institute of Physics, pp. 96–104.

Dorschner, J et al. (1995). "Steps toward interstellar silicate mineralogy. II. Study of Mg-Fe-silicate glasses of variable composition." In: *Astronomy and Astrophysics* 300, p. 503.

Draine, BT and Hyung Mok Lee (1984). "Optical properties of interstellar graphite and silicate grains". In: *The Astrophysical Journal* 285, pp. 89–108.

Duprat, Jean et al. (2010). "Extreme deuterium excesses in ultracarbonaceous micrometeorites from central Antarctic snow". In: *Science* 328.5979, pp. 742–745.

Fernández, Y. R. et al. (Sept. 2006). "Comet 162P/Siding Spring: A Surprisingly Large Nucleus". In: 132, pp. 1354–1360. DOI: 10.1086/506252. eprint: astro-ph/0608387.

Flynn, George J., Larry R. Nittler, and Cécile Engrand (June 2016). "Composition of Cosmic Dust: Sources and Implications for the Early Solar System". In: *Elements*

12.3, pp. 177–183. ISSN: 1811-5209. DOI: 10.2113/gselements.12.3.177. eprint: https://pubs.geoscienceworld.org/msa/elements/article-pdf/12/3/177/3111545/177_ELEM_v12n3.pdf. URL: https://doi.org/10.2113/gselements.12.3.177.

Giese, RH, B Kneissel, and U Rittich (1986). "Three-dimensional models of the zodiacal dust cloud: a comparative study". In: *Icarus* 68.3, pp. 395–411.

Giese, RH et al. (1978). "Large fluffy particles-A possible explanation of the optical properties of interplanetary dust". In: *Astronomy and Astrophysics* 65, pp. 265–272.

Girardi, L. et al. (June 2005). "Star counts in the Galaxy. Simulating from very deep to very shallow photometric surveys with the TRILEGAL code". In: 436, pp. 895–915. DOI: 10.1051/0004-6361:20042352. eprint: astro-ph/0504047.

Gondhalekar, PM (1990). "The ultraviolet starlight in the Galaxy". In: *Symposium-International Astronomical Union*. Vol. 139. Cambridge University Press, pp. 49–62.

Grun, E. et al. (May 1985). "Collisional balance of the meteoritic complex". In: 62, pp. 244–272. DOI: 10.1016/0019-1035(85)90121-6.

Hadamcik, E. et al. (2020). "Analogues of interplanetary dust particles to interpret the zodiacal light polarization". In: *Planetary and Space Science* 183. Special issue on Cosmic Dust X, p. 104527. ISSN: 0032-0633. DOI: https://doi.org/10.1016/j.pss.2018.04.022. URL: https://www.sciencedirect.com/science/article/pii/S0032063317304968.

Haikala, Lauri K et al. (1995). "Discovery and imaging of a Galactic cirrus cloud with the far ultraviolet space telescope". In: *The Astrophysical Journal* 443, pp. L33–L36.

Hanner, M. S. (Oct. 1999). "The Silicate Material in Comets". In: 90, pp. 99–108. DOI: 10.1023/A:1005285711945.

Hashimoto, J. et al. (June 2007). "Near-Infrared Polarization Images of the Orion Molecular Cloud 1 South Region". In: 59, pp. 481–486. DOI: 10.1093/pasj/59.3.481. eprint: astro-ph/0612519.

Heaney, James B et al. (1986). "The cyro-testing of infrared filters and beamsplitters for the Cosmic Background Explorer's instruments". In: *Cryogenic optical systems and instruments II*. Vol. 619. International Society for Optics and Photonics, pp. 142–147.

Heiles, C. (Feb. 2000). "9286 Stars: An Agglomeration of Stellar Polarization Catalogs". In: 119, pp. 923–927. DOI: 10.1086/301236. eprint: astro-ph/9910303.

Hirabayashi, M. et al. (2021). "Hayabusa2 extended mission: New voyage to rendezvous with a small asteroid rotating with a short period". In: *Advances in Space Research* 68.3, pp. 1533–1555. ISSN: 0273-1177. DOI: https://doi.org/10.1016/j.asr.2021.03.030. URL: https://www.sciencedirect.com/science/article/pii/S0273117721002556.

Jenniskens, Peter and Petrus Matheus Marie Jenniskens (2006). *Meteor showers and their parent comets*. Cambridge University Press.

Kelley, M. S. et al. (Apr. 2004). "Near-Infrared Polarimetry and Photometry of Recent Comets". In: 127, pp. 2398–2405. DOI: 10.1086/382240.

Kelsall, T. et al. (Nov. 1998). "The COBE Diffuse Infrared Background Experiment Search for the Cosmic Infrared Background. II. Model of the Interplanetary Dust Cloud". In: 508, pp. 44–73. DOI: 10.1086/306380. eprint: astro-ph/9806250.

Kimura, Hiroshi et al. (2016). "Light Scattering and Thermal Emission by Primitive Dust Particles in Planetary Systems". In: *Light Scattering Reviews, Volume 11*. Springer, pp. 363–418.

Korngut, P. M. et al. (Aug. 2013). "The Cosmic Infrared Background Experiment (CIBER): The Narrow-Band Spectrometer". In: 207, 34, p. 34. DOI: 10.1088/0067-0049/207/2/34. arXiv: 1307.0016 [astro-ph.CO].

Koschny, Detlef et al. (2019). "Interplanetary dust, meteoroids, meteors and meteorites". In: *Space science reviews* 215.4, pp. 1–62.

Lasue, J. et al. (Jan. 2009). "Cometary dust properties retrieved from polarization observations: Application to C/1995 O1 Hale Bopp and 1P/Halley". In: 199, pp. 129–144. DOI: 10.1016/j.icarus.2008.09.008.

Lasue, Jérémie et al. (2007). "Inferring the interplanetary dust properties-from remote observations and simulations". In: *Astronomy & Astrophysics* 473.2, pp. 641–649.

Leinert, C. and B. Blanck (Jan. 1982). "Stability and Symmetry of Zodiacal Light Polarization in the Antisolar Hemisphere". In: 105, p. 364.

Leinert, C. et al. (Jan. 1998). "The 1997 reference of diffuse night sky brightness". In: 127, pp. 1–99. DOI: 10.1051/aas:1998105.

Leinert, Ch et al. (1980). "The plane of symmetry of interplanetary dust in the inner solar system". In: *Astronomy and Astrophysics* 82, pp. 328–336.

Leinert, Christoph (1975). "Zodiacal light—a measure of the interplanetary environment". In: *Space Science Reviews* 18.3, pp. 281–339.

Leinert, Christoph and Eberhard Grün (1990). "Interplanetary dust". In: *Physics of the inner heliosphere I*. Springer, pp. 207–275.

Levasseur-Regourd, A. C. (1996). "Optical and Thermal Properties of Zodiacal Dust". In: *IAU Colloq. 150: Physics, Chemistry, and Dynamics of Interplanetary Dust*. Ed. by B. A. S. Gustafson and M. S. Hanner. Vol. 104. Astronomical Society of the Pacific Conference Series, p. 301.

Levasseur-Regourd, A. C. and R. Dumont (Apr. 1980). "Absolute photometry of zodiacal light". In: 84, pp. 277–279.

Magner, Thomas J (1987). "Diffuse Infrared Background Experiment (DIRBE) optics module breadboard alignment methods and results". In: *Optical Engineering* 26.3, p. 263264.

Matsumoto, T. et al. (Oct. 1996). "IRTS Observation of the Near-Infrared Spectrum of the Zodiacal Light". In: 48, pp. L47–L51.

Matsuura, Shuji et al. (2017). "New spectral evidence of an unaccounted component of the near-infrared extragalactic background light from the CIBER". In: *The Astrophysical Journal* 839.1, p. 7.

Mattila, K (1979). "Optical extinction and surface brightness observations of the dark nebulae LYNDS 134 and LYNDS 1778/1780". In: *Astronomy and Astrophysics* 78, pp. 253–263.

— (1980). "Synthetic spectrum of the integrated starlight between 3,000 and 10,000 A. I-Method of calculation and results". In: *Astronomy and Astrophysics Supplement Series* 39, pp. 53–65.

— (1990). "Observations of the extragalactic background light". In: *Symposium-International Astronomical Union*. Vol. 139. Cambridge University Press, pp. 257–268.

Nagata, T. et al. (1987). "Polarization Mapping of Infrared Reflection Nebulae". In: *Star Forming Regions*. Ed. by M. Peimbert and J. Jugaku. Vol. 115. IAU Symposium, p. 374.

Nesvorný, D. et al. (Apr. 2010). "Cometary Origin of the Zodiacal Cloud and Carbonaceous Micrometeorites. Implications for Hot Debris Disks". In: 713, pp. 816–836. DOI: 10.1088/0004-637X/713/2/816. arXiv: 0909.4322 [astro-ph.EP].

Nesvorný, David et al. (2011). "DYNAMICAL MODEL FOR THE ZODIACAL CLOUD AND SPORADIC METEORS". In: *The Astrophysical Journal* 743.2, p. 129. DOI:

10.1088/0004-637x/743/2/129. URL: https://doi.org/10.1088/0004-637x/743/2/129.

Ootsubo, T. et al. (June 1998). "IRTS observation of the mid-infrared spectrum of the zodiacal emission". In: *Earth, Planets, and Space* 50, pp. 507–511.

Ootsubo, T. et al. (Dec. 2009). "Mid-Infrared Spectrum of the Zodiacal Light Observed with AKARI/IRC". In: *AKARI, a Light to Illuminate the Misty Universe*. Ed. by T. Onaka et al. Vol. 418. Astronomical Society of the Pacific Conference Series, p. 395.

Pitz, E. et al. (Apr. 1979). "Colour and polarization of the zodiacal light from the ultraviolet to the near infrared". In: 74, pp. 15–20.

Reach, W. T. et al. (Aug. 2003). "The mid-infrared spectrum of the zodiacal and exozodiacal light". In: 164, pp. 384–403. DOI: 10.1016/S0019-1035(03)00133-7. eprint: astro-ph/0304289.

Reach, William T (1988). "Zodiacal emission. I-Dust near the earth's orbit". In: *The Astrophysical Journal* 335, pp. 468–485.

Rowan-Robinson, Michael and Brian May (2013). "An improved model for the infrared emission from the zodiacal dust cloud: cometary, asteroidal and interstellar dust". In: *Monthly Notices of the Royal Astronomical Society* 429.4, pp. 2894–2902.

Serkowski, K. (1973). "Interstellar Polarization (review)". In: *Interstellar Dust and Related Topics*. Ed. by J. M. Greenberg and H. C. van de Hulst. Vol. 52. IAU Symposium, p. 145.

Skrutskie, M. F. et al. (Feb. 2006). "The Two Micron All Sky Survey (2MASS)". In: 131, pp. 1163–1183. DOI: 10.1086/498708.

Soderblom, L. A. et al. (May 2002). "Observations of Comet 19P/Borrelly by the Miniature Integrated Camera and Spectrometer Aboard Deep Space 1". In: *Science* 296, pp. 1087–1091. DOI: 10.1126/science.1069527.

Srama, Ralf et al. (2011). "The cosmic dust analyser onboard cassini: ten years of discoveries". In: *CEAS Space Journal* 2.1, pp. 3–16.

Takimoto, Kohji et al. (2020). "Pre-flight optical test and calibration for the Cosmic Infrared Background ExpeRiment 2 (CIBER-2)". In: *Space Telescopes and Instrumentation 2020: Optical, Infrared, and Millimeter Wave*. Ed. by Makenzie Lystrup et al. Vol. 11443. International Society for Optics and Photonics. SPIE, pp. 861 –873. URL: https://doi.org/10.1117/12.2561917.

Tsumura, K. et al. (Aug. 2010). "Observations of the Near-infrared Spectrum of the Zodiacal Light with CIBER". In: 719, pp. 394–402. DOI: 10.1088/0004-637X/719/1/394. arXiv: 1004.5445 [astro-ph.EP].

Tsumura, K. et al. (Aug. 2013). "The Cosmic Infrared Background Experiment (CIBER): The Low Resolution Spectrometer". In: 207, 33, p. 33. DOI: 10.1088/0067-0049/207/2/33. arXiv: 1112.4217 [astro-ph.IM].

Tsumura, Kohji et al. (Dec. 2013a). "Low-Resolution Spectrum of the Diffuse Galactic Light and 3.3m PAH Emission with the AKARI InfraRed Camera". In: *Publications of the Astronomical Society of Japan* 65.6. 120. ISSN: 0004-6264. DOI: 10.1093/pasj/65.6.120. eprint: https://academic.oup.com/pasj/article-pdf/65/6/120/6030918/pasj65-0120.pdf. URL: https://doi.org/10.1093/pasj/65.6.120.

Tsumura, Kohji et al. (Dec. 2013b). "Low-Resolution Spectrum of the Extragalactic Background Light with the AKARI InfraRed Camera". In: *Publications of the Astronomical Society of Japan* 65.6. 121. ISSN: 0004-6264. DOI: 10.1093/pasj/65.6.121. eprint: https://academic.oup.com/pasj/article-pdf/65/6/121/19691709/pasj65-0121.pdf. URL: https://doi.org/10.1093/pasj/65.6.121.

Weinberg, J. L. and R. C. Hahn (1980). "Brightness and polarization of the zodiacal light - Results of fixed-position observations from SKYLAB". In: *Solid Particles in the Solar System*. Ed. by I. Halliday and B. A. McIntosh. Vol. 90. IAU Symposium, pp. 19–22.

Wooden, Diane H et al. (1999). "Silicate mineralogy of the dust in the inner coma of comet C/1995 01 (Hale-Bopp) pre-and postperihelion". In: *The Astrophysical Journal* 517.2, p. 1034.

Wooden, Diane H et al. (2000). "Mg-rich silicate crystals in Comet Hale–Bopp: ISM relics or solar nebula condensates?" In: *Icarus* 143.1, pp. 126–137.

Wright, E. L. (Mar. 1998). "Angular Power Spectra of the COBE DIRBE Maps". In: 496, p. 1. DOI: 10.1086/305345. eprint: astro-ph/9711261.

Wright, Edward L (1998). "Angular power spectra of the COBE DIRBE maps". In: *The Astrophysical Journal* 496.1, p. 1.

Wyatt, Stanley P and Fred L Whipple (1950). "The Poynting-Robertson effect on meteor orbits". In: *The Astrophysical Journal* 111, pp. 134–141.

Yang, Hongu and Masateru Ishiguro (2015). "ORIGIN OF INTERPLANETARY DUST THROUGH OPTICAL PROPERTIES OF ZODIACAL LIGHT". In: *The Astrophysical Journal* 813.2, p. 87. DOI: 10.1088/0004-637x/813/2/87. URL: https://doi.org/10.1088/0004-637x/813/2/87.

Zemcov, M. et al. (Aug. 2013). "The Cosmic Infrared Background Experiment (CIBER): A Sounding Rocket Payload to Study the near Infrared Extragalactic Background Light". In: 207, 31, p. 31. DOI: 10.1088/0067-0049/207/2/31. arXiv: 1112.1424 [astro-ph.IM].

Zubko, Evgenij et al. (2014). "Dust in comet C/1975 V1 (West)". In: *Monthly Notices of the Royal Astronomical Society* 440.4, pp. 2928–2943.